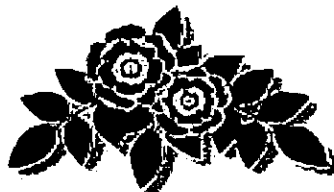


UNIVERSITY
OF CENTRAL
LANCASHIRE



**DEVELOPMENT OF AN EQCM-BASED
SENSOR FOR METAL IONS**

By

STEPHEN SHACKLEFORD

Being a thesis submitted to the University of Central
Lancashire in partial fulfillment for the requirements for the
degree of

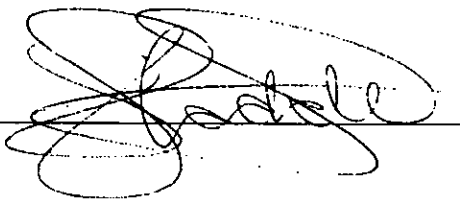
DOCTOR OF PHILOSOPHY

2002

The work presented in this thesis was carried out in the
Centre for Material Science, University of Central Lancashire,
Preston, Lancashire. PR1 2HE

DECLARATION

The work described in this thesis was conducted at the Centre for Materials Science, University of Central Lancashire and placement at BNFL Springfields, Salwick, Preston between October 1998 and December 2001. Unless otherwise stated, it is the work of the author and has been submitted in support of any other degree.

Signature: 

Stephen Shackleford

December 2002

ABSTRACT

A series of fundamental studies are presented of the components of a prototypical electrochemical quartz crystal microbalance (EQCM)-based sensor for metal ions. Designed for use in the nuclear industry, the sensor consists of a **gold (Au) piezoelectrode** modified by a **Nafion[®] polymer layer** impregnated with a cationic **hydroxamic acid (HA)**, a ligand showing oxidation state specific selectivity towards actinide 4+ ions and a non-radioactive **demonstrator ion, Fe³⁺**. In its final configuration, the polymer layer will also contain a **redox mediator**, methylene blue (MB), to facilitate electrochemical conditioning of the analyte. The following results have been obtained from EQCM and microelectrode voltammetry studies of each of the component parts.

The Gold Piezoelectrode – The dissolution and redeposition processes of Au in HNO₃ solution at pH 1 & 0 were investigated as a function of sweep rate (v). At pH 1 and $v \leq 10 \text{ mV s}^{-1}$, Au dissolves through a $3e^-$ oxidation at $E > +1.00 \text{ V (vs. SCE)}$, a process that, at $v \geq 10 \text{ mV s}^{-1}$, is kinetically hindered with respect to under potential deposition (UPD) of OH surface sublattices and subsequent 2-D-phase oxide formation. The inhibition arises from a closed packed layer of nitrate ions at the gold surface, although the layer is disrupted and the inhibition removed by the gold dissolution and reprecipitation processes that occur during potential cycling at low v .

The Hydroxamic Acid Ligand – Study of the oxidation of acetohydroxamic acid (AHA) in nitric acid revealed that three processes occur at Au electrodes at potentials in the vicinity of AHA oxidation at pH 0 & 1: (a) oxidation of the Au surface; (b) oxidation of the AHA; (c) complexation of the AHA with electrogenerated Au³⁺. The last process inhibits oxide formation and associated electrode passivation, so promoting the occurrence of the first two. The two current peaks associated with AHA oxidation show no associated mass change, indicating that AHA oxidation is controlled by semi-infinite

diffusion. The waves correspond to 1 and 2 electron processes with current onsets of +0.55 V and \sim +0.80 V (vs. SCE) respectively. Oxidation of AHA appears to be irreversible and blocked at electrodes with minimal microscopic roughness by close packing of nitrate ions at the surface.

The Polymer Layer and the Demonstrator Ion, Fe³⁺ – Microelectrogravimetric studies of the Fe^{2+/3+} couple were conducted at bare Au, Nafion[®] modified Au and Nafion[®] modified Au impregnated with the hydrophobic cationic HA ligand, desferrioximine (DFA⁺) electrode. In background nitric acid (pH 1 & 0), the electrochemistry of Nafion[®] layer partitioned Fe^{2+/3+} ions exhibits thin layer cell behaviour with the polymer layer increasing in mass during reduction of Fe(III) due to an influx of highly hydrated H⁺ ions necessary to maintain electroneutrality. Studies on Nafion[®] layers impregnated with DFA⁺ and Fe³⁺ show that while Fe³⁺ complexes with DFA⁺, Fe²⁺ does not and that, upon reduction of the complexed ferric ion, the resultant Fe(II)-DFA⁺ complex dissociates suggesting that electrochemical expulsion of the analyte is possible.

The Redox Mediator – At pH 7.9, the reduction of methylene blue (MB) to leucomethylene blue (LMB), occurs in two steps: (i) a reversible net 1.5 e⁻ transfer to form a solid charge transfer complex (LMB/LMB^{•+}) (ii) an irreversible reduction of LMB/LMB^{•+} to LMB, the onset of which can be directly observed as an inflection in the voltammogram, the first time that this has been reported. The reversibility of the MB to LMB reduction within the context of charge transfer complex electrogeneration suggests that MB may be a suitable mediator for actinide cation reduction within the polymer layer of the proposed sensor. It is known that the pender amino-groups of LMB are protonated below pH 1, so rendering the resultant LMBH₂²⁺ soluble in aqueous solution. This means (a) difficulties associated with the irreversible reoxidation of the solid LMB generated at pH 7.9 will be obviated at pH 1; and (b) being a large cation, we could expect LMBH₂²⁺ to be retained within the Nafion[®] layer.

CONTENTS

TITLE PAGE

Page i

DECLARATION

Page ii

ABSTRACT

Page iii

CONTENTS

Page v

ACKNOWLEDGEMENTS

Page viii

GLOSSARY OF TERMS

MAJOR SYMBOLS

Page ix

STANDARD ABBREVIATIONS

Page xii

**CHAPTER I - INTRODUCTION TO THE ELECTROCHEMICAL
QUARTZ CRYSTAL MICROBALANCE**

CONTENTS

Page 1

CHAPTER II - EXPERIMENTAL ASPECTS

CONTENTS

Page 82

CHAPTER III - GOLD OXIDATION & DISSOLUTION PROCESSES

CONTENTS

Page 102

**CHAPTER IV - ACETOHYDROXAMIC ACID OXIDATION
PROCESSES**

CONTENTS

Page 153

**CHAPTER V - THE ELECTROCHEMICAL BEHAVIOUR OF IRON
(II/III) ON AHA IMPREGNATED NAFION® COATED
ELECTRODES**

CONTENTS

Page 187

**CHAPTER VI - ELECTROCHEMICAL AND MICROELECTRO-
GRAVIMETRIC STUDIES OF METHYLENE
BLUE**

CONTENTS

Page 247

CHAPTER VII - CONCLUSIONS AND FURTHER WORK

CONTENTS

Page 278

APPENDICES

CONTENTS

Page 285

ACKNOWLEDGEMENTS

I would like to gratefully thank my Director of Studies Dr. C. Boxall for his help, guidance and encouragement throughout the term of study of this project. I would also like to thank him for his understanding of everything I could not quite grasp, but more importantly for his general support for my well being during the whole of the project.

I also wish to thank Dr. R. Taylor, Dr. G. Garnham & Dr. S.N. Port my industrial supervisors for their help and support.

I would also like to thank EPSRC for the case award and BNFL for the industrial sponsorship.

Through out this period of study I would like to whole-heartedly thank my wife who has been steady in her support, encouragement and patience. To this end I would also like to acknowledge that in part she owns the work that I have undertaken here.

Finally, to my children I thank for their understanding during this time and their persistence in ensuring that they got their moments during every day. To my boys I hope that I have at very least been pleasant at all times.

To

Beverley, Benedict & Luke

GLOSSARY OF TERMS

MAJOR SYMBOLS

ROMAN SYMBOLS

Symbol	Meaning	Dimensions	Section
<i>A</i>	Piezoelectric active area	m^2	<i>I.3</i>
<i>a</i>	Radius microdisc electrode	μm	<i>I.Appendix</i>
a_{min}	Radius of smallest electrode	μm	<i>I.Appendix</i>
<i>ads</i>	Adsorption	None	<i>1.7.1.1</i>
<i>c_f</i>	Differential sensitivity constant	$g Hz^{-1}$	<i>I.3</i>
<i>C_f</i>	Integral sensitivity constant	$g Hz^{-1} m^2$	<i>I.3</i>
<i>D₀</i>	Diffusion Coefficient	$m^2 s^{-1}$	<i>I.Appendix</i>
<i>E</i>	Potential	Volts	<i>II.3</i>
<i>E^θ</i>	Standard redox potential	Volts	<i>II.1</i>
<i>E_p</i>	Anodic peak potential.	Volts	<i>IV.4.1</i>
<i>E_r</i>	Constant reference potential	Volts	<i>IV.1.1</i>
<i>E_{1/2}</i>	Measured half-wave potential	Volts	<i>IV.1.1</i>
<i>E_{1/4}</i>	Measured potential where $i/i_d = 1/4$	Volts	<i>IV.1.1</i>
<i>E_{3/4}</i>	Measured potential where $i/i_d = 3/4$	Volts	<i>IV.1.1</i>
$(E_{3/4} - E_{1/4})$	Tomês potential	Volts	<i>IV.1.1</i>
<i>f₀</i>	Resonant frequency	Hz	<i>I.2.1</i>
Δf	Resonant frequency change	Hz	<i>I.3</i>
<i>F</i>	Faradays' constant	$96484.6 C mol^{-1}$	<i>II.4.2</i>

Hz	Hertz	s ⁻¹	1.2.1
i_p	Current peak	Amps	III.1
i	Current	Amps	
i_d	Current due to diffusive flux	Amps	
k_1	Propogation constant	None	1.4.1
k^θ	Standard electrochemical rate constant	ms ⁻¹	II.1
k^o	Standard heterogeneous rate constant	ms ⁻¹	I.Appendix
Δm	Mass change	g or kg	1.3
M_w	Molecular weight	g or kg	II.4.2
n	Total number of moles undertaking reaction	mol m ⁻³	1.7.1.1
Q	Charge	C	1.4.7
r	Distance coordinate	m	1.3
dr	Change in the distance coordinate	m	1.3
r	Radius	m	1.4.7
S	Sensitivity of crystal	g Hz ⁻¹	1.3
S_{ex}	Mass sensitivity	g Hz ⁻¹ m ²	II.5.2
T	Absolute Temperature	Kelvin	1.2.2
t_q	Thickness of crystal	m	1.2.2
Δt	Change of crystal thickness (also expressed as an areal area)	m	1.2.2
t	Time	s	1.4.1
v_{tr}	Transverse velocity of sound	3.34×10 ⁴ ms ⁻¹	1.2.2
z	Distance from crystal surface	m	1.4.1
z_i	Number of electrons per molecule oxidized or reduced; faradays per mole of substance electrolyzed	None	II.5.2

GREEK SYMBOLS

Symbol	Meaning	Dimensions	Section
α	Transfer coefficient	None	<i>II.1</i>
δ	Charge transfer	None	<i>1.7.1</i>
ϕ	Angle coordinates	Radians	<i>1.3</i>
γ	Partial charge of a species	None	<i>1.7.1</i>
η_f	Film viscosity	$\text{Kgm}^{-1}\text{s}^{-1}$	<i>1.4.2</i>
η_L	Liquid viscosity	$\text{Kgm}^{-1}\text{s}^{-1}$	<i>1.4.1</i>
κ^0	Dimensionless electrochemical rate constant	None	<i>I.Appendix</i>
v_0	Velocity of crystal	m s^{-1}	<i>1.4.1</i>
ν	Cyclic voltammetric scan rate	V s^{-1}	<i>III.1.1</i>
μ_f	Elasticity of a polymer film		<i>1.4.2</i>
μ_q	Shear modules of quartz crystal	$2.947 \times 10^{-9} \text{ kg}$ $\text{m}^{-1}\text{s}^{-2}$	<i>1.2.2</i>
ρ_f	Density of a film	k gm^{-3}	<i>1.4.2</i>
ρ_L	Density of a liquid	k gm^{-3}	<i>1.4.1</i>
ρ_q	Density of quartz	2.648 k gm^{-3}	<i>1.2.2</i>
ω_e	Cut off frequency of electrode plated regions	Hz	<i>1.3</i>
ω_q	Cut off frequency of unplated regions	Hz	<i>1.3</i>

STANDARD ABBREVIATIONS

<u>Abbreviation</u>	<u>Meaning</u>	<u>Section</u>
AHA	Acetohydroxamic acid	<i>I.0</i>
CME	Chemically modified electrodes	<i>I.11</i>
CV	Cyclic voltammetry	<i>I.4.7</i>
DFA ⁺	Desferrioxamine	<i>I.11</i>
DQCM	Dual quartz crystal microbalance	<i>I.6.2</i>
ECE	Electrochemical – chemical - electrochemical	<i>III.1</i>
EDTA	Ethylenediaminetetracetic acid	<i>V.1</i>
EE	Electrochemical - electrochemical	<i>III.1</i>
EQCM	Electrochemical quartz crystal microbalance	<i>I.0</i>
FTIRS	Fourier transform IR spectroscopy	<i>III.2.1</i>
GCE	Glassy carbon electrodes	<i>I.11</i>
GHA ⁺	Glycine hydroxamic acid	<i>I.11</i>
GPES	General purpose electrochemical system	<i>II.3</i>
HA	Monohydroxamic acids	<i>I.0</i>
HA/IEMAs	HA/ion exchange membrane assemblies	<i>V</i>
IR	Infra red spectroscopy	<i>I.9.2</i>
LMB	Leucomethylene blue	<i>III.1</i>
MB ⁺	Methylene blue	<i>III.1</i>
MS	Mass spectroscopy	<i>I.9.2</i>

NHE	Normal Hydrogen Electrode = SHE	<i>1.7.1.1</i>
NMR	Nuclear magnetic resonance	<i>1.9.2</i>
PDT	Photodynamic therapy	<i>III.1</i>
PTF	Polytetrafluoroethene	<i>II.4</i>
pzc	Point zero charge	<i>1.7.1.1</i>
QCM	Quartz crystal microbalance	<i>1.0</i>
RHE	Relative hydrogen electrode	<i>1.7.2</i>
RRDE	Rotating ring-disc electrode	<i>V.1</i>
RTO	Replacement turnover	<i>1.7.1.1</i>
SCE	Saturated calomel electrode	<i>1.7.1.2</i>
SERS	Surface-enhanced Raman Spectroscopy	<i>1.7.2</i>
SHE	Standard hydrogen electrode = NHE	
SIMs	Scanning tunneling microscope	<i>1.7.2</i>
SNIFTERS	Subtractively normalized interfacial Fourier transform IR spectroscopy	<i>III.2.1</i>
SSE	Silver/silver chloride electrode	<i>1.7.1.2</i>
UPD	Underpotential deposition	<i>III.2.1</i>
UV	Ultraviolet	<i>1.0</i>
XRD	X-ray defraction spectroscopy	<i>1.9.2</i>

CHAPTER I - INTRODUCTION TO THE ELECTROCHEMICAL QUARTZ CRYSTAL MICROBALANCE

CONTENT

<u>0 - AN ELECTROCHEMICAL BASED SENSOR FOR ACTINIDE IONS</u>	<i>Page 4</i>
<u>I.0 - INTRODUCTION AND PROJECT OBJECTIVES</u>	<i>Page 7</i>
<u>I.1 - PIEZOELECTRIC SENSORS</u>	<i>Page 9</i>
<u>I.2 - HISTORICAL PERSPECTIVE ON THE QCM</u>	<i>Page 10</i>
<i>I.2.1 - Piezoelectric Effect</i>	<i>Page 10</i>
<i>I.2.2 - Quartz Crystals</i>	<i>Page 11</i>
<u>I.3 - MASS FREQUENCY CORRELATIONS</u>	<i>Page 13</i>
<u>I.4 - EFFECTS OF VARIOUS PARAMETERS ON CRYSTAL OSCILLATIONS</u>	<i>Page 16</i>
<i>I.4.1 - Solution Effects</i>	<i>Page 16</i>
<i>I.4.2 - Viscoelastic Effects</i>	<i>Page 18</i>
<i>I.4.3 - High Mass Loadings</i>	<i>Page 19</i>
<i>I.4.4 - Surface Roughness</i>	<i>Page 19</i>

<i>1.4.5 - Surface Stress</i>	<i>Page 20</i>
<i>1.4.6 - Interfacial Slippage</i>	<i>Page 21</i>
<i>1.4.7 - Nonuniform Mass Distribution</i>	<i>Page 21</i>
<u>1.5 - ELECTROCHEMICAL QUARTZ CRYSTAL MICROBALANCE SENSORS</u>	<i>Page 23</i>
<u>1.6 - A HOLDER FOR THE ELECTROCHEMICAL QUARTZ CRYSTAL MICROBALANCE</u>	<i>Page 26</i>
<i>1.6.1 - Single Quartz Crystal</i>	<i>Page 26</i>
<i>1.6.2 - Dual Quartz Crystal Microbalance</i>	<i>Page 28</i>
<u>1.7 - GOLD ELECTROCHEMISTRY</u>	<i>Page 30</i>
<i>1.7.1 - Gold Oxidation</i>	<i>Page 30</i>
1.7.1.1 - Polarographic Gold Oxidation	<i>Page 32</i>
1.7.1.2 - Electrochemical Quartz Crystal Microbalance Studies of Gold Oxidation	<i>Page 43</i>
<i>1.7.2 - Gold Dissolution</i>	<i>Page 48</i>
<u>1.8 - NAFION[®] POLYMER FILMS</u>	<i>Page 52</i>
<u>1.9 - HYDROXAMIC ACIDS</u>	<i>Page 57</i>
<i>1.9.1 - Introduction</i>	<i>Page 57</i>
<i>1.9.2 - Structure of Hydroxamic Acids</i>	<i>Page 58</i>
<i>1.9.3 - Main Reactions</i>	<i>Page 58</i>
1.9.3.1 - Hydrolysis	<i>Page 58</i>

I.9.3.2 – Oxidation Reactions	<i>Page 60</i>
I.9.3.2.i – The Two Electron Process	<i>Page 65</i>
I.9.3.2.ii – The One Electron Process	<i>Page 67</i>
<u>I.10 - CO-ORDINATION CHEMISTRY OF IRON(III)</u>	<i>Page 69</i>
<u>I.11 - APPLICATIONS OF HYDROXAMIC ACIDS</u>	<i>Page 71</i>
<u>I.12 - REFERENCES</u>	<i>Page 73</i>

0 - AN ELECTROCHEMICAL BASED SENSOR FOR ACTINIDE IONS

The technological objective of this project was the development of an *Electrochemical Quartz Crystal Microbalance* (EQCM) based cation sensor specific to analytes that are of interest to the nuclear industry - specifically actinides metal ions. The purpose of such a sensor was to aid plant process control and determination for specific fission products.

The proposed sensor configuration and mode of operation is shown in *Figure 1.0*. It consists of a gold piezoelectrode modified with a polymer membrane. The membrane is impregnated with a ligand selective to the 4+ oxidation state of actinide (Ac) metal cations. The polymer layer will be engineered to be thin enough that electrochemical control of the complexed and uncomplexed actinides is possible in order that:

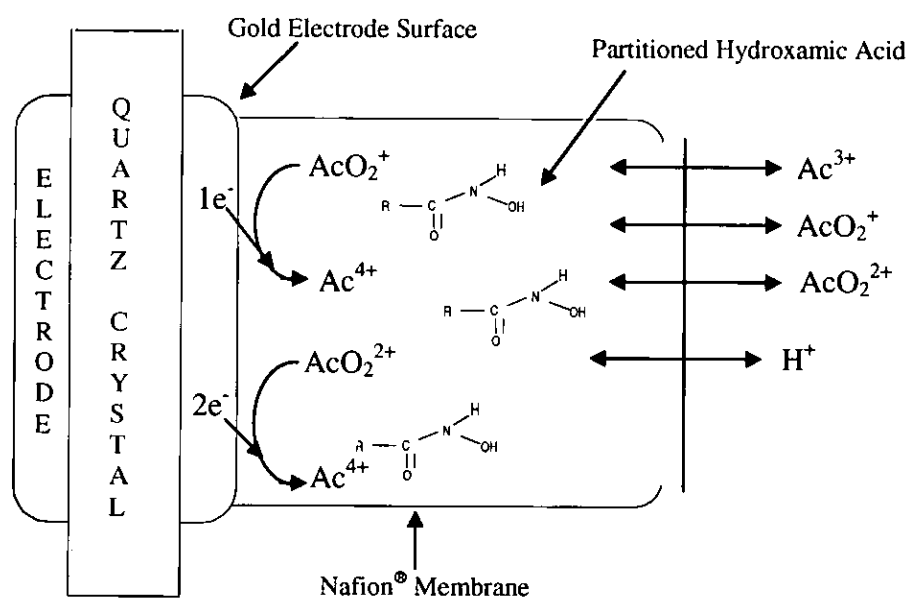


Figure 1.0: Representation of the Au piezoelectric electrode coated with a hydroxamic acid (whose simplified chemical structure is included) partitioned Nafion® polymer in contact with the nitric acid electrolyte. Analyte cations which may irreversibly oxidise the ligand, are reduced at the piezoelectrode surface to an oxidation state incapable of oxidising the ligand. In this way, the ligand is protected by the electrochemical conditioning of the polymer layer.

- (a) Ac(VI) and Ac(V) can be reduced to the Ac(IV). Complexation with the Ac^{4+} selective ligand will follow with an attendant mass change, so rendering possible indirect detection of actinides in higher oxidation states than 4+.
- (b) Electrochemical expulsion of the analyte. Once analysis has occurred, the metal ion of the Ac(IV)-ligand complex can be oxidized to the (V) or (VI) state or reduced to the (III) state. Neither of these forms a strong complex with the ligand and so the complex dissociates and the analyte is expelled.
- (c) Electrochemical protection of the ionophore ligand. The ligand chosen (see below) can be subject to irreversible oxidation by the higher oxidation state of some actinides - Pu^{4+} , PuO_2^+ , PuO_2^{2+} , NpO_2^+ and NpO_2^{2+} . Electrochemical reduction of these ions within the polymer layer would therefore protect the ligand against this and increase the lifetime of the sensor.

In order to facilitate electrochemical control of the environment within the polymer layer, and in recognition of the fact that the electrochemical kinetics of some actinide metal ions on gold are slow (leading to the imposition of large and undesirable overpotentials on certain Ac reduction processes). It is proposed to incorporate a redox mediator within the polymer layer, similar to the mediator concept employed in enzyme-based bioelectrochemical sensors.

So as to avoid the use of time-consuming safety-critical radiochemical techniques and active laboratories during the development of the sensor, initial work will be conducted on $\text{Fe}^{2+/3+}$ ions as a demonstrator system. Iron was chosen because the class of ligands to be used within the sensor exhibit oxidation state selectivity for Fe(III). Other components of the sensor are as follows.

Polymeric coatings with incorporated electroactive compounds are capable of modifying electrode surfaces, and a large area of research has been devoted to the study of such systems because of their potential as electrochemical sensors [1.1 & 1.2]. Of particular

utility to our ultimate sensor design are perfluorinated ion exchange polymer films that selectively preconcentrate hydrophobic ligands and ion selective chelating agents. Such films can enhance the electrochemical detection limit of the modified electrode compared to that of an uncoated electrode. Among the polymeric coatings that may serve such purposes, Nafion[®] is of special interest because of its high chemical stability, versatility and its ability to complex and retain organic cations. As a result of these features, Nafion[®] has been the subject of numerous investigations into the mechanisms of charge transport that occur for a range of redox couples incorporated into Nafion[®] as charge transport mediators.

Previous investigations of Nafion[®] coated electrodes have concentrated on hydrophobic redox-active cations such as ruthenium-bipyridine, cobalt-bipyridine and iron-phenanthroline complexes [1.3]. Consequently, there is ample evidence to demonstrate that Nafion[®] has an affinity for hydrophobic cations. We are interested in the interaction of Nafion[®] with the hydrophilic Fe²⁺/Fe³⁺ system [1.3, 1.4, 1.5, 1.6, 1.7 & 1.8] and the hydrophobic complexes iron yields with hydroxamic acids (HA) as a non-radioactive demonstrator system for analogous studies on actinide metal ions such as U⁴⁺, UO₂⁺, UO₂²⁺, Pu⁴⁺, PuO₂⁺, PuO₂²⁺, Np⁴⁺, NpO₂⁺ & NpO₂²⁺.

Hydroxamic ligands are useful reagents for the chemical analysis of metal ions. The preparation of chemically modified electrodes containing HA ligands for the purposes of electrochemical sensors has been proposed by several others [1.9, 1.10, 1.11, & 1.12]. The nature of HA as a strong chelator forming four or five membered chelates through the O-O or N-O type bond with ferrous, non-ferrous and rare earth metals make it an ideal ligand for the modification of electrode sensors.

1.0 - INTRODUCTION AND PROJECT OBJECTIVES

The last 15 – 20 years have seen electrochemists applying more sophisticated techniques to the study of electrode surfaces. These studies have provided detailed mechanistic information about film deposition and dissolution, surface morphology changes, and mass changes in thin films caused by redox or other chemical processes. This is due to the new availability of powerful tools for interfacial characterisation and because of an increase in electrochemical research on detailed determination of the structure and composition of the interface.

The *Quartz Crystal Microbalance* (QCM) represents a comprehensive method for the measurement of mass transfer process at the gas / solid and gas / liquid / solid interfaces. An extension of the QCM, the electrochemical quartz crystal microbalance (EQCM), was initially used in *ex situ* measurements of mass changes at electrode surfaces during electrodeposition of metals. Experimental studies into thin film formation on electrode surfaces required the use of an EQCM as an *in situ* mass sensor. This *in situ* technology has been developed so that the mass changes resulting from a range of processes involving thin films on electrode surfaces could be monitored in real time. We discuss these processes in considerable detail in later chapters.

The initial technological objective of this project was to develop a prototypical EQCM based sensor specific towards certain cationic actinide metal ions for the purposes of process control and the determination of isotope levels in effluent streams of interest to the nuclear industry. However, in the pursuit of that technological objective several scientific objectives needed to be addressed. These include, *inter alia*, a study of the oxidation dissolution of gold in a range of acid media, on investigation of the intrinsic electrochemistry of hydroxamic acids and an evaluation of the efficacy of various electrode coating and ligand preparation protocols.

Thus, the first section of this chapter gives an introduction to the principles of QCM and EQCM. The techniques are explained and a comprehensive overview of the work undertaken in this field to date is presented. Recent developments in QCM and EQCM construction will also be reviewed.

The second section of this chapter presents a review of the electrochemistry of gold and most especially the mechanisms by which gold oxide / oxyhydroxide layers are generated at the gold electrode surface. This is included for two reasons:

1. The majority of commercially available QCM resonators are coated with gold electrodes.
2. The oxidative electrochemistry of gold and that of *Acetohydroxamic Acid* (AHA) exhibit considerable overlap; consequently, the former must be fully characterised to enable the deconvolution of the latter. Due to the fact that Nafion[®] is the material of choice for the thin layer within which the impregnated AHA at the electrode surface.

The section on gold is then followed by a short discussion of the interrogation of Nafion[®] surface films using EQCM. Finally the chapter concludes with a discussion of the coordination chemistry and electrochemistry of hydroxamic acids.

1.1 - PIEZOELECTRIC SENSORS

Piezoelectrical transducers have widespread application within sensor devices due to their ease of modification, ruggedness, chemical inertness of substrate, conceptual simplicity, low cost and availability. Importantly, their response depends on the mass of the transducer per unit area, suggesting miniaturization without loss of sensitivity.

Piezoelectric sensors are most commonly fabricated by modification of the transducer with a coating that can interact with a desired analyte in such a way that the mass of the coating is increased. The most widespread of such devices is the quartz crystal microbalance.

Early examples of use of the QCM include the detection of hydrocarbons with quartz crystals coated with chromatographic substrates [1.13] and commercial instruments for moisture analysis and particle detection [1.14]. QCM-based systems for the detection of pollutants such as ammonia, formaldehyde, hydrogen sulphide, ozone, sulphur dioxide and mercury have also been extensively investigated [1.15].

1.2 - HISTORICAL PERSPECTIVE ON THE QCM

1.2.1 - Piezoelectric Effect

Jacques and Pierre Curie, in 1880, discovered that a mechanical stress applied to the surfaces of various crystals, including quartz, Rochelle salt ($\text{NaKC}_4\text{H}_4\text{O}_6 \cdot 4\text{H}_2\text{O}$) and tourmaline, produced a corresponding electrical potential whose magnitude was proportional to the stress applied [1.16]. This phenomenon is referred to as the *piezoelectric effect*. The charges generated in the quartz crystal upon application of a mechanical stress are due to the formation of dipoles that result from the displacement of atoms in an accentric crystalline material.

The Curies also discovered the *converse piezoelectric effect* [1.16]. Application of a voltage across a quartz crystal produces a corresponding mechanical strain; this effect later became the basis of the QCM.

During the 1920s, Cady determined that the converse piezoelectric effect could be utilised for the development of stable oscillator circuits [1.17] wherein the applied alternating electric field across a quartz crystal resulted in an alternating strain. This caused a vibrational, or oscillatory, motion in the quartz crystal, resulting in the generation of acoustic standing wave. Furthermore, the quartz crystal exhibited a preference to vibrate at a characteristic *resonant frequency* (f_0). Typical frequencies for these oscillations in QCMs are from 1 to 10 *MegaHertz* (MHz). As quartz crystals vibrate with minimal energy dissipation, they are nearly the ideal oscillators. This, combined with their low cost, ruggedness, low defect concentration, ease of fabrication and chemical inertness, has led to the establishment of their widespread use in frequency control and filter circuits.

1.2.2 - Quartz Crystals

The electromechanical coupling and stresses derived from the applied electric field depend upon the crystal symmetry, angle of cut of the crystal and the configuration of the electrodes used to apply the electric field.

The crystals are carefully cut and modified and the dimensions and configuration of the attached/deposited electrodes finely controlled. For QCM applications, the AT, BT and SC (stress-compensated) cuts have been frequently employed; [the terminology 'AT (alpha) & BT (beta)' simply refers to the orientation of the crystal with respect to the particular quartz rod face from which it is taken.]

The dependence of the resonant frequency, of a quartz crystal, on *temperature* (T) is caused by changes in ρ_q the *density of quartz*, and μ_q the *shear modulus of quartz* with temperature. AT-cut crystals are particularly popular, because they can be cut, at approximately 35° from the z -axis, to give nearly zero temperature coefficients at room temperature.

The two predominant types of AT-cut crystals used for QCM / EQCM mass measurements are the plano-plano and plano-convex. Plano-plano crystals have both faces parallel to each other, while plano-convex crystals have one face plane and the other a ground radius of curvature. The only major experimental limitation of the AT-cut quartz crystal is that it loses its piezoelectric activity above 573°C [1.18].

Application of an alternating field across the thickness of an AT-cut quartz crystal, by two electrodes on opposite sides of the crystal, results in shear strain proportional to the applied potential. The opposing polarity produces an identical strain, but in the opposite direction. Hence, an alternating potential across the crystal causes a vibrational motion within the quartz crystal with amplitude parallel to the surface of the crystal **Figure 1.1**. The resulting vibrational motion of the quartz crystal establishes a transverse acoustic

wave that propagates through the *thickness of the crystal* (t_q), reflecting back into the crystal at its surfaces.

A standing wave condition can now be established when the acoustic wavelength is equal to $2t_q$. The frequency of the acoustic wave in the resonant condition is given in *Equation 1.1*,

$$f_o = v_{tr} / 2t_q = (\mu_q^{1/2} / \rho_q^{1/2}) / 2t_q \quad (1.1)$$

where, f_o is the *resonant frequency* of the quartz crystal prior to a mass change, v_{tr} is the *transverse velocity of sound* in AT-cut quartz ($3.34 \times 10^4 \text{ m s}^{-1}$), t_q is the thickness of the crystal, $\rho_q = 2.648 \text{ kg m}^{-3}$, and $\mu_q = 2.947 \times 10^9 \text{ kg m}^{-1} \text{ s}^{-2}$.

Accordingly, when a uniform foreign layer is added to the surface of the quartz crystal the acoustic wave will travel across the interface between the quartz and the layer of foreign material. This is assuming that the acoustic properties of the foreign layer are identical to that of the quartz crystal.

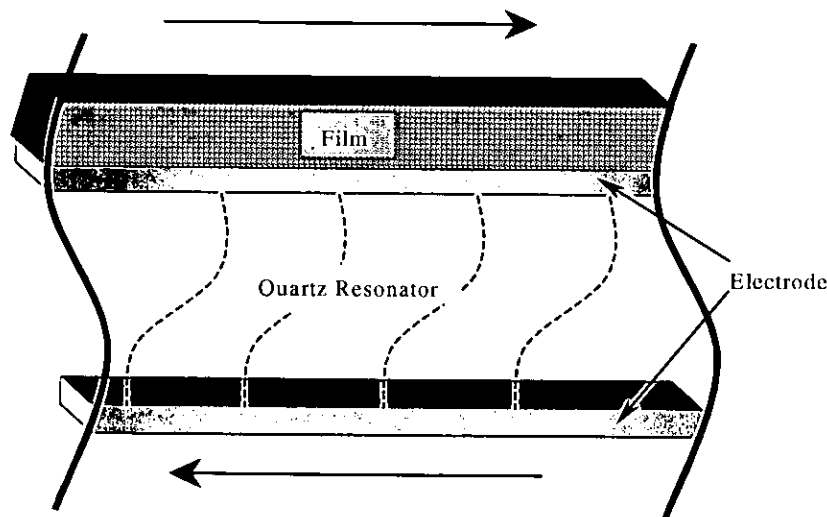


Figure 1.1: Schematic of the converse piezoelectric affect for shear motion. Application of an alternating field across the thickness of an AT-cut quartz crystal, by two electrodes on opposite sides of the crystal, results in shear strain proportional to the applied potential. The opposing polarity produces an identical strain, but in the opposite direction depicted by -----.

1.3 - MASS FREQUENCY CORRELATIONS

By 1957 Sauerbrey had developed a description and experimental proof of the *mass-frequency relation* for mass deposited on thickness-shear mode crystals [1.19]. This proof is still used today for the determination of mass changes at the surface of shear mode transducers. This mass sensing technique is commonly what is being referred to when discussing the QCM. The mass-frequency relationship relies upon the assumption that a deposited mass exists entirely at the antinode of the standing wave propagating across the thickness of the quartz crystal. The mass deposited could be treated as an extension of the quartz crystal, hence, the frequency change can be calculated as though it were the result of an increase in the thickness of the quartz crystal.

Noting that Δt is expressed as an *areal density* $\Delta m/A$, obtained from Equation 1.1.a it can therefore be seen from Sauerbrey, that a *fractional change in thickness* ($\Delta t / t_q$) results in a fractional change in frequency ($\Delta f / f_o$). Substitution of Equation 1.1 into Equation 1.2 and then gives the Sauerbrey equation (Equation 1.3)

$$\Delta t = \Delta m / \rho_q A \quad (1.1.a)$$

$$\Delta f / f_o = -\Delta t / t_q = -2f_o \Delta t / v_{tr} \quad (1.2)$$

$$\Delta f = -2f_o^2 \Delta m / A(\mu_q \rho_q)^{1/2} \quad (1.3)$$

where, Δf is the *measured frequency shift*, Δm the *mass change* and A the *piezoelectrically active area*.

Therefore an intrinsic assumption of the above treatment is that the density and transverse wave velocity associated with the foreign material is identical to that of the quartz resonator.

The Sauerbrey relationship also assumes that the frequency change due to mass deposition at some radial distance from the centre of the crystal will be the same regardless of the radial distance. However, the actual frequency response due to the mass

change is dictated by the *differential sensitivity constant*, c_f , which represents the differential frequency shift for a corresponding mass change at that point on the surface of the QCM *Equation 1.4*. Integration of c_f over the total surface area of the QCM produces the *integral sensitivity constant*, C_f , which corresponds to the $2f_0^2/(\mu_q \rho_q)^{1/2}$ term in (*Equation 1.3*).

$$c_f = df / dm = S \quad (1.4)$$

$$C_f = \int_0^{2\pi} \int_0^r S(r, \Phi) r dr d\Phi \quad (1.5)$$

Φ and r are the *angle and distance co-ordinates for a polar coordinate system*, the origin of which is at the centre of the QCM disc and S the sensitivity of the crystal.

The Sauerbrey relationship requires that the deposited film has a uniform thickness across the entire active area of the resonator. However, studies of metal deposits sputtered onto localised areas of a QCM have indicated that c_f is not uniform across the entire active area of the resonator. c_f is found to be highest at the centre of the QCM, but decreases in a Gaussian like manner as a radial line is traversed from the centre, and becomes negligible at and beyond the electrode boundary [1.19 & 1.20].

This behaviour can be explained by energy trapping that results from the confinement of crystal oscillations within the electrode region of the resonator. Ideally only the portion of crystal located in the electric field induced by the two electrodes encounters the stress field responsible for oscillation. The unplated portion of the crystal serves to clamp the crystal confining the oscillations to the electrode boundary. Energy trapping is thus a result of the mass loading produced by the electrodes which increases the effective density of the resonator in this region compared to the unplated region.

As a result the electroded and unplated regions have cut-off frequencies (ω_e) and (ω_q) respectively below which acoustic waves cannot propagate without attenuation. These cutoff frequencies are equivalent to the frequencies of the fundamental resonant thickness shear modes in these regions. The amplitudes of acoustic waves with

frequencies between ω_e and ω_q decrease exponentially in the unplated region while frequencies greater than ω_q propagate freely through the unplated region until damped by contacts.

The result is that the energy of the fundamental modes is trapped in the electrode region, with the amplitude greatest at the centre and minimal at the edges. Note that the fact the sensitivity is not constant across the surface does not invalidate the Sauerbrey equation, it merely requires film thickness uniformity.

It should be noted that for plano-convex crystals, the region of the crystal which undergoes displacement during oscillation will be confined to the area defined by the electrodes. However, for plano-plano crystals this region extends past the edge of the electrodes, onto the face of the quartz disc.

1.4 - EFFECTS OF VARIOUS PARAMETERS ON CRYSTAL OSCILLATION

1.4.1 - Solution Effects

When a plano-plano crystal that is oscillating in a shear mode is immersed into a liquid medium, a shear wave propagates away from the crystal surface into that medium. The energy dissipation caused by the viscous nature of the liquid medium produces an exponential damping of the shear wave as it travels through the liquid away from the electrode surface.

This effect has been quantitatively investigated by Kanazawa and Gordon [1.21], and Bruckenstein and Shay [1.22] giving the equation for shear wave velocity as a function of distance from the surface of the oscillating crystal (*Equation 1.6*)

$$v(z,t) = v_o \exp(-k_1 z) \cos(k_1 z - 2\pi f_o t) \quad (1.6)$$

where $v(z,t)$ is the *shear velocity* (parallel to the crystal surface), which is a function of *distance* (z) from the crystal surface and *time* (t), v_o is the *velocity* of the crystal surface, k_1 is the *propagation constant*. The propagation constant is given by *Equation 1.7* showing the dependence of the damping on the density and viscosity of the medium

$$k_1 = \left(\frac{\pi f_o \rho_L}{\eta_L} \right)^{1/2} \quad (1.7)$$

where ρ_L and η_L are the *solution density* (*i.e.* the effective mass of the solution that is being moved along the QCM surface) and *viscosity* (*i.e.* a measure of loss of the shear wave amplitude by momentum transfer to the solution) respectively. **Figure 1.2** shows the shear velocity profiles in a liquid at three different times [1.21].

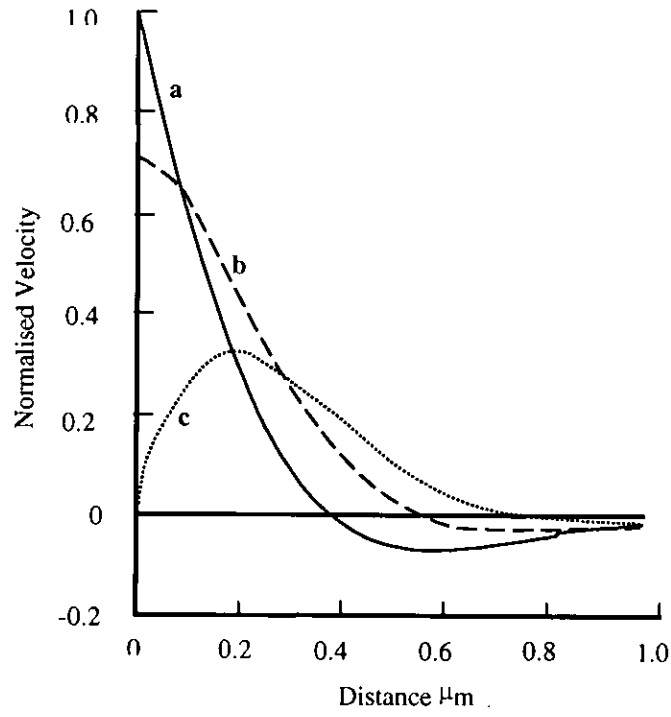


Figure 1.2: Graphic interpretation of the shear velocity profiles in a fluid adjacent to a QCM at three different times: (a) peak surface velocity, (b) intermediate surface velocity and (c) zero surface velocity.

Kanazawa's treatment of the influence of the solution properties on the crystal permits the prediction of the change in resonant frequency, which accompanies immersion of the crystal into viscous medium (*Equation 1.8*)

$$\Delta f = -f_o^{3/2} \left(\frac{\rho_L \eta_L}{\pi \rho_q \mu_q} \right)^{1/2} \quad (1.8)$$

where the change in resonant frequency, Δf , is seen to be proportional to $(\rho_L \eta_L)^{1/2}$. Under ideal conditions, $\rho_L \eta_L$ is constant in a QCM experiment and the Sauerbrey equation is applicable.

1.4.2 - Viscoelastic Effects

The EQCM has been used to investigate the mass changes that occur in redox-active films during electrochemical cycling, so providing information about the transport of counter ions and solvent molecules into and out of the film. The possibility of viscoelastic changes in the film due to their large molecular weights and the resulting chain entanglements from cross linking, and also changes in the morphology and swelling has not been well-documented [1.18]. However, it is apparent that the ingress and egress of counter ions and solvent can result in changes in the viscosity and elasticity of the film. As such, this behaviour can lead to erroneous conclusions about mass transport in the film because of the contributions of $\rho_f \eta_f$ described below.

Polymer films are viscoelastic in nature and the contributions made to the resonant frequency by the immobilised film's *viscosity* (η_f), *density* (ρ_f) and *elasticity* (μ_f) must be considered. If the polymer film is rigid throughout the experiment or if $\rho_f \eta_f$ does not change during the experiment, then contributions from $\rho_f \eta_f$ can be ignored.

Under these conditions, one could assume that the film exhibits liquid like behaviour wherein the contributions from the liquid remain constant. Under these conditions, the resonant frequency upon the application of a polymer film to the electrode surface can be simply expressed by combination of *Equation 1.3* and *Equation 1.8*, which describes the frequency change derived from immersing the electrode in a viscous medium (*Equation 1.9*) [1.23].

$$\Delta f_o = - \left[2f_o^2 / (\mu_q \rho_q) \right]^{1/2} \left[(\Delta m / A) + [\rho_f \eta_f / 4\pi f_o]^{1/2} \right] \quad (1.9)$$

Whilst non-rigorous, this treatment does however point out that Δf_o can be affected by both terms in *Equation 1.9*.

Although truly quantitative models of the behaviour of the polymer film-coated QCM are not yet in place, the above analysis indicates that viscoelastic effects must not be ignored in EQCM experiments. This is especially true for polymer films that experience insertion

of counter ions or incorporation of solvent that may lead to film swelling and so changes in $\rho_f \eta_f$.

The relative contributions of the rigid mass and $\rho_f \eta_f$ terms to Δf_o can be quantified by impedance analysis [1.24].

1.4.3 - High Mass Loadings

As the mass deposited on the QCM is increased, the sensitivity of the device, $\Delta f_o / \Delta m$ decreases. This effect can be understood by inspection of the Sauerbrey equation (Equation 1.3). A high mass loading will result in a decrease in f_o during the deposition/adsorption process. This will result in a decrease in the numerator of the Sauerbrey equation with a corresponding decrease in the QCM sensitivity.

Typically, QCM measurements are considered accurate provided the mass of the film does not exceed 2% of the mass of the crystal. Higher mass loadings of up to 10% can be tolerated by using the “Z-match” method, but the μ_f and ρ_f must be known. The “Z-match” method has not been employed in EQCM applications because in most cases μ_f and ρ_f are not known [1.23].

1.4.4 - Surface Roughness

The roughness of the QCM electrode surface can play an important role in the behaviour of the QCM in a liquid medium. Trapping of liquid in the surface cavities will result in an additional mass component whose magnitude will depend upon the amount of trapped liquid and the size of the cavities. This effect has been observed during the oxidation of gold electrodes in neutral and basic media, in which it was discovered that the observed frequency shift during electrochemical oxidation was significantly larger than that expected from oxide formation. This was attributed to water trapped in surface cavities formed during the oxidation step [1.25 & 1.26].

Attempts have been made to explain these discrepancies by modeling the surface as having hemispherical undulations, which trapped solution, and further assuming that this trapped solution behaved as a mass rigidly attached to the surface. However, some disagreement exists between the predicted behaviour of this model and the data observed [1.25 & 1.26].

1.4.5 - Surface Stress

QCM experiments are usually performed with one side of the AT-cut quartz crystal immersed in a liquid medium with the opposite side facing air. This arrangement will result in stress on the quartz crystal due to hydrostatic pressure exerted by the liquid medium. These effects in QCM experiments have not been well characterised, but it seems likely that they will not be of great importance if the pressure remains constant through out the experiment.

Strain effects arising from thick films can also affect the conformance of the transducer to the Sauerbrey equation [1.27 & 1.28]. Compressive stresses in metal films on the QCM and EQCM are known to result in frequency shifts unrelated to mass changes, with a decrease in f_0 observed for AT-cut crystals [1.29].

1.4.6 - Interfacial Slippage

The QCM and its mass sensing properties rely on the “no-slip” condition, *i.e.* the first layer of solvent at the QCM metal electrode surface is tightly bound and does not slip against the metal surface during the shear motion of the quartz crystal. Thus, the vibrating QCM electrode and the adjacent molecular layer of the liquid move at the same velocity.

A correlation between contact angles and Δf_0 was observed upon immersion in liquids, under conditions where the surface energy of the QCM electrodes were controlled by

treatment with salines of differing hydrophobicity. It was determined that the time required to reach the final stable value of f_0 in liquid depended upon the nature of the electrode surface [1.30, 1.31 & 1.32].

1.4.7 - Non-uniform Mass Distribution

An experimental study into the physical behaviour of quartz resonators using a tungsten probe to measure the surface motion of AT-cut quartz resonators has corroborated the radial dependence of the shear velocity and amplitude in water [1.33]. This behaviour is unlike that observed for the QCM in a vacuum as the shear motion extends beyond the electroded region of the resonator consistent with field fringing due to the dielectric contribution from water.

It is apparent that in liquid media the regions beyond the electrode boundary can contribute to the sensitivity of the resonator. The observation of field fringing dictates that the integral sensitivity constant for a given crystal frequency, contour, electrode thickness and electrode geometry should be determined electrochemically prior to quantitative experiments. One such standard procedure involves Cu electrodeposition [1.23].

In situ measurements of the radial mass sensitivity of the electrochemical quartz crystal microbalance (EQCM *vide infra*) in liquid media performed via Cu electrodeposition through holes in a photoresist polymer deposited over the QCM surface have produced simultaneous *cyclic voltammetry* (CV) and frequency change (Δf) measurements, from which the electrochemical charge passed and hence the mass sensitivity can be determined as a function of position. This calibration can also be conducted in a manner to account for the electrode tabs where electrochemical events take place despite their being located on piezoelectrically inactive regions of the crystal [1.23]. The plano-plano resonator exhibits significant sensitivity to mass changes beyond the electrode edges. In

contrast, the plano-convex resonator exhibits greater sensitivity in the centre of the crystal with little field fringing due to greater energy trapping of the fundamental mode

Figure 1.3.

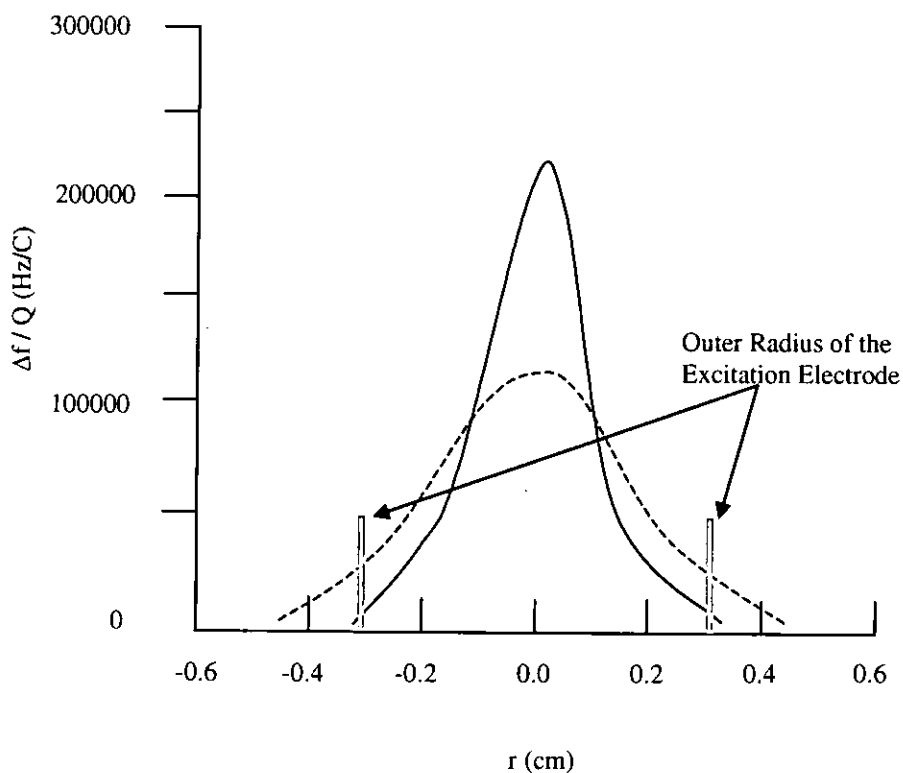


Figure 1.3: Sensitivity dependence on radial position of 0.025-in. holes aligned parallel to the x - axis ($\phi = 0^\circ$) for radius of the excitation electrode = 0.32cm on plano-plano and plano-convexed — quartz crystals, expressed as $\Delta f / Q$ ratios measured during copper electroplating. Where Q is the charge passed during electroplating and r the radius of the electrode[1.23].

1.5 - ELECTROCHEMICAL QUARTZ CRYSTAL MICROBALANCE SENSORS

The use of the QCM in an electrochemical context to monitor mass changes at electrodes was first demonstrated by Jones and Meire [1.34 & 1.35], who showed that trace metal determinations were possible by plating metals onto a QCM electrode and measuring the change in resonant frequency of the crystal in air following its removal from the electrochemical cell.

However, since the first report in 1980 that the QCM could be used for *in situ* experiments in conjunction with electrochemical measurements, [1.36] there has been a widening interest in its use to monitor mass changes at electrode surfaces and in thin films on electrodes.

This configuration of the QCM, commonly referred to as the electrochemical quartz crystal microbalance, presents one of the resonator excitation electrodes (see below), to the solution. This solution-facing electrode may then be used as a working electrode in a conventional electrochemical cell. The EQCM may then be used to provide correlation between electrochemically induced mass changes at the electrode surface and the charge consumed in that process. Such measurements can allow determination of the composition of the deposit, its stoichiometry, and the efficiency of the use of charge in its deposition.

The applications of this device to the measurement of electrochemical kinetics was first reported by Bruckenstein [1.37] and Kaufman [1.38]. The former “weighed” one monolayer of oxygen during gold oxidation in perchloric acid. The latter showed that during the electroreduction of a polypyrrole polymer film, the charge compensation is limited by the diffusion of Li^+ in the film and not by the diffusion of the ClO_4^- in the solution.

The EQCM has been used to investigate the electrochemical formation, on metal electrodes, of monolayers of adsorbed oxides [1.24, 1.26 & 1.36], halides [1.39] and metal atoms [1.40, 1.41 & 1.42]. The frequency changes associated with these changes in the surface monolayer are not only affected by the mass of the electrochemically formed monolayer, but also by mass changes due to solvent or ion content of the monolayer. Interactions of the bare surface and adsorbed species with solvent and ions in the electrical double layer must also be accounted for these frequency changes.

The study of multilayer deposition and dissolution processes is a mature area of electrochemistry [1.43 & 1.44]. Recently, the deposition of semiconductor materials [1.45], the growth and cycling behaviour of oxide layers [1.46], and the deposition and dissolution mechanisms of electrochromic films [1.47 & 1.48] have been popular topics of investigation. All of these studies have used the EQCM to probe processes such as nucleation, growth & dissolution, and to characterise properties such as current efficiency for deposit formation/dissolution, the physical state of the deposit and the stoichiometry of the deposit.

Mass transport processes, which accompany redox transformations in polymer films adsorbed on electrode surfaces, have been extensively studied with the EQCM [1.49]. Properties which can be characterised for such systems using EQCM include the current efficiency for deposition in electropolymerisation reactions, the extent of film swelling and changes in swelling which occur during redox reactions [1.50, 1.51 & 1.52], ion and solvent transport, [1.49 to 1.51 & 1.53] and changes in the viscoelastic properties of the deposit [1.49 to 1.51 & 1.54].

The identification of ionic species undergoing transport, in supporting electrolyte, during redox switching reaction is important for manipulating the properties of conducting polymers in many applications [1.55]. The EQCM can provide qualitative and quantitative information on the extent of solvent swelling or deswelling which occurs

during the switching process [1.49 to 1.51]. Mechanistic information can then be obtained, allowing correlation to be drawn between the amount of deposited material and the deposition conditions [1.56].

1.6 - A HOLDER FOR THE ELECTROCHEMICAL QUARTZ CRYSTAL MICROBALANCE

1.6.1 - Single Quartz Crystal Microbalance

Despite the growth in the use of EQCM there are few commercially available EQCM holders which can satisfactorily meet all the requirements of an EQCM experiment carried out over a wide range of pH or ion concentration in aqueous solutions and which can also be used in non-aqueous solutions. Although a simple electrical and mechanical device in principle, EQCM holders have been somewhat difficult to use successfully so that, until recently the EQCM was utilised only by specialist laboratories.

Several designs of the EQCM holder have been presented in the literature [1.15, 1.18, 1.57, 1.58 & 1.59]. The basic feature of the EQCM is that only one face of the quartz crystal needs to be in contact with the solution. In earlier holder constructions, the crystal was sealed with adhesive. Unfortunately, a crystal mounted in this way is difficult (if not impossible) to change; additionally it can prohibit measurement in non aqueous solvents. More recent designs utilise an o-ring compression seal so removing both of these disadvantages.

Three general orientations exist for the mounted crystal holder [1.15, 1.18 & 1.57 to 1.59]. Two involve horizontal mountings, where either the bottom or the top crystal face is exposed to the solution. The third arrangement involves a vertical mounting. The drawback of the horizontal mounting with the bottom face exposed is that visual observation of the working crystal face is difficult. In addition, undesirable, gas bubbles may attach to the Au/quartz electrode during solution purging or gas evolution at the electrode which may then be difficult to remove. A horizontal mounting in which the top face is in contact with the solution is free of the later disadvantage. However, in this design solution stirring becomes difficult under anaerobic conditions. Moreover, in this

horizontal mounting, any solid which is formed in the bulk solution can fall by gravity onto the crystal face, causing an erroneous EQCM reading.

A vertical crystal mounting has none of these disadvantages and so allows for ease of handling and operation *Figure 1.4*.

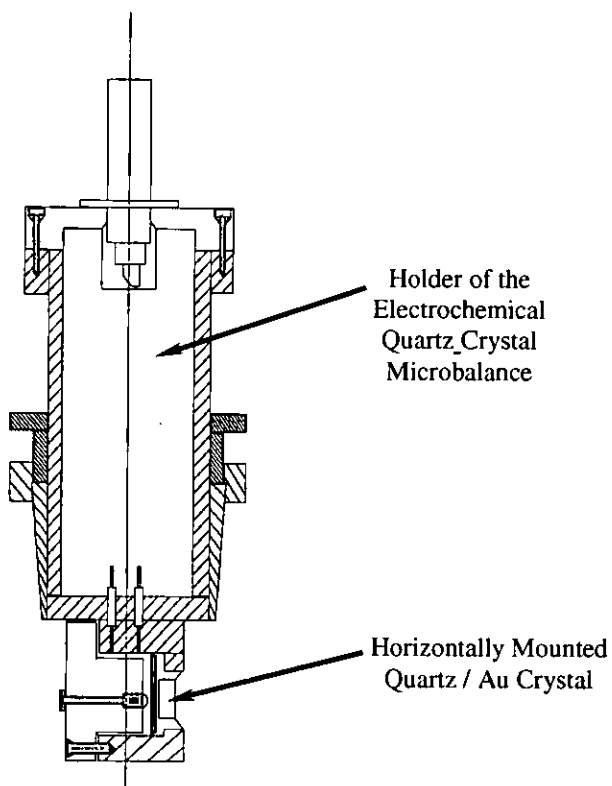


Figure 1.4: Holder for the electrochemical quartz crystal microbalance – cross sectional view.

1.6.2 - Dual Quartz Crystal Microbalance (DQCM)

The use of QCM in the measurement of deposition and dissolution, electrochemical oxidation and reduction, biological cell growth and viscosity of liquids is well known. However, an obvious problem with QCM and EQCM in liquids, is that the resonant oscillation frequency, f_0 , of the crystal and hence the sensitivity of the EQCM depends on the three factors: the properties of the quartz, the properties of a rigidly attached film, and the properties of the liquid. For sensing applications, it is more often the case that, for simplicity of interpretation of measurement, an analyte dependent response of only one of these properties is desired. Previous authors have attempted to compensate for undesirable variations in the other two properties by applying theoretical or empirical corrections, thereby largely isolating the effect of interest [referenced in 1.23 & 1.28]. This approach may yield unsatisfactory results if the real systems deviate from the theoretical predictions. An alternative approach is the development of a self-compensating QCM able to produce a frequency change directly proportional only to the phenomenon we wish to measure.

S. Bruckenstein and G.C. Dunham and co-workers have developed new generations of dual quartz crystal microbalance probes [1.60 & 1.61]. The DQCM have found utility for operations in gases and conducting or viscous liquids with no need for corrections due to effects associated with conductivity, viscosity or temperature changes over reasonable ranges of those parameters. Application to the two exposed faces of thin selective layers with different chemical sensitivities creates a chemical sensor capable of functioning in air or liquid. The simultaneous sensitivity to mass change and insensitivity to environmental effects stimulates interest in this type of probe as a generic precursor of a chemical sensor with applications including, mass monitoring during electrochemical deposition, electroless plating and etching processes, and changes in elasticity of the added layer.

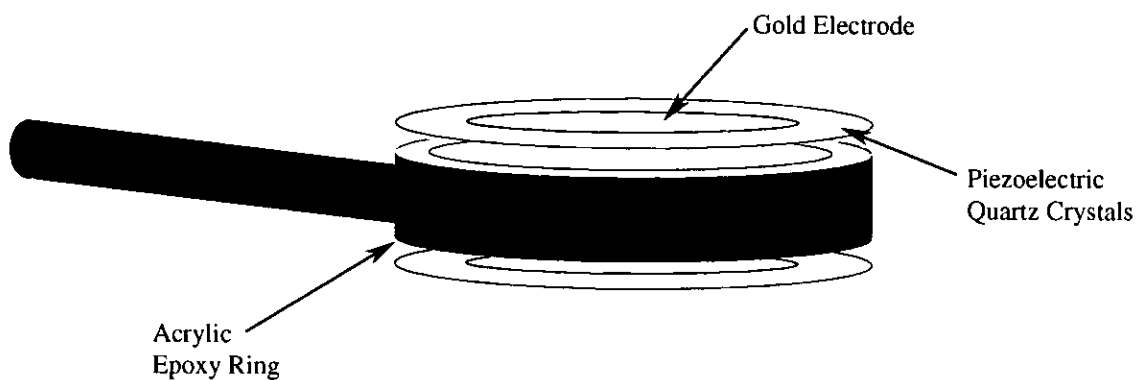


Figure 1.5: Holder for the Dual quartz crystal microbalance.

One significant feature of the DQCM *Figure 1.5* is the isolation of the excited electrode on each crystal from the solution by placing it in the air gap of the probe. By preventing electrical leakage, the probe's operating range is extended into very conductive solutions.

1.7 - GOLD ELECTROCHEMISTRY

1.7.1 - Gold Oxidation

The anodic behaviour of metals is of major interest to industrialists and electrochemists alike, and the behaviour of gold is especially important due to: (i) its role as a model system for fundamental studies; and (ii) its technological applications in, for example, in the electronics industry where its corrosion resistance and ease of electro-deposition are major advantages.

Electrochemical studies of gold in aqueous solutions provide a powerful means by which to study the mechanisms of, *inter alia*, generic oxidation and dissolution processes at the metal surface [1.62, 1.63 & 1.64]. The subject has been studied extensively, the literature up to 1972 having been reviewed by Schmid and Curley [1.62]. This review led to an ongoing debate about the mechanism by which gold electro-oxidation actually occurs.

More recently, the advent of more sensitive electrochemical equipment and techniques have allowed for the resolution and characterisation of sub-monolayer processes at electrodes, especially at the early stages of metal oxidation. Gold oxidation and reduction in acid and alkaline solutions has been widely investigated upon monocrystalline gold electrodes (presenting, *inter alia*, the Au (100), (111), (110) and (910) crystal planes to solution), polycrystalline gold electrodes and EQCM gold electrodes in the works of Angerstein-Kozlovska *et al* [1.65, 1.66 & 1.67] Gordon and Johnson [1.68], Hamelin [1.69], Hamelin *et al*, [1.70 & 1.71] Strbac *et al*, [1.72 & 1.73] Sotto, [1.74] Chialvo *et al*, [1.75] Ferro *et al*, [1.76 & 1.77] Hoare, [1.78] Piela and Wrona [1.79], Rand and Woods, [1.80] Oesch and Janata, [1.81] Burke and O'Leary, [1.82] Burke *et al*, [1.83, 1.84 & 1.85] Bruckenstein and Shay, [1.37] Johnson and LaCourse [1.86], Gerlache *et al*, [1.87] Ye *et al*, [1.88] Shengli *et al* [1.89] and Juodkazis *et al* [1.90 & 1.91].

The generic consensus for gold oxidation provided by the authors above is known to involve the formation of gold oxide / oxyhydroxide layers on the electrode surface observed in *Figure 1.6* peak E_a . Depending on the formation conditions, these oxides / oxyhydroxides layers can be from one molecular layer to several nanometers thick. During cathodic polarisation of an electro-oxidised Au surface, these oxidation compounds are reduced with associated cathodic current peaks in the cyclic voltammogram see *Figure 1.6* peak E_c .

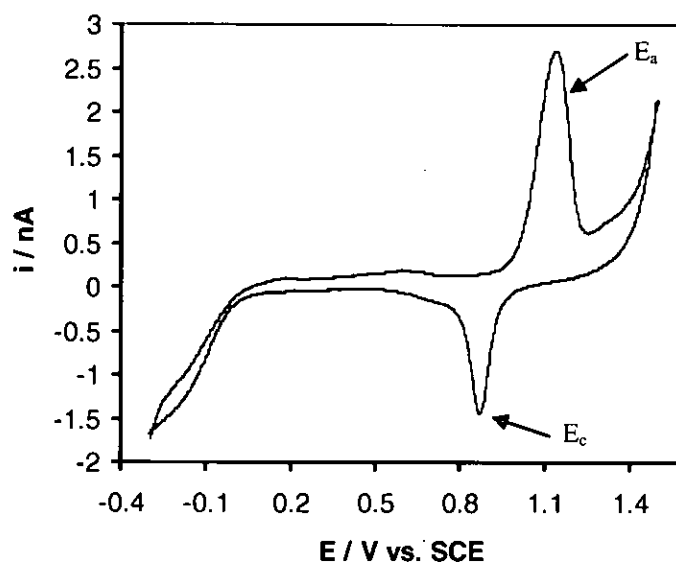
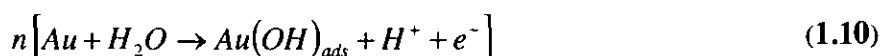


Figure 1.6: Typical CV recorded in house of $100 \text{ mol m}^{-3} \text{ HNO}_3$ using a $25 \mu\text{m}$ Au microdisc electrode at v 1 mV/s .

Due to its extensive use as an electrode material in EQCM-based studies, the next section will therefore provide a short review of the mechanisms by which the electro-oxidation and reduction of gold are known to occur in acidic medium typical of those in which our final sensor might be deployed.

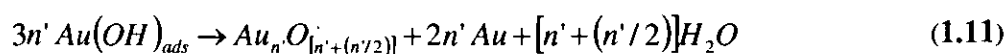
1.7.1.1 - Polarographic Gold Oxidation

Following a series of studies in sulphuric and perchloric acid, Ferro *et al* [1.76] have suggested gold oxidation occur at potentials higher than 1.35 V (vs. NHE). They have proposed that the process begins with the participation of water molecules



where n is the number of reacting surface atoms.

Equation 1.10 is followed by the generation of a more stable surface oxide, (comparable to Au_2O_3) and partial regeneration of free metal surface

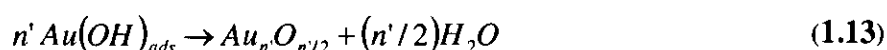


where $3n' \leq n$ and n' is the number of reacting atoms during hydroxide adsorption.

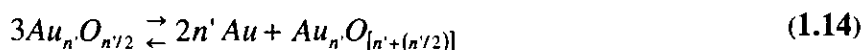
The simultaneous existence of $Au_n O_{[n'+(n'/2)]}$ and Au implies the existence of a surface equilibrium given by Equation 1.12.



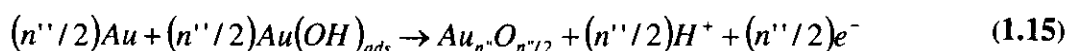
Ferro *et al* also suggest that the establishment of this surface equilibrium from $Au(OH)_{ads}$ as a starting point could occur via



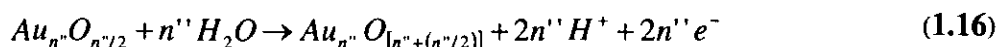
and



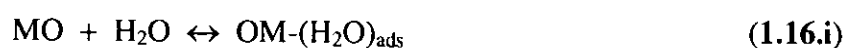
they then postulate that $Au(OH)_{ads}$ and free metal Au undergo further electrochemical oxidation via:



where $[(n''/2) + 3n'] \leq n$ and n'' is the number of reacting atoms which ultimately leads to the resultant surface oxide approaching the stoichiometry of Au_2O_3 . Finally, further oxidation produces an Au_2O_3 structure by the following overall reaction.



Angerstein-Kozłowska *et al* [1.65] have also suggested that adsorption of OH species occurs as a precursor to gold oxidation in the absence of anions in solution. They posit that OH adsorption / gold oxidation occurs through the formation of three successive, energetically different, overlaying metal (M)-OH lattices, the three energy states arising from repulsion between metal-oxygen dipoles. The formation of all three lattices is reversible on a metal surface. However, the reactions become progressively less reversible with increasing oxide coverage. Monolayer coverage always shows hysteresis due to the occurrence of the place exchange or turn-over reaction, wherein the metal-oxygen dipole reorientates at the electrode surface in accordance with *Equation 1.16.i*:



A summary of the Angerstein-Kozłowska mechanism in anion-free solution is shown in *Figure 1.7*. The stages (1), (2) and (3) represent the successive overlaying of lattices of oxygen species on the gold surface. The symbols O_{A1} , O_{A2} etc and O_{C1} , O_{C2} etc refer to peak features in the forward sweep oxidation and reverse sweep reduction currents on Au respectively. An example of their placement / locations may be seen in *Figure 1.8.a*, although it should be noted that this voltammogram was recorded in the presence of nitrate anions. As the results presented in *Chapters 3-5* were recorded in the presence of anions, we present the mechanism of *Figure 1.7* for purposes of comparison only. Detailed elucidation of the mechanism can be found in the literature cited above, to which the interested reader should refer for further detail.

Angerstein-Kozłowska *et al* [1.65] report that the presence of the anions in perchloric and sulphuric acids have profound effects on the mechanism of electrochemical oxidation of polycrystalline gold surfaces. These effects derive from the specific adsorption of the anions at the Au surface and can be summarized as being due to the following:

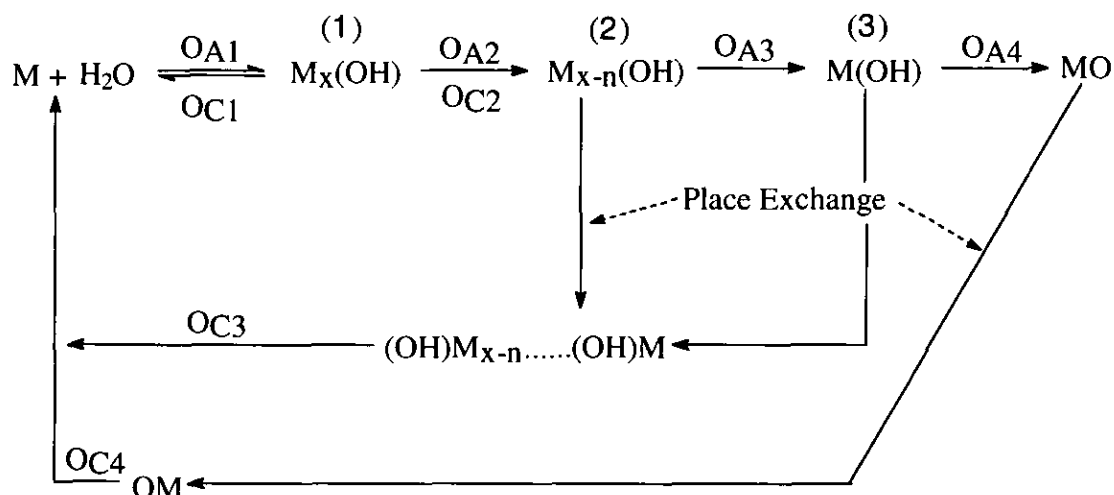


Figure 1.7:- Reaction pathway for the oxidation and reduction of gold in a solution where anion adsorption does not take place.

- Anion adsorption being competitive with OH/O deposition, so blocking initial oxidative coverage and causing the potential at which the initial oxidation commences to be displaced to more positive potentials.
- As a consequence of (a), the interfacial field experienced by electrodeposited OH or O species is higher than it would be in the absence of anion adsorption, which in turn accelerates the place exchange process.
- Lateral repulsion between the anions and the metal-oxygen dipoles, which also facilitates place exchange.
- Anion adsorption changes the composition of the Helmholtz plane and consequently the interfacial field in the double layer in a direction that assists place exchange.

Angerstein-Kozłowska *et al* observed in **Figure 1.8.a** that peak O_{A1} , which is associated with the very initial stage of surface oxidation (+1.19 to +1.30 V (vs. NHE)) and which is reversible with O_{C1} , can be suppressed by the addition of SO_4^{2-} and replaced by peak O_{A1A} , reversible with peak O_{C1A} , and which corresponds to the formation of the first hydroxide lattice overlayer in the presence of co-adsorbed anions.

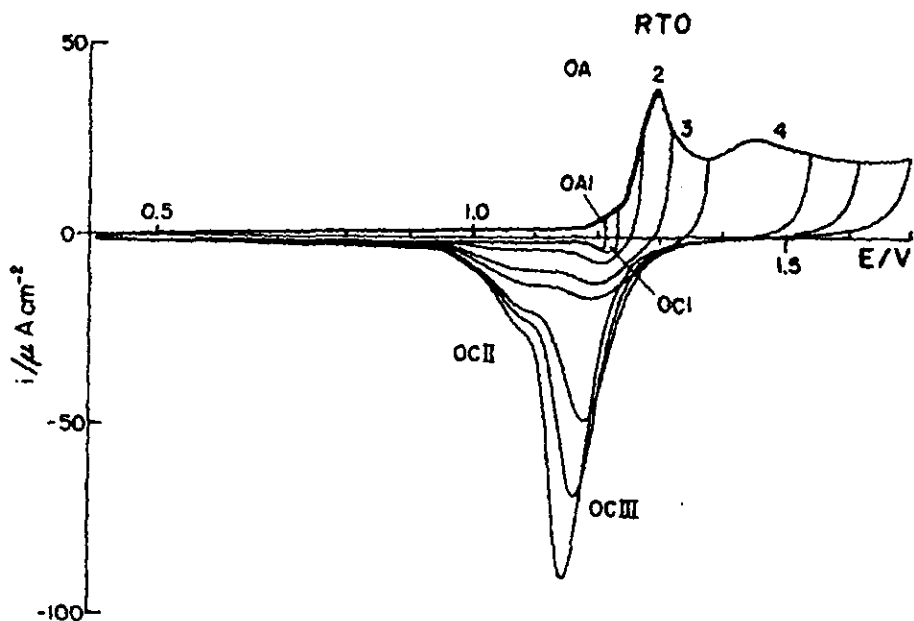


Figure 1.8.a: Cyclic voltammogram of 100 mol m^{-3} perchloric acid (pH1) using a polycrystalline Au electrode at 20 mV/s was produced by Angerstein-Kozłowska *et al* depicting the anodic oxidation peaks (O_{A1} , O_{A2} , O_{A3} and O_{A4}) and associated cathodic peaks (O_{C1} , O_{C3} and O_{C4}) [1.53].

They also observed that peak O_{A2} (+1.30 V (vs. NHE)) is reduced in size in the presence of SO_4^{2-} while peak O_{A3} (+1.35 V (vs. NHE)) increases in size. Neither feature exhibits a change in peak potential upon introduction of SO_4^{2-} . From these observations, Angerstein-Kozłowska *et al* concluded that the presence of SO_4^{2-} results in an interchange of population between the two species responsible for the two peaks. Specifically, sulphate induced suppression of the oxidation of $\text{M}_x(\text{OH})\text{A}$ to $\text{M}_{x-n}(\text{OH})\text{A}$ in peak O_{A2} (i.e. suppression of the value of n) results in a higher population of M atoms participating in $\text{M}_{x-n}(\text{OH})\text{A}$ to $(x-n)\text{MOH}$ plus free anion A in peak O_{A3} . As in anion free systems, peak O_{A4} corresponds to the formation of the oxide MO.

Figure 1.9 summaries one of the first mechanisms developed by Angerstein-Kozłowska *et al* to explain their observations of the electrochemistry of gold oxidation and reduction in sulphate-containing acid media. Stage (1) is normally reversible; stage (2) can be

reversible but may appear experimentally irreversible, depending upon the extent of reaction of the concurrent place exchange process. Stage (3) is normally irreversible due to the involvement of the following place exchange process to form OHM. Further oxidation to the MO results in hysteresis with respect to all reduction processes due to place exchange to OM disrupting the order of the metal surface.

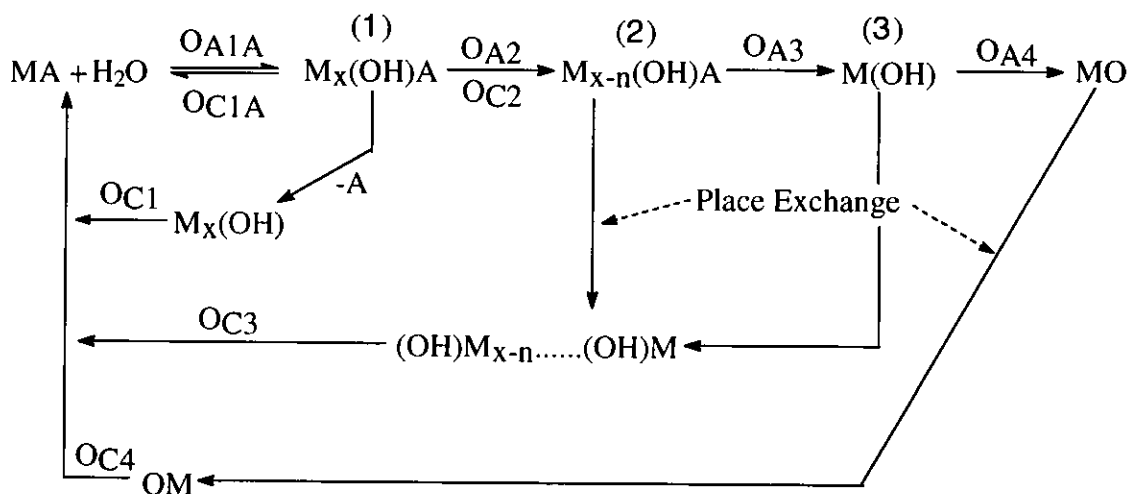


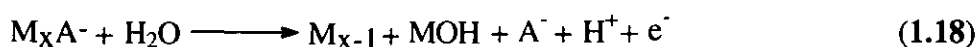
Figure 1.9:- Reaction pathway for the oxidation of gold electrode in a solution where anion adsorption takes place [1.65].

Subsequent work by Angerstein-Kozłowska *et al* [1.66] in solutions containing sulphate and perchlorate anions led to some refinement of the mechanism of **Figure 1.9**, especially with relation to the reactions assigned to peaks OA2 and OA3. The refined mechanism may be summarized as follows.

The first anodic peak, O_{A1A} **Figure 1.8.a** corresponds to formation of the first sub-lattice of OH on the surface wherein OH deposition occurs between adsorbed anions:



The second anodic peak is observed as the first sharp peak having a potential of +1.30 V (vs. NHE) **Figure 1.8.a** and corresponds to simultaneous deposition of the second OH sublattice and anion desorption:



Equations 1.17 & 1.18 are followed by the place exchange process:



Indeed, anion desorption and place exchange occur in one simultaneous *replacement turnover* (RTO) process, the reduction of this material occurring in peak O_{C3} .

The third oxidation peak O_{A3} , corresponds to OH deposition between the existing sublattices, so completing the OH monolayer:



Stoichiometrically, peaks O_{A1A} - O_{A3} correspond to the transfer of the first electron in the oxidation of the gold surface. Peak O_{A4} corresponds to the transfer of the second electron and is usually seen as a broad feature on a polycrystalline gold surface:



Reactions 1.18 – 1.22, and the EQCM response associated with them, are discussed in detail in *Chapter 3*. We do not propose to discuss the mechanistic details of the cathodic processes of the reverse sweep of *Figure 1.8.a* in this thesis. The interested reader is directed to the references cited above and articles cited therein.

Angerstein-Kozłowska *et al* also studied the electrochemical oxidation of Au in perchloric and sulphuric acids at a series of low index Au crystal faces – specifically the Au(100), Au(110) and Au(111) faces [1.65]. The results obtained were not inconsistent with the mechanism described in *Reactions 1.18 – 1.21*. However, the relative sizes and peak potentials of peaks O_{A1} – O_{A4} do exhibit some variations from plane to plane due to the differing facilities with which the tetrahedrally symmetric sulphate and perchloric anions pack at the surface – symmetry & dimensions of the anions most closely match those of the Au(111) face, least closely those of the Au(100) face. This investigation highlighted the idea that sulphate and perchloric anions, which are adsorbed with some charge transfer (see *Equations 1.22 to 1.25* below), can be regarded as forming an

overlying lattice at the electrode surface on these highly ordered crystal planes. The strength and extent of this adsorption is higher on those planes on which the symmetry and arrangement of the atoms on the surface is compatible with symmetry of the anion. Thus, in the case of the Au(111) plane, the overlying lattice of anions is nearly completely discharged and forms an orderly anion network with holes through which OH species can fit and adsorb at Au surface sites of different energies. Saturation of the surface anion population at the Au(111) plane does not therefore block the electrogeneration of surface OH species.

When the symmetry of the surface lattice is not compatible with that of the anion *i.e.* Au(100) plane, then adsorption is much weaker and the charge transfer is small. Because of the mismatch of geometry between anion and lattice, no orderly network of anions is formed – however, the field arising from the non discharged anions partially shields the surface, inhibiting OH deposition to such an extent that none occurs without concurrent place exchange.

Angerstein-Kozłowska *et al* further suggest that the co-ordination deposition of the OH species occurs from the H-bonded waters of hydration of the anions [1.66], its facility necessarily being dependent on the geometry of the anions and arrangement of metal atoms at the Au surfaces. Expressed in relation to the geometry of the H-bonded H₂O, the H-bond between the O of discharged OH and the anion can either be preserved, as is the case for the Au(111) face, or broken, as is the case for the Au(100) face. The specifically adsorbed, H-bonded anions also seem to stabilise the OH sublattices on the surface and desorption of the anions appears necessary for place exchange to occur.

Given the importance of the role played by ClO₄⁻, SO₄²⁻ or HSO₄⁻ anion adsorption in the oxidation of Au, it is unsurprising that Angerstein-Kosłowska *et al* have also studied the processes of anion adsorption and premonolayer OH adsorption on polycrystalline gold [1.66]. In particular, they studied the so-called “double layer” potential range of

voltammograms of Au in acid perchloric and sulphate media *Figure 1.10* produced in-house). They showed that, at potentials positive of the point of zero charge (pzc) but negative of peak O_{A1}, a sizable passage of charge could be observed, giving rise to a group of peaks designated D *Figure 1.10* [1.65]. They noted that the origin of the extra charge could not be linked to the under potential deposition of OH⁻ because; (a) the potential at which peaks D were observed did not change with solution pH; and (b) the amount of charge passed changed when the concentration of the adsorbing anion was increased.

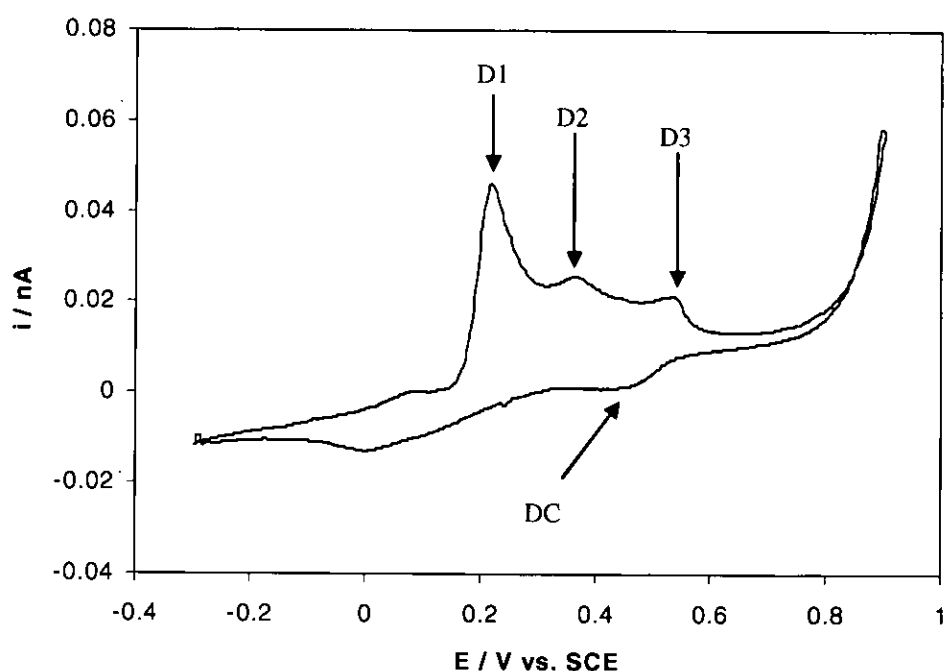
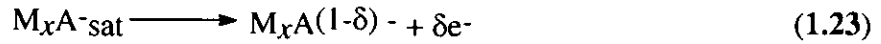


Figure 1.10:- A cyclic voltammogram of 2 mol m⁻³ acetohydroxamic acid with a pH of 1 using a 25 μm Au microdisc electrode at ν 1 mV/s was produced in house to represent the double-layer potential region observed by Angerstein-Kozłowska et al [1.66].

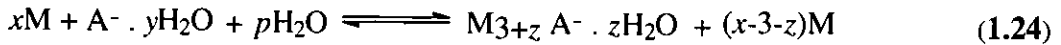
Angerstein-Kozłowska *et al* suggested that anion adsorption occurs via:



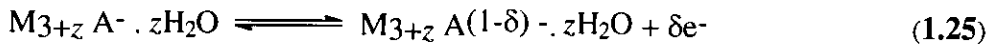
The charge transfer (δ) associated with the D peaks then only occurs once the surface anion population reaches saturation:



Analogous processes that explicitly involve the waters of hydration of the anion may be written as follows:

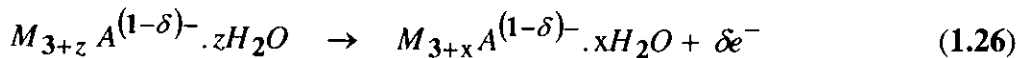


where z the hydration number = $y + p$.



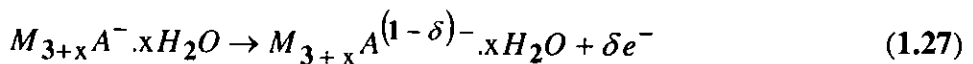
Thus it can be seen that the adsorbed anions disrupt the patches of H-bonded water network on the metal surface by abstracting H_2O molecules and forming, with H_2O strongly H-bonded complexes.

Strong chemisorption of the sulphate and perchloric anions, i.e. $\delta=1$ or near complete discharge of the anions in *Equations 1.24 & 1.26*, is geometry and symmetry facilitated on the Au(111) plane. As the concentration of discharged anions at the surface increases, the hydration number z can decrease, potentially leading to a reconstruction of the anion overlay lattice and giving rise to the sharp peak D1:



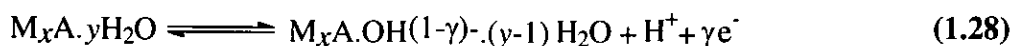
where, $z > x$ and x is a small number of hydration instead of z .

Further discharge of anions can then occur in the D2 peaks (*Equation 1.27*), but with a reduced number, x , of hydration H_2O 's instead of hydration associated with z :



At increased anodic potentials, the partial discharge of the H_2O H-bonded to the O atoms in the anions starts to be possible and occurs on the Au(111) face in two energy states, usually in a series of fast reactions which occurs at peaks O_{A1} and O_{A2} peaks *Figure*

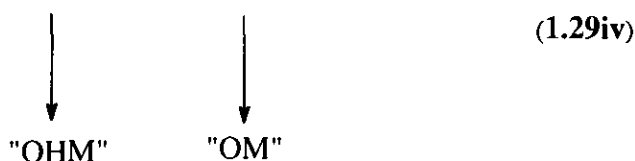
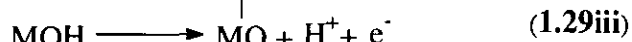
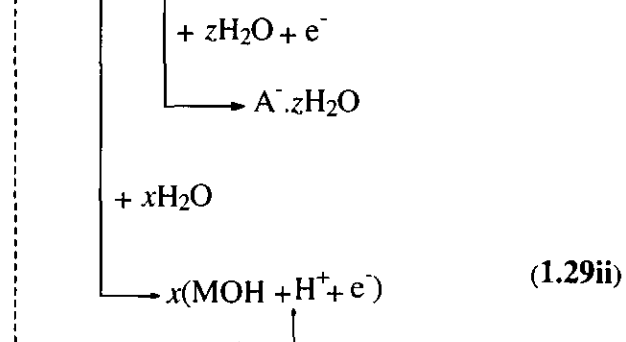
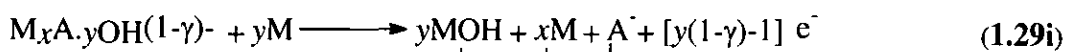
1.18.a&b. The net reaction, involving a fully discharged anion species, is shown in *Equation 1.28*



where γ is the partial charge of a species.

Similar processes can occur on polycrystalline Au surfaces and the mechanism by which peaks $O_{A1} - O_{A4}$ are produced through the discharge of anion-bonded water molecules on polycrystalline Au surfaces is described in detail in *Chapter 3*. However, a short summary will be presented here for the convenience of the reader.

The process in *Equation 1.29i* involves desorption of the anion followed by MOH or MO turnover. Angerstein-Kozłowska and co-workers suggest that this desorption involves a change in the H-bonding of the OH group to the O-atoms of the discharged oxyanions. As OH is converted to O and/or as MOH is converted to OHM, the local environment of the discharged anions changes, forcing them to be recharged and desorbed back into solution as soon as the process of gold oxide formation commences. The remainder of the gold oxide generation process is then as described by *Equations 1.29i – 1.29iv*.



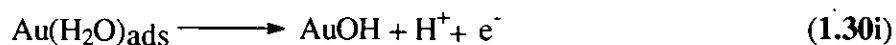
It must be noted that an alternative form of the anionic species $OH_{ads}^{(1-\gamma)-}$, posited by Angerstein-Kosłowska *et al* as being responsible for premonolayer oxide formation in acidic media [1.65], has been suggested. Burke and co-workers [1.92 & 1.93] have also investigated this premonolayer oxide region and they interpret their cyclic voltammetric data on the basis of the formation of a submonolayer of hydrous oxide at gold atoms in low coordination sites, i.e. adatoms of the form $[Au_2(OH)_9]^{3-}$ in base/acid media.

It is worth stressing with regard to premonolayer oxidation that Burke and Lee [1.93] were aware of strong spectroscopic evidence for such behaviour in the case of gold in base. However, no such evidence exists for the existence of premonolayer oxidation for gold in acid. Indeed, in Burke's experiments in acid solution, the generation of premonolayer adsorbed OH groups may also have been masked by the degree of adsorption of anions other than OH^- . Furthermore, a degree of uncertainty is not unreasonable, as the surface coverage by the hydroxy species in acid solution would be expected to be so minute that a precise determination of its composition, structure and state of charge would be extremely difficult.

1.7.1.2 - Electrochemical Quartz Crystal Microbalance Studies of Gold Oxidation

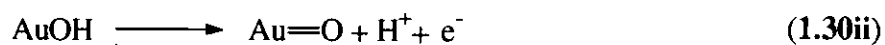
Application of the quartz crystal microbalance device to electrochemical kinetics was first conducted by Bruckenstein and Shay in 1984 in an investigation of the mechanism for the formation of the first monolayer of electroadsorbed oxygen at a gold electrode [1.37]. The mechanism was deduced by determining the in situ change in weight of the gold electrode during simultaneous cyclic voltammetry using the oscillating quartz crystal method. Using a 10MHz vacuum evaporated gold quartz crystal electrode in perchloric acid they observed an increase in resonator mass between +0.02 and +0.80 V (vs. SCE) in the anodic going sweep. They propose that this increase in mass, in the double layer region, is due to the adsorption of perchlorate ions.

According to Bruckenstein and Shay the onset of gold oxidation involves a one electron transfer process that oxidises adsorbed water to form an adsorbed hydroxyl radical *Equation 1.30i*;

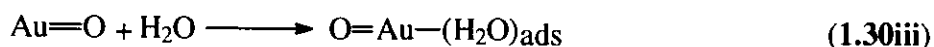


The change in mass accompanying the loss of a hydrogen ion during the first electron transfer process is too small to be detected.

The second electron transfer forms an oxide ion *Equation 1.30ii*;



Concurrent with *Equation 1.30ii* place exchange takes place and the oxide ion moves below the plane of the surface gold atoms and a water molecule is adsorbed onto the surface gold atom *Equation 1.30iii*;



The rate of the second electron transfer reaction and the subsequent place exchange reaction with consequent mass increase is not significant until nearly a monolayer of adsorbed hydroxyl radicals has formed.

Broadly in keeping with Angerstein-Koslowska the net effect of the Bruckenstein and Shay mechanisms is to introduce an oxygen atom into the gold lattice just below the electrode/solution interface. The mass increase observed in the potential range +1.10 V to +1.39 V (vs. SCE), is reported by Bruckenstein and Shay to be $(20.1 \pm 0.4) \times 10^{-9} \text{ g Hz}^{-1}$ which is equivalent to approximately one monolayer of adsorbed oxygen atoms.

The EQCM was also used in a similar study by Stockel and Schumacher [1.27], who reported that the mass increased only in the voltammetric region corresponding to gold oxide formation. However, in a subsequent investigation the authors [1.94] used a higher current sensitivity to record the cyclic voltammetric profile and they observed a small anodic wave in the pre-oxide region which developed simultaneously with a decrease in frequency. They concluded in agreement with Bruckenstein and Shay [1.37] and the findings of Angerstein-Koslowska that the specific adsorption of anions is responsible for the small anodic wave as well for the increase in surface mass. Stockel and Schumacher also reported that on the basis of capacitance and voltammetric data, Cl^- , Br^- and I^- are adsorbed reversibly in the preoxide region; however, they concluded that SO_4^{2-} is adsorbed irreversibly [1.94].

The formation of a gold oxide in a sulphuric acid medium was investigated by Bourkane *et al* [1.95] by using electrochemical impedance techniques. The experimental results obtained from this investigation were compared to those obtained by means of cyclic voltammetry. It was shown that gold oxidation occurs in three monoelectronic steps in sulphuric acid. According to Bourkane *et al* the impedance technique provided information on the number of elementary steps, on the number of adsorbed intermediates and an estimation of the rate constants.

A complementary EQCM-based impedance technique was employed in an investigation by Bourkane *et al* [1.96] in order to obtain information on the mass changes at the

electrode. Bourkane *et al* [1.96] used this study to verify their previously postulated mechanism of gold oxidation specifically:



where M represents gold and were AuOH, Au(OH)₂ respectively correspond to the adsorbed intermediates MX₁, MX₂, and Au₂O₃ is the final oxide formation MX₃. The mass change observed during this investigation, using a pure gold quartz crystal was measured as 60 ng cm⁻² over the potential range +0.40 to +1.10 V (*vs.* SSE). The change in mass involved during gold oxidation is of the same order as that observed by Bruckenstein and Shay [1.37].

EQCM was also employed in a study by Gordon and Johnson [1.68] to investigate surface mass changes during cyclic voltammetry in perchloric acid. They observed that a large increase in mass observed during the positive potential scan in the preoxide region at ≈+0.50 V (*vs.* SCE), well negative of the potential for the onset of formation of surface oxide (AuO), is independent of acid concentration and can be interpreted as the adsorption of water. Such adsorption could occur via hydrogen bonding of the H₂O molecules *Figure 1.11* to a submonolayer of hydrous oxide (AuOH), in low coordination sites, which were generated at low coordination number gold sites in the preoxide potential range. As such they explicitly state that their findings support the work of Burke *et al* [1.92 & 1.93] *vide supra*, whose submonolayer preoxide generation of AuOH groups at Au low coordination sites to explain certain electrocatalytic effects on Au.

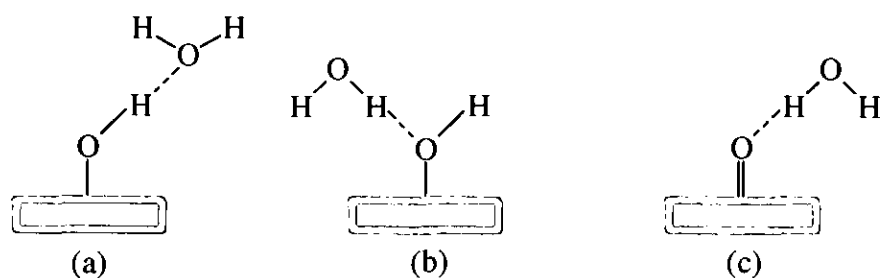
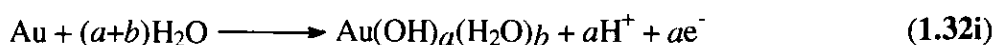


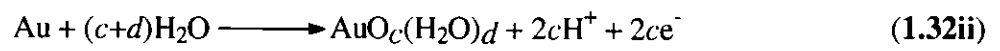
Figure 1.11:- Diagram suggesting possible H bonding of H₂O to (a, b) AuOH formed in the peroxide region $\approx +0.90$ V (vs. SCE) and (c) AuO formed in the oxide formation region $+1.60$ V (vs. SCE) [1.68].

Gordon and Johnson also investigated the EQCM response of Au in HNO₃ and CF₃SO₃H media, the anions of which (i) are significantly different masses from HClO₄, (ii) have been suggested as being incapable of chemisorbing at the gold surface by Yeager *et al* [1.97] on the basis of in-situ FTIR data. The data obtained from cyclic voltammetry and voltamassograms for repetitive measurements were virtually independent of the identity and concentration of the acids chosen.

Hence, Gordon and Johnson in contradiction to Bruckenstein and Shay [1.37] and Stockel and Shumacher [1.94], concluded that the observed change in mass in the preoxide potential range is not the result of adsorption of anions from these supporting electrolytes and that, the frequency changes observed in the preoxide region $< \approx +0.90$ V (vs. SCE) and the oxide formation region $\approx +1.60$ V (vs. SCE) were as a result of increased surface hydration and of the formation of Au(OH)_a and AuO_c respectively, where *a* and *c* represent the fractional surface coverages by the hydroxyl and oxide species respectively.

Gordon and Johnson therefore suggested that the following reactions occur during the positive scan region at $< \approx +0.90$ V (vs. SCE) (Equation 1.32i) and in the range $+0.90$ to $+1.60$ V (vs. SCE) (Equation 1.32ii):





where b and d represent the increase in the average effective number of H_2O molecules adsorbed per Au site as a consequence of the anodic reactions.

1.7.2 - Gold Dissolution

Gold is known to have an excellent inherent chemical stability. However, this becomes unstable and dissolves in the anodic positive potential region [1.61, 1.62, 1.98, 1.99, 1.100, 1.101, 1.102 & 1.103] especially in solutions containing acidic media and trace chloride ions [1.90]. This property is of particular interest to the electronic industry for design, manufacture and production of certain thin films and integrated circuits.

The first investigation into gold oxidative dissolution electrochemistry using a quartz crystal microbalance for cyclic voltammetric and gravimetric responses was indirectly conducted by Bruckenstein and Shay [1.37]. They observed during their investigation into the mechanism for the formation of the first monolayer of electrosorbed oxygen at a gold electrode in 200 mol m⁻³ perchloric acid, they observed a difference between the initial and final frequencies at +0.02 V (vs. SCE). They posited that some dissolution of gold occurs during the electrogeneration and reduction of gold oxide, some of which could be redeposited from solution after the reduction of the gold oxide surface phase.

Initial direct investigation into the dissolution of gold during anodic oxidation was conducted by Heumann and Panesar potentiostatically in sulphuric acid containing various concentrations of chloride ion [1.104]. They proposed that the gold dissolution reaction involved both the 1e⁻ and the 3e⁻ oxidation pathways in the anodic potential region of $E^0 = +1.00$ V to $E^0 = +1.15$ V (vs. RHE) respectively.



A further investigation was conducted by Gaur and Schmid [1.105] in the potential region of +1.00 to +1.20 V (vs. SCE) in 100 mol m⁻³ HClO₄ containing 10 to 200 mol m⁻³ KCl. From their observations, they suggest that gold dissolution and oxide formation are competitive reactions in the anodic oxidative potential region and that gold is dissolved as AuCl₄⁻ (Equation 1.33b) at oxygen-free sites on the gold electrode surface.

A rotating-ring disc electrode system was employed by Cadle and Bruckenstein [1.101], to study the behaviour of the gold electrode in $200 \text{ mol m}^{-3} \text{ H}_2\text{SO}_4$, containing trace amounts of Cl^- ion. They detected dissolved Au(III) (Equation 1.33a) species at the gold ring electrode held at -0.20 V (vs. SCE) when cycling the disc in the range of $+1.00 \text{ V}$ (vs. SCE). They also encountered trace amounts of Au(I) (Equation 1.33b) species on the disc during the cathodic scan. Frankenthal *et al* [1.102 & 1.106] reported potentiostatic measurements from i vs. E curves, that in acidic and basic sulphate solutions containing additions of HCl and chloride salt gold is dissolved as Au(I) (Equation 1.33a) species at positive potentials less than $+0.80 \text{ V}$ (vs. SCE) and an Au(III) species (Equation 1.33b) at positive potential region $+1.10 \text{ V}$ (vs. SCE). More interestingly they propose that in the absence of Cl^- gold is oxidised to a soluble Au(III) species or to a film of $\text{Au}(\text{OH})_3$ at potentials in the passive and transpassive regions.

Further investigation of the anodic dissolution and passivation of gold electrodes, in neutral and acidic sulphate solutions with and without Cl^- ions, using a rotating disc electrode was studied by Loverecek *et al* [1.103]. They confirmed a diffusion activation control of the dissolution process and suggested that AuCl_4^- (Equation 1.33b) was the final dissolution product and that no dissolution process was observed in acidic media without Cl^- ion, with consequent probable formation of a layer of the type Au_2O_3 .

Diaz *et al* [1.100] studied gold dissolution and deposition on a gold coated Pt rotating disc electrode in HCl solutions with different Au(I)/Au(III) molar ratios, pH values and Cl^- concentrations. From their findings they proposed that gold dissolved as AuCl_2^- (Equation 1.33a) and as AuCl_4^- (Equation 1.33b) at more positive potentials. Using in situ surface-enhanced Raman spectroscopy (SERS) measurements, Loo [1.107] found that both the AuCl_2^- (Equation 1.33a) and AuCl_4^- (Equation 1.33b) complexes were detected in a solution of $100 \text{ mol m}^{-3} \text{ KCl}$ on a gold electrode surface during the anodic

cycle in the presence of Cl^- ion. At high potentials greater than +0.90 V (*vs.* SCE) the surface complexes were predominately found to be AuCl_4^- ions (*Equation 1.33b*).

Interestingly Trevor *et al* [1.108] and Honbo *et al* [1.109] have independently investigated the dissolution process of a monocrystalline (Au 111) gold crystal surface in a solution of HClO_4^- with and without trace amounts of Cl^- ion using in situ scanning tunnelling microscopy (SIMs). They propose that the terraces of the gold substrate in a Cl^- containing solution seemed smoother than the terraces in Cl^- free solution.

Finally, Ye *et al* [1.88] undertook an investigation into the dissolution process of a gold electrode in perchloric acid solution containing various chloride ion concentrations using in situ EQCM. Ye *et al* [1.88] report that gold dissolution occurs via a $3e^-$ oxidation process (*Equation 1.33b*) and that they could find no evidence for a $1e^-$ dissolution (*Equation 1.33a*).

Initially Ye *et al* [1.88] measured standard cyclic voltammetric and voltamassogram profiles in a perchloric acid solution containing no chloride ions at 50 mV/s. The observed CV and voltamassogram was similar to that obtained by previous workers [1.26, 1.37, 1.78 & 1.96] for gold oxidation and reduction processes. During the gold oxidation phase a mass increase was observed from the voltamassogram between +1.20 V and +1.70 V (*vs.* RHE), conversely as reduction of the gold oxide takes place a mass loss was detected between +1.20 V to +1.10 V (*vs.* RHE). The initial and final frequency responses after one potential sweep were found to be near its starting value.

Upon the introduction of 100 mol m^{-3} of chloride ion the CV remains relatively unchanged. However, the voltamassogram response shows a surface mass decrease starting at the onset of the gold oxidation current at +1.25 V (*vs.* RHE). Calculation of the mass change and the charge passed indicate a $3e^-$ gold dissolution process. The rate of mass loss becomes smaller after the second gold oxidation anodic peak at +1.53 V (*vs.* RHE), with the mass became nearly constant around +1.60 V (*vs.* RHE) due to

passivation brought about by the formation of the gold oxide layer. Ye *et al* [1.88] reports a mass loss of ~300 ng during the anodic cycle from +0.8 to +1.7 V (*vs.* RHE).

This was followed by a further mass loss during the gold oxide reduction potential range of the reverse sweep. The mass decreased upon the appearance of the first gold oxide reduction peak at +1.20 V (*vs.* RHE). The surface mass continued to decrease until +1.14 V (*vs.* RHE) where a current minimum between the first and the second anodic peaks was observed.

The surface mass started to increase, as the potential moved negative of +1.14 V (*vs.* RHE), due to the redeposition of the soluble gold species produced during the oxide stripping phase. The mass did not return to its original value at +0.80 V (*vs.* RHE) and a net mass loss of ~200ng was reported after a potential cycle to +1.80 V (*vs.* RHE).

Ye *et al* also reported the potential dependence of the current and the mass change as the sweep rate was decreased. They showed that as the sweep rate was reduced from 20, 10 to 5 mV/s in a 100 mol m⁻³ HClO₄ solution containing 1 mol m⁻³ Cl⁻ the anodic and cathodic peaks shifted to more negative and positive potentials respectively. Also the relative peak heights became larger for the first oxide peak at +1.30 V (*vs.* RHE) than that of the second one at +1.50 V (*vs.* RHE). Furthermore, it was observed that the lower the sweep rate the larger the observed capacitance (*iv*⁻¹) (*i.e.* currents were divided by their respective sweep rates) of both the anodic and cathodic peaks and the larger the mass loss.

Ye *et al* [1.88] also observed a Cl⁻ concentration dependence of mass loss. As chloride ion concentration was increased and sweep rate decreased, an anodic peak was observed at +1.30 V (*vs.* RHE), due to the instability of the gold oxide, which as reported could be destroyed by concentrated Cl⁻ solution.

1.8 - NAFION[®] POLYMER FILMS

The first report of an EQCM study of a polymer film on an electrode was by Kaufman *et al* [1.38] who observed the transport of both ionic species and solvent in polypyrrole during electrochemically induced doping and undoping. Their work demonstrated the potential of EQCM in studies of the solvent/solute transport processes which accompany the injection, or removal of electrons in thin polymer films. It has been shown that it is possible to use the EQCM to monitor electrochemically initiated nucleation and growth of polymer films, the transport of charged species, solvent, and other neutral species which occur during the redox chemistry of these films, and chemical reactions within polymer films [see 1.15 & 1.23 and references therein]. Furthermore, correlation of the compositional information gained from the mass measurement with typical electrochemical observables (such as charge, current, *etc.*) provides a tool with which to determine mechanisms of the processes mentioned above.

Nafion[®] is a perfluorosulfonic acid cation exchange membrane that offers both outstanding chemical resistance and application in a variety of electrolytic processes. This permselective cation exchange membrane permits the migration of cations from the anode to the cathode, while blocking the migrations of anions in the opposite direction.

The application of EQCM to determine the directionality of ion transport and the use of this information to manipulate charge transport rates was the subject of a study of the composite films of Nafion[®] and poly(aniline) [1.110]. Earlier work on ion transport during switching in poly(aniline) revealed that anion transport was dominant at pH 1 to 10 [1.109]. It was considered that higher charge transport rates could be attained by

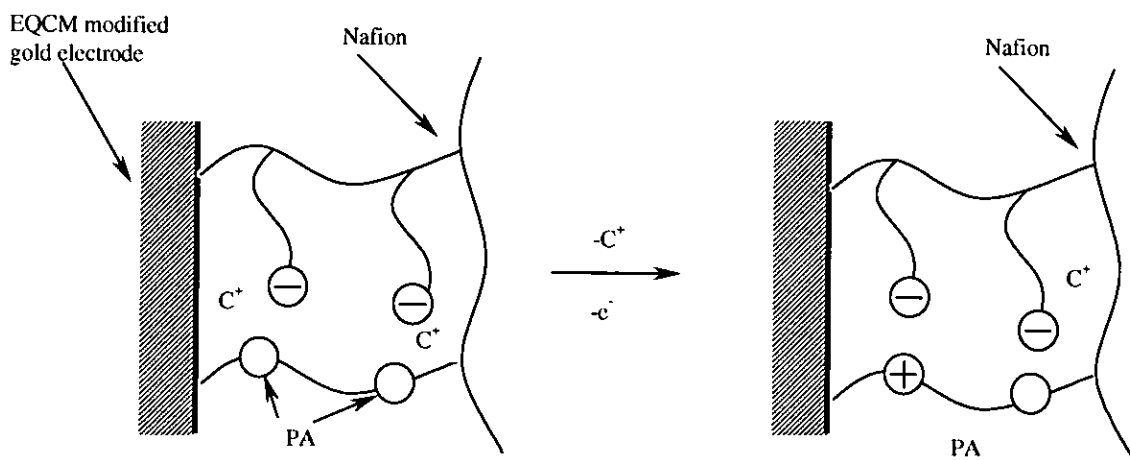


Figure 1.12: Schematic depiction of cation transport during switching in a PA/Nafion® composite film.

manipulating the ion transport in such a way as to achieve electroneutrality via proton transport, the thought being that the higher mobility of the proton compared to other ions would allow for faster switching. Hence, as the permselectivity of the cation exchange membrane should preclude the rapid transport of anions within the Nafion® film, the switching reaction should be accompanied solely by cation exchange.

This phenomena was also investigated by Reynolds and co-workers [1.111] when they studied electrochemically synthesised copolymers of pyrrole and 3-(pyrrol-1-yl)-propanesulfonate in which the pendent sulfonate groups were neutralised with Li^+ , K^+ or H^+ . By the use of EQCM they monitored ion transportation during the switching process and demonstrated that cation transport was the dominant mode of ion transport during the switching reaction. In this latter system, the cations exist in the film as the counter ions of the fixed sulfonate sites of the Nafion® matrix. In the former system, *i.e.* in acidic solutions, protons would be the only available cations, so they should be the only species involved in ion transport ***Figure 1.12.***

Such a model of ion transport based on the maintenance of electroneutrality is an over simplified view of the multiplicity of possible mass transport processes that can occur in such films during redox switching. The over simplification offered by this explanation was highlighted by Bruckenstein and Hillman [1.112], who through thermodynamic

analysis demonstrated that electroneutrality alone cannot account for all of the transport processes in thin films.

It has been previously observed that the electrochemical responses exhibited by multiple charged electroactive counter ions incorporated in Nafion[®] coatings on electrodes can change dramatically with the water content of the coatings. The sensitivity of the responses to the state of hydration of the coatings is high when the electroactive counter ion is the only counter ion present in the Nafion[®] coating.

A factor that influences the electrochemical responses of Nafion[®] coatings containing electroactive counter ions is the ionic impedance of the coatings which is a strong function of their water content. Shi and co-workers [1.113 & 1.114] proposed a model that accounts for the cyclic voltammetric behaviour of Os(bpy)₃^{3+ / 2+} loaded Nafion[®] coatings. This model correlates the response of the Nafion[®] with the impedance of the coating and the mass changes resulting from electrochemically induced incorporation of water into the coatings *Figure 1.13*. The model is a function of the structure of Nafion[®], which consists of pores connected by narrow channels through which the counter ions move when ionic current is passed through the coatings.

The schematic model of *Figure 1.13* thus depicts the structure of a freshly cast Nafion[®] film in its protonated form (A). This coating can be converted to (B) by immersing in pure water for a few minutes producing a fully hydrated film. Shi *et al* [1.114] propose that cation exchange will be facile with a fully hydrated membrane because there is adequate water present to hydrate both the sulphonate groups and the counter ions.

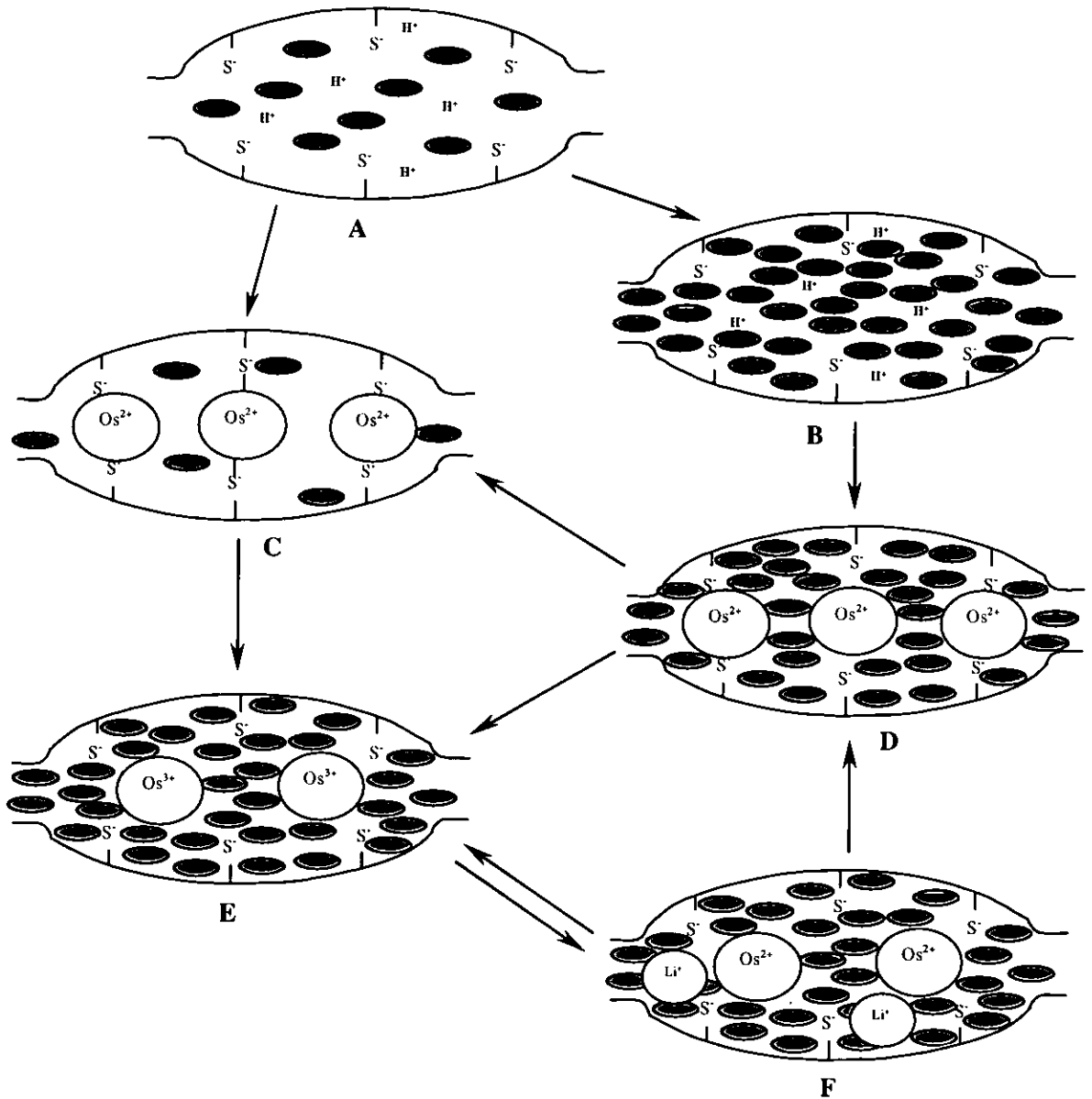


Figure 1.13: *The schematic depiction of the states of hydration of Nafion® coatings fully saturated with $Os(bpy)_3^{2+/3+}$ ($Os^{2+/3+}$) and subjected to the indicated treatments. Where Li^+_{aq} (Li^+), H^+_{aq} (H^+), SO_3^- (S^-) and H_2O (●) [1.114].*

Thus, (B) can be readily converted to (D) by exposure to the counter ion solution. Water is expelled from (D) due to the exchange of larger and hydrophobic cations *i.e.* $Os(bpy)_3^{2+}$, for the highly hydrated protons. However, if the newly cast Nafion® coating is exposed to the cation prior to hydration (C) is believed to be formed. Proportionately more water is expelled from structure (C) than that of (D) because of the stronger tendency of the Nafion® matrix to incorporate the more hydrophobic cations. The

resulting membrane will be dehydrated as the sulphonate groups lose a portion of their hydration spheres to bind strongly to the cations, so forming a 'Nafionate salt'. Such dehydrated films have a high (ionic) impedance because of the low mobility of the cations in this salt.

The conversion of structure (A) to (C) requires a much longer time than that of structure (A) to (B). This is due to the large tightly bound counter ions blocking the narrow channels within Nafion[®] through which the incorporating cations and departing hydrated protons and water molecules must pass in order to produce the fully loaded, dehydrated structure shown in (C).

The conversion of structure (D) to (C) by air drying of (D) proceeds slowly. This is because the water molecules leaving the hydrated coating forms a Nafionate salt structure at the outermost portion of the film. Thus, the resulting clogging reduces the rate of further water loss. However, exposure to water at these Nafionate salt sites causes partial rehydration and a recommencing of ionic exchange.

Structure (E) results from the electrooxidation of either structures (C) or (D). When the fully hydrated coating, (D), is oxidised, the expulsion of one-third of the $\text{Os}(\text{bpy})_3^{2+}$ cations is accompanied by the incorporation of water molecules into the coating. The electrooxidation of structure (C) induces the incorporation of such large amounts of water molecules that the mass of the membrane increases despite the expulsion of the massive $\text{Os}(\text{bpy})_3^{2+}$ cations.

The electroreduction of structure (E) in the presence of supporting electrolyte leads to structure (F), in which Li^+ cations from the supporting electrolyte are incorporated to maintain electroneutrality.

Structures (E) and (F) constitute steady-state structures that can be repeatedly converted by electrochemical cycling without further structural changes.

1.9 - HYDROXAMIC ACIDS

1.9.1 - Introduction

Hydroxamic acids play an important role in both chemistry and biology. They have been used in the past as colorimetric and gravimetric reagents in analytical chemistry [1.115]. They have also been extensively studied for their role in the biological transport of iron in certain strains of yeast and bacteria [1.116].

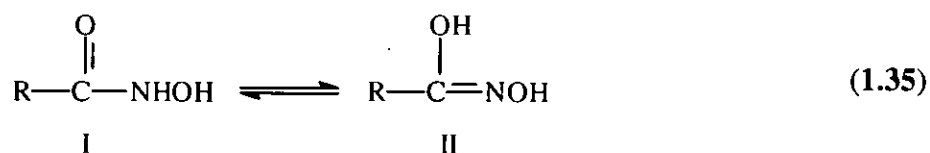
The first example of a hydroxamate group was oxalohydroxamic acid isolated by Lossen in 1869 [1.117] from the reaction of ethyl oxalate and hydroxylamine. Hydroxamic acids are more typically formed by the reaction of an activated acyl group with hydroxylamine (*Equation 1.34*) [1.118]



where X is typically Cl. This type of preparation is carried out under basic conditions with the extraction of the hydroxamic acid by direct precipitation after acidification.

1.9.2 - Structure of Hydroxamic Acids

Between the discovery of the hydroxamate group in 1869 and the advent of spectroscopy, great debate existed over the structure of hydroxamic acids. Yale attempted to end this controversy in 1943 when he proposed that two tautomers existed (*Equation 1.35*) [1.118]. Evidence obtained from modern techniques (XRD, UV, IR, MS and NMR) indicated that tautomer I was the predominant species in both the solid state and in solution [1.119 & 1.120].



1.9.3 - Main Reactions

1.9.3.1 - Hydrolysis

Acid or base catalysed hydrolysis of hydroxamic acids yields carboxylic acids and hydroxylamine [1.116, 1.117, 1.121, 1.122 & 1.123]. Difuria [1.123] suggests that the acid catalysed hydrolysis occurs via nucleophilic attack of water on the N-protonated conjugate acid. This step is the rate determining step and gives rise to a tetrahedral intermediate, which then yields the products almost irreversibly *Figure 1.14*.

Base catalysed hydrolysis takes place on either the un-ionised hydroxamic acid or the deprotonated hydroxamate anion [1.122 & 1.123].

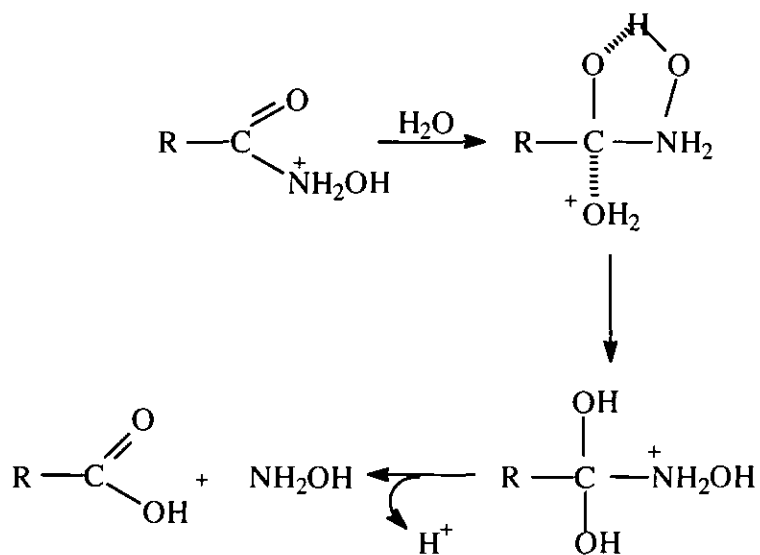


Figure 1.14: The scheme depicts the acid catalysed hydrolysis occurring via nucleophilic attack of water on the N-protonated conjugate acid.

This anionic mechanism is however, open to criticism since the structure of the anion has not been settled. Nevertheless, if the anion is the reacting species, the tautomer shown is the most suitable for nucleophilic attack, as the negative charge is located at the remote atom

Figure 1.15.

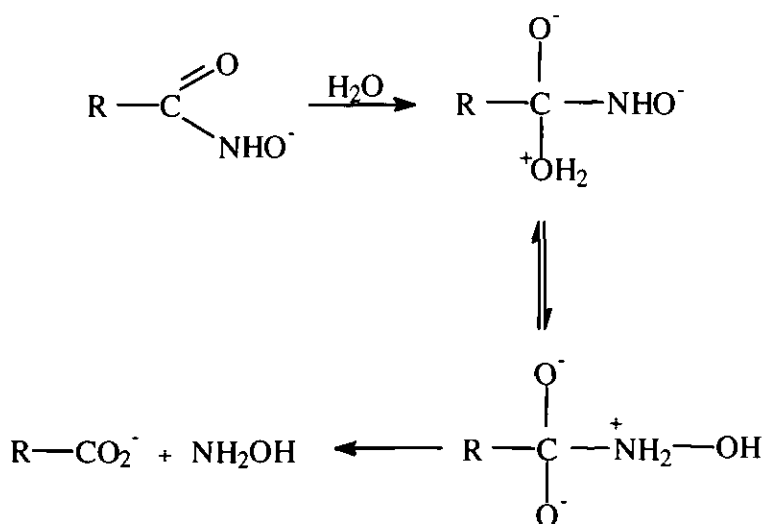


Figure 1.15: The tautomer shown is the most suitable for nucleophilic attack, as the negative charge is located at the remote oxygen atom.

1.9.3.2 - Oxidation Reactions

Minor *et al* [1.124] proposed a mechanism for chemical oxidation of hydroxamic acids which involved the formation of the nitroso compound followed by intramolecular rearrangement. However, two other papers on the subject agreed that the mechanism might involve the formation of a free radical centered on the nitrogen, the subsequent dimerisation and intramolecular rearrangement [1.125 & 1.126].

In 1971 Oliver and Waters [1.127] made a detailed study of the mechanism and products of the oxidation of $\text{PhCH}_2\text{-CO-NHOH}$ using alkaline ferricyanide and aqueous cerium ammonium nitrate. The following schemes were presented **Figure 1.16**.

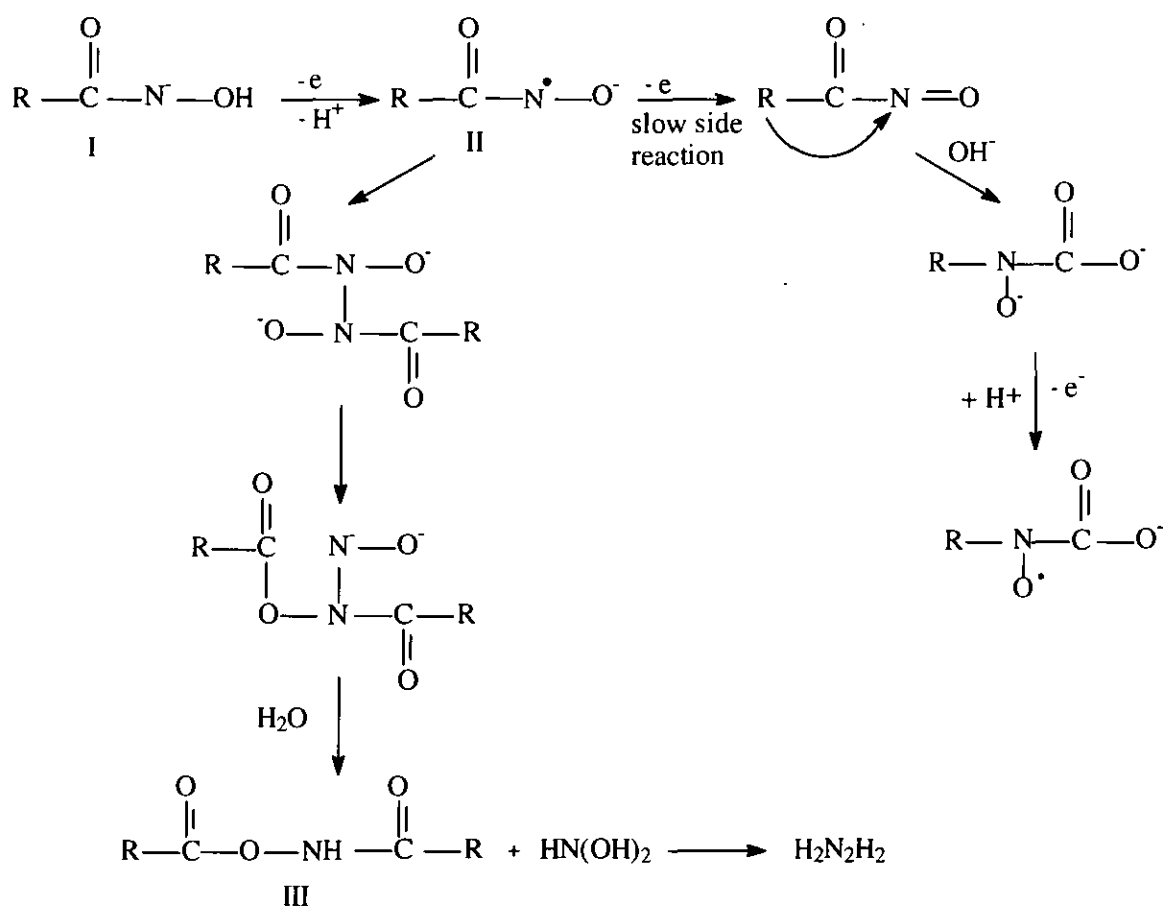


Figure 1.16: A detailed scheme of the mechanism and products of the oxidation of $\text{PhCH}_2\text{-CO-NHOH}$ using alkaline ferricyanide and aqueous cerium ammonium nitrate.

The slow side reaction occurs via the mechanism earlier proposed for the main oxidation by Minor *et al* [1.124].

Using aqueous ceric ammonium nitrate oxidising agent in neutral ethanol again results in formation of compound (III) as shown in *Figure 1.16* but in lower yield and with further hydrolysis to the carboxylic acid *Figure 1.17*.

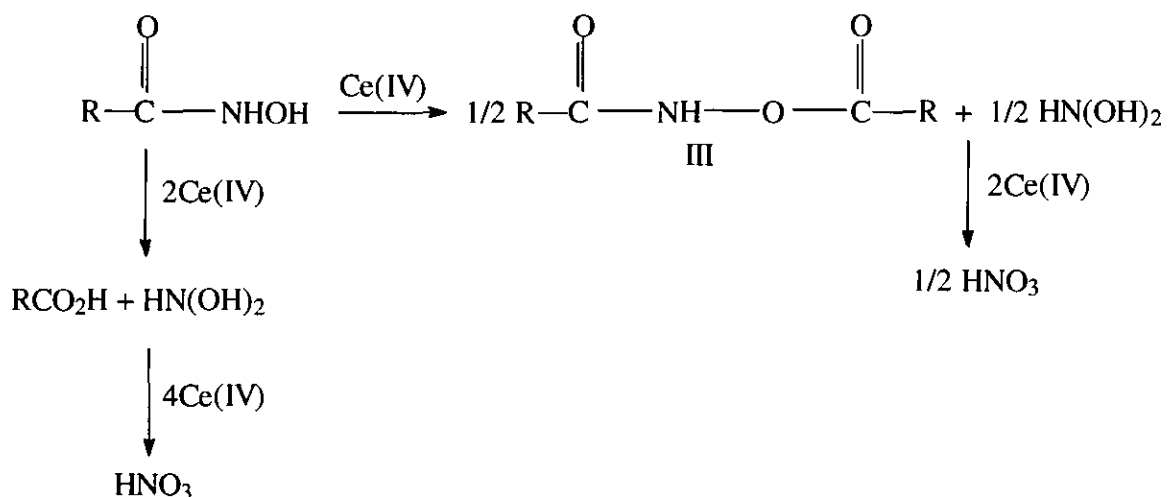


Figure 1.17: The scheme depicts the slow side reaction occurring via a mechanism previously proposed as the main oxidation mechanism.

For the N-substituted acids studied, again a dimerisation is postulated, but this time the transient radical is located on the oxygen atom *Figure 1.18*.

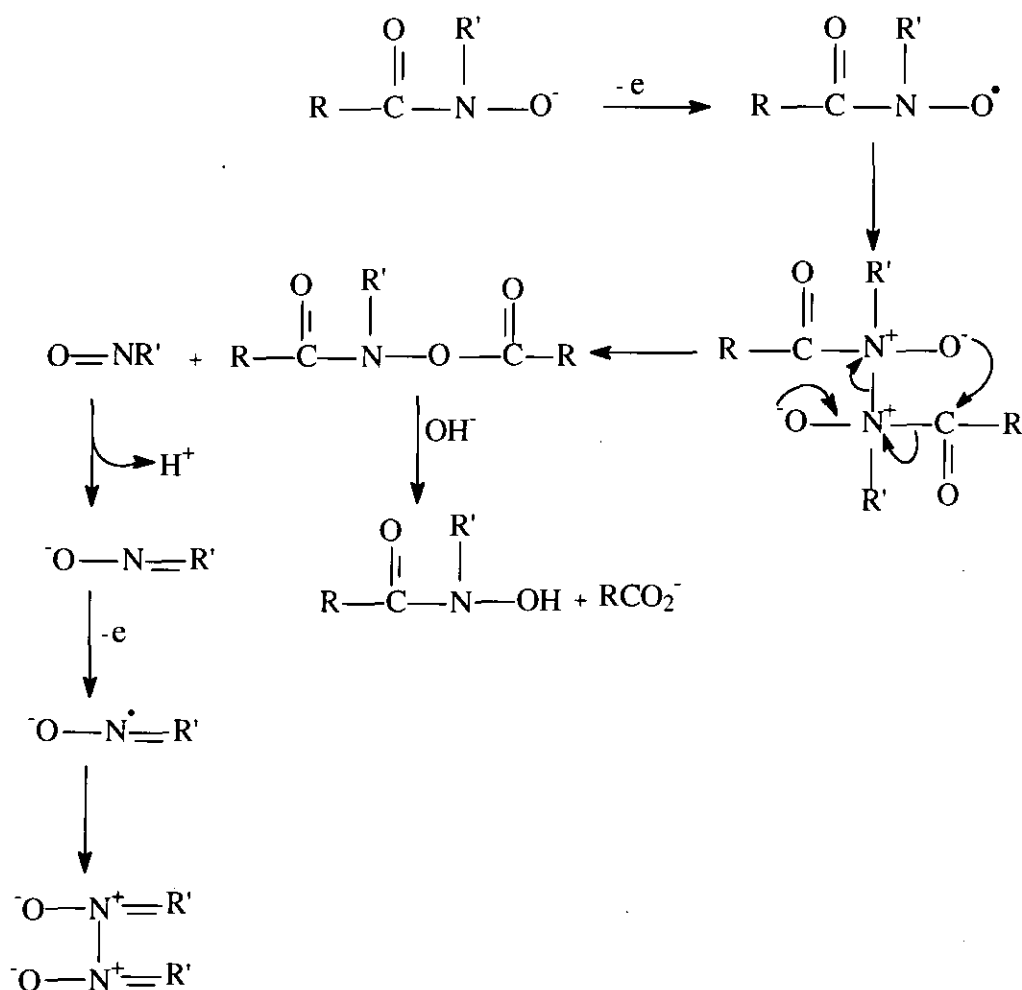


Figure 1.18: For *N*-substituted acids dimerisation is proposed, but the transient radical is located on the oxygen atom.

The electrochemical behaviour of hydroxamic acids has received little attention in the past and the majority of that which has been published has concentrated on the reduction reaction. Much of the early work was conducted by Prytz and Osterud [1.128 & 1.129].

In order to develop an electrochemical method for determination of hydroxamic acids, Prytz and Osterud [1.128 & 1.129] developed a polarographic technique using as a supporting electrolyte, tetraalkylammonium salts, in ethanoic solution so allowing measurements down to ≈ -2.5 V (vs. SCE). They found that the two acids studied, acetohydroxamic acid (CH_3CONHOH), and propinohydroxamic acid ($\text{C}_2\text{H}_5\text{CONHOH}$), gave two distinct waves;

however only the first was at low enough potential to be clearly defined and suitable for analytical purposes.

They explained their results by assuming that it is the hydroxamic tautomer, which is involved in the reduction process, *i.e.* that the process will affect the carbon-nitrogen double bond. By 1959 the same authors [1.130] reported a polarographic method for the determination of acetohydroxamic acid in the presence of hydroxylamine, but no attempt was made to elucidate the electroreduction mechanism.

It was not until 1977 that Japanese workers Ozaki and Masui published the results of *electro-oxidation* studies of some hydroxamic acids [1.131]. Using a glassy carbon working electrode and ethyl-tri-n-butylammonium tetrafluoroborate as supporting electrolyte, unsubstituted, O-substituted and N-substituted hydroxamic acids were investigated, and the following mechanisms were proposed **Figure 1.19, 1.20 & 1.21**.

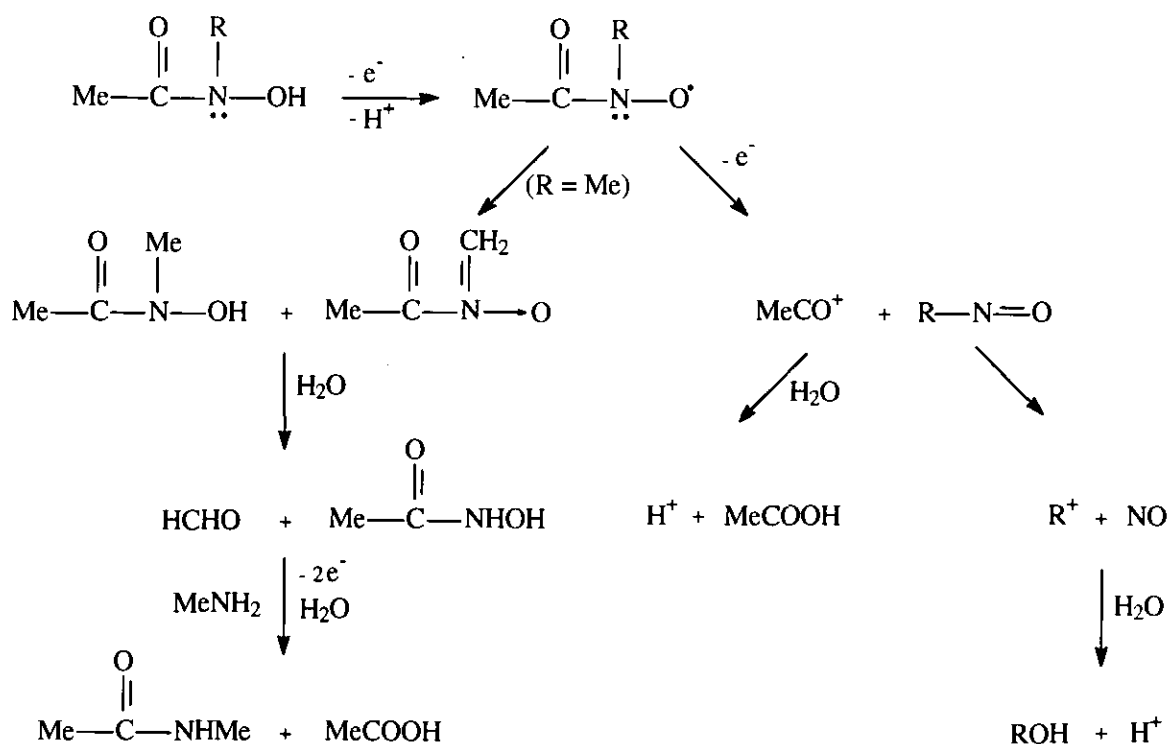


Figure 1.19: Electrooxidation mechanism for N-substituted hydroxamic acids by Ozaki et al [1.131].

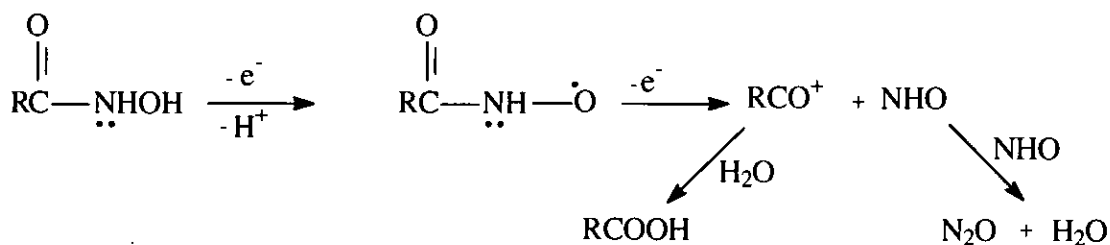


Figure 1.20: Electrooxidation mechanism for unsubstituted hydroxamic acids by Ozaki et al [1.131].

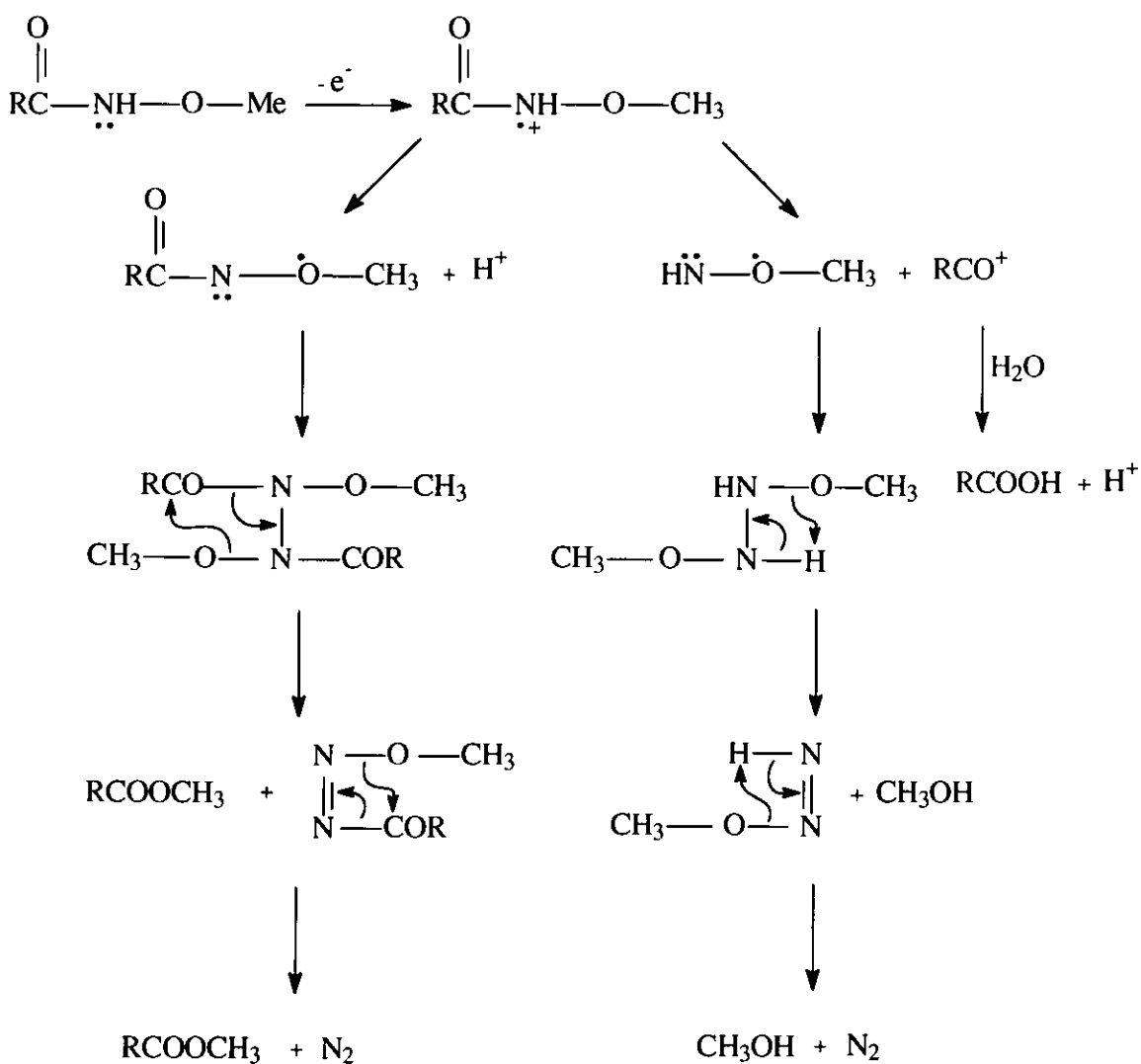


Figure 1.21: Electrooxidation mechanisms for O-substituted hydroxamic acids by Ozaki et al [1.131].

Although a comprehensive study of the products formed during constant potential electrolysis was carried out using mainly gas chromatography for identification, no attempt was made to study the acid-base behaviour of the hydroxamic acids.

Masui *et al* later reported [1.132 & 1.133] effects of a number of bases on the oxidation potentials of some hydroxamic acids. They found that the anodic oxidation of hydroxamic acids in a base solution acquired an irreversible wave at a less anodic potential than that observed in the absence of base. As the base acid complex is more easily oxidised than the acid, the difference in the potential between these two peaks can be taken as a measure of the hydrogen bond strength: therefore, the stronger the base the greater the difference in potential. Furthermore, it was found from plots of peak current vs. base concentration that the ratio of base to acid was 1:1 or for an acid having more than one acidic proton, 1:1 for each of the protons.

More recently Amberson and co-workers have published the results of electrooxidation studies on some hydroxamic acids [1.8 & 1.134]. Using cyclic voltammetry and a glassy carbon working electrode to investigate the electrooxidation of Glutaro and Adipo dihydroxamic acids, they identify two oxidation processes, a two electron process and a single electron process, the latter occurring at a more positive potential than the former.

1.9.3.2.i - The Two Electron Process

Amberson *et al* propose that the two electron oxidation of the neutral hydroxamate group involves the loss of a proton, followed by the formation of a cationic nitroso compound. This compound then reacts with the water to form a carboxylic acid and possibly hydroxylamine or nitrous or nitric acid *Figure 1.22*.

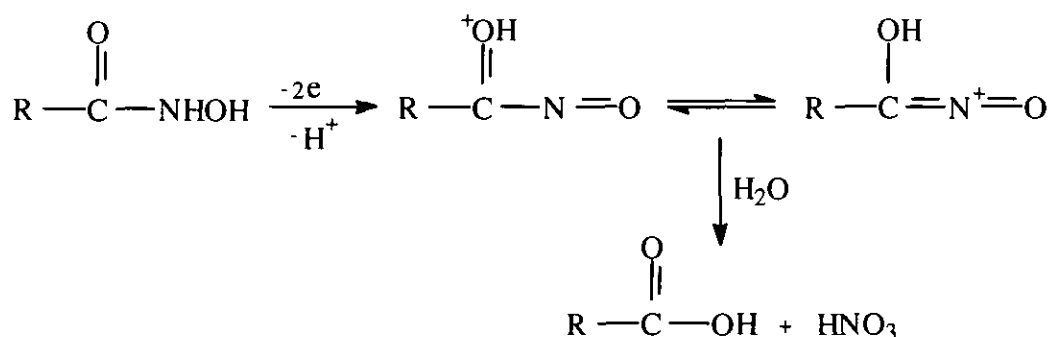


Figure 1.22: A proposal for a two electron oxidation of a neutral hydroxamate group involving the loss of a proton, followed by the formation of a nitroso group.

Further results obtained by Amberson indicate that the two electron oxidation does not occur easily in acidic solution. As the protonated cation form of the hydroxamic acid predominates, this process would necessitate the removal of two protons from the hydroxamate group to enable the formation of the cationic nitroso compound.

After ionisation of the hydroxamate group in neutral or basic solution the oxidation proceeds without the involvement of protons **Figure 1.23**.

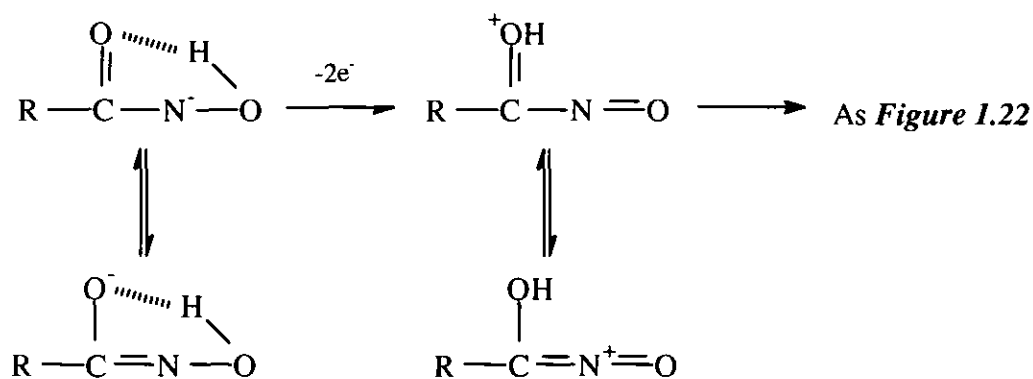


Figure 1.23: After ionisation of the hydroxamate group the oxidation proceeds without the involvement of any protons.

1.9.3.2.ii - The One Electron Process

The one electron oxidation of both the cation and the neutral hydroxamate group involves the loss of one proton, and is probably followed by a dimerisation reaction as proposed by Oliver and Waters [1.127] *Figure 1.24 & 1.25*.

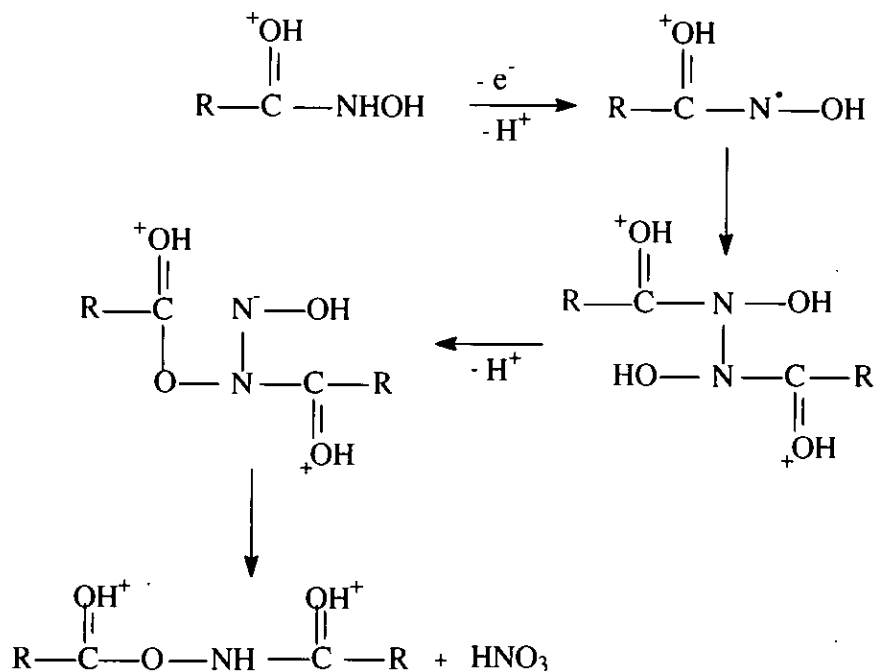


Figure 1.24: The one electron oxidation of both the cation and the neutral hydroxamate groups involves the loss of one proton.

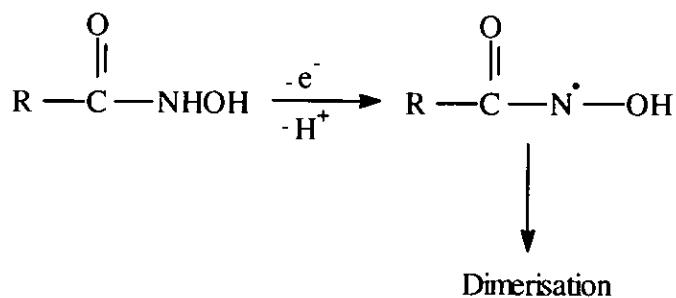


Figure 1.25: This mechanism is followed by a dimerisation reaction.

After ionisation of the hydroxamate group to form the anionic species the electrode reaction proceeds without the release of a proton *Figure 1.26*.

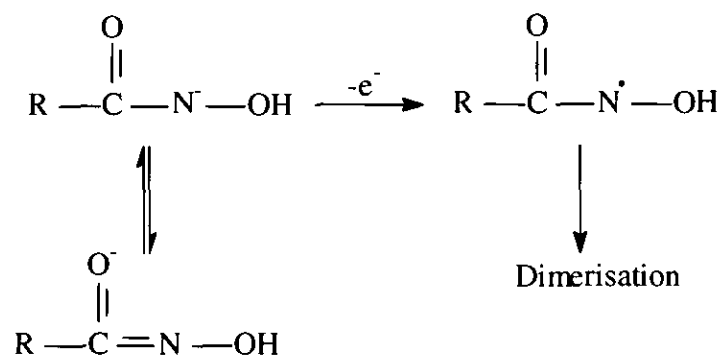


Figure 1.26: The ionisation of the hydroxamate group proceeds without the release of a proton.

1.10 - CO-ORDINATION CHEMISTRY OF IRON(III)

Monohydroxamic acids (HA) form either 3:1 (orange-brown), 2:1 (red-brown), or 1:1 (purple) HA:Fe complexes, depending on the pH and the relative proportions of HA to Fe [1.135]. It has been observed from the measurement of stability constants that hydroxamic acids have a high affinity for spherically symmetrical 3^+ ions. Thus they exhibit a high specificity for iron(III) [1.136].

X-ray studies of iron(III) complexes with both synthetic and naturally occurring hydroxamic acids show that the hydroxamate ion binds to the iron to form a five membered chelate ring.

Figure 1.27 [1.137, 1.138 & 1.139].

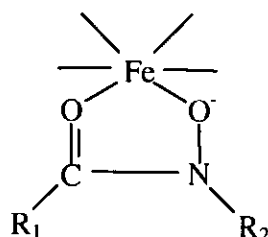


Figure 1.27: The hydroxamate ion binds to the iron to form a five membered chelate ring.

Thermodynamic and kinetic studies have been carried out on several hydroxamic acids to systematically investigate the electronic influence of substituent on the carbon (R_1) and the nitrogen (R_2) atoms, on the stability's of their iron(III) complexes [1.140 & 1.141]. It was found that the stability of the complex increases with the electron donor ability of R_2 . This can be interpreted in terms of the substituent's ability to delocalise the lone pair of electrons on the nitrogen. Three resonance forms illustrate this **Figure 1.28**:

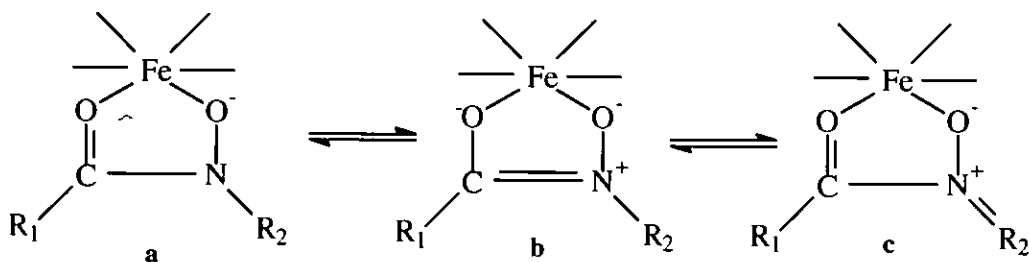


Figure 1.28: The resonance forms of the iron / hydroxamate five membered chelate ring.

As R_2 becomes more electron donating, resonance form (b) becomes important; there is an increase in electron density on the carbonyl oxygen which increases the oxygen-iron bond strength, which in turn results in higher stability constants. But if R_2 becomes more electron accepting, resonance form (c) predominates, resulting in lower electron density at the carbonyl oxygen and consequently lower stability constants.

Similar results were obtained from the investigation of the influence of the R_1 group on complex stabilities *i.e.* As R_1 becomes stronger electron donor, complex stability increases.

Therefore the greatest complex stability, both thermodynamically and kinetically, is achieved when both the R_1 and R_2 groups are capable of electron donation, although the R_2 plays the dominant role through inductive stabilisation of the nitrogen lone pair delocalisation into the carbon-nitrogen bond.

1.11 - APPLICATIONS OF HYDROXAMIC ACIDS

Hydroxamic acids have proved versatile reagents in both inorganic and organic analysis. The use of hydroxamic acids for the extraction and spectrophotometric determination of various metal ions (V, Al, Bi, Cd, Ce, Co, Cu, Fe, Hf, Mn, Hg, Mo, Nb, Pa, Sn, Ti, W, U and Zr.) was extensively reviewed by Brandt in 1960 and Agrawal in 1980 [1.142 & 1.143]. Due to the facts that hydroxamic acids can form strong complexes with most of the valuable metallic oxide minerals, and show good selectivity and collecting power, they have been used extensively in the field of extraction metallurgy [1.144 & 1.145].

A hydroxamic acid-based ion exchange resin specific for iron has also been developed and evaluated for its performance in removing iron from water supplies [1.146]. The resin was synthesised by converting the carboxylic acid groups of Chelex 100 to hydroxamate groups by reaction with ethylchloroformate followed by hydroxylamine. It was found that the resin could be regenerated by reduction of the Fe(III) to Fe(II) with hydrosulphate, followed by washing with distilled water. An important function of these chelating resins of relevance to work presented in this report has been the extraction of actinides from the environment and waste streams [1.147, 1.148 & 1.149]. Reports of metals separated by hydroxamate chelating resins include; Pb and Cu [1.150 & 1.151] Fe, Sc, Ti, Zr, Hf and Tl; [1.152] Mo, W, U, and V [1.150 & 1.153].

The development and application of *chemically modified electrodes* (CMEs) for metal ion determination has received much attention in recent years. Immobilisation of metal ion binding reagents at or on an electrode surface can lead to selective accumulation of the analyte of interest with subsequent determination by a voltammetric technique [1.154 & 1.155]. Examples of ligands that have been immobilised include ethylenediamine, [1.156] phthalocyanine, [1.157] and hydroxamic acids [1.10 & 1.11]. The analytical utility of CMEs

is a result of the ability of the electrode to accumulate the analyte and so serve to concentrate the analyte from dilute solution onto the electrode surface.

An example of this is the incorporation of hydroxamic acid ligands, *desferrioxamine* (DFA⁺) and *glycine hydroxamic acid* (GHA⁺) into Nafion[®] coated glassy carbon electrodes (GCE) as investigated by Arrigan and co-workers [1.11]. They reported that the modified electrode allowed the presence of the ligand to be detected in the Nafion[®] film both visually (by its reaction with the iron(III) to form a deep red complex) and electrochemically (by oxidative voltammetry) in a 100 mol m⁻³ nitric acid electrolyte. The visual detection of the electroactive film retained hydroxamic acid Fe(III) species; producing a deep red colour, is characteristic of an octahedral iron(III) hydroxamate complex, which indicated the formation of a 1:1 DFA⁺-iron(III) and 3:1 GHA⁺-iron(III) complexes within the film. Furthermore, they determined that the complexes had retained a net positive charge and thus were retained within the Nafion[®] matrix. The electrochemistry obtained from the CVs of the iron(III) / hydroxamate / Nafion[®] complex shows two reduction waves upon the cathodic going sweep corresponding to the reduction of ion exchanged and complexed iron(III) within the Nafion[®] membrane. The oxidation wave observed on the returning anodic going sweep indicated the reoxidation of the non-complexed iron (III) only in the Nafion[®] membrane.

1.12 – REFERENCES

- 1.1 L.D. Whiteley and C.R. Martins. *Anal. Chem.* **59**, (1987), 1746
- 1.2 M.W. Espenchied, A.R. Ghatak-Roy, R.B. Moore III, R.M. Penner, M.N. Szentirmay and C.R. Charles. *J. Chem. Soc. Faraday Trans.* **82**, (1986), 1051
- 1.3 D.A. Buttry and F.C. Anson. *J. Electroanal. Chem.* **130**, (1981) 333
- 1.4 J. Langmaier, A. Trojanek, I. Weber and Z. Samec. *J. Electroanal. Chem.* **469**, (1999), 11
- 1.5 Z. Lu and S. Dong. *J. Electroanal. Chem.* **233**, (1987), 19
- 1.6 C.P. Andrieux, P. Audebert, B. Divisia-Blohorn, P. Aldebert and F. Michalak. *J. Electroanal. Chem.* **296**, (1990), 117
- 1.7 E. Juzeliunas and K. Juttner. *Electrochimica Acta.* **43**, (1998), 1691
- 1.8 J.A. Amberson and G.H. Svehla. *Anal. Pro.* **23**, (1986), 443
- 1.9 T.S.I. Cordoba, L.G.A. Hugot and R. Torresi. *J. Electrochem. Soc.* **138**, (1991), 1548
- 1.10 D.W.M. Arrigan, J.D. Glennon and G. Svehla. *Anal. Proc.* **30**, (1993), 141
- 1.11 D.W.M. Arrigan, B. Deasy, J.D. Glennon, B. Johnston and G. Svehla. *Analyst.* **118**, (1993), 355
- 1.12 S. Dong and Y. Wang. *Electroanalysis.* **1**, (1989), 99
- 1.13 W.H. King, Jr. *Anal. Chem.* **36**, (1964), 1735
- 1.14 M.H. Ho, in: *Applications of Piezoelectric Quartz Crystal Microbalances, Methods and Phenomena.* C. Lu and A.W. Cazanderna, (Ed.), Elsevier, New York. **10**, (1984), 351
- 1.15 M.D. Ward and D.A. Buttry. *Science.* **249**, (1990), 1000
- 1.16 P. Curie and J. Curie. *C. R. Acad. Sci.* **91**, (1880), 294
- 1.17 W.G. Cady, in: *Piezoelectricity*, (Ed.), McGraw-Hill, Dover, New York. (1964), 308

-
- 1.18 D.A. Buttry, in: *Electroanalytical Chemistry*, A.J. Bard, (Ed.), Marcel Dekker, New York. **17**, (1990), 1
- 1.19 G. Sauerbrey. *Z. Phys.* **155**, (1959), 206
- 1.20 D.M. Ullevig, J.M. Evans and M.G. Albrecht. *Anal. Chem.* **54**, (1982), 2341
- 1.21 A. Kanazawa and J.G. Gordon. *Anal. Chem.* **57**, (1985), 1770
- 1.22 S. Bruckenstein and M. Shay. *Electrochim. Acta.* **30**, (1985), 1295
- 1.23 D.A. Buttry and M.D. Ward. *Chem. Rev.* **92**, (1992), 1355
- 1.24 S.J. Martin, V.E. Granstaff and G.C. Frye. *Anal. Chem.* **63**, (1991), 2272
- 1.25 R. Schumacher, G. Borges and K. Kanazawa. *Surf. Sci.* **163**, (1985), L621
- 1.26 R. Schumacher, J. Gordon and O.J. Melroy. *J. Electroanal. Chem.* **216**, (1987), 127
- 1.27 W. Stockel and R. Schumacher. *Ber. Bunsen-Ges. Phys. Chem.* **91**, (1987), 345
- 1.28 J.W. Coburn, in: *Applications of Piezoelectric Quartz Crystal Microbalance*, Methods and Phenomena. C. Lu and A.W. Cazanderna, (Eds.), Elsevier, New York. **7**, (1984), 221
- 1.29 G.T. Cheek and W.E. O'Grady. *J. Electroanal. Chem.* **277**, (1990), 341
- 1.30 L.V. Rajakovic, B.A. Cavic-Vlasak, V. Ghaemmaghami, K.M.R. Kallury, A.L. Kipling and M. Thompson. *Anal. Chem.* **63**, (1991), 615
- 1.31 A.L. Kipling and M. Thompson. *Anal. Chem.* **62**, (1990), 1514
- 1.32 M. Thompson, C.L. Arthur and G.K. Dhaliwal. *Anal. Chem.* **58**, (1986), 1206
- 1.33 B.A. Martin and H.E. Hager. *J. Appl. Phys.* **65**, (1989), 2630
- 1.34 J.L. Jones and J.P. Meiore. *Anal. Chem.* **41**, (1969), 484
- 1.35 J.P. Meiore and J.L. Jones. *Talanta.* **16**, (1969), 149
- 1.36 T. Nomura and O. Hattori. *Anal. Chim. Acta.* **115**, (1980), 323
- 1.37 S. Bruckenstein and M. Shay. *J. Electroanal. Chem.* **188**, (1985), 131

-
- 1.38 K. Kaufman, K.K. Kanazawa and G.B. Street. *J. Phys. Rev. Lett.* **53**, (1984), 2461
- 1.39 M.R. Deakin, T.T. Li and O.R. Melroy. *J. Electroanal. Chem.* **243**, (1988), 343
- 1.40 M.R. Deakin and O.R. Melroy. *J. Electroanal. Chem.* **239**, (1988), 321
- 1.41 S. Bruckenstein and S. Swathirajan. *Electrochim. Acta.* **30**, (1985), 851
- 1.42 O. R. Melroy, K. Kanazawa, J.G. Gordon II and D. Buttry. *Langmuir.* **2**, (1986), 697
- 1.43 Mori, C.K. Baker, J.R. Reynolds and K. Rajeshwar. *J. Electroanal. Chem.* **252**, (1988), 441
- 1.44 M. Hepel, K. Kanige and S. Bruckenstein. *J. Electroanal. Chem.* **266**, (1989), 409
- 1.45 H.K. Park, K. Podolske, Z. Munshi, W.H. Smyrl and B.B. Owens. *J. Electrochem. Soc.* **138**, (1991), 627
- 1.46 A. Grezegorzewski and K.E. Heusler. *J. Electroanal. Chem.* **228**, (1987), 455
- 1.47 G.S. Ostrom and D.A. Buttry. *J. Electroanal. Chem.* **256**, (1988), 411
- 1.48 T.S.I. Cordoba, L.G.A. Hugot and R. Torresi. *J. Electrochem. Soc.* **138**, (1991), 1548
- 1.49 R.W. Murray, in: *Electroanalytical Chemistry*, A.J. Bard, (Ed.), Marcel Dekker, New York. **13**, (1984), 191
- 1.50 S.J. Lasky and D.A. Buttry. *J. Am. Chem. Soc.* **110**, (1988), 6258
- 1.51 R. Borjas and D.A. Buttry. *J. Electroanal. Chem.* **280**, (1990), 73
- 1.52 A.J. Kelly, T. Ohsaka, N. Oyama, R.J. Forster and J.G. Vos. *J. Electroanal. Chem.* **287**, (1990), 185
- 1.53 P.T. Varineau and D.A. Buttry. *J. Phys. Chem.* **91**, (1987), 1292
- 1.54 R. Borlas and D.A. Buttry. *Chem. Mater.* **3**, (1991), 872
- 1.55 R.M. Penner, L.S. Van Dyke and C.R. Martin. *J. Phys. Chem.* **92**, (1988), 5274
- 1.56 C.K. Baker and J.R. Reynolds. *J. Electroanal. Chem.* **251**, (1988), 307
- 1.57 M.R Deakin and D.A. Buttry. *Anal. Chem.* **61**, (1989), 1147A

-
- 1.58 R. Schumacher. *Angew. Chem. Int. Ed. Engl.* **29**, (1990), 329
- 1.59 D.A. Buttry, in: *Electrochemical Interfaces*, H.D. Abruna, (Ed.), VCH Inc., New York. (1991), 531
- 1.60 S. Bruckenstein, M. Michalski, A. Fensore, L. Zhufen and A.R. Hillman. *Anal. Chem.* **66**, (1994), 1847
- 1.61 G.C. Dunham, N.H. Benson, D. Petelenz and J. Janata. *Anal. Chem.* **67**, (1995), 267
- 1.62 G.M. Schmid and M.E. Curley-Fiorino, in: *Encyclopedia of Electrochemistry of the Elements IV*, A.J. Bard, (Ed.), Marcel Dekker, New York. **4**, (1975), 87
- 1.63 D.W. Kirk, F.R. Foulkes and W.F. Graydon. *J. Electrochem. Soc.* **127**, (1980), 1069
- 1.64 G.H. Kelsall, N.J. Welham and M.A. Diaz. *J. Electroanal. Chem.* **361**, (1993), 13
- 1.65 H. Angerstein-Kozłowska, B.E. Conway, B. Barnett and J. Mozota. *J. Electroanal. Chem.* **100**, (1979), 417
- 1.66 H. Angerstein-Kozłowska, B.E. Conway, A. Hamelin and L. Stoicoviciu. *Electrochimica. Acta.* **31**, (1986), 1051
- 1.67 H. Angerstein-Kozłowska, B.E. Conway, A. Hamelin and L. Stoicoviciu. *J. Electroanal. Chem.* **288**, (1987), 429
- 1.68 J.S. Gordon and D.C. Johnson. *J. Electroanal. Chem.* **365**, (1994), 267
- 1.69 A. Hamelin. *J. Electroanal. Chem.* **407**, (1996), 1
- 1.70 A. Hamelin, M.J. Sottomayor, F. Silva, Si-Chung Chang and M.J. Weaver. *J. Electroanal. Chem.* **295**, (1990), 291
- 1.71 A. Hamelin and A.M. Martins. *J. Electroanal. Chem.* **407**, (1996), 13
- 1.72 S. Strbac and R.R. Adzic. *J. Electroanal. Chem.* **403**, (1996), 169
- 1.73 S. Strbac, N.A. Anastasijevic and R.R. Adzic. *J. Electroanal. Chem.* **323**, (1992), 179
- 1.74 M. Sotito. *J. Electroanal. Chem.* **72**, (1976), 287

-
- 1.75 A.C. Chialvo, W.E. Triaca and A.J. Arvia. *J. Electroanal. Chem.*, **171**, (1984), 303
- 1.76 C.M. Ferro, A.J. Calandra and A.J. Arvia. *J. Electroanal. Chem.* **59**, (1975), 239
- 1.77 C.M. Ferro, A.J. Calandra and A.J. Arvia. *J. Electroanal. Chem.* **65**, (1975), 963
- 1.78 J.P. Hoare. *Electrochimica. Acta.* **11**, (1966), 203
- 1.79 B. Piela and P.K. Wrona. *J. Electroanal. Chem.* **388**, (1995), 69
- 1.80 D.A.J. Rand and R. Woods. *J. Electroanal. Chem.* **31**, (1971), 29
- 1.81 U. Oesch and J. Janata. *Electrochimica. Acta.* **28**, (1983), 1237
- 1.82 L.D. Burke and O'Leary. *J. Appl. Electrochem.* **19**, (1989), 758
- 1.83 L.D. Burke, D.T. Buckley and J.A. Morrissey. *Analyst.* **119**, (1994), 841
- 1.84 L.D. Burke and P.F. Nugent. *J. Electroanal. Chem.* **444**, (1998), 19
- 1.85 L.D. Burke and J.F. O'Sullivan. *J. Electroanal. Chem.* **285**, (1990), 195
- 1.86 D.C. Johnson and W.R. La Course. *Electroanalysis.* **4**, (1992), 367
- 1.87 M. Gerlache, Z. Seturk, G. Quarin and J.M. Kauffmann. *Electroanalysis.* **9**, (1997),
1088
- 1.88 S. Ye, C. Ishibashi, K. Shimazu and K. Uosaki. *J. Electrochem. Soc.* **145**, (1998),
1614
- 1.89 C. Shengli, W. Bingliang and Z. Hong. *J. Nat. Sci.* **3**, (1998), 102
- 1.90 K. Juodkazis, J. Juodkazyte, T. Juodiene and A. Lukinskas. *J. Electroanal. Chem.*
441, (1998), 19
- 1.91 K. Juodkazis, J. Juodkazyte, B. Sebeko and A. Lukinskas. *Electrochem. Comm.* **1**,
(1999), 315
- 1.92 L.D. Burke and J.F. O'Sullivan. *Electrochim. Acta.* **37**, (1992), 2087
- 1.93 L.D. Burke and B.H. Lee. *J. Electroanal. Chem.* **330**, (1992), 637
- 1.94 W. Stockel and R. Schumacher. *Ber. Bunsenges. Phys. Chem.* **93**, (1989) 600

-
- 1.95 S. Bourkane, C. Gabrielli, F. Huet and M. Keddami. *Electrochimica. Acta.* **38**, (1993), 1023
- 1.96 S. Bourkane, C. Gabrielli, and M. Keddami. *Electrochimica. Acta.* **38**, (1993), 1827
- 1.97 E.B. Yeager, D. Scherson, X. Xing and I.T. Bae. *Anal. Chem.* **61**, (1989), 1154
- 1.98 D.A.J. Rand and R. Woods. *J. Electroanal. Chem.* **35**, (1972), 209
- 1.99 S.H. Cadle and S. Bruckenstein. *Anal. Chem.* **46**, (1974), 16
- 1.100 M.A. Diaz, G.H. Kelsall and N.J. Welham. *J. Electroanal. Chem.* **361**, (1993), 25
- 1.101 S.H. Cadle and S. Bruckenstein. *J. Electroanal. Chem.* **48**, (1973), 325
- 1.102 R.P. Frankenthal and D.E. Thompson. *J. Electrochem. Soc.* **123**, (1976), 799
- 1.103 B. Lovrecek, K. Moslavac and D.J. Matic. *Electrochimica. Acta.* **26**, (1981), 1087
- 1.104 T. Heumann and H.S. Panesar. *Z. Phys. Chem.* **229**, (1965), 84
- 1.105 J.N. Gaur and G.M. Schmid. *J. Electroanal. Chem.* **24**, (1970), 279
- 1.106 R.P. Frankenthal and D.J. Siconolfi. *J. Electrochem. Soc.* **129**, (1982), 1192
- 1.107 B.H. Loo. *J. Phys. Chem.* **86**, (1982), 433
- 1.108 D.J. Trevor, C.E.D. Chidsey and D.N. Loiacono. *Phys. Rev. Lett.* **62**, (1989), 929
- 1.109 H. Honbo, S. Sugawara and K. Itaya. *Anal. Chem.* **62**, (1990), 2424
- 1.110 D. Orata and D.A. Buttry. *J. Electroanal. Chem.* **257**, (1988), 71
- 1.111 J.R. Reynolds, N.S. Sundaresan, M. Pomerrantz, S. Basak and C.K. Baker. *J. Electroanal. Chem.* **250**, (1988), 355
- 1.112 S. Bruckenstein and A.R. Hillman. *J. Phys. Chem.* **92**, (1988), 4837
- 1.113 M. Shi and F.C. Anson. *J. Electroanal. Chem.* **415**, (1996), 41
- 1.114 M. Shi and F.C. Anson. *J. Electroanal. Chem.* **425**, (1997), 117
- 1.115 Y.K. Agrawal and R.D. Roshania. *Bull. Soc. Chim. Belg.* **89**, (1980), 159

-
- 1.116 K.N. Raymond and T.P. Tufano, in: *The Biological Chemistry of Iron*, H.B. Dunford, D. Dolphin, K.N. Raymond and L. Sleiker, (Eds.), D. Reidel Publishing C^o, Dordecht Holland. (1982), 85
- 1.117 H. Lossen. *Ann. Chem.* **150**, (1869), 314
- 1.118 H.L. Yale. *Chem. Rev.* **33**, (1943), 209
- 1.119 L. Bauer and O. Exner. *Angew. Chem. Int. Ed. Engl.* **13**, (1974), 376
- 1.120 C.K. Lowe-Ma and D.L. Decker. *Acta Cryst.* **C42**, (1986), 1648
- 1.121 D.C. Berndt and I.E. Ward. *J. Org. Chem.* **41**, (1976), 3297
- 1.122 B.S. Mane and M.H. Jagdale. *Gazz. Chim. Ital.* **107**, (1977), 487
- 1.123 F. Difuria, G. Modena and P. Scrimin. *Nouv. J. Chim.* **8**, (1984), 45
- 1.124 D.F. Minor, W.A. Waters and J.V. Ramsbottom. *J. Chem. Soc.* **B180**, (1967)
- 1.125 J.E. Rowe and A.D. Ward. *Aust. J. Chem.* **21**, (1968), 2761
- 1.126 J.H. Cooley, M.W. Mosher and M.A. Khan. *J. Am. Chem. Soc.* **90**, (1967), 1867
- 1.127 T.R. Oliver and W.A. Waters. *J. Chem. Soc.* **B677**, (1971), 677
- 1.128 T. Osterud and M. Prytz. *Acta. Chem. Scand.* **10**, (1956), 451
- 1.129 M. Prytz and T. Osterud. *Acta. Chem. Scand.* **11**, (1957), 1530
- 1.130 T. Osterud and M. Prytz. *Acta. Chem. Scand.* **13**, (1959), 2114
- 1.131 S. Ozaki and M. Masui. *Chem. Pharm. Bull.* **25**, (1977), 1179
- 1.132 M. Masui, Y. Kaiho and S. Ozaki. *Chem. Pharm. Bull.* **29**, (1981), 1772
- 1.133 M. Masui, Y. Kaiho, T. Ueshima and S. Ozaki. *Chem. Pharm. Bull.* **30**, (1983), 3225
- 1.134 J.A. Amberson. *Ph.D. Thesis*, Queens University Belfast. (1987)
- 1.135 P. Desaraju and A. Winston. *J. Co-ord. Chem.* **14**, (1986), 241
- 1.136 L.G. Sillen and A.E. Martell. *Chem. Soc. Spec. Publ. No.* 17, (1964)
- 1.137 H. Linder and S. Gottlicher. *Acta. Cryst.* **B25**, (1969), 832

-
- 1.138 A. Zalkin, J.C. Forrester and D.H. Templeton. *J. Am. Chem. Soc.* **88**, (1965), 1810
- 1.139 D. van der Helm and M. Doling. *J. Am. Chem. Soc.* **98**, (1986), 82
- 1.140 C.P. Brink and A.L. Crumbliss. *Inorg. Chem.* **23**, (1984), 4708
- 1.141 L.L. Fish and A.L. Crumbliss. *Inorg. Chem.* **24**, (1985), 2198
- 1.142 W.W. Brandt. *Record. Chem. Progr.* **21**, (1960), 159
- 1.143 Y.K. Agrawal and S.A. Patel. *Rev. Anal. Chem.* **4**, No4, (1980), 238
- 1.144 D.W. Fuerstenau in: *Pradip, Reagents, Miner Ind. Pap*, M.J. Jones and R. Oblatt. (Eds.) Inst. Min. Metall. London U.K. (1984), 161
- 1.145 R.J. Philips and J.S. Fritz. *Anal. Chim. Acta.* **139**, (1982), 237
- 1.146 A. Winston, C.R. Jenkins, W. Lerdthusnee and S.J. Masten. Report (1981), WRI-WVU-81-03, Information-17, W82-05282, OWRT-A-043-WVA(1), Order No. PB82-224593 Avail. NTIS. From Gov. Rep. Announce. Index (US). **82**, (21), 4376, (1982), 1
- 1.147 T. Hirotsu, S. Katoh, K. Sugasak and M. Sakuragi. *J. Polym. Sci.* **24**, Part A, (1986), 1953
- 1.148 F. Vernon. *Appl. Chem.* **54**, (1982), 2151
- 1.149 A. Gopalan, V. Huber, N. Koshti, H. Jacobs, O. Zincircioglu, P. Smith and G. Jarvinen. *Proc. Am. Chem. Soc. Symp.* (1994), 77
- 1.150 A. Shah and S. Devi. *Anal.* **110**, (1985), 1501
- 1.151 M. Ahuja, A.K. Rai and P.N. Mathur. *Talanta.* **43**, (1996), 1955
- 1.152 T.F. Vertinskaya, G.V. Kudryavtsev, T.I. Tikomirova and V.I. Fadeeva. *Zh. Anal. Khim.* **40**, (1985), 1387
- 1.153 C.Y. Liu and P.J. Sun. *Fresenius Z. Anal. Chem.* **325**, (1986), 553
- 1.154 J. Wang. *Anal. Chimi. Acta.* **234**, (1990), 41

1.155 J. Wang. *Electro. Anal.* **3**, (1991), 255

1.156 G.T. Cheek and R.F. Nelson. *Anal. Let.* A11, **5**, (1978), 393

1.157 J. Wang. *Talanta.* **36**, No 1 / 2, (1986), 279

CHAPTER II - EXPERIMENTAL ASPECTS

CONTENT

<u>II.1 - INTRODUCTION TO VOLTAMMETRY</u>	<i>Page 84</i>
<u>II.2 - EQUIPMENT FOR ELECTROCHEMICAL EXPERIMENTS</u>	<i>Page 85</i>
<u>II.3 - EQUIPMENT FOR ELECTROCHEMICAL QUARTZ CRYSTAL MICROBALANCE EXPERIMENTS</u>	<i>Page 86</i>
<u>II.4 - THE REMOTE SCE REFERENCE ELECTRODE EQUIPMENT USED FOR THE DETERMINATION OF ACID ASSISTED GOLD DISSOLUTION.</u>	<i>Page 88</i>
<u>II.5 - EQCM CALIBRATION USING Ag⁺/Ag ELECTRO-DEPOSITION / ELECTRODISSOLUTION PROCESSES</u>	<i>Page 90</i>
<i>II.5.1 - Preparation of Ag⁺ Solution</i>	<i>Page 90</i>
<i>II.5.2 - Results from the Calibration of the EQCM</i>	<i>Page 91</i>
<u>II.6 - PREPARATION OF ACETOHYDROXAMIC ACID SOLUTION</u>	<i>Page 95</i>
<u>II.7 - GOLD MICRO-DISC ELECTRODE FABRICATION</u>	<i>Page 95</i>
<i>II.7.1 - Electrode Fabrication</i>	<i>Page 95</i>
<i>II.7.2 - Fabrication of Electrical Contact</i>	<i>Page 96</i>

<u>II.8 - GOLD MICRODISC ELECTRODE POLISHING PROCEDURE</u>	<i>Page 96</i>
<u>II.9 - GOLD MICRODISC ELECTRODE ELECTROCHEMICAL CLEANING PROCEDURE</u>	<i>Page 97</i>
<u>II.10 - IRON(III) DETERMINATION USING QCM/EQCM EXPERIMENTS</u>	<i>Page 97</i>
<u>II.11 - PREPARATION OF THE EQCM/NAFION/DEFERRIOXAMINE COMPOSITE ELECTRODE</u>	<i>Page 98</i>
<u>II.12 - PREPARATION OF DESFERRIOXAMINE SOLUTION</u>	<i>Page 98</i>
<u>II.13 - PREPARATION OF IRON(III) NITRATE NONHYDRATE SOLUTION</u>	<i>Page 99</i>
<u>II.14 - CLEANING PROCEDURE FOR THE EQCM CHROMIUM, TITANIUM AND PURE GOLD BACKED ELECTRODES</u>	<i>Page 99</i>
<u>II.15 - EQCM Au NAFION/(DFA) COMPOSITE ELECTRODE CLEANING PROCEDURE</u>	<i>Page 100</i>
<u>II.16 - PREPARATION OF METHYLENE BLUE SOLUTION</u>	<i>Page 100</i>
<u>II.17 - REFERENCES</u>	<i>Page 101</i>

II.1 - INTRODUCTION TO VOLTAMMETRY

In voltammetry, a voltage is applied to the working electrode and the resulting current flow is measured. The origin of voltammetry can be traced back to Salomen [2.1] who in 1897 studied current-voltage curves for the electrolysis of silver ions. Such current-voltage curves are recorded when a gradually changing voltage is applied to a working electrode immersed in a cell containing an electrolyte, a reference electrode and an auxiliary electrode. In 1922 Heyrovsky first described the principles of polarography, where the working or indicator electrode was a dropping mercury electrode [2.2]. Modern voltammetry is now a powerful analytical technique that offers increasing current sensitivity with low cost instrumentation.

Voltammetry is applicable to analysis in the organic, inorganic, physical, electrochemical, geochemical, medicinal and pharmaceutical fields. Electrochemical detectors, for example, are becoming increasingly important for chromatographic and flow injection techniques and recently an increased development has been seen in EQCM-based techniques, their main advantage being their extremely low detection limits.

In situ microweighing with the EQCM in the course of an experiment provides quantification of the mass change occurring at the electrode surface; which can be correlated to the ongoing electrochemical processes. It can also measure the electrochemical variables (*e.g.* E° the *standard redox potential*, k° the *standard rate constant* and α the *transfer coefficient*). For this reason, the combination of electrochemical voltammetry and mass measurements has proven useful for analytical applications and for gaining an insight into many physicochemical phenomena that can occur at the electrode surface.

II.2 - EQUIPMENT FOR ELECTROCHEMICAL EXPERIMENTS

In order to assess the thermodynamic stability of various hydroxamic acids, CV experiments were performed using a conventional three-electrode cell. An in house fabricated gold microdisc electrode (see Section II.7, gold microdisc electrode fabrication) served as a working electrode, a platinum wire coil (250 μm diameter, 99.99+% purity, Advent Research Materials Ltd., Halesworth, Suffolk, UK) served as the counter electrode, and a *saturated calomel electrode* (SCE) (Russel, type CRL/s7, Auchtermuchty, Fife, UK) was used as reference electrode in all electrochemical studies of hydroxamic acid stability. All CVs were recorded using a commercially available specialist low current potentiostat (Autolab PGSTAT 10, Windsor Scientific Ltd., Slough, UK). A schematic diagram of the experimental setup is shown in *Figure 2.1*.

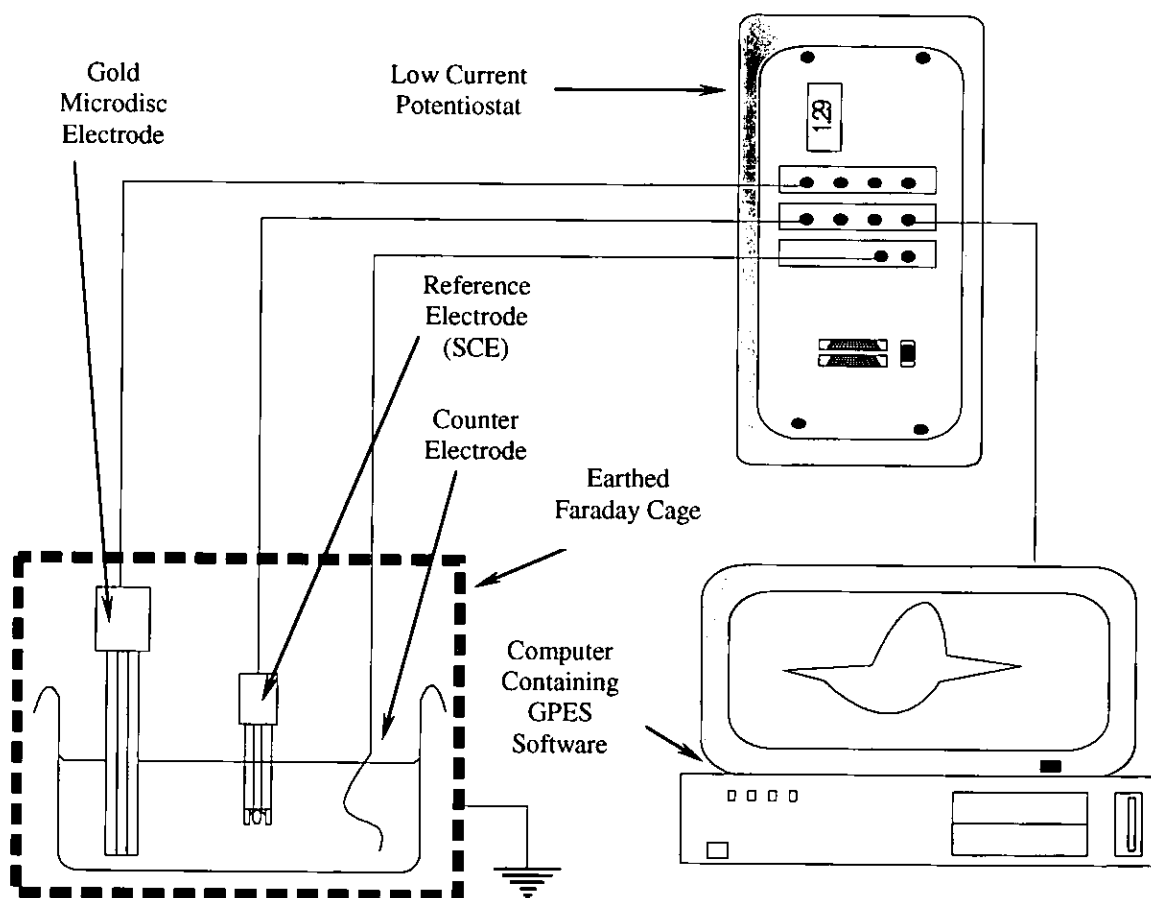


Figure 2.1: Schematic of the cyclic voltammogram experiments.

II.3 - EQUIPMENT FOR ELECTROCHEMICAL QUARTZ CRYSTAL MICROBALANCE

EXPERIMENTS

The EQCM apparatus (10 MHz, Windsor Scientific Ltd.) was constructed in the workshop of the Institute of Physical Chemistry, Polish Academy of Sciences (Warsaw, Poland) [2.3] and utilises an electronic design of the type described elsewhere [2.4]. The mass sensitive oscillators (Institute of Physical Chemistry, Polish Academy of Sciences (Warsaw, Poland)) were 14mm in diameter, plano-plano, AT-cut quartz crystals of a 10MHz nominal f_0 . The 6mm-diameter “key-hole” gold electrode patterns were deposited on both oscillator faces. The Au layer which faces the solution was connected to the working electrode input of a potentiostat. The high frequency signal was electronically separated so that any standard potentiostat could be utilised.

The EQCM experiments were performed with a conventional three-electrode cell. The solution side face of the EQCM oscillator served as the working electrode, a platinum wire coil served as the counter electrode and a SCE was used as the reference electrode. All potentials are reported with respect to the SCE.

Simultaneous EQCM and CV experiments were performed using an electrochemical setup which consisted of a *general purpose electrochemical system* (GPES) consisting of a PGSTAT 10 potentiostat (Autolab PGSTAT 10, Windsor Scientific Ltd.) driven by the appropriate proprietary software.

The frequency was measured with a Philips PM6680 High Resolution Programmable Timer/Counter (J.Fluka, Mfg. Co., Inc., Everett, WA.). Simultaneous CV and Δf versus E (*potential*) curves were recorded by interfacing the output of the frequency counter to a second channel input of the GPES via an analogue digital converter to the computer software GPES. The calibrated sensitivity of the EQCM system was calculated to be 1.242 ng Hz^{-1} (vide infra). The high-frequency signal waveform was also monitored with

a Tektronix 60MHz 1GS/s Model TDS 210 Digital Storage Oscilloscope (T.E.R. Instruments Ltd. Manchester. U.K.)

Nitrogen (Whitespot grade, BOC Ltd., Guildford, Surrey, UK) was purged through the solution to remove any oxygen prior to EQCM experiments. All experiments were carried out at ambient temperature ($22 \pm 1^\circ\text{C}$). A schematic diagram of the experimental setup is shown in *Figure 2.2*.

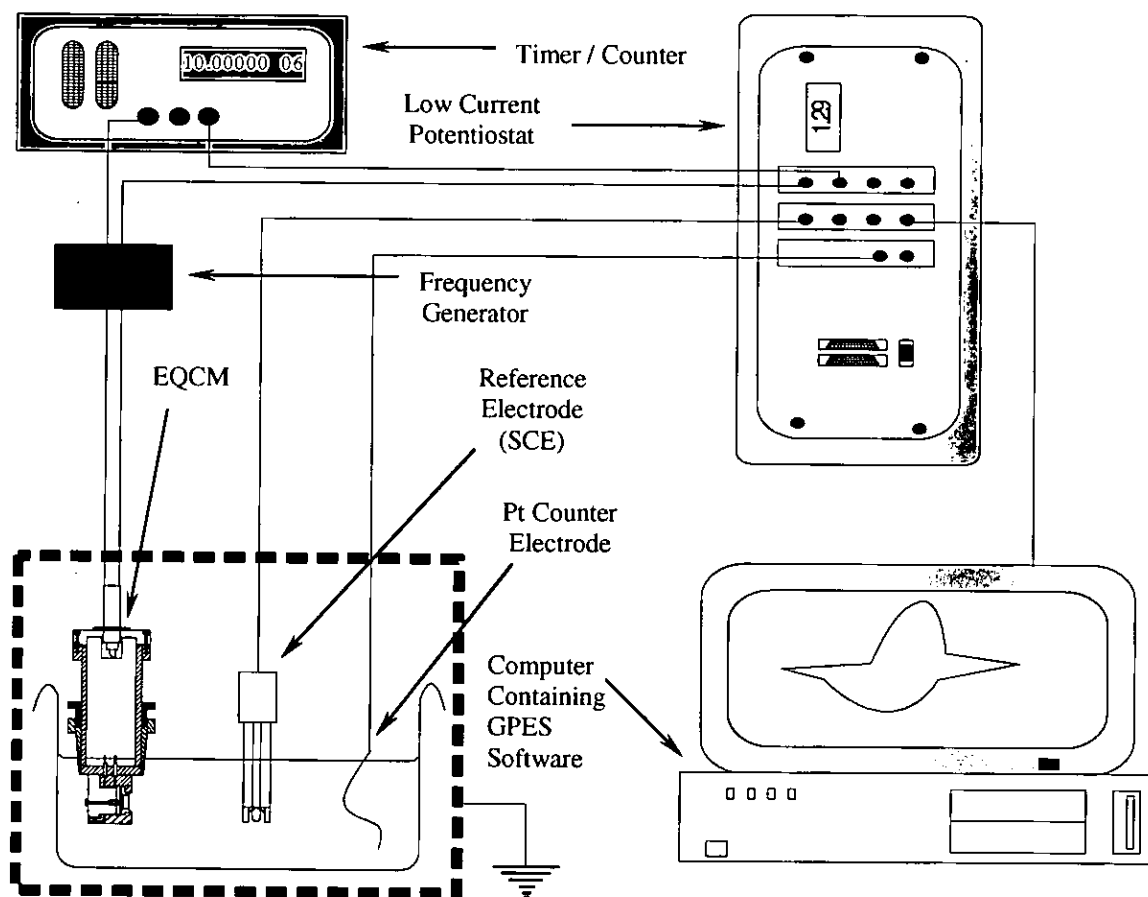


Figure 2.2: Schematic diagram of the EQCM experimental set up.

II.4 - THE REMOTE SCE REFERENCE ELECTRODE EQUIPMENT USED FOR THE DETERMINATION OF ACID ASSISTED GOLD DISSOLUTION.

In order to determine if gold dissolution is assisted by acidic media a series of experiments were carried out using an in house constructed remote SCE reference electrode. There by removing any possible convection effects that may be brought about by the use of the 10 MHz quartz crystal electrode resonator.

The remote SCE reference electrode was constructed by inserting a platinum wire (250 μm diameter, 99.99+% purity, Advent Research Materials Ltd., Halesworth, Suffolk, UK) into a Flexible PTF tube. The end of the *polytetrafluoroethene* (PTF) tube was sealed using an agar stopper and was filled with a saturated solution of KCl, which was filled using a syringe. The syringe was secured to the wire/PTF/agar stopper assembly and acted as the reservoir and holder for the main reference SCE electrode.

Gold dissolution CV, chronoamperometry and UV-visible experiments could now be performed within a cuvette using a conventional three-electrode cell. A gold wire (0.5 mm diameter, 99.99+% purity, Advent Research Materials Ltd., Halesworth, Suffolk, UK) served as a working electrode, a platinum gauze mesh (100 woven mesh 0.0762 mm thick, 99.99+% purity, Alfa Aesar, Johnson Matthey Company, Royston, Herts, UK) served as the counter electrode, and a saturated calomel electrode of the (SCE) (Russel, type CRL/s7, Auchtermuchty, Fife, UK), was inserted into the syringe KCl reservoir, and was used as reference electrode in all electrochemical studies.

All CVs were recorded using a commercially available specialist low current potentiostat (Autolab PGSTAT 10, Windsor Scientific Ltd., Slough, UK). All CVs recorded were used as a source of calibration to ensure that the system design was properly operating prior to any investigation and can be seen **Section III.2.4, Figure 3.10.**

Nitrogen (Whitespot grade, BOC Ltd., Guildford, Surrey, UK) was purged through the solution to remove any oxygen prior to EQCM experiments. All experiments were carried out at ambient temperature ($22 \pm 1^\circ\text{C}$). A schematic diagram of the experimental setup is shown in *Figure 2.3*.

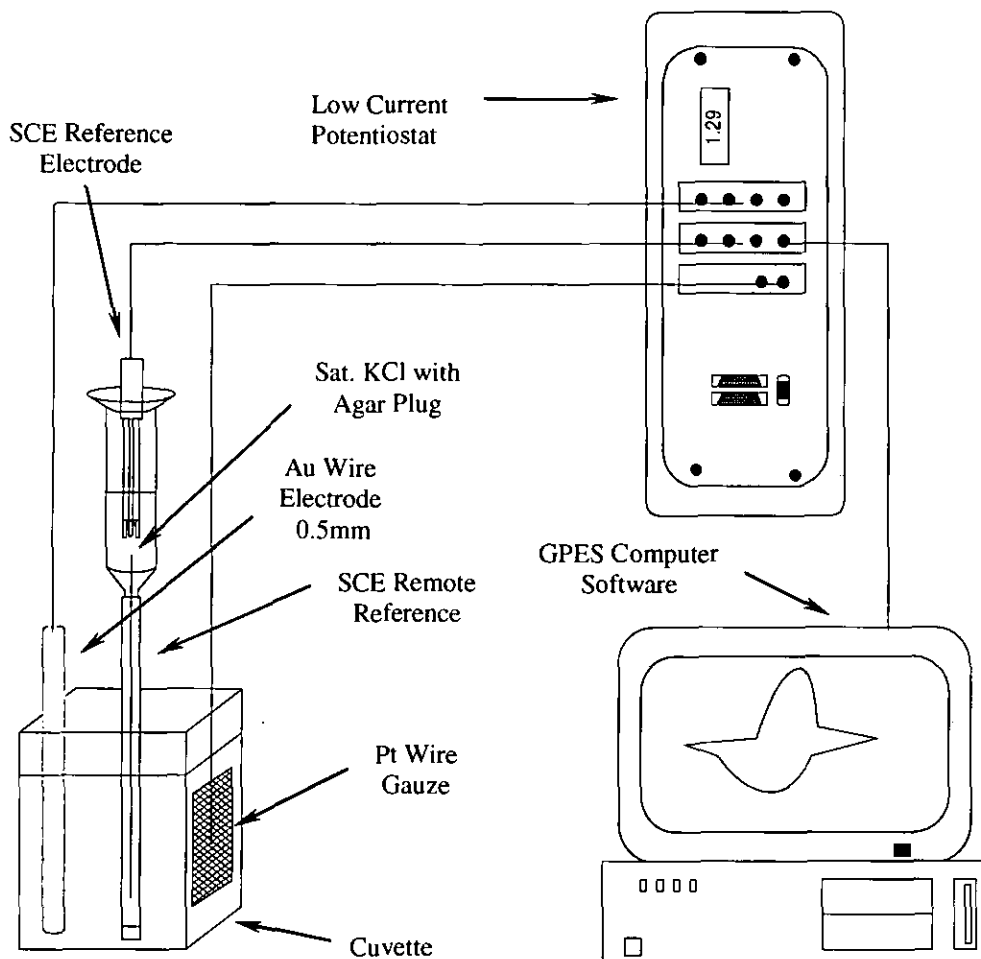


Figure 2.3: Schematic diagram of the remote SCE experimental set up for the determination of gold dissolution.

II.5 - EQCM CALIBRATION USING Ag^+/Ag ELECTRO-DEPOSITION / ELECTRODISSOLUTION PROCESSES

The EQCM has been used to determine Ag^+ and Cu^{2+} in solution and these processes have been commonly used for EQCM calibration [2.5 & 2.6]. The mass sensitivity of the crystal oscillator has been previously determined under both potentiostatic [2.7] and galvanostatic [2.4 to 2.7] conditions and it was shown that for the same amount of charge passed, Δf of the quartz oscillator is independent of the applied current density. Previous work also established that the crystal oscillator could be calibrated by cyclic voltammetry [2.3]. We have calibrated our device using the cyclic voltammetric deposition of Ag from Ag^+ .

II.5.1 - Preparation of Ag^+ Solution

Unless specified otherwise all solutions were prepared using distilled water from a home made still that was further purified by an E-pure deionisation system (Barnstead/Thermodyne, model 04642, Dubuque, Iowa, US) to a resistivity of $1.8 \times 10^5 \Omega\text{m}$. For simplicity, it will be referred to as E-pure water for the remainder of this thesis. 0.0427 g of AgNO_3 (Sigma-Aldrich C^o. Ltd., Poole, Dorset, UK) were mixed with 250 cm^3 of 100 mol m^{-3} HClO_4 (AnalaR, BDH Chemicals Ltd., Poole, Dorset, UK) in a 250 cm^3 volumetric flask to give a 1.01 mol m^{-3} solution of AgNO_3 / 100 mol m^{-3} HClO_4 . 40 cm^3 of this solution were placed into a Pyrex beaker, which was purged with nitrogen for 600 s to remove all O_2 . All measurements were carried out under a continuous blanket of N_2 .

The EQCM was adjusted to its resonant frequency, and this frequency was recorded. The EQCM was placed into the AgNO_3 / HClO_4 solution under N_2 and simultaneous cyclic voltammetry and EQCM frequency responses were recorded.

II.5.2 - Results from the calibration of the EQCM

The QCM was calibrated as per references [2.3 & 2.5]. This method, which is summarised below, can be used as a self-diagnostic tool for both the QCM and new quartz crystal / electrode assemblies. The QCM was placed into the $\text{AgNO}_3 / \text{HClO}_4$ solution under N_2 as described in **Section II.5.1** and simultaneous cyclic voltammetric and EQCM frequency responses recorded **Figure 2.4**.

The values for frequency shift derived from the electrodeposition of Ag **Figure 2.4** were used in conjunction with charge passed to obtain a value of S_{ex} , the *mass sensitivity* of the device. Charges passed during the Ag electrodeposition and stripping processes was determined by a simple Trapezium Rule integration of the current passed as a function of time. A linear correlation of Δf versus *Charge (Q)* is observed for both electrodeposition **Figure 2.5** and electrodedissolution **Figure 2.6**.

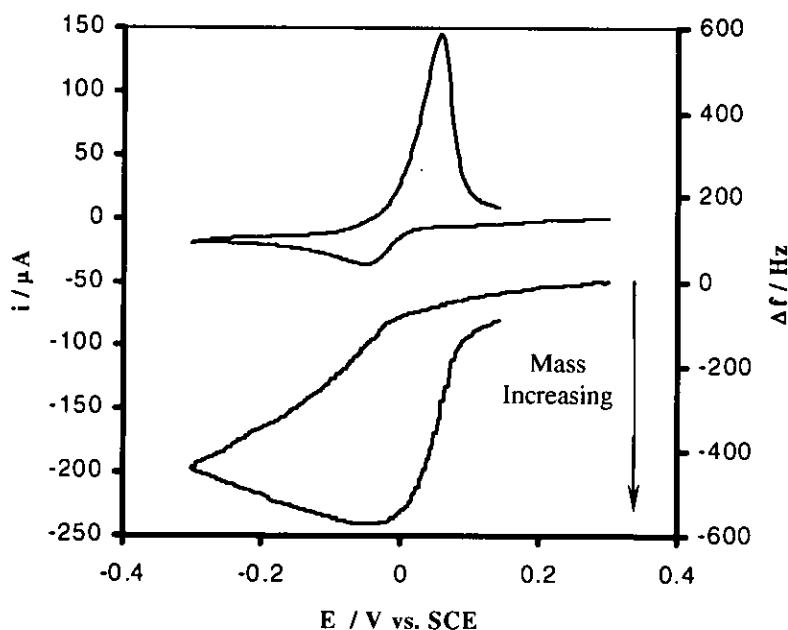


Figure 2.4: Simultaneous cyclic voltammetry and frequency response for a solution containing 1 mol m^{-3} AgNO_3 , 100 mol m^{-3} HClO_4 , at a Scan Rate 20 mV/s . The cathodic current is due to silver electrodeposition and is accompanied by a frequency decrease due to the mass gain at the electrode surface; the converse is true for the anodic current.

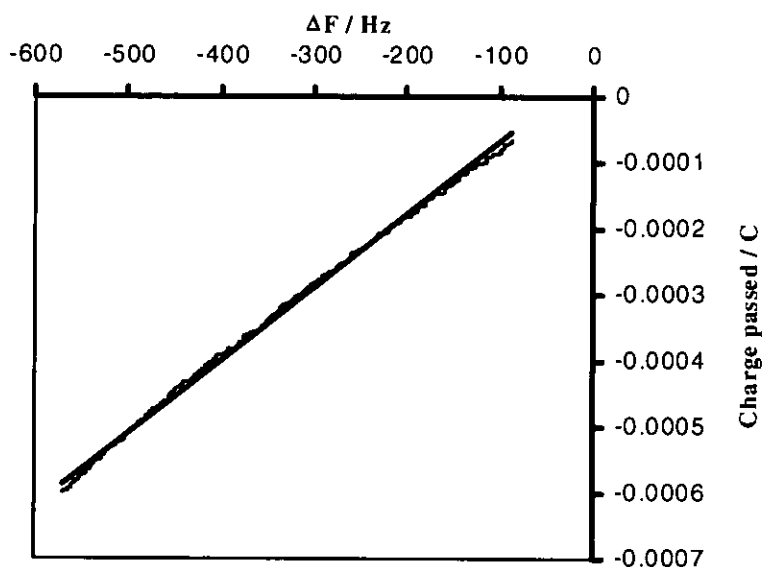


Figure 2.5: Charge passed during the reductive deposition of silver vs. the associated frequency change.

Regression analysis indicates a linear relation between charged passed and frequency given by $Q = (1.11 \times 10^{-6})\Delta f + (4.21 \times 10^{-5})$. The associated line has an R^2 value of 0.998.

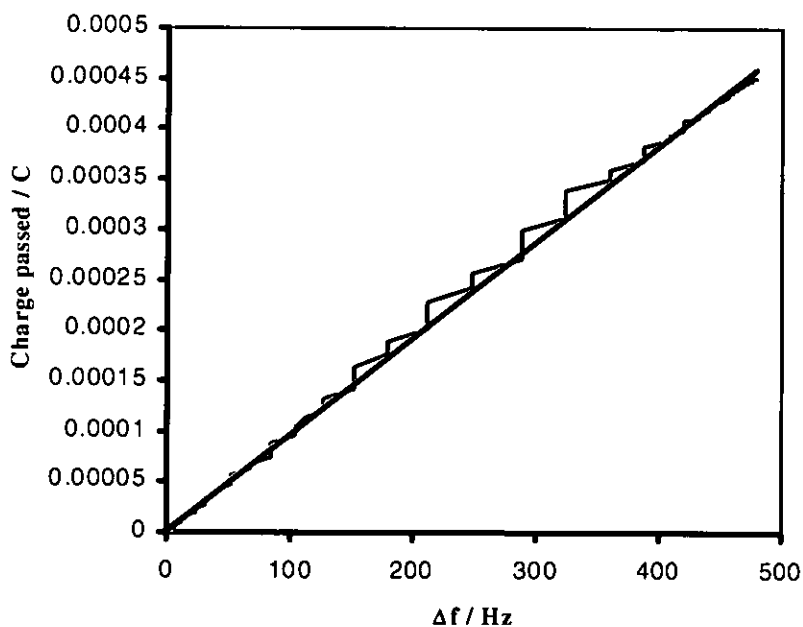


Figure 2.6: Charge passed during the oxidative dissolution of silver vs. the associated frequency change.

Regression analysis indicates a linear relation between charged passed and frequency given by $Q = (1.1 \times 10^{-6})\Delta f + (9.13 \times 10^{-7})$. The associated line has an R^2 value of 0.999.

The measured mass change may be obtained from the charge by using Faraday's Law:

$$\Delta m = \frac{QM_w}{z_i F} \quad (2.1)$$

Where, Δm is the *mass change*, Q is the *charge passed* during electro deposition / stripping, F is *Faradays constant*, M_w the *molecular weight* of the deposit and z_i is the *number of electrons* involved during the deposition / stripping phases. A plot of measured mass change versus frequency gives an experimental mass sensitivity. The mass sensitivity, determined from the average of the values for electrodeposition from **Figure 2.7** and electrodisolution from **Figure 2.8** is 1.242 ng Hz^{-1} .

Koh *et al* [2.3] found that mass sensitivities determined by simultaneous cyclic voltammetry and frequency response were closer to the theoretical sensitivity of $17.7 \text{ ng Hz}^{-1} \text{ cm}^{-2}$, calculated by the Sauerbrey equation, (*Equation 1.3*) than mass sensitivities determined by galvanostatic electrodeposition using a 5 MHz quartz crystal. The theoretical sensitivity of a 10 MHz quartz crystal is $4.417 \text{ ng Hz}^{-1} \text{ cm}^{-2}$ calculated by the Sauerbrey equation. For a 10 MHz quartz crystal with a 6 mm dia. Au electrode, the theoretical mass sensitivity is 1.249 ng Hz^{-1} . The experimental and theoretical values of mass sensitivity differ slightly because (i) the Sauerbrey equation is derived for application in a vacuum and (ii) assumes that the frequency change is due to a mass change associated with a rigidly attached deposit that is uniformly spread over the electrode surface.

The Sauerbrey equation predicts that a plot of Δm vs Δf is linear and has an intercept of zero. The intercept of the plot is non zero due to the double layer processes, which contribute to silver deposition [7.8].

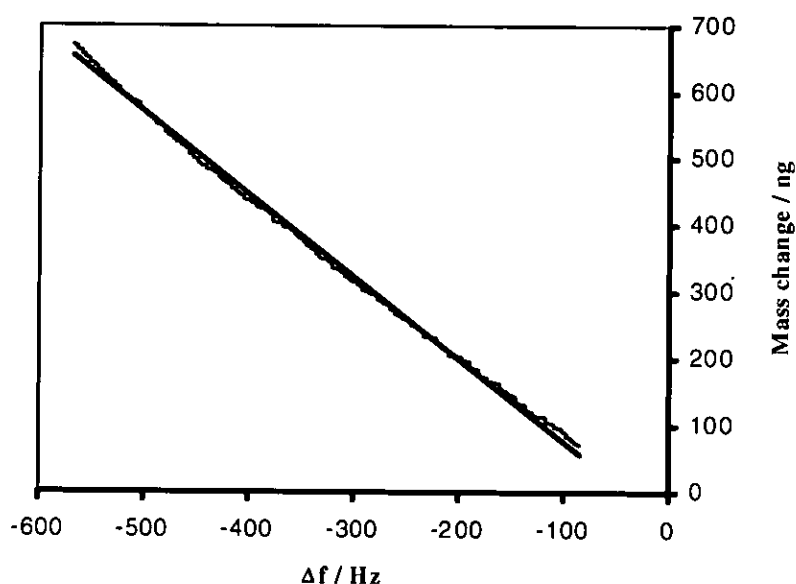


Figure 2.7: The mass change during electrodeposition of silver on the Au piezoelectrode (calculated using Faradays' law) versus the frequency change. Linear regression analysis indicates a linear relation between mass deposited in ng and frequency change is given by $\Delta M = 1.23\Delta f - 46.1$. The associated line has an R^2 value of 0.998.

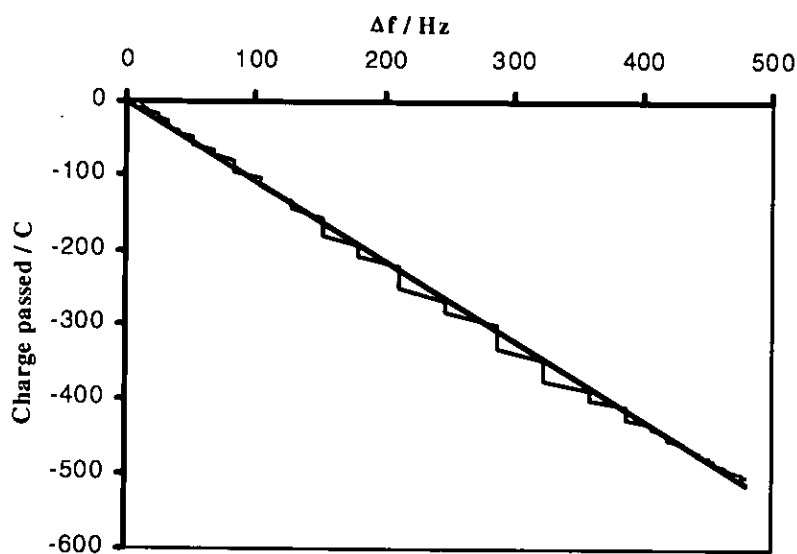


Figure 2.8: The mass change during electrodisolution of silver from the piezoelectrode (calculated using Faradays' law) versus the frequency change. Linear regression analysis indicates a linear relation between mass dissolved in ng and frequency change is given by $\Delta M = 1.23\Delta f - 1.02$. The associated line has an R^2 value of 0.999.

II.6 - PREPARATION OF ACETOHYDROXAMIC ACID SOLUTION

0.075 g of *aceto hydroxamic acid* (AHA) (Sigma-Aldrich C^o. Ltd.) were mixed with 500 cm³ of 100 mol m⁻³ HNO₃ (dilution of conc. HNO₃, AnalaR, BDH Chemicals Ltd.) in a 500 cm³ volumetric flask to give a 2 mol m⁻³ solution of AHA. 30 cm³ of this solution were placed into a Pyrex beaker, which was purged with N₂ for 600 s to remove all O₂. All measurements were carried out under a continuous blanket of nitrogen.

II.7 - GOLD MICRO-DISC ELECTRODE FABRICATION

Smaller electrodes, not manufactured in house, were purchased from commercial suppliers. These include a 0.6 μm diameter platinum microdisc electrode and a 5 μm diameter gold microdisc electrode (both from BAS Technicol Ltd., West Lafayette, US). Those made in house were fabricated as follows.

II.7.1 - Electrode Fabrication

Borosilicate glass Pasteur pipettes (John Poulton Ltd., Barking, Essex, UK) were trimmed so as to remove tapered ends. The pipette bodies and gold wire (250, 125, 50, and 25 μm diameter, 99.99+%, pure, Advent Research Chemicals Ltd.) were washed by sonication, for 900 s, in chloroform, acetone, ethanol (AnalaR grade, BDH Chemicals Ltd.) and E-pure water. After each wash, excess solvent was removed by a lens cloth. The glass tubes and gold wire were then dried for 900 s at 383 K. The gold wires and glass tubes were then washed in 5000 mol m⁻³ HNO₃ for 3600 s, finishing with a wash in E-pure water. The gold wires and glass tubes were then oven dried at 383 K for 1800 s.

Approximately 20 mm lengths of the washed gold wires were then sealed into the glass tubes by use of a bunsen burner, ensuring that ~5 mm of gold wire protruded from either side of the glass seal.

II.7.2 - Fabrication of Electrical Contact

For electrodes prepared in house, the electrical contact with the interior exposed gold wire was established by the following method. Woods metal (Bi 50/Cd 12.5/Pb 25/Sn 12.5, Advent Research Materials Ltd.) was cut into 2.5 mm pieces and dropped into the sealed glass tubes and melted by immersing the tubes in boiling water. An electrical contact was then made by placing a length of Cu wire (1-3 mm diameter, 99.99+% pure, Advent Research Materials Ltd.) into the molten woods metal, which was cooled to form a set. The sealed glass tube was given additional strength by injecting the interior of the glass tube with Araldite CY1300 and CY1301 (Ciba-Geigy Plastics, Duxford, Cambridge, UK). The excess gold wire protruding from the distal end of the sealed glass tube was trimmed and a gold disc shaped surface exposed with light sanding.

II.8 - GOLD MICRODISC ELECTRODE POLISHING PROCEDURE

The above fabricated gold microdisc electrodes were polished using diamond pastes of a decreasing granular size; 6 μm , 3 μm , and 1 μm , (Marcon Diamond Products Ltd., Hitchin, Hertfordshire, UK) upon a synthetic micro polishing cloth (product no. 40-7212, Buehler, Lake Bluff, Illinois, USA) and were washed with sonication in ethanol for 15min between each polish. Finally, the gold microdisc electrodes were polished with a slurry of Al_2O_3 (AnalaR, BDH Chemicals Ltd.) in a 10 mol m^{-3} solution of $\text{NaCN}_{(\text{aq})}$ (AnalaR, BDH Chemicals Ltd.) and sonicated in E-pure water for 900 s, so removing

any embedded alumina particles which could potentially act in an electrocatalytic fashion [2.9].

II.9 - GOLD MICRODISC ELECTRODE ELECTROCHEMICAL CLEANING PROCEDURE

Finally, the gold disc microelectrodes were polished electrochemically. This was accomplished by immersing the electrode in question in a solution of appropriate buffer ($100 \text{ mol m}^{-3} \text{ HNO}_3$) and sweeping 5 times between the solvent limits at a sweep rate of 90 mV/s . The electrochemical polishing procedure always terminated at the end of an anodic going sweep.

II.10 - IRON(III) CONTENT DETERMINATION USING QCM/EQCM EXPERIMENTS

The iron(III) content of a solution under investigation can be obtained by EQCM via the medium exchange technique. This involves first impregnation the Nafion/DFA composite layer overlying the Au/quartz crystal oscillator with Fe(III). The amount of Fe(III) adsorbed by the Nafion/DFA layer will then be proportional to Fe(III) concentration in the solution in question. Fe(III) uptake in the layer is then assessed by CV and QCM measurements. The former is accomplished by immersing the oscillator composite in the solution under interrogation for 30 to 60 s. The latter is accomplished by extracting the oscillator from the solution under investigation, rinsing and drying it and then immersing it an electrochemical cell containing $100 \text{ mol m}^{-3} \text{ HNO}_3$.

II.11 - PREPARATION OF THE EQCM/NAFION/DEFERRIOXAMINE COMPOSITE ELECTRODE

The EQCM electrode was cleaned as described in **Section II.14**. The polished and dried EQCM electrodes were coated with 5 to 20 μl of 5% Nafion solution in lower aliphatic alcohols and 10% water (Dupont 950 E.wt. Mfg Co., Solution Technology, Inc., Mendenhall, Pennsylvania, USA.). This volume covered the total area of the gold electrode and flags and also any quartz crystal presented to the solution. The solvent was allowed to evaporate at room temperature giving a Nafion coated gold/quartz electrode.

The Nafion coated gold/quartz crystal was then immersed in an aqueous solution of the desferrioxamine mesylate (DFA) (Sigma-Aldrich C^o. Ltd.) ligand for 18 hours. The (DFA) ligand partitioned into the Nafion film producing a Nafion/(DFA) composite modified gold/quartz crystal electrode.

II.12 - PREPARATION OF DESFERRIOXAMINE SOLUTION

1.642 g of (DFA) were mixed with 500 cm^3 of E-pure water in a 500 cm^3 volumetric flask to give a 5 mol m^{-3} solution of AHA. 30 cm^3 of this solution were placed into a Pyrex beaker, which was used for the incorporation of the (DFA) ligand into the EQCM/Nafion composite membrane.

II.13 - PREPARATION OF IRON(III) NITRATE NONHYDRATE SOLUTION

2.02 g of iron(III) nitrate nonhydrate (Fisher Scientific, Loughborough, Leicestershire, UK) were mixed with 500 cm³ of 5 mol m⁻³ HNO₃ (dilution of conc. HNO₃, AnalaR, BDH Chemicals Ltd.) in a 500 cm³ volumetric flask to give a 10 mol m⁻³ solution of iron(III). 10 cm³ of this solution were placed into a Pyrex beaker, which was used for the incorporation of iron(III) into the Nafion/DFA composite.

II.14 - CLEANING PROCEDURE FOR THE EQCM CHROMIUM, TITANIUM AND PURE GOLD BACKED ELECTRODES

All EQCM electrodes were washed in copious amounts of ethanol to remove all traces of grease produced during manufacture. This was followed by repetitive washing with E-pure water. Finally, the EQCM electrodes were electrochemically polished see **Section II.9.**

II.15 - EQCM Au NAFION/(DFA) COMPOSITE ELECTRODE CLEANING PROCEDURE

The Au quartz crystal oscillator coated with the Nafion/(DFA) composite is immersed into an activated carbon (Norit[®] Lancaster Synthesis Ltd. Morecambe, Lancashire, UK) organic solvent solution and sonicated for 300 s. The activated carbon organic solvent solution is prepared by placing 25 g of activated carbon into 500 ml of butan-1-ol. (Lancaster Synthesis Ltd.) The clean EQCM electrode is washed with copious amounts of E-pure water and finally polished electrochemically see **Section II.9**.

II.16 - PREPARATION OF METHYLENE BLUE SOLUTION

Methylene blue chloride (reagent grade) was purchased from BDH Chemicals (UK) and used without further purification. All other chemicals were of analytical grade or better and used without further purification. Prior to electrochemical use; all solutions were purged for 900 s with N₂ (white spot grade, BOC Ltd.) to remove dissolved O₂. The supporting electrolyte was a solution of 50 mol m⁻³ potassium dihydrogen phosphate/sodium hydroxide (both compounds AnalaR, BDH Chemicals Ltd.) buffer (pH 7.9) prepared in E-pure water.

II.17 - REFERENCES

- 2.1 E. Salomon. *Z. Phys. Chem.* **24**, (1897), 55
- 2.2 J. Heyrovsky. *J. Chem. Listy.* **16**, (1922), 256
- 2.3 W. Koh, W. Kutner, M.T. Jones and K.M. Kadish. *Electroanal.* **5**, (1993), 209
- 2.4 W. Stockel and R. Schumacher. *Ber. Bunsen-Ges. Phys. Chem.* **91**, (1987), 345
- 2.5 M. Benje, M. Eiermann, U. Pittermann and K.G. Weil. *Ber. Bunsen-Ges. Phys. Chem.* **90**, (1986), 435
- 2.6 C. Gabrielli, M. Keddam and R. Torresi. *J. Electrochem. Soc.* **138**, No 9, (1991), 2657
- 2.7 S. Bruckenstein and M. Shay. *Electrochim. Acta.* **30**, (1985), 1295
- 2.8 S. Bruckenstein and S. Swathirajan. *Electrochim. Acta.* **30**, (1985), 851
- 2.9 J. Zak and T. Kuwana. *J. Electroanal. Chem.* **39**, (1983), 645

CHAPTER III - GOLD OXIDATION & DISSOLUTION PROCESSES

CONTENT

<u>III.1 - ELECTROCHEMICAL STUDIES OF GOLD OXIDATION USING MICRODISC & EQCM ELECTRODES</u>	<i>Page 104</i>
<i>III.1.1 - Cyclic Voltammetric Study of Gold Oxidation in a 100 mol m⁻³ Nitric Acid Solution using Varied Sized Microdisc Electrodes</i>	<i>Page 109</i>
<i>III.1.2 - Cyclic Voltammetric & Gravimetric Study of Gold Oxidation and Reduction in Varying Anion Solutions</i>	<i>Page 112</i>
<i>III.1.2.i - The Angerstein-Kozłowska Model of Oxide Monolayer Formation on Gold</i>	<i>Page 113</i>
<u>III.2 - SIMULTANEOUS CYCLIC VOLTAMMETRIC & VOLTAMASSOGRAM SWEEP RATE STUDIES IN VARYING ANION SOLUTIONS</u>	<i>Page 117</i>
<i>III.2.1 - Assessment of the High Sweep Rate Simultaneous Cyclic Voltammetric and Voltamassogram Results</i>	<i>Page 117</i>
<i>III.2.2 - Assessment of the Low Sweep Rate Simultaneous Cyclic Voltammetric and Voltamassogram Results During Sweep Rate Dependent Studies</i>	<i>Page 125</i>

III.2.3 - Response of Au in HNO₃ as a Function of Increasing Sweep Rate *Page 141*

III.3 - CONCLUSIONS *Page 147*

III.4 - REFERENCES *Page 148*

III.1 - ELECTROCHEMICAL STUDIES OF GOLD OXIDATION USING MICRODISC & EQCM ELECTRODES

The initial technological objective of this project was to develop a prototypical EQCM based sensor specific towards actinide metal ions of interest to the nuclear industry. However, as the project progressed, it became apparent that two factors in the sensor design would necessitate an exploration of the electrochemistry of the gold.

(i) Selectivity is to be achieved by immobilising actinide-specific hydroxamic acid ligands at the electrode surface. For reasons pertaining to sensor robustness, an exploration of the oxidative stability of hydroxamic acids needs to occur. However, the oxidative electrochemistry of hydroxamic acids exhibits considerable overlap with that of gold. Thus, the latter must be fully characterised in order to facilitate the deconvolution of the former. This would be a trivial matter were it not for the second factor:

(ii) The sensor is to be deployed in nuclear reprocessing streams – consequently, it needs to function in concentrated nitric acid media. To our knowledge, the oxidative behaviour of Au at the EQCM has never been studied in nitric acid media.

Thus, it was against this background that we commenced an exploration of the oxidative electrochemistry of gold in nitric acid solution.

Gold is renowned for its chemical stability. However, this stability is compromised in acid solutions under anodic conditions [3.1, 3.2, 3.3 & 3.4] and in the presence of certain anions such as chloride [3.5, 3.6, 3.7, 3.8, 3.9, 3.10, 3.11, 3.12, 3.13, 3.14, 3.15 & 3.16]. This instability can be manifested as one or several of the following processes: anion-assisted dissolution, electro-oxidative dissolution, surface reconstruction of the electrode and electrogeneration of the metal oxide / hydroxide.

The mechanism and products of these processes have been widely investigated in acid and also neutral and basic media by a number of authors, including Burke and co-workers [3.17, 3.18, 3.19, 3.20, 3.21, 3.22, 3.23 & 3.24], Rand and Woods [3.25 & 3.26], Ferro and co-workers [3.27 & 3.28], Angerstein-Kozłowska and co-workers [3.29, 3.30, 3.31 & 3.32] and Hamelin and co-workers [3.33, 3.34, 3.35, 3.36, 3.37, 3.38 & 3.39], and a number of reviews have been published on the subject [3.40, 3.41, 3.42, 3.43, 3.44 & 3.45]. Electro-oxidation of gold has been studied using a wide range of techniques including: classical macroelectrode potentiometry [3.5], a.c impedance, [3.46], coulometry coupled with atomic absorption spectroscopy [3.9 & 3.25], SEM [3.47 & 3.48], STM [3.15, 3.16 & 3.49], in-situ IR reflectance spectroscopy, [3.50 & 3.51], in-situ surface enhanced raman spectroscopy [3.14], rotating ring-disc electrodes [3.4, 3.8 & 3.10 to 3.13], square wave voltammetry [3.52] and the electrochemical quartz crystal microbalance [3.48, 3.53, 3.54, 3.55, 3.56, 3.57, 3.58, 3.59 & 3.60].

EQCM has been used in the study of dissolution [3.8, 3.26, 3.53, 3.54 & 3.61] and adsorption processes at electrode surfaces [3.62, 3.63, 3.64, 3.65, 3.66 & 3.67], including those associated with the oxidation of small organic molecules [3.68 & 3.69]. While it is true that the EQCM cannot yield any information concerning the identity of the adsorbed and/or dissolving species or products, it does provide a profile of changes in electrode surface morphology (dissolution, surface oxide formation, adsorption etc). The resultant mass profiles, recorded alongside electrochemical experiments, have been found to be particularly valuable in identifying both the general nature of the morphological process occurring and the potential at which that process commences.

It is well established that the oxidative electrochemistry of gold is highly dependent on the structure of the gold / aqueous electrolyte interface. It is particularly dependent upon the crystal face presented to solution. The crystal face in turn determines the observed

differences in the electrochemical behaviour associated with: (a) deposition / adsorption of OH; (b) reconstruction processes involving turnover of OH-Au dipoles of the lattice; (c) adsorption and desorption of anions; and (d) dissolution of the Au surface. Given its capability to interrogate the mass changes associated with adsorption and dissolution processes at electrode surfaces, EQCM offers a powerful technique with which to study the electro-oxidative processes that occur at gold electrodes. This is especially true with respect to gold dissolution, which must otherwise be studied by quantitative analysis of product generated during potentiostatic polarization measurements. The elucidation of the mechanism of the dissolution process is impossible to achieve by use of potentiostatic polarisation measurements alone as analysis is usually carried out after a prolonged electrolysis because of low sensitivity of the analytical techniques. However, EQCM can detect mass changes on the nanogram scale with a time resolution of < 1 s, so facilitating real-time study of the metal dissolution reaction(s).

As mentioned above, a number of authors have used the EQCM in the study of the anodic processes on Au in acidic media. While much is understood about the mechanism of electrogeneration of the pseudo-2D phase oxide monolayer that precedes formation of bulk oxide at the gold surface, there is still some debate in the literature concerning aspects of this process, especially:

- (i) whether the oxide monolayer arises from chemisorption of oxidised water molecules or direct oxidation of Au [3.70];
- (ii) the chemical nature of the monolayer – if formed by Au oxidation, what is the extent of Au(III) formation within that monolayer [3.71, 3.72 & 3.73];
- (iii) the extent of Au dissolution – does any Au(III) formed within the monolayer participate in any dissolution process, so competing with oxide formation [3.59 & 3.74]; and

- (iv) the nature of the anion adsorption processes that occur in the so-called “double layer” charging region that precedes the potential range over which surface oxide formation occurs [3.56 & 3.59].

Previous studies concerning the role of anion adsorption in oxide monolayer formation and Au dissolution have for the most part been concerned with measurements in hydrochloric [3.53 & 3.58] and sulphuric acid [3.57 to 3.59, 3.75 & 3.76], whose anions are strongly adsorbed at gold electrode surfaces [3.29 & 3.31], and perchloric [3.48, 3.53, 3.54 & 3.56] acid, whose anions are (comparatively) weakly adsorbed [3.31, 3.38 & 3.77]. Particular attention has been paid to the latter pair as the tetrahedral trigonal face symmetry and dimensions of these ions are compatible with the trigonal symmetry and internuclear distance of the densely packed Au(111) plane - the distances between the gold atoms on the Au(111) plane is 0.288 nm, while the distances between the O atoms of the anions are 0.272 nm for sulphate and 0.236 nm for perchlorate [3.31].

As stated above, to our knowledge, there have to date been no EQCM-based studies on the electro-oxidative behaviour of gold electrodes in nitric acid, the anion of which exhibits a strength of adsorption on Au intermediate between that of perchlorate and sulphate [3.30 & 3.31]. In situ FTIRS measurements of the adsorption of nitrate on gold indicate that the NO_3^- most likely adsorbs with a two-fold co-ordination, perpendicular to the Au surface [3.50 & 3.51]. Further, the distance between the O atoms of the nitrate anion is 0.235 nm [3.78] which, like that of perchlorate (0.236 nm), is compatible with the Au internuclear distance (0.28841 nm) on the Au(111) plane. Thus, unlike the perchlorate and sulphate anions, whose trigonal-face symmetry is completely mismatched with that of the respective two and four fold symmetries of the Au(110) and Au(100) faces, both the two-fold symmetry and dimensions of the adsorbing nitrate anion are compatible with those of all three low index crystal planes of gold, so facilitating the study of electrochemical

phenomena associated with high densities of anion adsorption on polycrystalline gold surfaces.

Further, virtually all of the voltammograms reported for gold electrodes in mineral acid media have been recorded at sweep rates, v , of 20 mV/s or above. However, slow scan rate experiments offer the opportunity to study any reactions that, thermodynamically, should occur at potentials cathodic of monolayer oxide formation, but which, kinetically, are much slower than that process.

This section therefore explores the microelectrogravimetric responses of Au in HNO₃, H₂SO₄ and HClO₄ on piezoelectrodes of a range of material composition. Furthermore an explanation for the response of Au in HNO₃, H₂SO₄ and HClO₄ over a range of sweep rates down to $v = 1$ mV/s will be addressed. The information that is obtained, complementary to that acquired in HClO₄ & H₂SO₄ media at higher sweep rates, will provide a further understanding of Au redox mechanisms.

III.1.1 - Cyclic Voltammetric Study of Gold Oxidation in a 100 mol m⁻³ Nitric Acid Solution using Varied Sized Microdisc Electrodes

The CV profiles for microdisc electrodes with a gold polycrystalline disc electrode diameter of 250, 50, 25 & 5 μm respectively, obtained in a 100 mol m⁻³ nitric acid solution, are compared in *Figures 3.1* to *3.4* and show typical gold cyclic voltammetric response.

For all electrode radii, during the initial positive-going scan hydrogen evolution wave can be seen from 0.00 to +0.30 V (vs. SCE). Between +0.30 to +0.70 V (vs. SCE) the scan appears featureless although a small oxidation peak, due to possible submonolayer production of an ill-characterised anion adsorption process, exists according to Angerstein-Kozłowska and co-workers [3.30].

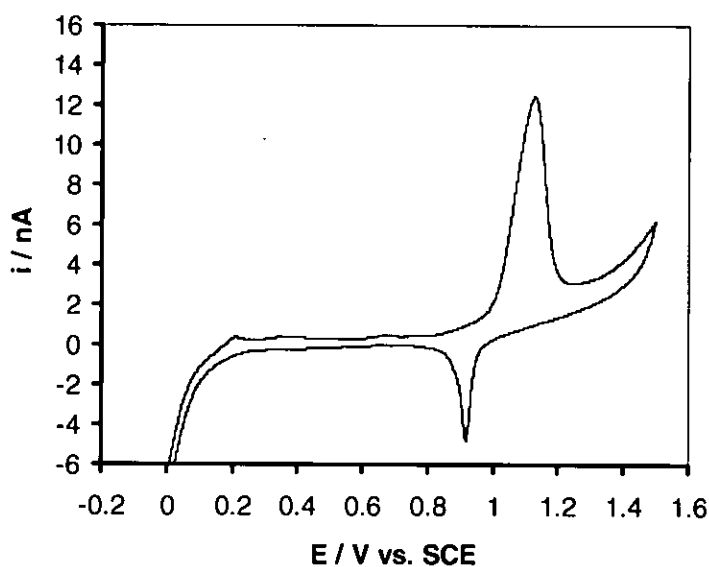


Figure 3.1: Cyclic voltammogram of 100 mol m⁻³ nitric (pH1) acid using a 250 μm Au microdisc electrode at ν 1 mV/s.

A large broad oxidation wave is observed in *Figures 3.1* to *3.4* with an onset of +0.90 V (vs. SCE) followed by a smaller peak with an onset of +1.30 V (vs. SCE).

Comparison of the CV profiles in *Figures 3.1 to 3.4*, with those recorded by Angerstein-Koslowska *et al* [3.29 to 3.32], and Burke *et al* [3.19, 3.21 & 3.79], indicate that the oxidation waves at +0.90 V and +1.30 V (*vs.* SCE) are due to the formation of several sublattice hydroxide layers. This sublattice hydroxide layers in turn form a passivating layer of gold at the electrode surface.

From the switching potential during the reverse cathodic going scan, a reduction peak associated with gold oxide dissolution is observed in the potential range of +1.00 V to +0.80 V (*vs.* SCE). A more detailed peak assignment for the data of *Figures 3.1 to 3.4* can be achieved using the combined technique of cyclic voltammetry and gravimetry provided by the EQCM.

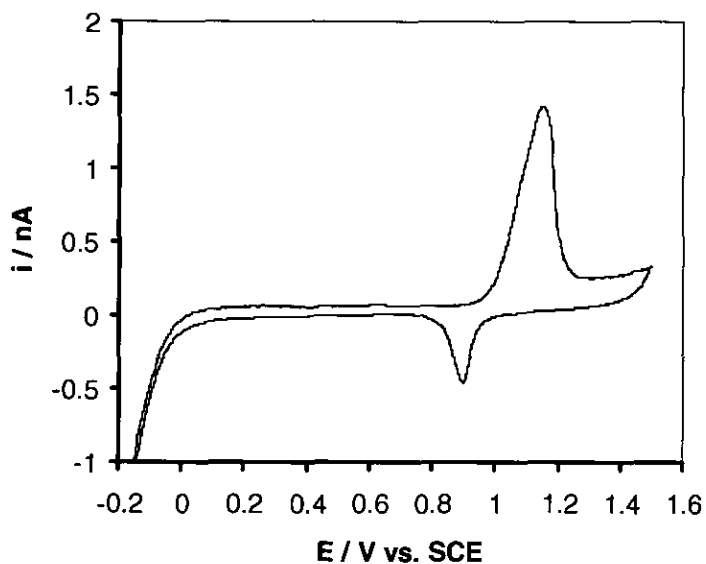


Figure 3.2: Cyclic voltammogram of 100 mol m⁻³ nitric (pH1) acid using a 50 μm Au microdisc electrode at v
1 mV/s.

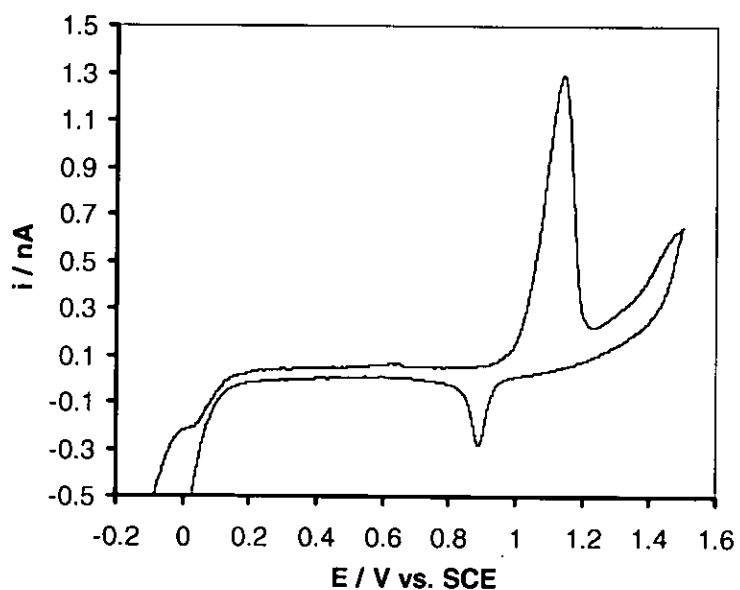


Figure 3.3: Cyclic voltammogram of 100 mol m⁻³ nitric (pH1) acid using a 25 μm Au microdisc electrode at v
1 mV/s.

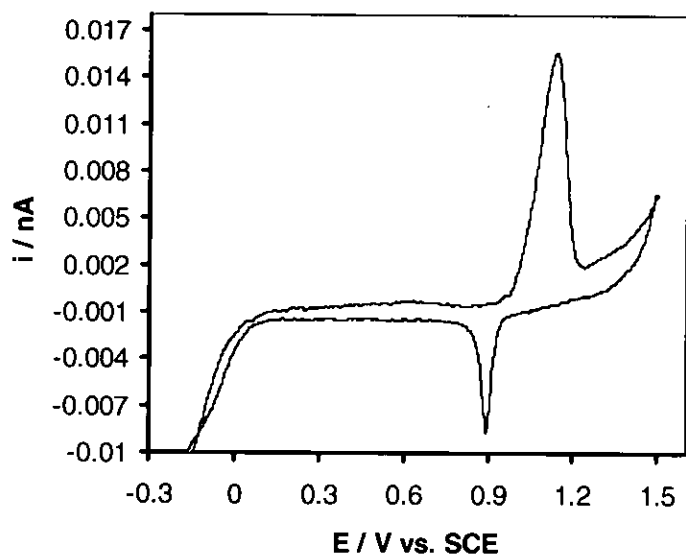


Figure 3.4: Cyclic voltammogram of 100 mol m⁻³ nitric (pH1) acid using a 5 μm Au microdisc electrode at v
1 mV/s.

III.1.2 - Cyclic Voltammetric & Gravimetric Study of Gold Oxidation and Reduction in Varying Anion Solutions

Figure 3.5 shows a CV and cyclic voltamassogram recorded in house for a polycrystalline Au piezoelectrode in $100 \text{ mol m}^{-3} \text{ HNO}_3$. The positive switching potential is $+1.40 \text{ V}$ (vs. SCE) and it is generally accepted that bulk phase oxide formation on gold at pH 1 only commences once the potential exceeds this value [3.46, 3.52, 3.59 & 3.60]. Comparison of the CV of **Figure 3.5** with that recorded in $100 \text{ mol m}^{-3} \text{ HClO}_4$ [3.56 & 3.53] reveals the two to be virtually identical, suggesting that processes occurring on polycrystalline Au in HClO_4 also occur in HNO_3 . Thus, it seems appropriate that we bear in mind models developed for Au in perchloric acid when developing a model to explain our results in nitrate and sulphate media. As discussed in **Chapter 1**, oxide formation on Au electrodes in HClO_4 and H_2SO_4 media has been extensively studied by Angerstein-Kozłowska *et al* [3.29 to 3.32] and a discussion was presented in that chapter of the generation of gold oxide layers at monocrystalline electrode surfaces. However, our studies were conducted at polycrystalline surfaces. Therefore, the next section presents a summary of the findings of Angerstein-Kozłowska *et al* pertaining to the mechanism of gold oxide formation on polycrystalline surfaces. For the convenience of the reader, we will first summarise those aspects of their work that are relevant to the Au/nitric system, but which are generically inherent and well established for the Au/sulphuric and Au/perchloric systems as well.

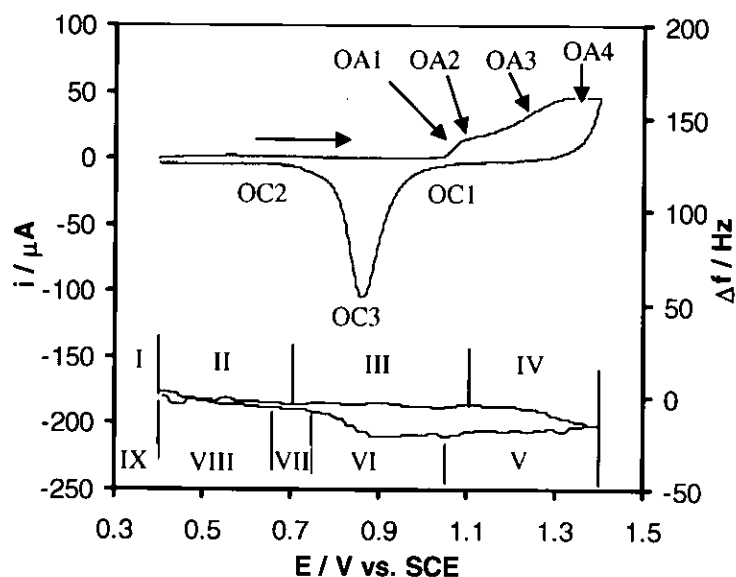


Figure 3.5: Cyclic voltammogram of 100 mol m^{-3} nitric (pH1) acid using a 14 mm Au(Ti) EQCM crystal at 90 mV/s .

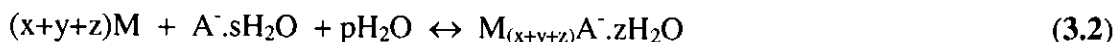
III.1.2.i - The Angerstein-Kozłowska Model of Oxide Monolayer Formation on Gold

Using the peak designation of **Figure 3.5**, Angerstein-Kozłowska *et al* have suggested that oxide formation at the metal (M) surface proceeds in two, one electron steps [3.29 to 3.32]:



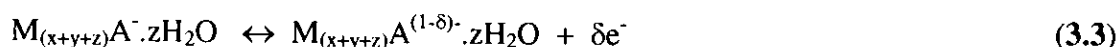
When sites of various energies are present on the surface the transfer of at least the first of the two electrons will produce a number of peaks, one for each energy state. These sites arise during the electrochemical oxidation of solid metal electrodes on which anions are adsorbed. Thus, “MOH” here represents not a stoichiometric phase compound, but a state of OH electroadsorption in some 2D surface lattice. The representations MO, OHM and OM

used below are similarly symbolic. At potentials positive of the point of zero charge ((pzc), ca. +0.16 V (vs. SCE) for Au [3.29]) but negative of OH adsorption, a reversible electrostatic adsorption of hydrated anions is observed:

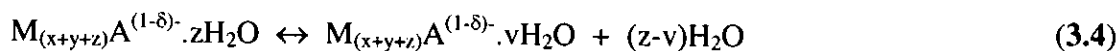


where $s + p = z$, z is the hydration number.

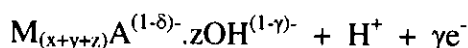
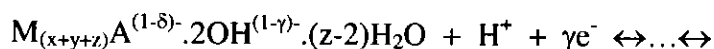
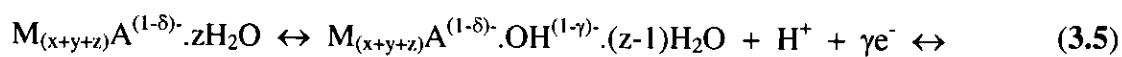
Depending on the compatibility of the anion's dimensions and symmetry with that of Au crystal face, they may then undergo partial or full charge transfer to form chemisorbed species:



The stronger the chemisorption, the larger δ . For strongly chemisorbed ions, as coverage by discharged anions increases, the hydration number z diminishes [3.31]:

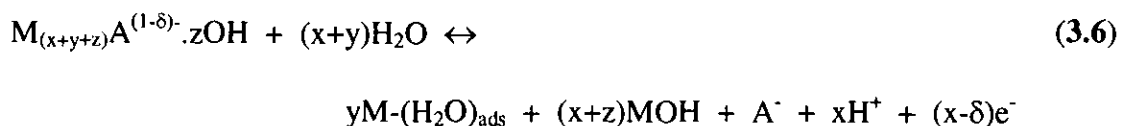


Angerstein-Kozłowska *et al* propose that *Reaction 3.1a* then occurs by 3 overlapping processes, each forming a 2D lattice of OH species at the Au surface. As a result of the "pre-adsorption" of anions, the initial stages of OH deposition occur within the overlay lattice of adsorbed anions from the H-bonded hydration water of the anions:



where $\gamma \cong 0.5 e^-$ per OH.

Reaction 3.3 gives rise to peak OA1 in *Figure 3.5* and has been shown to be reversible. At any single crystal Au face, where long-range order can arise on the surface, the OH's become partially discharged ($\gamma \cong 0.5 e^-$ per OH). The resultant H-bonded complexes involving the anions then stabilise the overlay lattice formed on the surface, making the OH-M turnover process (*vide infra*) and anion desorption more difficult. At polycrystalline Au, no long range order can develop. The deposition of OH species then seems to occur between the chemisorbed anions with complete discharge of the OH i.e. $\gamma \cong 1$. Thus, Angerstein-Kozłowska *et al* suggest that the effect of the chemisorbed anions is twofold [3.31]: (i) to hinder oxidation of Au by blocking the surface for discharge of water from the free water network; and (ii) to facilitate full or partial discharge of the H₂O H-bonded to the anions, so providing a path for H₂O discharge which occurs at less positive potentials than the main oxidation reaction. *Reaction 3.5* may therefore be regarded as underpotential deposition of OH between the adsorbed anions [3.30 & 3.43]. In the case of polycrystalline Au, peak, OA2 corresponds to the to the development of the second sublattice of OH via deposition of OH accompanied by anion desorption.



Concomitant with this is reconstructive surface turn-over (RTO) of the MOH dipoles:



which ultimately gives rise to a quasi-2-D phase oxide, the precursor of a 3-D phase oxide. If anion adsorption effects are sufficiently strong, then place exchange is forced to occur at higher fields in the double-layer and hence can be established beyond the potential for the

initial stages of OH deposition (OA1). Peak OA3, corresponds to the deposition of OH into the third sublattice, so completing the OH monolayer:



Reaction 3.1b occurs in peak OA4 which is broad on polycrystalline Au [3.30], due to:

(i) *Reaction 3.1b* occurring simultaneously with TO of MOH (*Reaction 3.7*) and MO [3.54]:



(ii) The reorientation of the MOH and MO dipoles during TO disturbing the symmetry of the sublattices; consequently, they are not seen as separate peaks in the oxidation to MO (OA4) or in the reduction process of the turned over material (OC3) [3.31].

III.2 - SIMULTANEOUS CYCLIC VOLTAMMETRIC & VOLTAMASSOGRAM SWEEP RATE STUDIES IN VARYING ANION SOLUTIONS

III.2.1 - Assessment of the High Sweep Rate Simultaneous Cyclic Voltammetric and Voltamassogram Results

To ensure that the observations discussed herein for the nitric acid system are generic and wholly applicable to gold in a range of anions, CVs and voltamassograms of gold in perchloric and sulphuric acids are included for the purpose of reference comparison with our findings. As such **Figures 3.6 & 3.7** can be observed to be in keeping with those of the nitric acid system **Figures 3.8 & 3.9** and also with that gleaned from literature sources. Consequently, this section contains some discussion of the processes observed into the perchlorate and sulphate systems as a basis for the interpretation of results from the nitric acid / gold system.

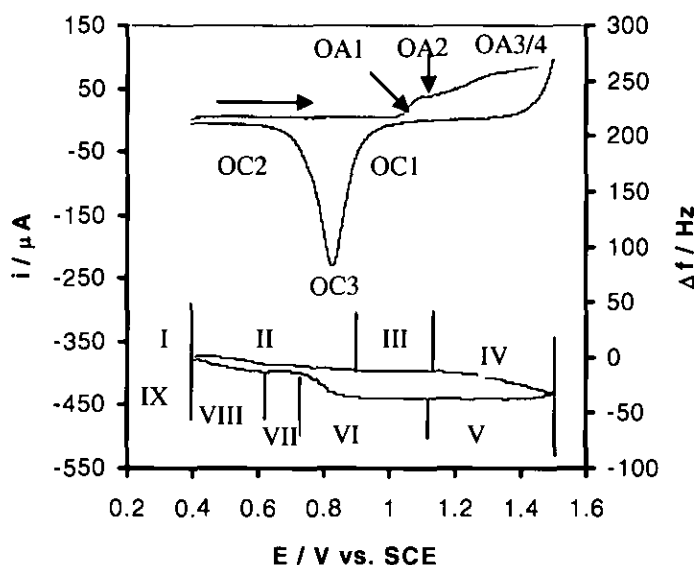


Figure 3.6: Cyclic voltamassogram of 100 mol m⁻³ perchloric (pH1) acid using a 14 mm Au(Cr) EQCM crystal at v 100 mV/s.

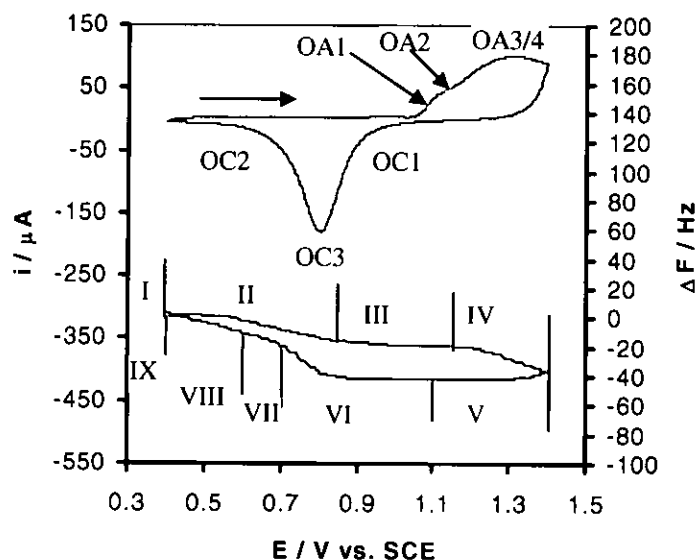


Figure 3.7: *Cyclic voltammogram of 50 mol m⁻³ sulphuric (pH 1.3) acid using a 14 mm Au(Cr) EQCM crystal at ν 100 mV/s.*

Figures 3.8 & 3.9 show CVs and voltamassograms recorded for a polycrystalline Au electrode at $\nu = 90 \text{ mV s}^{-1}$ in 100 and 1000 mol m⁻³ HNO₃. The scans were started at +0.40 V (vs. SCE), reversed at +1.40 V (vs. SCE) at pH 1 and +1.50 V (vs. SCE) at pH 0, and stopped at the initial potential. As the data at pH 0 & 1 are broadly similar, this section will be concerned with a discussion of **Figure 3.8**, although observations analogous to those made at pH 1 may also be made for the data of **Figure 3.9** / pH 0. Based upon comparison with the ClO₄⁻ system, the processes occurring in zones I to IX of **Figure 3.8** are as follows:

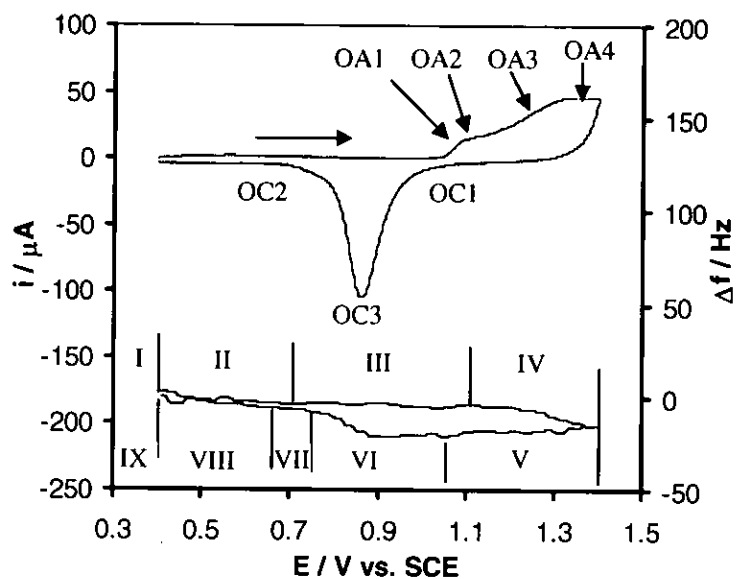


Figure 3.8: Cyclic voltammogram of 100 mol m^{-3} nitric (pH1) acid using a 14 mm Au(Ti) EQCM crystal at v 90 mV/s.

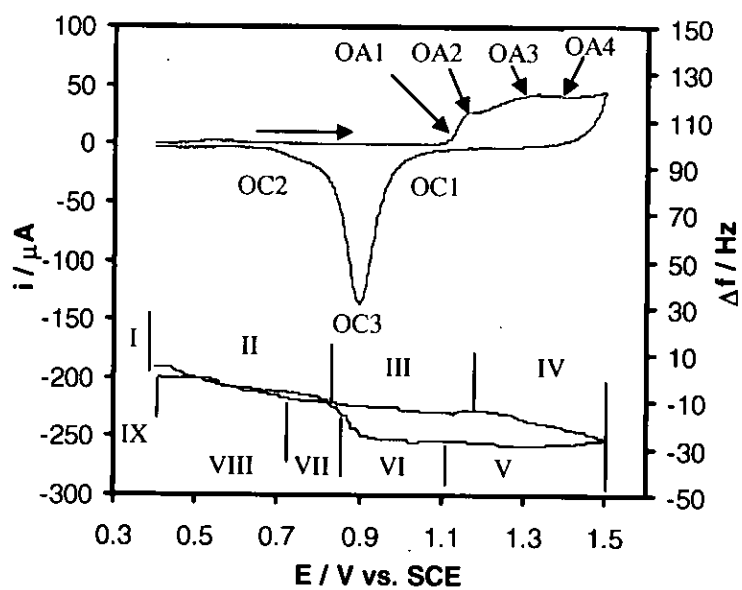


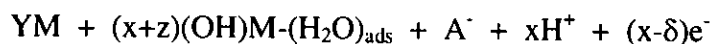
Figure 3.9: Cyclic voltammogram of 1000 mol m^{-3} nitric (pH0) acid using a 14 mm Au(Ti) EQCM crystal at v 90 mV/s.

ZONE I –The non-faradaic region, associated with changes in the structure of the double layer at the Au surface. Current flow and mass changes are negligible [3.54].

ZONE II – The small peak observed at $+0.40 \text{ V} < E < +0.60 \text{ V}$ (vs. SCE) and the simultaneous electrode mass increase are due to two effects: (i) the formation of a sub monolayer of AuOH species at Au (ad)atoms in low coordination sites; (ii) the adsorption of NO_3^- ions and their associated waters of hydration. The former was first suggested by Burke *et al* as a means to explain electrocatalytic effects in the pre-oxide region [3.19, 3.21 & 3.79]. Burke *et al* estimate that $< 1\%$ of the Au sites are converted to the hydrous oxide in the pre-oxide region. Gordon & Johnson [3.55] suggest that these sites facilitate the adsorption of H_2O molecules via H-bonding, so leading to an increase in mass. The latter effect, the nitrate analogue of Reactions 3.2 & 3.3, has been previously investigated for Au electrodes in HClO_4 [3.29 to 3.32, 3.53 & 3.54], H_2SO_4 [3.29 to 3.32 & 3.57] and HCl [3.53 & 3.57] media.

ZONE III – The processes of *zone II* are complete, so little variation of mass with potential is observed in this region. The current peak $+1.09 \text{ V}$ (vs. SCE) has been attributed to Reaction 3.5 [3.29 to 3.32, 3.43 & 3.54] and corresponds to peak OA1. As suggested by Bruckenstein & Shay, the change in weight accompanying the loss of H^+ is too small to be detected, and so no mass change is seen in that region of the voltamassogram [3.54].

ZONE IV – The current in this region has been attributed to the RTO process [3.29 to 3.32] described by Reactions 3.6 (corresponding to peak OA2) & 3.7 or the net process:



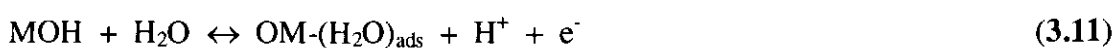
i.e. A^- has been replaced by xOH and $(x+z)H_2O$ at the electrode surface, so leading to the small mass increase observed in the corresponding region of the voltammogram.

The mass increase in this zone has been attributed to two sources: (i) formation of a place exchanged surface monolayer of 2-D-phase oxide; and (ii) entrapment of solvent at the surface due to roughening induced by oxide formation. The latter phenomenon in particular has been extensively investigated in the literature. It has been demonstrated by means of capacitance and SEM measurements that the Au surface remains smooth upon a single potential scan in basic and neutral electrolytes [3.48]. Further, STM measurements [3.15, 3.16, 3.49 & 3.80] have shown that, for Au(111) in $10 \text{ mol m}^{-3} \text{ HClO}_4$, clusters of gold are produced during the last stage of oxidation i.e. the RTO step. This cluster generation leads to hollow formation during the reduction of the oxide and to the expectation that liquid trapped within these hollows will be dragged along as the crystal oscillates, so increasing the effective mass of the electrode [3.47]. However, it has been observed that these hollows are removed when the electrode is returned to potentials negative of its p.z.c. (ca. $+0.16 \text{ V}$ (vs. SCE)).

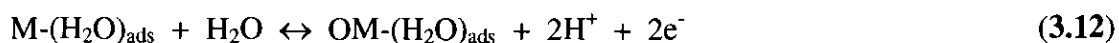
The electrode potential is well positive of the p.z.c at all times in *Figure 3.8*, suggesting that hollows/roughening generated during the potential scan will be retained at scan end. The most obvious manifestation of an increase in surface roughening would be the presence of a gap between the frequency at $+0.40 \text{ V}$ (vs. SCE) at the start and end of the cycle. As no such gap is observed in *Figure 3.8* and potentials at which removal of surface oxide-associated roughening occurs have not been accessed, we conclude that our electrode maintains a constant level of surface roughness throughout the experiment. Further, given that a significant level of 3-D-phase oxide formation would involve considerable disruption of the metal surface lattice [3.87] which would ultimately lead to roughening of the surface. We also conclude that, by reversing the scan at $+1.40$ & $+1.50 \text{ V}$ (vs. SCE) at pH 1 & 0, we

are forming little more than a monolayer of the 2-D-phase oxide at the surface at $v > 50 \text{ mV s}^{-1}$. These conclusions are in keeping with the findings of Cadle & Bruckenstein [3.8] and Gordon & Johnson [3.55] who both report that significant roughening of Au (with the possibility of entrapment of solution) is only observed at $E > +1.80 \text{ V (vs. SCE)}$.

Thus, the mass change in *zone IV* is associated with formation of surface oxide species via *Reaction 3.1b*. This occurs in concert with the place exchange process of *Reaction 3.9* with a resultant increase in the electrode mass [3.54], the net process being given by:



From the total charge passed, Q , the corresponding change in frequency, Δf , and *Reaction 3.3c*, we can calculate the mass change per mol-equivalent electron (mpe) for this region which, for *Figure 3.8*, has a value of $+11.5 \text{ g / mol-e}$. The theoretical mpe for *Reaction 3.11* is $+17 \text{ g / mol-e}$ which, in conjunction with the broadness of the current feature in *zone IV* [3.30] is suggestive of at least two parallel processes occurring [3.46]. Further, it is reasonable to expect *Reaction 3.8* to occur at least in part in *zone V*, the product of the reaction then participating in *Reaction 3.11*. The net process is then:



which has a theoretical mpe of 8 g / mol-e . The concurrence of *Reaction 3.12* with *Reaction 3.11* would then lead to an observed mpe value less than that predicted on the basis of *Reaction 3.11* alone. Thus, the *i-E* profile in *zone IV* is comprised of peaks OA3 & OA4 in the Angerstein-Kozłowska description of the electrochemistry of Au.

The total increase in mass during oxide formation is 46.5 ng cm^{-2} . Interestingly, *Reactions 3.11* & *3.12* lead to a net increase in mass of 17 & $16 \text{ g per mol of Au turned over}$. Using the smaller of these two values, the total mass increase corresponds to the inclusion of ca.

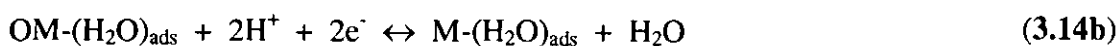
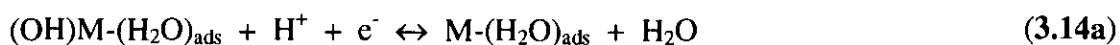
1.7×10^{15} atoms of oxygen cm^{-2} . Given that the number of Au atoms cm^{-2} is ca. 1.2×10^{15} , this further supports our earlier conclusion that little more than a monolayer of 2-D oxide is being generated during the experiment of *Figure 3.8*.

ZONE V – Neither current nor mass change is observed until +1.10 V (vs. SCE) at pH 1 and +1.20 V (vs. SCE) at pH 0, suggesting that the electrode has been passivated by the oxide layer.

ZONE VI – In agreement with the results recorded in HClO_4 solution [3.54], ~20% of the charge in the large cathodic, oxide stripping peak passes before a mass change occurs. Angerstein-Kozłowska *et al* [3.29 to 3.32] have suggested that the current in this region, peak OC1, is due to reduction of non-place-exchanged MOH sites, the mass increase upon the gain of H^+ being too small to be detected:



Besides non-place-exchanged MOH groups, the main constituents of the oxide layer are place-exchanged MO and MOH groups (*Reactions 3.7 & 3.9*) [3.31 & 3.33]. Calculation of the mpe at $+0.90 \text{ V} > E > +0.80 \text{ V}$ (vs. SCE), where the current is accompanied by a change in mass, gives an value of -10.8 g / mol-e . The turn-over and subsequent reduction of place-exchanged MOH & MO groups can be expressed as the following net *Reactions*:



with mpe values of -17 and -8 g / mol-e respectively. Thus, in analogy with *zone IV*, the observed mpe is due to two parallel processes occurring in this range which, in accordance with Angerstein Kozłowska *et al* [3.30], are given by *Reactions 3.14a & 3.14b*.

ZONE VII – A small mass increase can be observed in *zone VII* due to (i) readsorption of NO_3^- and their water molecules of hydration at the freshly regenerated Au surface; and (ii) the redeposition of any dissolved Au(III) species. The former effect has been discussed above; the latter will be discussed in more detail below.

ZONES VIII & IX – The small cathodic peak at $+0.40 \text{ V} < E < +0.60 \text{ V}$ (*vs.* SCE) and the simultaneous electrode mass decrease is then due to the desorption of nitrate anions and their associated waters of hydration from the electrode surface i.e. the reverse of the process occurring in *zone II*. *Zone IX* is the non-faradaic region, as in *zone I*.

III.2.2 - Assessment of the Low Sweep Rate Simultaneous Cyclic Voltammetric and Voltamassogram Results During Sweep Rate Dependent Studies

Figures 3.10-3.14 & 3.15-3.19 show CVs and voltamassograms for titanium backed Au electrodes in 100 and 1000 mol m⁻³ HNO₃, recorded sequentially from $\nu = 50 \text{ mV s}^{-1}$ to 1 mVs⁻¹. Both responses change with ν . In the forward scan of the CV, the relative height of peak OA1 first decreases with ν . However, at $\nu < 10 \text{ mV s}^{-1}$, a new peak, OA0, appears in the vicinity of OA1, its relative size increasing as ν decreases. The relative size of peak OA2 simply increases as ν is decreased. While little or no change is observed in peak OC3 in the reverse sweep, the relative height of the shoulder OC2 on the negative side of peak OC3 increases as ν decreases. However, when ν is further reduced to $\leq 3 \text{ mV s}^{-1}$ at pH 0, OC3 disappears and a pair of anodic peaks are observed at $+1.20 \text{ V} > E > +0.90 \text{ V}$ (vs. SCE).

More profound changes are observed in the voltamassogram. Whilst *zone II* is relatively unaffected by sweep rate, *zone III* shows significant variation in form with ν especially at $\nu < 10 \text{ mV s}^{-1}$ where a two stage mass decrease becomes apparent, said mass decreases increasing in magnitude with decreasing ν . The magnitude of the more positive and substantial mass decrease is attenuated with increasing E in *zone IV*, and a small mass increase is recorded in *zone IV*, the magnitude decreasing with ν . At pH 1, the voltamassogram is unaffected by variation in ν in *zones V & VI* whilst a large mass increase is observed as the potential is driven to more negative values in *zone VII* the size of this change increasing with decreasing ν see **Figures 3.11-3.14**. Similar behaviour is exhibited at pH 0 at $\nu > 4 \text{ mV s}^{-1}$ see **Figure 3.15**. However, at $\nu \leq 3 \text{ mV s}^{-1}$, the voltamassogram exhibits a substantial mass loss in *zone IV*, coincident with the onset of the more positive of

the two anodic peaks seen in the reverse sweep of the CV. This decrease continues throughout zones V & VI until the onset of the mass increase in zone VII see *Figure 3.19*.

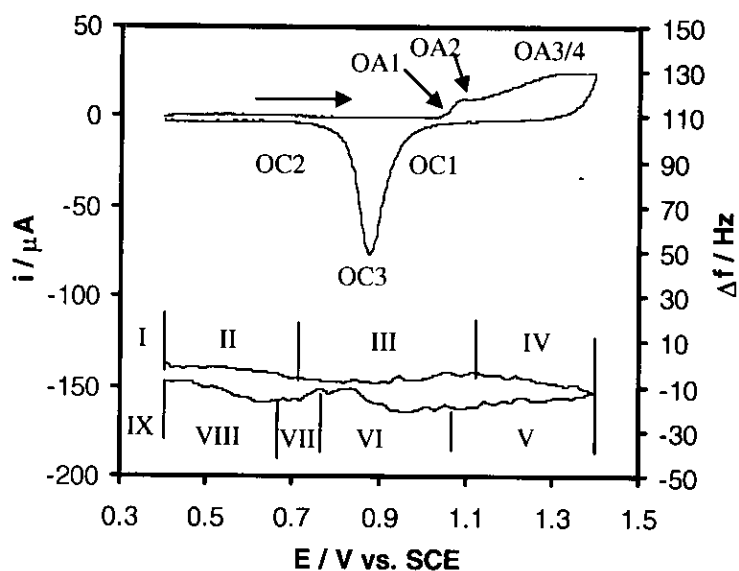


Figure 3.10: Cyclic voltammogram of 100 mol m^{-3} nitric (pH1) acid using a 14 mm Au(Ti) EQCM crystal at $v = 50 \text{ mV/s}$.

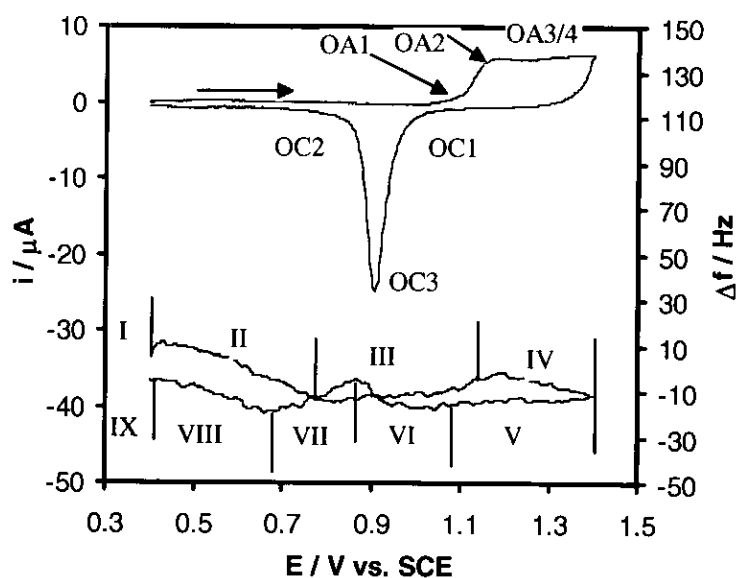


Figure 3.11: Cyclic voltammogram of 100 mol m^{-3} nitric (pH1) acid using a 14 mm Au(Ti) EQCM crystal at $v = 10 \text{ mV/s}$.

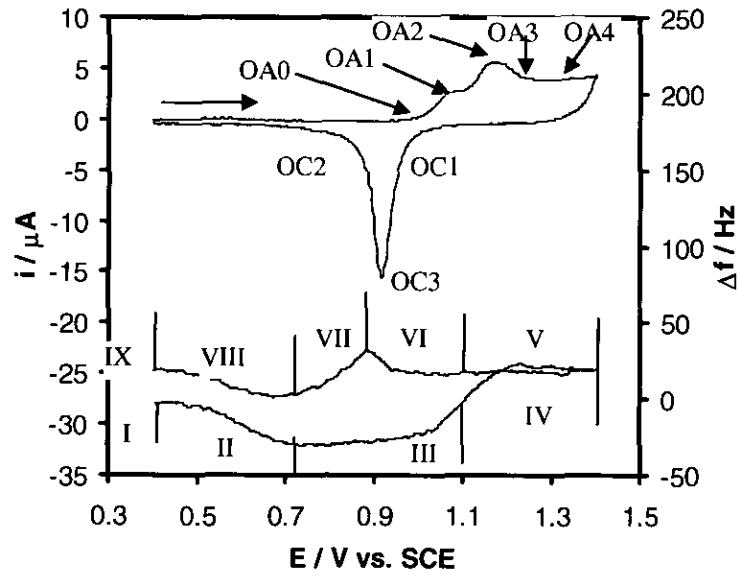


Figure 3.12: Cyclic voltammogram of 100 mol m^{-3} nitric (pH1) acid using a 14 mm Au(Ti) EQCM crystal at $v6 \text{ mV/s}$.

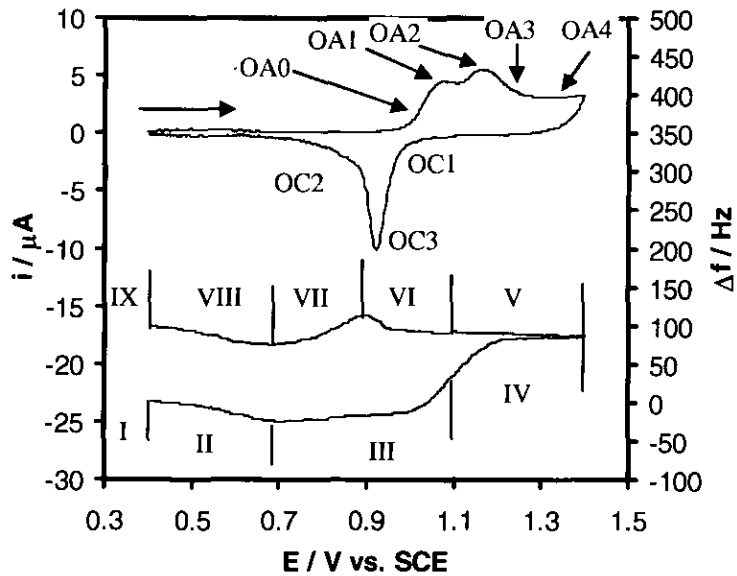


Figure 3.13: Cyclic voltammogram of 100 mol m^{-3} nitric (pH1) acid using a 14 mm Au(Ti) EQCM crystal at $v4 \text{ mV/s}$.

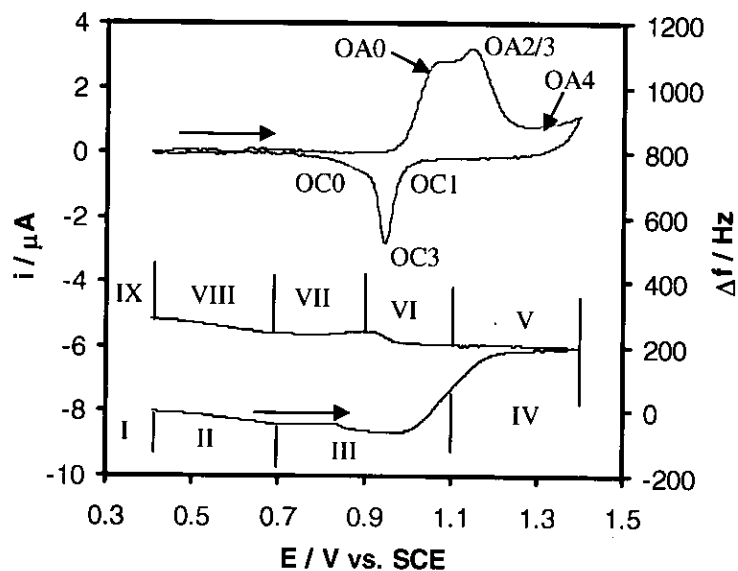


Figure 3.14: Cyclic voltammogram of 100 mol m^{-3} nitric (pH1) acid using a 14 mm Au(Ti) EQCM crystal at $v 1 \text{ mV/s}$.

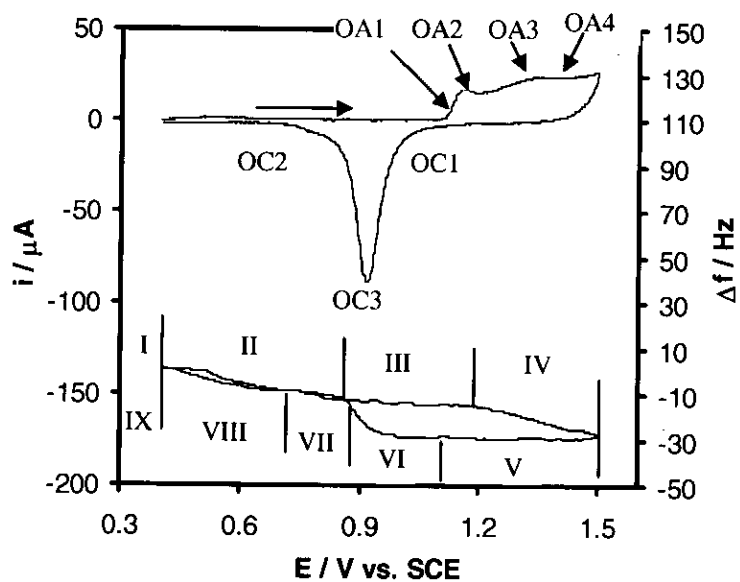


Figure 3.15: Cyclic voltammogram of 1000 mol m^{-3} nitric (pH0) acid using a 14 mm Au(Ti) EQCM crystal at $v 50 \text{ mV/s}$.

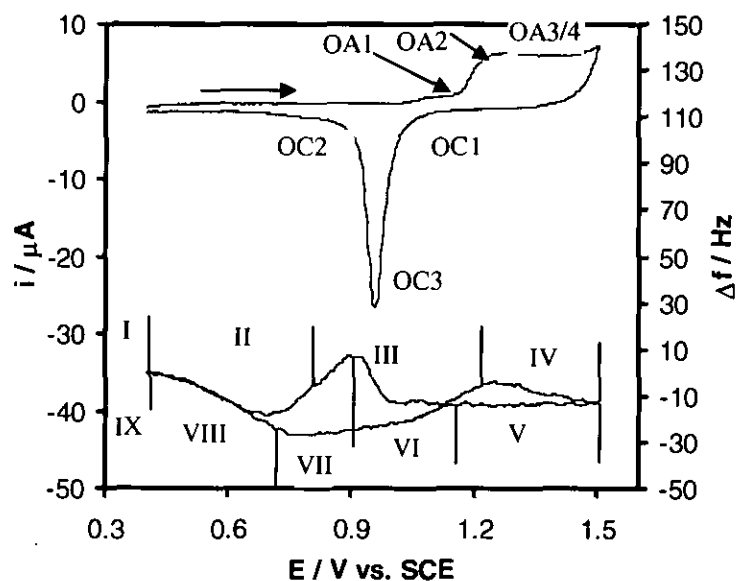


Figure 3.16: Cyclic voltammogram of 1000 mol m^{-3} nitric (pH0) acid using a 14 mm Au(Ti) EQCM crystal at $v 10 \text{ mV/s}$.

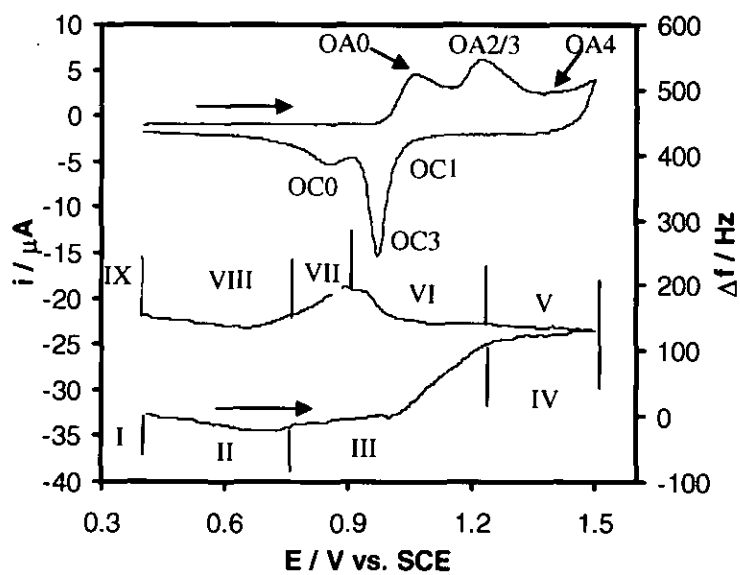


Figure 3.17: Cyclic voltammogram of 1000 mol m^{-3} nitric (pH0) acid using a 14 mm Au(Ti) EQCM crystal at $v 6 \text{ mV/s}$.

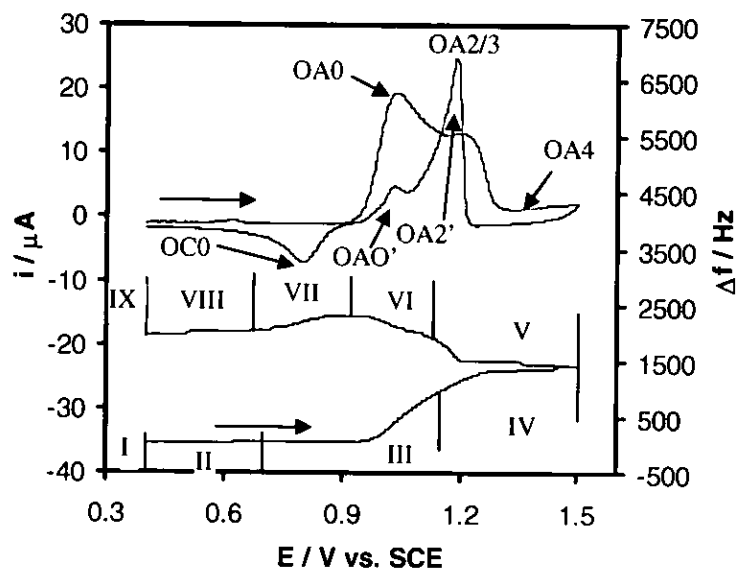


Figure 3.18: Cyclic voltammogram of 1000 mol m^{-3} nitric (pH0) acid using a 14 mm Au(Ti) EQCM crystal at $v 2 \text{ mV/s}$.

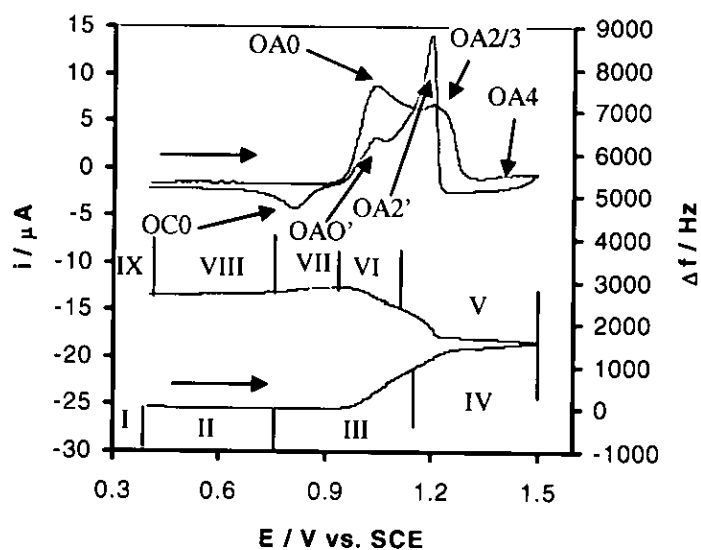


Figure 3.19: Cyclic voltammogram of 1000 mol m^{-3} nitric (pH0) acid using a 14 mm Au(Ti) EQCM crystal at $v 1 \text{ mV/s}$.

By comparing with the ClO_4^- , SO_4^{2-} and NO_3^- systems at $v > 50 \text{ mV s}^{-1}$, it is possible to identify the processes occurring in zones I to IX under slow sweep ($v \leq 4 \text{ mV s}^{-1}$) conditions. This identification will be facilitated by comparison between results obtained from the ClO_4^- , **Figure 3.20.b** SO_4^{2-} **Figure 3.20.a** and NO_3^- systems **Figure 3.14** at $v < 4 \text{ mV s}^{-1}$ at pH1. **Figure 3.21** shows the mass change as a function of charge passed for **Figure 3.14**. The mpe for any of the potential regions can be calculated from the slope of the curve. For the most part, results at pH 0 are similar and thus analogous conclusions can be made to those at pH 1. Where differences occur, we shall address those directly.

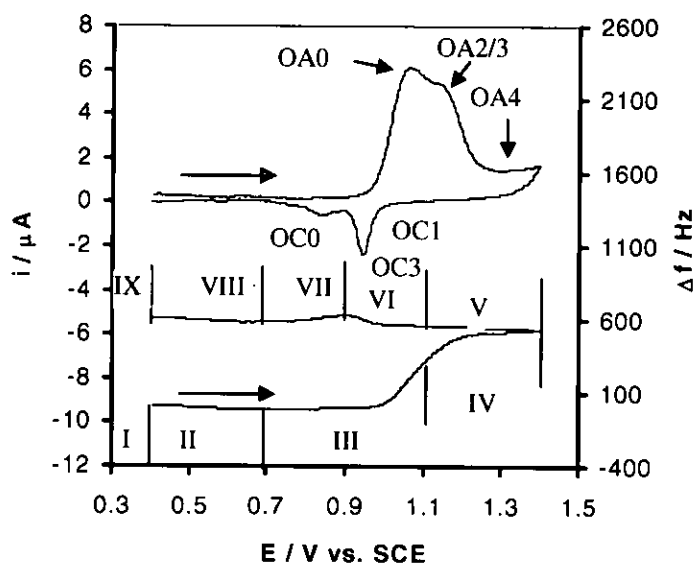


Figure 3.20.a: Cyclic voltammogram of 100 mol m^{-3} sulphuric (pH1) acid using a 14 mm Au(Ti) EQCM crystal at $v 1 \text{ mV/s}$.

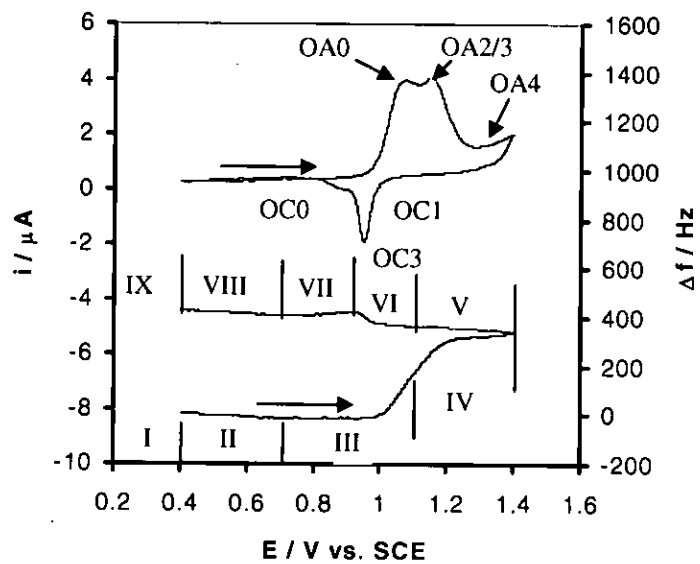


Figure 3.20.b: Cyclic voltammogram of 100 mol m^{-3} perchloric (pH1) acid using a 14 mm Au(Ti) EQCM crystal at $v 1 \text{ mV/s}$.

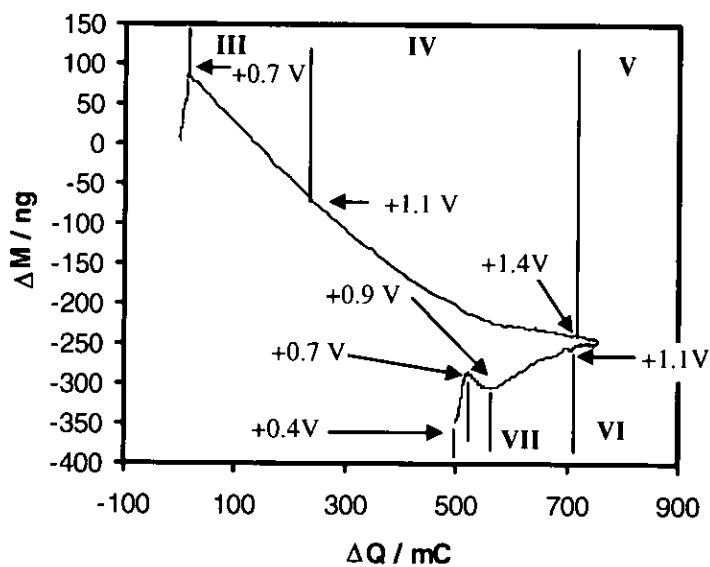


Figure 3.21: Mass change as a function of charge passed for Figure 3.14.

ZONE I – The non-faradaic region, as in *Figure 3.8 & 3.9*.

ZONE II – As in *Figure 3.8*, little charge is passed but a significant mass increase is observed which we have attributed to the absorption of anions and water molecules at submonolayer AuOH groups. That the size of this change increases with decreasing v is indicative of the greater time afforded for these processes to occur at slower v .

ZONE III – A two stage mass decrease is seen in this zone. The first decrease, which occurs at $E < +1.00$ V (vs. SCE) and is most readily seen at $v \geq 4$ mV s⁻¹ *Figures 3.12 & 3.13*, is accompanied by little or no passage of charge and is therefore most likely derived from the dehydration of adsorbed anions (*Reaction 3.4*) [3.31]. The second, larger change occurs at $E > +1.00$ V (vs. SCE) and is accompanied by significant passage of charge. The mpe value for this mass change is -64.5 g / mol-e *Figure 3.21*, a value consistent with the electrodisolution of Au via:



a conclusion supported by the finding that the peak potential of the associated current peak is invariant with pH e.g. $E_p(\text{OA0}) = +1.06$ & $+1.07$ V (vs. SCE) at $v = 1$ mV s⁻¹ at pH 0 & 1 respectively *Figures 3.14 & 3.19*. The metal stripping of *Reaction 3.15* / peak OA0 at $v < 10$ mV s⁻¹ is in contrast to the discharge of waters of hydration of adsorbed anions, *Reaction 3.5* / peak OA1, observed at similar potentials at $v > 50$ mV s⁻¹. This contrast is consistent with *Reaction 3.15* being thermodynamically more favourable than *Reaction 3.5*, *Reaction 3.5* being kinetically more facile than *Reaction 3.15* at high v , and can be explained as follows.

Angerstein-Kozłowska *et al* have noted that close-packed, specifically adsorbed anions hinder the oxidation of Au by blocking the access of free water to the electrode surface [3.31]. In the case of the tetrahedrally symmetric ClO_4^- and SO_4^- ions, close packing is most readily achieved on the Au(111) plane, while the symmetry and dimensions of NO_3^- are compatible with all three low index planes of Au. This, in conjunction with the occurrence at high v of peak OA1 *Figures 3.10 & 3.15*, a feature facilitated by the anion adsorption, suggests that our electrodes initially present a crystal plane or planes to solution on which relatively high levels of NO_3^- packing are possible. In accordance with this, a high level of NO_3^- adsorption at the electrode would hinder access of water from the free water network to the electrode surface and so inhibit the kinetics of the hydration and dissolution of Au^{3+} ions formed via *Reaction 3.15*. However, the waters in the anion hydration sphere provide a kinetically favourable route by which OH upd can occur via *Reaction 3.57*. Thus, at fast sweep rates, $v > 50 \text{ mV s}^{-1}$, *Reaction 3.5* occurs in preference to the *Reaction 3.15*. Once *Reaction 3.5* commences, the onset of *Reaction 3.6* with concomitant place exchange rapidly follows further blocking the electrode surface, so preventing Au dissolution from occurring at higher applied potentials.

The slower the sweep rate, the greater the extent of the kinetically hindered Au^{3+} dissolution that can occur before the onset of the more kinetically viable but thermodynamically less likely OH upd process of *Reaction 3.5*. This proceeds until, at $v < 10 \text{ mV s}^{-1}$, *Reaction 3.15* becomes the dominant process, said dissolution disrupting the anion packing to such an extent that *Reaction 3.5* / peak OA1 can no longer obtain. In accordance with *Reaction 3.6*, OH sublattice formation then only commences once anion desorption occurs, the accompanying place-exchange reaction leading ultimately to electrode passivation. Chemisorption of anions stabilises the Au surface by preventing the

turn-over of the MOH dipoles [3.31]. Thus, it appears that a critical surface concentration of anions must be retained during dissolution – once the concentration drops below this critical level, place exchange and, consequently, passivation begin.

ZONE IV – The rate of mass decrease with increasing potential starts to decline *Figures 3.14 & 3.19*, as does the mpe value *Figure 3.21*. This decline is coincident with the occurrence in the CV of a current peak in the vicinity of peak OA2 and can be attributed to inhibition of Au dissolution caused by blocking of the electrode surface by *Reactions 3.6 and 3.7*. The current in this zone is invariant with E whilst the decrease in mass has been very nearly arrested. Interestingly, at $v > 6 \text{ mV s}^{-1}$, a small mass increase can be seen see e.g. *Figures 3.11 & 3.12*, while at $v < 6 \text{ mV s}^{-1}$, a small mass decrease is observed *Figures 3.13 & 3.14*. As for *Figures 3.8 & 3.9*, the former effect can be attributed to the formation of a surface oxide. The latter seems to indicate that, despite the formation of the phase oxide, the electrode is not completely passivated, and that dissolution is still occurring, albeit at a much reduced rate.

ZONES V & VI– Whilst similar behaviour is seen at pH 1 & 0 at $v > 4 \text{ mV s}^{-1}$, differences occur at $v < 4 \text{ mV s}^{-1}$. Therefore, each pH will be dealt with separately.

Behaviour at pH 1 at $v > 4 \text{ mV s}^{-1}$ Figures 3.10-3.17

As in *Figure 3.8*, little current above that expected for double charging is seen in *zone V* at pH 1. However, compared with *Figure 3.8*, a gradual mass loss is observed at $v < 6 \text{ mV s}^{-1}$ *Figures 3.13, 3.14 & 3.17*, suggesting that Au^{3+} ions are still disengaging from the electrode surface. The total mass change in this zone at $v = 1 \text{ mV s}^{-1}$ *Figure 3.14*

corresponds to the loss of 1.2×10^{14} atoms of gold cm^{-2} , compared to a surface density of $\sim 1.2 \times 10^{15}$ atoms of gold cm^{-2} for polycrystalline Au. One possible explanation for this mass loss is provided by assuming that the slower the scan, the greater the opportunity for formation of 3-D-phase oxide. Such an oxide would be less well characterised than that formed at $v > 50 \text{ mV s}^{-1}$ **Figure 3.8**, primarily due to its generation occurring simultaneously with gold dissolution in *zone V*, so preventing the calculation of reliable mpe values in that zone. If such an oxide were to be formed at $v < 6 \text{ mV s}^{-1}$, then it is not unreasonable to postulate the possibility of Au^{3+} ions, generated via *Reaction 3.14a&b*, being trapped in the oxide matrix and gradually diffusing to solution. This theory is supported by a rotating ring-disc electrode study conducted by Cadle & Bruckenstein [3.8], who have detected Au^{3+} ions on the ring disc electrode during cathodic dissolution of gold oxide on the disc.

Moving to *zone VI*, it can be seen that the cathodic peak OC3, attributed to the reduction of turned over metal oxide / hydroxide species [3.30], is accompanied by a mass loss at $+1.00 \text{ V} < E > +0.90 \text{ V}$ (vs. SCE) **Figures 3.13, 3.14 & 3.17**. At pH 1, the mpe is found to be -18 , -33.3 and -40 g / mol-e at 6, 4 and 1 mV s^{-1} respectively, the latter being substantially larger than the theoretical values of -17 and -8 g / mol-e obtained for *Reactions 3.14a* and *3.14b*. Ye *et al* have reported a similar phenomenon in Cl^- media at scan rates of 50 mV s^{-1} [3.53]. As suggested in the discussion for *zone VI*, at $v < 6 \text{ mV s}^{-1}$, the multilayer oxide formed at the electrode surface may contain entrapped Au^{3+} ions. Stripping of the oxide would release those ions to solution, so leading to a net mass decrease over and above that which would be expected for the removal of the oxide layer alone.

Behaviour at pH 0 at $v < 4 \text{ mV s}^{-1}$ Figures 3.18 & 3.19

Little current or mass change is observed during the reverse sweep in *zone V* until $E \cong +1.20 \text{ V}$ (*vs.* SCE) where a substantial anodic current begins to flow, forming a pair of anodic peaks at $+1.20 \text{ V} > E > +0.90 \text{ V}$ (*vs.* SCE) *Figures 3.18 & 3.19*. A large surface mass decrease is observed from $+1.20 \text{ V}$ (*vs.* SCE), corresponding well to the anodic current flow. Since the potential for the onset of mass loss is more positive than that for oxide dissolution at $v > 4 \text{ mV s}^{-1}$ see e.g. *Figures 3.16 & 3.17*, the oxide seems to be unstable and can be partly destroyed at $[\text{HNO}_3] = 1000 \text{ mol m}^{-3}$, especially under conditions of low v . These two anodic peaks, designated OA0' and OA2', can be regarded as the net current observed from two opposing parallel processes, one cathodic and one anodic, occurring in *zone V*. The former process can be attributed to the reduction of turned over metal oxide/hydroxide species, preceded by reduction of non-place exchanged AuOH groups in accordance with *Reaction 3.13*. Indeed, comparison of *Figures 3.18* with *3.17* indicates that the onset of the anodic peak during the reverse sweep at $v = 2 \text{ mV s}^{-1}$ is coincident with the onset of the current associated with *Reaction 3.13* at $v = 6 \text{ mV s}^{-1}$. It therefore appears that *Reaction 3.13* triggers the depassivation process. The positions of peaks OA0' & OA2' indicate that the latter of the two opposing parallel processes occurring in *zone V* can be attributed to the electrodisolution of Au in accordance with *Reaction 3.15*. Confirmation of this assignment by calculation of reliable mpe values for the two peaks is difficult given the suppression of the net current in the region by the cathodic current associated with the oxide stripping reaction. However, the current onset on the positive side of peak OA2' overlays the leading edge of the cathodic current due to *Reaction 3.13*.

The current observed in **Figure 3.17**, due to **Reaction 3.13**, in region OA2' is small – less than 0.5 μA – while the net current associated with peak OA2' in **Figure 3.18** quickly rises to almost 30 μA . This indicates that the mpe calculation for the rising part of the positive side of peak OA2' would be subject, at worst, to a ~2% error. Calculation gives an mpe value of -70 g / mol-e , consistent with the theoretical value of -66 g / mol-e for the electrodisolution of Au via **Reaction 3.14**.

ZONE VII – A substantial mass increase is observed with an associated cathodic current feature in the CV (**Figures 3.14 & 3.17-3.19**). This current feature, designated OC0, manifests itself as a shoulder peak on the negative side of OC3 at pH 1 and as a separate peak at pH 0, the peak potential of OC0 being invariant with potential e.g. $E_p(\text{OC0}) = +0.825 \text{ V (vs. SCE)}$ and $+0.834 \text{ V (vs. SCE)}$ at 4 mV s^{-1} at pH 0 & 1 respectively. The experimental mpe value in this zone is found to be -68.7 and -63.8 g / mol-e at $v = 1 \text{ mV s}^{-1}$ at pH 0 & 1 respectively, values consistent with the redeposition of solution phase Au^{3+} ions generated via **Reaction 3.15** in preceding zones. That the redeposition process of OC0 is the reverse counterpart of **Reaction 3.15** / peak OA0 is further supported by the data of **Figure 3.22**, wherein the positive switching potential is restricted to $+1.10 \text{ V (vs. SCE)}$ at pH 0. Switching at $+1.10 \text{ V (vs. SCE)}$ restricts the available processes in the positive going sweep to that described by **Reaction 3.15** / OA0 i.e. no OH sublattice formation or RTO processes can occur. Under these circumstances, a single peak is observed in the return sweep with a peak potential consistent with it being peak OC0 e.g. $E_p(\text{OC0}) = +0.873 \text{ V (vs. SCE)}$ and $+0.856 \text{ V (vs. SCE)}$ at 6 mV s^{-1} , pH 0 at switching potentials of $+1.10 \text{ V (vs. SCE)}$ and $+1.50 \text{ V (vs. SCE)}$ respectively.

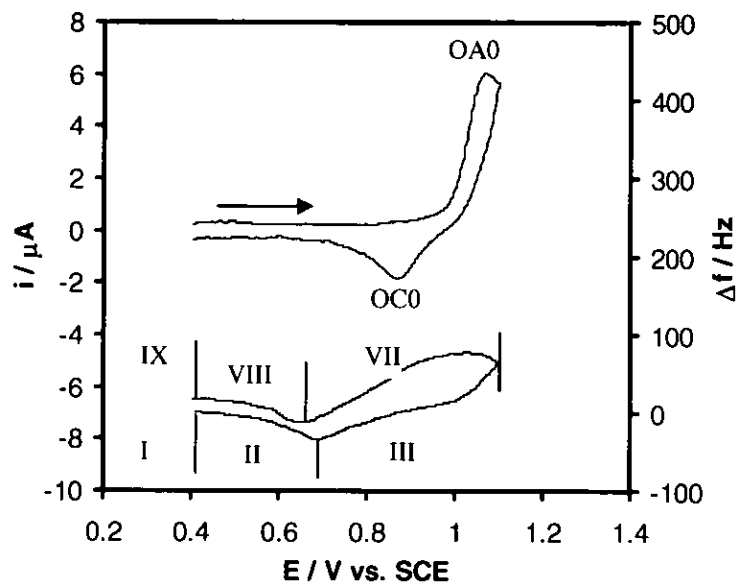


Figure 3.22: Cyclic voltammogram of 1000 mol m^{-3} nitric (pH0) acid using a 14 mm Au(Ti) EOCM crystal at $v6 \text{ mV/s}$. With a switching potential of 1.10 V (vs. SCE) .

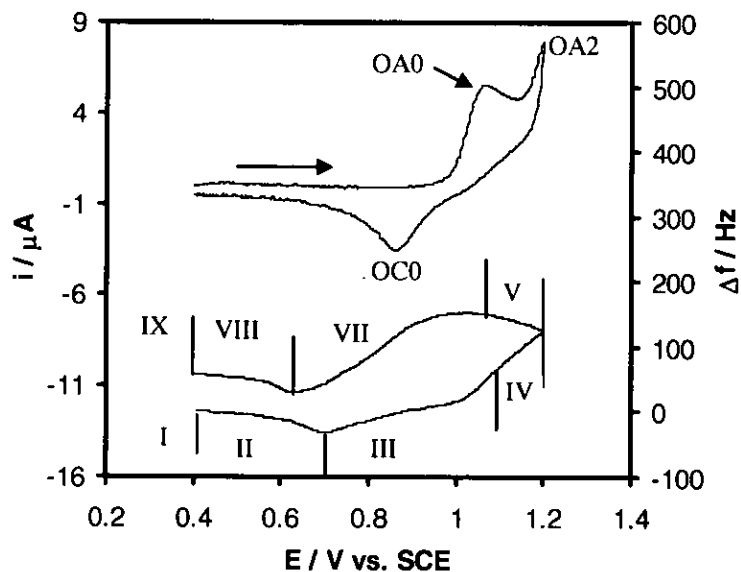


Figure 3.23: Cyclic voltammogram of 1000 mol m^{-3} nitric (pH0) acid using a 14 mm Au(Ti) EOCM crystal at $v6 \text{ mV/s}$. With a switching potential of 1.20 V (vs. SCE) .

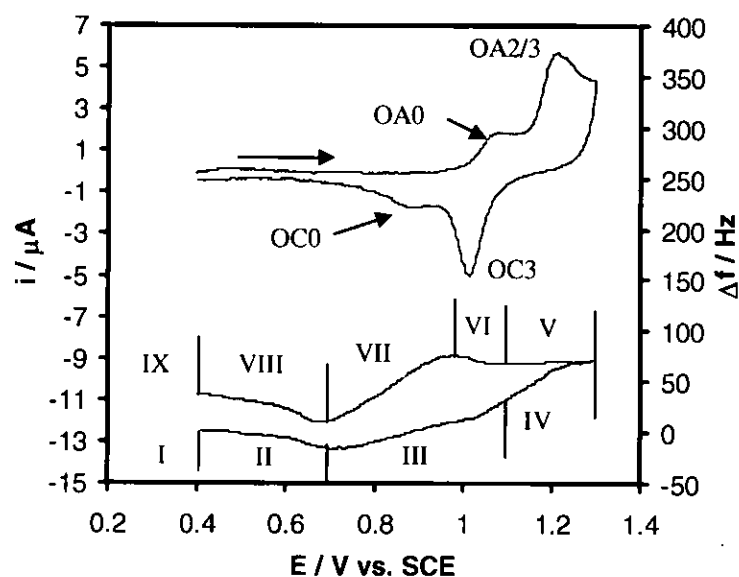


Figure 3.24: Cyclic voltammogram of 1000 mol m^{-3} nitric (pH0) acid using a 14 mm Au(Ti) EQCM crystal at $v6 \text{ mV/s}$. With a switching potential of 1.30 V (vs. SCE)

Figures 3.23 & 3.24 show the effect of increasing the switching potential from +1.10 to +1.20 and +1.30 V (vs. SCE) respectively. Whilst the onset of peak OA2 is observed at a switching potential of +1.20 V (vs. SCE), little or no current associated with peak OC3 is observed in the reverse sweep, indicating that little or no RTO has occurred during the forward going sweep. Peak OC3 can be observed in the reverse sweep when the switching potential is increased beyond $E_p(\text{OA2})$ to +1.30 V (vs. SCE) **Figure 3.24**, the size of OC3 increasing with the switching potential. Interestingly, $E_p(\text{OC0})$ moves in a negative direction as the switching potential and size of OC3 increase, indicating that oxide/hydroxide reduction processes make some contribution to the overall current in peak OC0. Angerstein-Kozłowska *et al* suggest that the current in the region of peak OC0, which they designate OC2, is due to OH sublattice reduction. Whilst there appears to be no reason to discount such a process making a contribution to the current of OC0/OC2 when the

switching potential is beyond E_p (OA2), our findings seem to indicate that, at $v < 10 \text{ mV s}^{-1}$, the majority process in this region is the redeposition of Au from Au^{3+} ions.

ZONE VIII & IX – Results are analogous to those obtained at $v > 50 \text{ mV s}^{-1}$.

That Au dissolution does occur in proceeding zones is supported by the observation that, at $v \leq 10 \text{ mV s}^{-1}$, the mass does not return to the original value at +0.40 V (vs. SCE). At pH 1, net losses of 15, 27, 121 & 354 ng are seen at $v = 10, 6, 4 \text{ \& } 1 \text{ mV s}^{-1}$ in *Figures 3.11-3.14* respectively. Assuming a polycrystalline surface, these correspond to dissolution of 0.13, 0.23, 1.04 and 3.04 monolayers of Au respectively, the loss increasing due to the longer time available for dissolution at smaller v ; the mass loss is linearly proportional to v^{-1} .

Other reports [3.60] have suggested that the mass loss is due to decreasing electrode roughness during cycling, so reducing the number and size of liquid pockets at the Au surface. However, this is not the source of the net losses observed in *Figures 3.13 & 3.14* for several reasons: (i) Other authors have reported the formation of Au^{3+} in solution during cycling experiments over similar potential ranges [3.8, 3.54, 3.70 & 3.72]; (ii) Cycling of a 0.5 mm diameter Au wire at 1 mV s^{-1} between -0.30 V (vs. SCE) & $+1.65 \text{ V}$ (vs. SCE) for 150 minutes at pH 1 results in a mass loss from the wire of 6.2 mg and the precipitation of a purple solid on the floor of the cell. Elemental analysis reveals this solid to be pure Au; (iii) Inspection of piezoelectrodes after repetitive cycling at 1 mV s^{-1} between $+0.40 \text{ V}$ & 1.50 V (vs. SCE) at pH 1 reveals a loss of Au coating from the crystal visible to the naked eye.

III.2.3 - Response of Au in HNO_3 as a Function of Increasing Sweep Rate

The structure of the Au/electrolyte interface depends upon the history, and type of electrochemical perturbation, applied to the electrode. This is supported by the observation made by several workers that freshly immersed electrodes must be subjected to several

rounds of cycling, usually at $\nu > 20 \text{ mV / s}$, before a reproducible CV is obtained [3.56, 3.57 & 3.75]. Thus, given the profound differences observed between data recorded at $\nu > & < 10 \text{ mV s}^{-1}$, we elected to study the behaviour of Au in HNO_3 as a function of increasing ν after electrode pre-treatment by 2-3 cycles at 1 mV s^{-1} .

Figure 3.25 to 3.29 shows the resultant data, recorded by increasing ν from $\nu = 1$ to 300 mV s^{-1} in HNO_3 at pH 1. As can be seen from Figures 3.25 & 3.26, results at $\nu \leq 6 \text{ mV s}^{-1}$ are similar to those recorded over the same ν when ν is decreased from 100 mV s^{-1} . However, unlike the results of Figures 3.8, 3.10 & 3.14 this behaviour is retained as ν is increased above 6 mV s^{-1} Figure 3.26, indicating that pre-treatment by cycling $\nu < 10 \text{ mV s}^{-1}$ results in a Au surface structure different to that obtained when the electrode is pre-treated by cycling at $\nu > 10 \text{ mV s}^{-1}$.

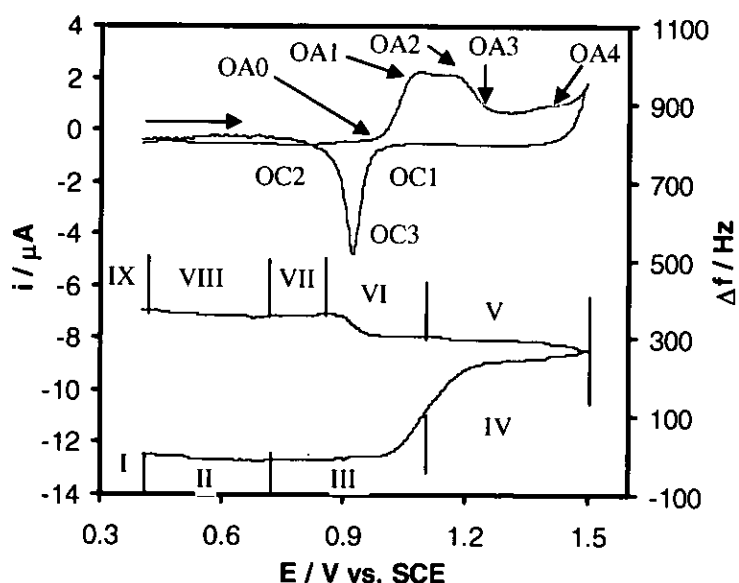


Figure 3.25: Cyclic voltammogram of 100 mol m^{-3} nitric (pH1) acid using a $14 \text{ mm Au(Ti) EQCM}$ crystal at $\nu 1 \text{ mV/s}$.

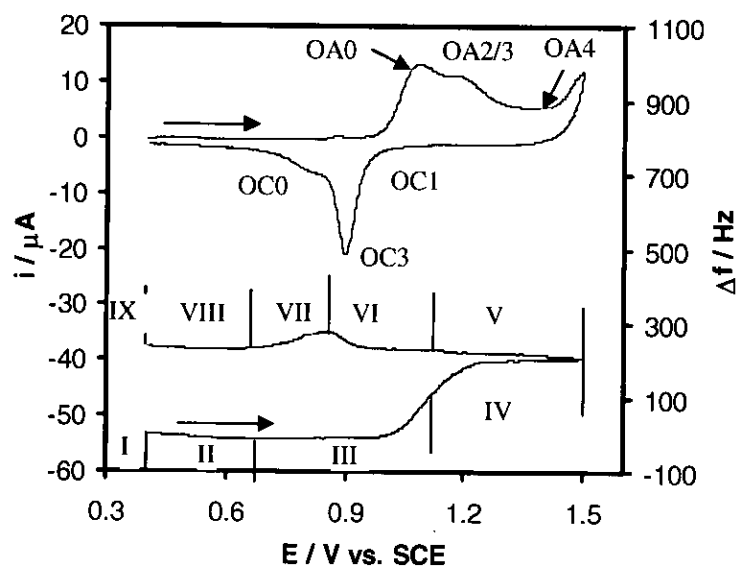


Figure 3.26: Cyclic voltammogram of 100 mol m^{-3} nitric (pH1) acid using a 14 mm Au(Ti) EQCM crystal at 6 mV/s .

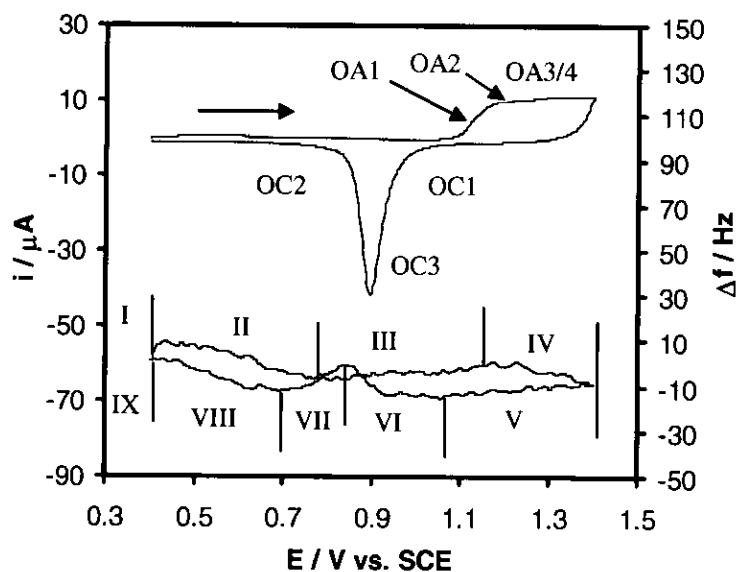


Figure 3.27: Cyclic voltammogram of 100 mol m^{-3} nitric (pH1) acid using a 14 mm Au(Ti) EQCM crystal at 20 mV/s .

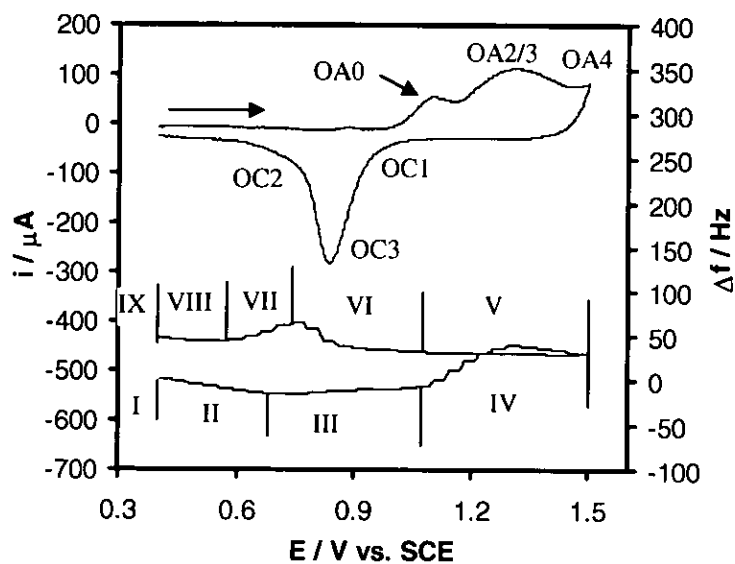


Figure 3.28: Cyclic voltammogram of 100 mol m^{-3} nitric (pH1) acid using a 14 mm Au(Ti) EQCM crystal at $v 100 \text{ mV/s}$.

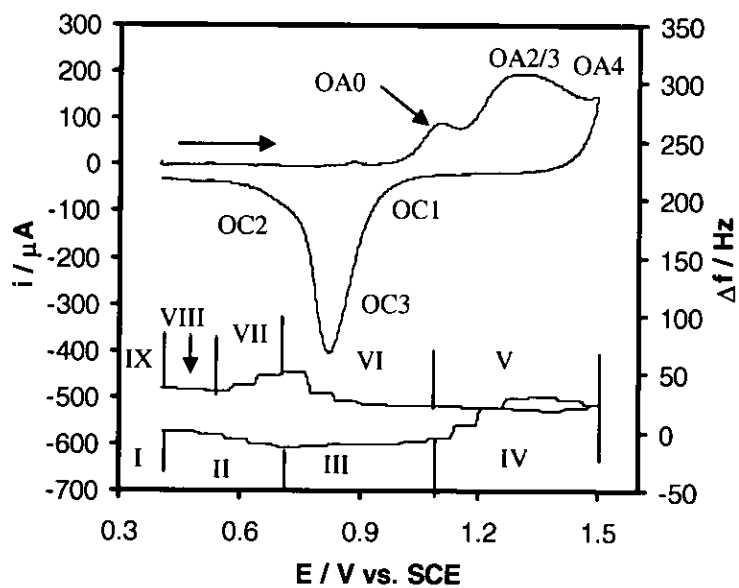


Figure 3.29: Cyclic voltammogram of 100 mol m^{-3} nitric (pH1) acid using a 14 mm Au(Ti) EQCM crystal at $v 300 \text{ mV/s}$.

One possible explanation for these results can be derived from a consideration of the mechanism of Au surface regeneration during the reverse sweep at high and low v . At high v , over the potential range employed in our experiments, little more than a monolayer of oxide is formed during the forward sweep (*vide supra*). Regeneration of the metal surface during the return sweep then involves reversal of the dipoles associated with OM and (OH)M groups followed by reductive dissolution of the resultant surface OH lattices. At no point in this process do the participating Au atoms disengage from the surface. Thus, it is reasonable to conclude that the crystal planes presented to solution by the electrode at the start of the cycle are regenerated during oxide monolayer removal. This is a conclusion supported by the CV and voltamassogram being reproducible over many cycles at $v > 20$ mV s^{-1} , the form of the CV in particular being critically dependent upon the crystal structure of the electrode surface [3.43 & 3.44]. On the other hand, dissolution of the Au surface occurs at low v , the resultant ions being redeposited during the return sweep, so generating a new electrode surface.

Bearing these differences in mind, the observations made from *Figures 3.8, Figures 3.10 & 3.14* and *Figures 3.25 to 3.29* are consistent with the following. Crystals that are pre-treated by potential cycling at $v > 10$ mV s^{-1} initially present a crystal plane or planes to solution on which relatively high levels of NO_3^- packing are possible. The anions hinder access of water from the free water network to the electrode surface, so inhibiting the kinetics of Au^{3+} dissolution in favour of OH sublattice and subsequent oxide monolayer formation (*vide supra*). The crystal structure of the electrode surface is retained during oxide monolayer generation and removal at fast v . However, as v is decreased, the thermodynamically favoured Au dissolution reaction becomes more dominant and Au^{3+} ions are released to

solution during the forward sweep. These ions are redeposited during the reverse sweep producing an electrode surface with a more open structure than that obtained at an electrode that has been subjected to potential cycling at fast sweep rates only, the associated crystal planes now being incapable of supporting the relatively high levels of anion adsorption achieved on the electrode of *Figures 3.8 & 3.10 & 3.11*. Water from the free water network can now gain access to the electrode, so facilitating the Au dissolution reaction. This more open structure is then retained by the dissolution / reprecipitation processes as v is increased. That the surface structure of the electrode has changed to a more open morphology is supported by a comparison of the surface roughness before and after slow potential cycling.

Using the method of Brummer & Makrides [3.81], the data of *Figure 3.8* provide an electrode roughness factor of ca. 1.1, whilst those of *Figure 3.28* provide a value of ca. 1.8 i.e. a 60% increase upon treatment by slow cycling. By use of in situ IR spectroscopy and STM, Bunge *et al* have observed the restructuring of the Au surface through dissolution / redeposition processes in the presence of complexants such as tetra-methylthiourea [3.82].

III.3 - CONCLUSIONS

The dissolution and redeposition processes of Au in HNO₃ solution at pH 1 & 0 were investigated as a function of sweep rate by in situ EQCM experiments. The results demonstrate that, at pH 1 and $v \leq 10 \text{ mV s}^{-1}$, Au dissolves through a $3e^-$ oxidation at $E > +1.00 \text{ V (vs. SCE)}$, a process that, at $v \leq 10 \text{ mV s}^{-1}$, is kinetically hindered with respect to upd of OH surface sublattices and subsequent 2-D-phase oxide formation. The inhibition arises from the presence of a closed packed layer of nitrate oxyanions at the gold surface, although the layer is disrupted and the inhibition removed by the gold dissolution and reprecipitation processes that occur during potential cycling at low v .

III.4 - REFERENCES

- 3.1 G.M. Schmid and M.E. Curley-Fiorino, in: A.J. Bard (Ed.), "Encyclopaedia of Electrochemistry of Elements", vol. 4, Marcel Dekker, Inc., New York, 1975
- 3.2 D.W. Kirk, F.R. Foulkes and W.F. Grayford. *J. Electrochem. Soc.* **127**, (1980), 1069
- 3.3 G.H. Kelsall, N.J. Welham and M.A. Diaz. *J. Electroanal. Chem.* **361**, (1993), 13
- 3.4 M. Pourbaix, in: "Atlas of Electrochemical Equilibria in Aqueous Solution", NACE, Houston, Texas, 1974
- 3.5 T. Heumann and H. S. Panesar. *Z. Phys. Chem.* **229**, (1965), 84
- 3.6 J. N. Gauer and G. M. Schmid. *J. Electroanal. Chem.* **48**, (1973), 325
- 3.7 J.N. Gauer and G.M. Schmid. *J. Electroanal. Chem.* **24**, (1970), 279
- 3.8 S.H. Cadle and S. Bruckenstein. *J. Electroanal. Chem.* **48**, (1973), 325
- 3.9 T. Horikoshi, S. Yoshimura, N. Kubota and E. Sato. *Nippon Kagakukaishi.* **1118**, (1983)
- 3.10 R.P. Frankenthal and D.E. Thompson. *J. Electrochem. Soc.* **123**, (1976), 799
- 3.11 R.P. Frankenthal and D.J. Siconolfi. *J. Electrochem. Soc.* **129**, (1982), 1192
- 3.12 B. Lovrecek, K. Moslavac and D.J. Matic. *Electrochimica. Acta.* **26**, (1981), 1087
- 3.13 M.A. Diaz, G.H. Kelsall and N.J. Welham. *J. Electroanal. Chem.* **361**, (1993), 25
- 3.14 B.H. Loo. *J. Phys. Chem.* **86**, (1982), 433
- 3.15 D.J. Trevor, C.E.D. Chidsey and D.N. Loiacono. *Phys. Rev. Lett.* **62**, (1989), 929
- 3.16 H. Honbo, S. Sugawara and K. Itaya. *Anal. Chem.* **62**, (1990), 2424
- 3.17 L.D. Burke, V.J. Cunnanae and B.H. Lee. *J. Electrochem. Soc.* **139**, (1992), 393
- 3.18 L.D. Burke and O. Leary. *J. Appl. Electrochem.* **19**, (1989), 758
- 3.19 L.D. Burke, D.T. Buckley and J.A. Morrissey. *Analyst.* **119**, (1994), 841
- 3.20 L.D. Burke and J.F. O'Sullivan. *J. Electroanal. Chem.* **285**, (1990), 195

-
- 3.21 L.D. Burke and J.F. O'Sullivan. *Electrochim. Acta.* **37**, (1992), 585
- 3.22 L.D. Burke and J.F. O'Sullivan. *Electrochim. Acta.* **37**, (1992), 2087
- 3.23 L.D. Burke and M. Mc Rann. *J. Electroanal. Chem.* **125**, (1981), 387
- 3.24 L.D. Burke. *Plat. Metal. Rev.* **38**, (1994), 166
- 3.25 D.A.J. Rand and R. Woods, *J. Electroanal. Chem.* **31**, (1971), 29
- 3.26 D.A.J. Rand and R. Woods. *J. Electroanal. Chem.* **35**, (1972), 209
- 3.27 C.M. Ferro, A.J. Calandra and A.J. Arvia. *J. Electroanal. Chem.* **59**, (1975), 239
- 3.28 C.M. Ferro, A.J. Calandra and A.J. Arvia. *J. Electroanal. Chem.* **65**, (1975), 963
- 3.29 H. Angerstein-Kozłowska, B.E. Conway, B. Barnett and J. Mozota. *J. Electroanal. Chem.* **100**, (1979), 417
- 3.30 H. Angerstein-Kozłowska, B.E. Conway, A. Hamelin and L. Stoicoviciu. *J. Electroanal. Chem.* **31**, (1986), 1051
- 3.31 H. Angerstein-Kozłowska, B.E. Conway, A. Hamelin and L. Stoicoviciu. *J. Electroanal. Chem.* **288**, (1987), 429
- 3.32 H. Angerstein-Kozłowska, B.E. Conway, K. Tellefsen and B. Barnett. *Electrochimica. Acta.* **34**, (1989), 1045
- 3.33 A. Hamlin, in: B.E. Conway, R.E. White and J.O'M. Bockris (Eds.), "*Modern Aspects of Electrochemistry*", vol. **16**, Plenum Press, New York, 1985
- 3.34 A. Hamelin and M.J. Weaver. *J. Electroanal. Chem.* **209**, (1986), 109
- 3.35 A. Hamelin and M.J. Weaver. *J. Electroanal. Chem.* **223**, (1987), 171
- 3.36 A. Hamelin. *J. Electroanal. Chem.* **210**, (1986), 303
- 3.37 A. Hamelin and L. Stoicoviciu. *J. Electroanal. Chem.* **229**, (1987), 107
- 3.38 A. Hamelin. *J. Electroanal. Chem.* **138**, (1987), 395
- 3.39 A. Hamelin. *J. Electroanal. Chem.* **101**, (1979), 285

-
- 3.40 G. Belanger and A.K. Vijh, in: A.K. Vijh (Ed.), "*Oxides and Oxide Films*", vol. 5, Marcel Dekker, New York, 1977, Ch.1
- 3.41 L.D. Burke and M.E.G. Lyons, in: R.E. White, J.O'M. Bockris and B.E. Conway, (Eds.), "*Modern Aspects of Electrochemistry*", vol. 18, Plenum Press, New York, 1986
- 3.42 E. Yeager, in: J.O'M. Bockris, B.E. Conway and S. Sarangapani, (Eds.), "*Comprehensive Treatise of Eelectrochemistry*", vol. 9, Plenum Press, New York, 1984
- 3.43 A. Hamelin. *J. Electroanal. Chem.* **407**, (1996), 1
- 3.44 A. Hamelin and A.M. Martins. *J. Electroanal. Chem.* **407**, (1996), 13
- 3.45 A. Hamlin, in: B.E. Conway, R.E. White and J.O'M. Bockris, (Eds.), "*Modern Aspects of Electrochemistry*", vol. 16, Plenum Press, New York, 1985. Ch. 1
- 3.46 B. Piela and P.K. Wrona. *J. Electroanal. Chem.* **388**, (1995), 69
- 3.47 R. Schumacher, J. Gordon and O.J. Melroy. *J. Electroanal. Chem.* **216**, (1987), 127
- 3.48 R. Schumacher, G. Borges and K.K. Kanazawa. *Surf. Sci.* **163**, (1985), L621
- 3.49 A. Hamlin, in: A.A. Gewirth and H. Seigenthaler (Eds.), "*Nanoscale Probes of the Solid/Liquid Interface*", NATO ASI, Ser. C, Sophia Antipolis, France, Kluwer Academic, Dordrecht, Netherlands, 1995
- 3.50 N.S. Marinkovi, J.J. Calvente, A. Kloss, Z. Kováčová and W.R. Fawcett. *J. Electroanal. Chem.* **467**, (1999), 325
- 3.51 M.C.P.M. da Cunha, M. Weber and F.C. Nart. *J. Electroanal. Chem.* **414**, (1996), 163
- 3.52 A.C. Chialvo, W.E. Triaca and A.J. Arvía. *J. Electroanal. Chem.* **171**, (1984), 303
- 3.53 S. Bruckenstein and M. Shay. *J. Electroanal. Chem.* **188**, (1985), 131

-
- 3.54 X. Zeng and S. Bruckenstein. *J. Electroanal. Chem.* **461**, (1999), 131
- 3.55 J.S. Gordon and D.C. Johnson. *J. Electroanal. Chem.* **365**, (1994), 275
- 3.56 W. Stöckel and R. Schumacher. *Ber. Bunsenges. Phys. Chem.* **91**, (1987), 345
- 3.57 W. Stöckel and R. Schumacher. *Ber. Bunsenges. Phys. Chem.* **93**, (1989), 600
- 3.58 R. Schumacher, G. Borges and K.K. Kanazawa. *Surf. Sci.* **163**, (1985), L621
- 3.59 S.L. Chen, B.L. Wu and H. Zhang. *Wuhan Univ. J. Nat. Sci.* **3**, (1998), 102
- 3.60 S.L. Chen, B.L. Wu and C.S. Cha. *J. Electroanal. Chem.* **431**, (1997), 243
- 3.61 T. Dickinson, A.F. Povey and P.M.A. Sherwood. *J. Chem. Soc. Faraday Trans.* **71**, (1975), 298
- 3.62 S. Bruckenstein and M. Shay. *Electrochim. Acta.* **30**, (1985), 1295
- 3.63 D.A. Buttry and M.D. Ward. *Chem. Rev.* **92**, (1992), 1355
- 3.64 D.A. Buttry, in: A.J. Bard (Ed.), “*Electroanalytical Chemistry*”, vol. **17**, Marcel Decker, New York, 1990
- 3.65 R. Schumaker. *Angew. Chem. Intl. Ed. Eng.* **29**, (1990), 329
- 3.66 M.D. Ward and D.A. Buttry. *Science.* **249**, (1990), 190
- 3.67 Z.X. Shu and S. Bruckenstein. *J. Electroanal. Chem.* **317**, (1991), 263
- 3.68 C.P. Wilde and M. Zhang. *J. Chem. Soc. Faraday Trans.* **89**, (1993), 385
- 3.69 C.P. Wilde and M. Zhang. *J. Chem. Soc. Faraday Trans.* **90**, (1994), 1233
- 3.70 K. Juodkazis, J. Juodkazyté, B. Šebeka and A. Lukinskas. *Electrochem. Comm.* **1**, (1999), 315
- 3.71 T. Dickinson, A.F. Povey and P.M.A. Sherwood. *J. Chem. Soc. Faraday Trans.* **71**, (1975), 298
- 3.72 K. Juodkazis, J. Juodkazyté, T. Juodienė and A. Lukinskas. *J. Electroanal. Chem.* **441**, (1998), 19

-
- 3.73 U. Oesch and J. Janata. *Electrochim. Acta.* **28**, (1983), 1237
- 3.74 S.H. Cadle and S. Bruckenstein. *Anal. Chem.* **46**, (1974), 16
- 3.75 S. Bourkane, C. Gabrielli, F. Huet and M. Keddam. *Electrochimica. Acta.* **38**, (1993), 1023
- 3.76 S. Bourkane, C. Gabrielli and M. Keddam. *Electrochimica. Acta.* **38**, (1993), 1827
- 3.77 J. Clavilier and C. Nguyen van Huong. *J. Electroanal. Chem.* **80**, (1977), 101
- 3.78 N.N. Greenwood and A. Earnshaw, in: "*Chemistry of the Elements*", Butterworth Heinemann, Oxford 1997 2nd Edn.
- 3.79 L.D. Burke and B.H. Lee. *J. Electroanal. Chem.* **330**, (1992), 637
- 3.80 X. Gao and M.J. Weaver. *J. Electroanal. Chem.* **367**, (1994), 259
- 3.81 S.B. Brummer, A.C. Makrides. *J. Electrochem. Soc.* **111**, (1964), 1122
- 3.82 E. Bunge, S.N. Port, B. Roelfs, H. Meyer, H. Baumgärtel, D.J. Schiffrin and R.J. Nichols. *Langmuir.* **13**, (1997), 85

CHAPTER IV - ACETOHYDROXAMIC ACID OXIDATION PROCESSES

CONTENT

<u>IV.1 - INTRODUCTION</u>	<i>Page 154</i>
<u>IV.2 - AN ELECTROGRAVIMETRIC STUDY OF THE OXIDATION OF ACETOHYDROXAMIC ACID USING THE EOCM AT LOW SWEEP RATE</u>	<i>Page 155</i>
<u>IV.3 - DETERMINATION OF THE FORM OF THE ACETOHYDROXAMIC ACID ASSISTED GOLD DISSOLUTION AS A FUNCTION OF SWEEP RATE</u>	<i>Page 160</i>
<i>IV.3.1 - The Evolution of the Forms of the Cyclic Voltammograms and Voltamassograms of AHA in Nitric Acid as a Function of Decreasing Sweep Rate</i>	<i>Page 169</i>
<u>IV.4 - THE ELECTROCHEMISTRY OF ACETOHYDROXAMIC ACID STUDIED BY CYCLIC VOLTAMMETRY USING DISC MICROELECTRODES</u>	<i>Page 173</i>
<u>IV.5. - CONCLUSIONS</u>	<i>Page 185</i>
<u>IV.6 - REFERENCES</u>	<i>Page 186</i>

IV.1 - INTRODUCTION

Hydroxamic acid (HA) ligands are useful reagents for the chemical analysis of metal ions. Voltammetric studies of these ligands and their metal ion complexes have been undertaken and mechanisms for their oxidation proposed. A detailed investigation by Amberson *et al* proposed a 2 electron irreversible oxidation at glassy carbon electrodes resulting in the cleavage of the C-N bond [4.1 & 4.2]. The preparation of chemically modified electrodes containing HA ligands for the purposes of developing electrochemical sensors has been proposed by several authors [4.3, 4.4, 4.5, & 4.6]. The nature of HA as a strong chelator forming four of five membered chelates through the O-O or N-O type bond with ferrous, non-ferrous and rare earth metals and its important role in microbial iron metabolism make it an ideal ligand for the modification of electrode sensors.

Thus, in order to assess the thermodynamic and kinetic stability of HA ligands within an electrochemical sensing system, we elected to study the electrochemistry of a representative HA by use of (i) the simultaneous cyclic voltammetric and voltamassogram profiles afforded by the EQCM (ii) a polarography using a range of disc microelectrodes of various sizes. As will be described in **Chapter 5, Section V.2.1**, we studied three common hydroxamic acids in order to assess their potential for use as the ionophore within our proposed sensor - desferrioxamine hydroxamic acid (DFA⁺), glycine hydroxamic acid (GHA⁺) and acetohydroxamic acid (AHA). The former pair are more hydrophobic than AHA. Thus, as the potential for the oxidation of the HA group exhibits little dependence upon its substituents, and in order to simplify the interpretation of the electrogravimetric data in particular, we elected to commence the study of the electrochemistry of our candidate HAs with AHA.

IV.2 - AN ELECTROGRAVIMETRIC STUDY OF THE OXIDATION OF ACETOHYDROXAMIC ACID USING THE EQCM AT LOW SWEEP RATE

As discussed in **Chapter 3, Section III.2.2** the anodic dissolution of a gold electrode in acidic media forms a necessary backdrop to the investigation of AHA oxidation using the EQCM. As is the case with the gold-nitric acid system (**Chapter 3**) to our knowledge, there are no reports in the literature pertaining to the cyclic voltammetric and voltamassogram response for the oxidation of AHA gold electrodes. The majority of the literature in this area concerns various hydroxamic acid GC electrode systems [4.1 to 4.5]. Thus, it was against this background that we commence an exploration of the electrochemistry of Au in AHA/HNO₃ systems, nitric being the acid used in the overwhelming majority of nuclear reprocessing streams.

A typical voltammogram and voltamassogram, recorded in 2 mol m⁻³ AHA in nitric acid background electrolyte at pH 1 using the EQCM under polarographic conditions (*i.e.* slow sweep rates of <1 mV/s) are shown in **Figure 4.1**. Comparison with **Figure 3.14** in **Chapter 3** indicates that, whilst the voltammogram is significantly different to that recorded in the absence of AHA, the voltamassogram is very similar. The specific similarities to, and differences between the results obtained in the absence of AHA at pH 1 in the *Zones I to IX* (related to, but not identical to those identified in **Chapter 3**) of **Figure 4.1** are as follows.

ZONE I –

The behaviour in this zone is identical to that described in **Chapter 3, Section III.2.2** *i.e.* in *Zone 1* in the absence of AHA at pH 1.

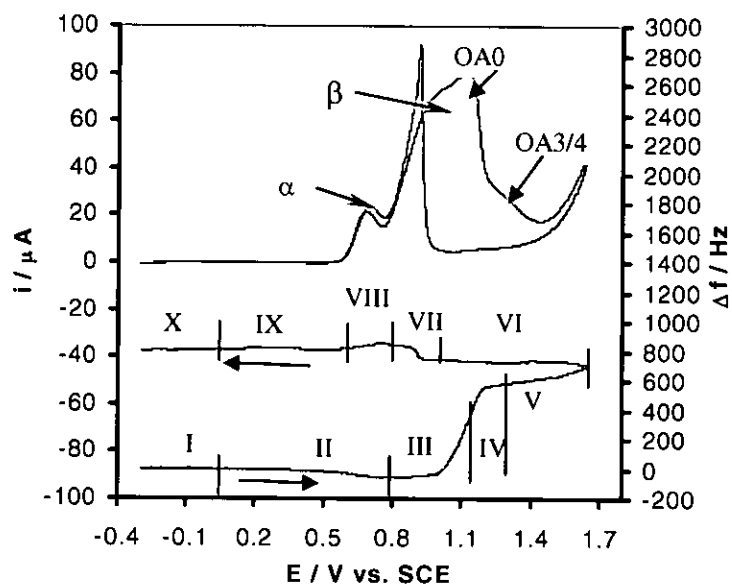


Figure 4.1: Cyclic voltammogram of 2 mol m^{-3} acetohydroxamic acid in 100 mol m^{-3} nitric (pH1) acid using a $14 \text{ mm Au(Cr) EOCCM}$ crystal at $v 1 \text{ mV/s}$.

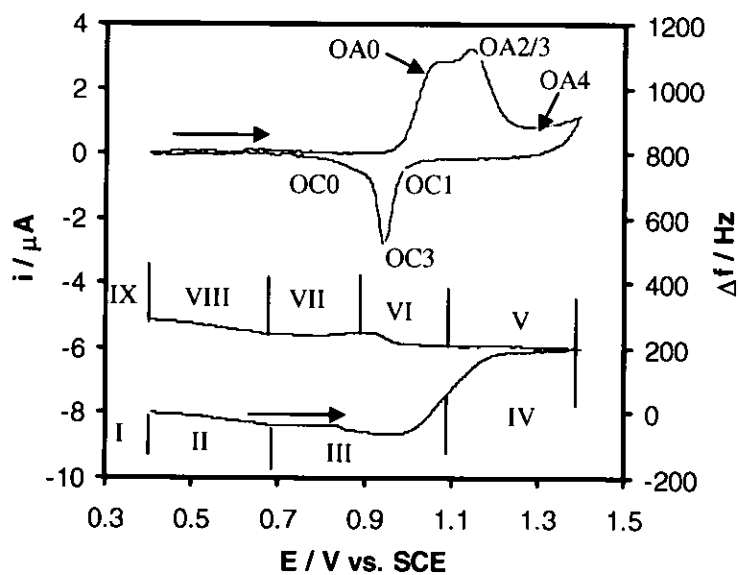


Figure 4.1.i: Cyclic voltammogram of 100 mol m^{-3} nitric (pH1) acid using a $14 \text{ mm Au(Ti) EOCCM}$ crystal at $v 1 \text{ mV/s}$. Being identical to **Figure 3.14** of **Chapter 3** and is used as comparison herein.

ZONE II –

Identical to that described in *Zone II* in the absence of AHA at pH 1, **Chapter 3, Section III.2.2**, even down to the total mass change observed as a result of the formation of the submonolayer hydroxide species. That the mass change of 59.1 ng in *Zone II* of **Figure 4.1** is approximate to that of 55.7 ng in *Zone II* of **Figure 4.1.i** is indicative of there being no specific interaction between AHA and the hydrophilic electrode surface generated as a result of submonolayer hydroxide formation. The implication of this observation is that the AHA oxidation reactions occurring in the potential range +0.60 to + 1.00 V (*vs.* SCE) (*vide infra*) are solution diffusion and not surface processes. This assertion is supported by the fact that there is no mass change associated with *peaks alpha & beta* in the voltamassogram of **Figure 4.1** over and above those observed in the corresponding voltamassogram recorded in nitric acid in the absence of AHA – **Figure 4.1.i**.

ZONES III & IV–

As in the case of *Zones III & IV* of **Figure 3.14** of **Chapter 3**, a two stage mass decrease is seen in this zone. The first decrease, which occurs at $E < +1.00$ V (*vs.* SCE) and corresponds with the onset of peak β in the voltammogram. This is most likely derived from the dehydration of adsorbed anions (**Reaction 3.6** of **Chapter 3, Section III.X**) [4.7]. The second, larger change occurs at $E > +1.00$ V (*vs.* SCE) and is accompanied by significant passage of charge which can be explained as follows. In both **Figures 4.1 & 4.1.i**, the second, more substantial mass loss in *Zone III* has an onset of +1.00 V (*vs.* SCE). This is coincident with the onset of peak OA0 in **Figure 4.1.i** which is associated with the Au/Au³⁺ oxidation process (**Reaction 3.17**) as discussed in **Section III.2.2** of **Chapter 3**. The onsets of both peaks α and β in **Figure 4.1** are substantially negative of +1.00 V (*vs.* SCE),

indicating that the associated AHA oxidation process occurs independently of the Au/Au³⁺ oxidation reaction. Thus, the substantial currents passed at $E > 1.00$ V (vs. SCE) in **Figure 4.1** is due to both AHA oxidation / peak β and Au/Au³⁺ oxidation / peak OA0 overlaying each other. Once gold oxide formation and passivation occurs at $\sim +1.20$ V (vs. SCE), both reactions are arrested.

Interestingly, the total mass loss observed in *Zones III & IV* of **Figure 4.1** is greater than that observed in the corresponding *Zones III & IV* of **Figure 4.1.i** (~ 750 ng in the former compared with ~ 360 ng in the latter), indicating the presence of a third process in this potential range – AHA assisted electro-dissolution of gold. This conclusion is further supported by the observation that the total mass change between the start and end of the voltamassogram is greater in the presence of AHA **Figure 4.1** than in its absence **Figure 4.1.i** – ~ 990 ng in the former compared with ~ 370 ng in the latter.

Furthermore, the mass loss calculated from the frequency change in *Zones III & IV* of the voltamassogram of **Figure 4.1** is found to be ~ 750 ng. This is much less than a mass change of $\sim 10,900$ ng that may be estimated from the charge passed under peaks β and OA0 in **Figure 4.1**, assuming that those waves are associated with a three electron transfer, gold electro-dissolution reaction. This disparity in calculated mass changes is again indicative of those peaks of **Figure 4.1** observed in addition to those of **Figure 4.1.i** – peaks α and β – being predominantly due to the electrochemistry of AHA. Although, it should be noted that the differences between **Figure 4.1 & 4.1.i** in the final mass change and the mass change recorded in *Zone III & IV* are strongly suggestive of the existence of a minority process involving AHA-assisted gold stripping. This putative AHA-assisted gold dissolution reaction will be discussed in more detail below.

ZONES V to X –

Zones V to X are identical in detail to those described as *zones IV to IX* in **Chapter 3, Section III.2.2** (please note the difference in labelling) and need no further explanation here.

In summary, the results obtained from *Figures 4.1 & 4.1.i* indicate that the existence of three processes in *Zones III & IV*:

- (i) conventional gold stripping in accordance with *Equation 3.17*;
- (ii) some oxidation reaction of AHA; and
- (iii) an AHA assisted gold dissolution reaction.

A number of points raised in this section will be addressed in the following section.

IV.3 - DETERMINATION OF THE FORM OF THE ACETOHYDROXAMIC ACID ASSISTED GOLD DISSOLUTION AS A FUNCTION OF SWEEP RATE

In order to interrogate the intrinsic electrochemistry of AHA and the AHA-assisted dissolution of Au, a set of cyclic voltammograms were recorded using gold piezoelectrodes in solutions of AHA in pH 1 nitric acid at sweep rates between 1 and 100 mV/s *Figures 4.2i-xi*. The following observations were made:

- (i) At any one sweep rate, the mass increase in *Zone II* is the same in both the absence (*Figure 3.8* of Chapter 3, Section III.2.1) and the presence *Figure 4.2.i* of AHA, indicating that, as in the low sweep rate experiments, no surface adsorption of AHA takes place at the gold electrode surface at high sweep rates.
- (ii) At high sweep rates, the oxidation of AHA and the electrogeneration of the gold oxide layer at the electrode surface occur independently of each other. This can be plainly seen in *Figure 4.2.i* where the AHA oxidation peaks, α and β , appear as a compound feature in the potential range +0.80 - +1.00 V (*vs.* SCE), whereas the gold oxidation peaks exhibit an onset of $\sim +1.05$ V (*vs.* SCE). Thus, the two processes are reasonably well separated in the voltammogram. The gold oxidation onset potential and the peak at $\sim +1.30$ V (*vs.* SCE) is consistent with these features being analogous to, respectively, peaks OA1 and OA3/4 recorded in pH 1 nitric acid in the absence of AHA (see e.g. *Figure 3.10* in Chapter 3).
- (iii) A mass gain is recorded in *Zones III and IV* in the absence and presence of AHA at high sweep rate *Figure 3.8* and *4.2.i* respectively, but a corresponding mass loss is observed in the presence of AHA at low sweep rate *Figure 4.2.xi* and this is due to a number of possible processes described as follows.

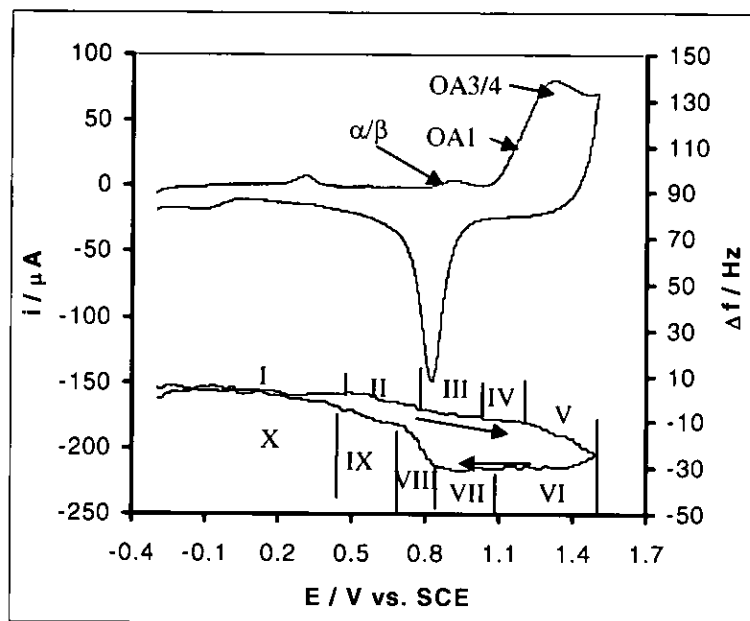


Figure 4.2.i: Cyclic voltammogram of 2 mol m^{-3} acetohydroxamic acid in 100 mol m^{-3} nitric (pH1) acid using a $14 \text{ mm Au(Ti) EQCM}$ crystal at $v 100 \text{ mV/s}$.

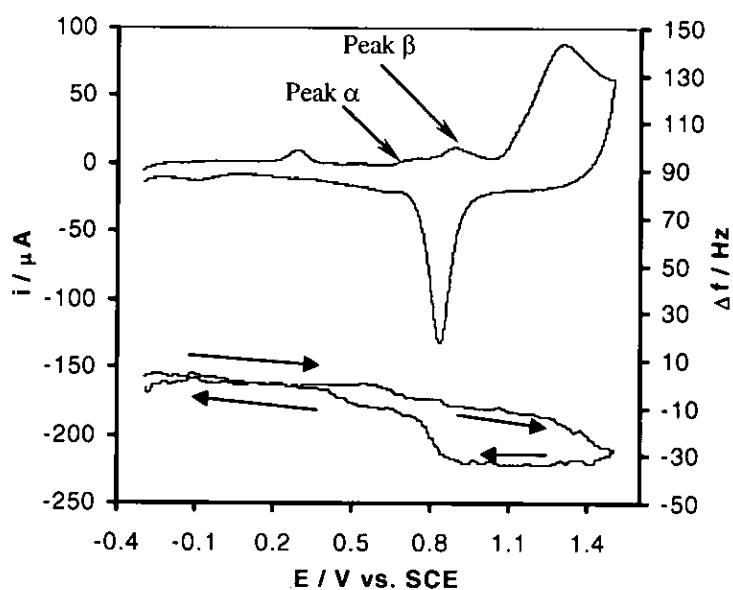


Figure 4.2.ii: Cyclic voltammogram of 2 mol m^{-3} acetohydroxamic acid in 100 mol m^{-3} nitric (pH1) acid using a $14 \text{ mm Au(Ti) EQCM}$ crystal at $v 80 \text{ mV/s}$. Zones are consistent with those shown in **Figure 4.2.i**.

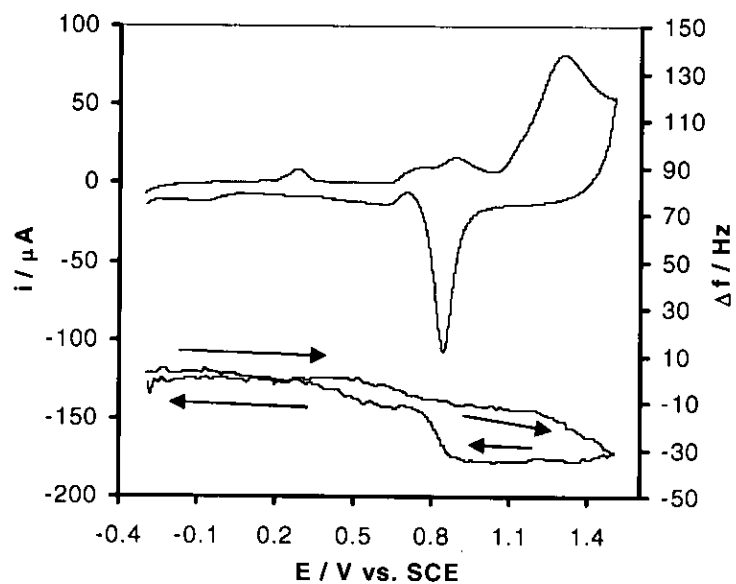


Figure 4.2.iii: Cyclic voltammogram of 2 mol m^{-3} acetohydroxamic acid in 100 mol m^{-3} nitric (pH1) acid using a 14 mm Au(Ti) EOCM crystal at $v60 \text{ mV/s}$. Zones are consistent with those shown in **Figure 4.2.i**.

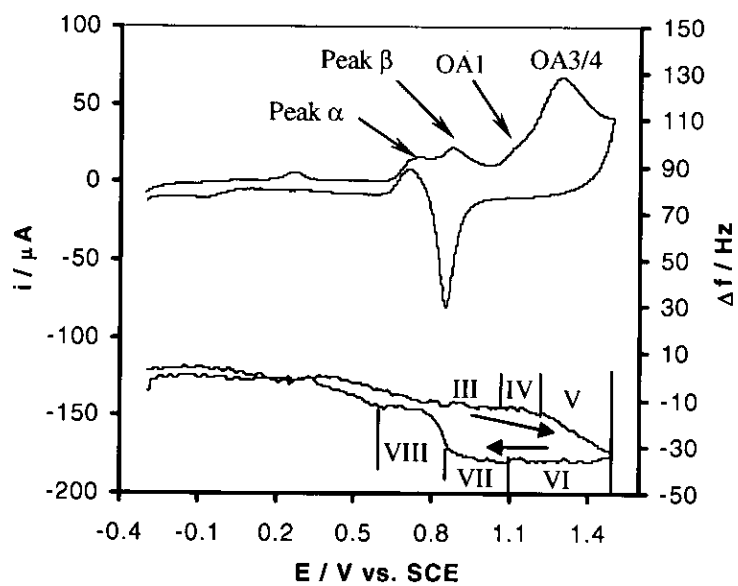


Figure 4.2.iv: Cyclic voltammogram of 2 mol m^{-3} acetohydroxamic acid in 100 mol m^{-3} nitric (pH1) acid using a 14 mm Au(Ti) EOCM crystal at $v40 \text{ mV/s}$.

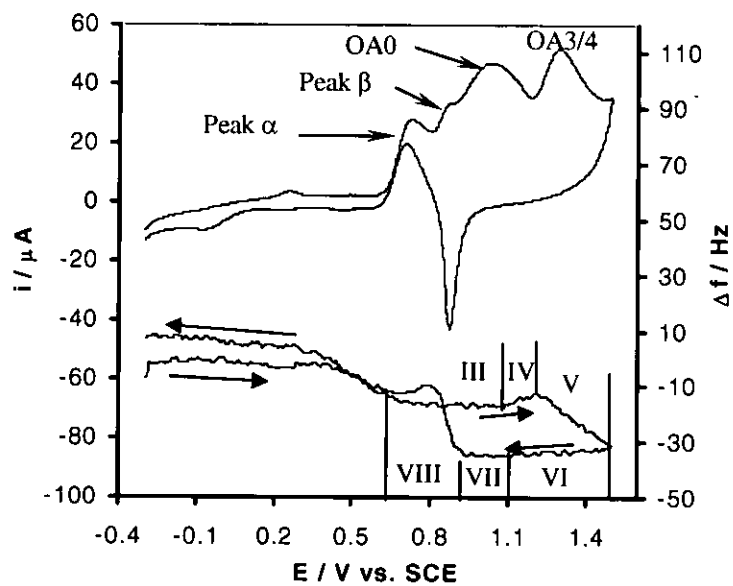


Figure 4.2.v: Cyclic voltammogram of 2 mol m^{-3} acetohydroxamic acid in 100 mol m^{-3} nitric (pH1) acid using a 14 mm Au(Ti) EQCM crystal at $v 20 \text{ mV/s}$.

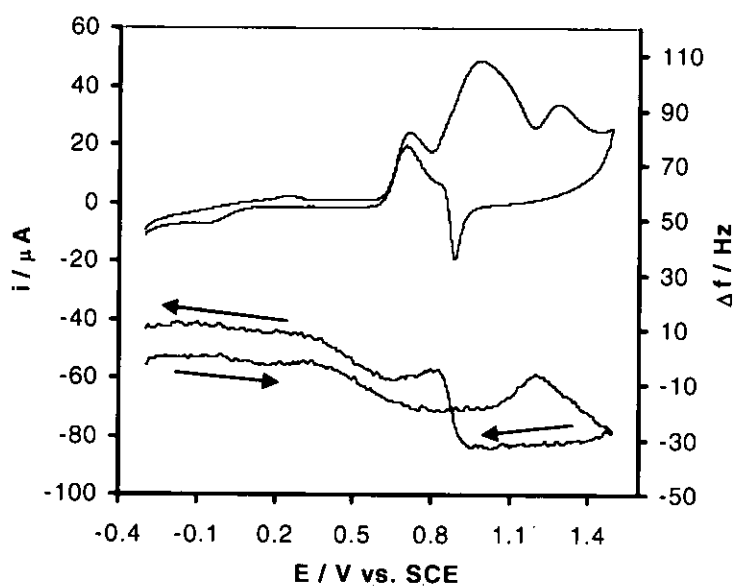


Figure 4.2.vi: Cyclic voltammogram of 2 mol m^{-3} acetohydroxamic acid in 100 mol m^{-3} nitric (pH1) acid using a 14 mm Au(Ti) EQCM crystal at $v 10 \text{ mV/s}$. Zones are consistent with those shown in Figure 4.2.v.

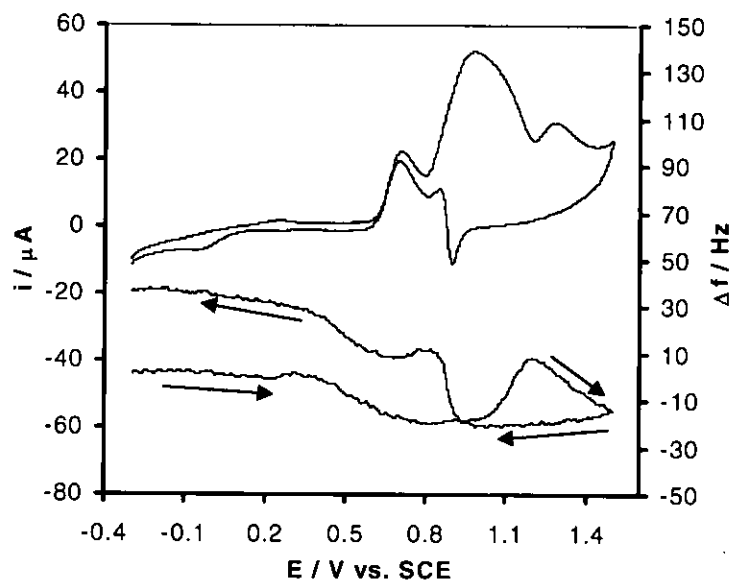


Figure 4.2.vii: Cyclic voltammogram of 2 mol m^{-3} acetohydroxamic acid in 100 mol m^{-3} nitric (pH1) acid using a 14 mm Au(Ti) EQCM crystal at $v8 \text{ mV/s}$. Zones are consistent with those shown in **Figure 4.2.v**.

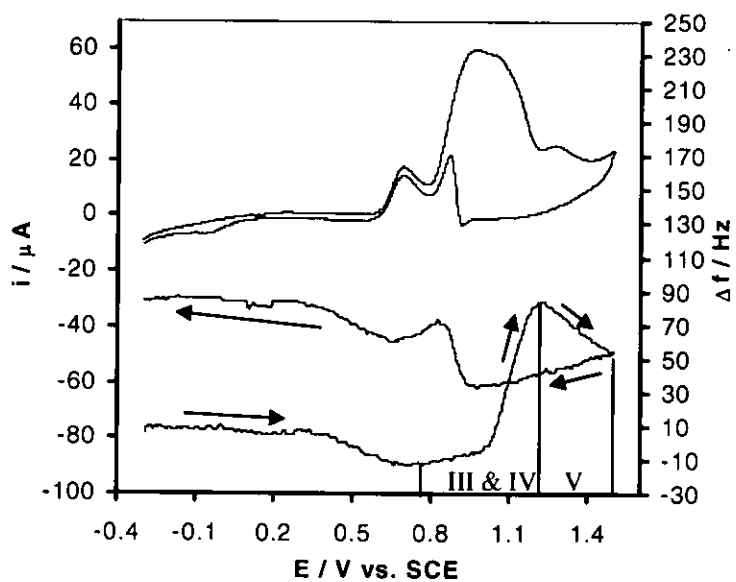


Figure 4.2.viii: Cyclic voltammogram of 2 mol m^{-3} acetohydroxamic acid in 100 mol m^{-3} nitric (pH1) acid using a 14 mm Au(Ti) EQCM crystal at $v6 \text{ mV/s}$.

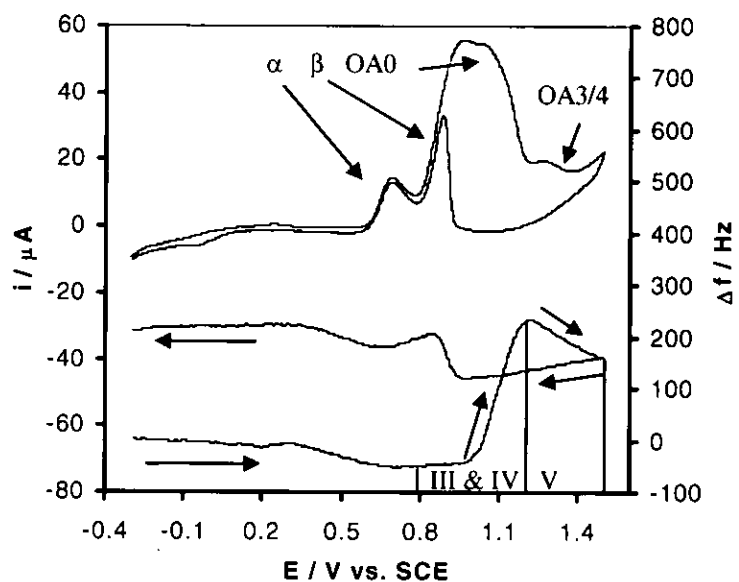


Figure 4.2.ix: Cyclic voltammogram of 2 mol m^{-3} acetohydroxamic acid in 100 mol m^{-3} nitric (pH1) acid using a 14 mm Au(Ti) EOCM crystal at $v4 \text{ mV/s}$.

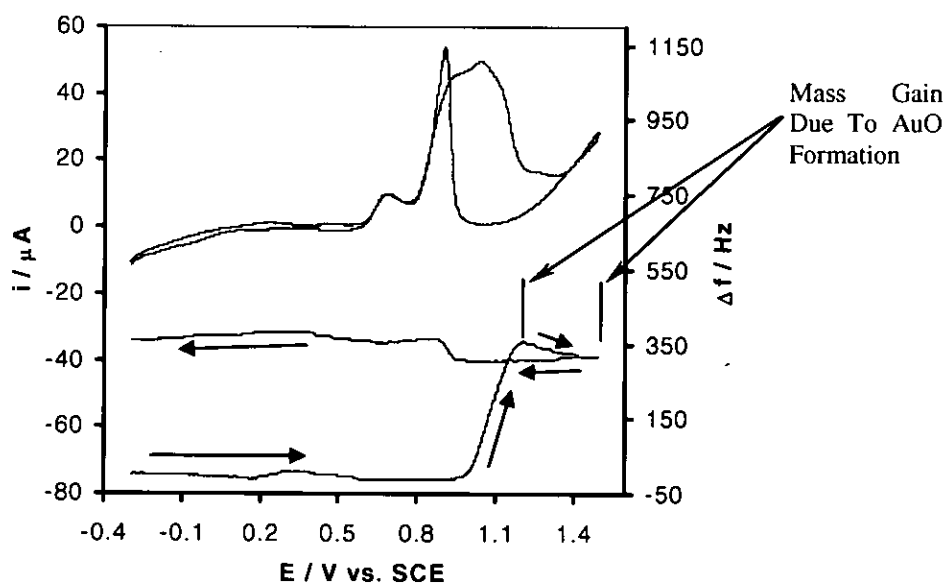


Figure 4.2.x: Cyclic voltammogram of 2 mol m^{-3} acetohydroxamic acid in 100 mol m^{-3} nitric (pH1) acid using a 14 mm Au(Ti) EOCM crystal at $v2 \text{ mV/s}$. Zones are consistent with those shown in Figure 4.2.ix.

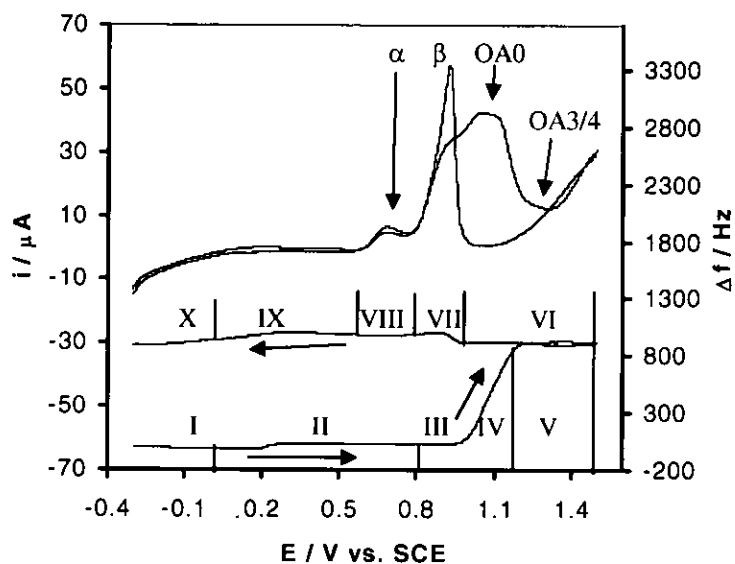


Figure 4.2.xi: Cyclic voltammogram of 2 mol m^{-3} acetohydroxamic acid in 100 mol m^{-3} nitric (pH1) acid using a 14 mm Au(Ti) EQCM crystal at $v 1 \text{ mV/s}$.

Firstly, there is as expected a shorter time available for the Au stripping reaction to occur at higher sweep rates. This is supported by **Figures 4.2.iv to 4.2.vii**, that show that as the sweep rate is decreased from 20 to 6 mV/s, a net mass loss is recorded between the starting and end potentials of the cycles, corresponding to gold dissolution. This mass loss increases as v is reduced.

Secondly, in keeping with the observations of **Chapter 3**, as the sweep rate decreases, proportionately more Au stripping occurs with respect to oxide formation i.e. the amount of electrogenerated surface oxide decreases with sweep rate. As a result of the decrease in surface oxide generation, the electrode depassivates more readily and the AHA oxidation peaks observed in the return sweep become more prominent at lower v **Figures 4.2.iv-xi**.

(iv) The mass loss corresponding to gold stripping in *Zones III & IV* in the absence of AHA *Figure 3.15*, is less than that observed in the corresponding zone in the presence of AHA *Figures 4.1 & 4.2.xi*. This is strongly indicative of AHA assisted gold stripping, probably via the formation of a complex between acetohydroxamic acid and the product of the Au/Au³⁺ oxidation reaction see **Section I.10** of **Chapter 1**. Such a complex formation reaction would increase the effective local solubility of the gold species, so displacing to more anodic potentials the point at which passivation by the formation of insoluble gold oxide species occurs. This assertion is supported by the proximity of our system at pH 1 to the Au³⁺ (SOLUBLE)/ Au(OH)₃ (INSOLUBLE) boundary at E > 1.20 V (vs. SCE) in the Pourbaix diagram for the Au-H₂O system *Figure 4.3*.

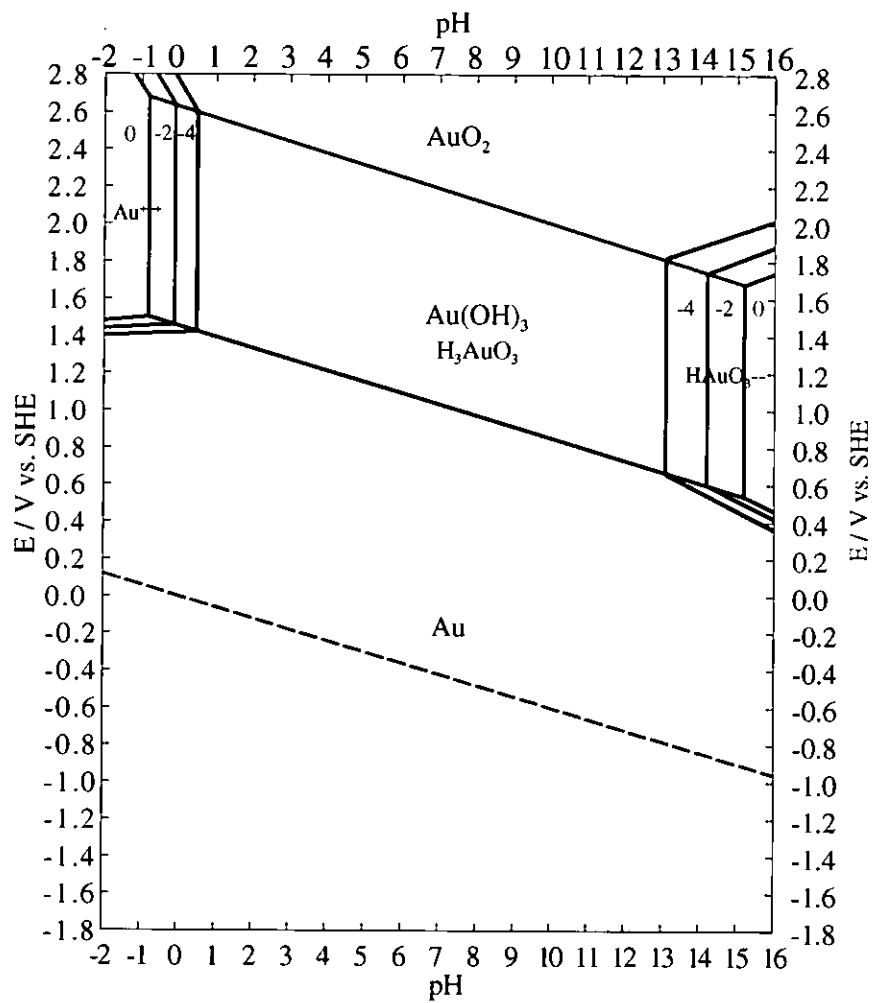


Figure 4.3: The Pourbaix diagram of the gold water system at 25°C.

IV.3.1 - The Evolution of the Forms of the Cyclic Voltammograms and Voltamassograms of AHA in Nitric Acid as a Function of Decreasing Sweep Rate

Complete interpretation of the simultaneous cyclic voltammograms and voltamassograms obtained at high and low sweep rates on Au piezoelectrodes in the absence and presence of AHA in solution have been presented in **Chapter 3 Sections III.2.1 & III.2.2**, and in this chapter, **Sections IV.2 & IV.3**. In light of these findings, it is now possible to present a discussion of how the forms of the voltammograms and voltamassograms of AHA evolve as a function of decreasing v . To this end, **Figures 4.2.i-ix** show CVs and voltamassograms of Au piezoelectrodes in the presence of AHA in pH 1 nitric acid, recorded over a range of sweep rates from $v = 100$ to 1 mV/s.

The data of **Figure 4.2.i**, taken at 100 mV/s, comprise a standard simultaneous CV and voltamassogram response and requires little detailed explanation, the results having been dealt with in detail in **Section IV.3.1**. Particular attention should be paid to the broad peak between $+0.60$ to $+1.00$ V (*vs.* SCE), peaks α and β , which arise from diffusion controlled AHA oxidations processes (see **Section IV.2**).

As the sweep rate is decreased from 80 to 60 mV/s in **Figures 4.2.ii** and **4.2.iii** the AHA oxidation peaks α and β , with onsets of $+0.60$ and $+0.90$ V (*vs.* SCE) respectively, become more distinct. The AHA oxidation peak α at a potential of $+0.70$ V (*vs.* SCE) begins to emerge during the 80 mV/s cathodic scan and is well established in the 60 mV/s cycle – so well established that it can also be seen as anodic feature once the electrogenerated gold oxide surface has been reduced during the negative-going reverse sweep at 60 mV/s in **Figure 4.2.iii**. This feature becomes more prominent as v decreases due to the greater proportion of gold oxide removal that can be effected at higher positive (measured)

potentials at slower sweep rates, so exposing the Au surface sooner during the reverse sweep. It should be noted that there is no difference between the measured frequency at the start and the end of the potential scans in any of *Figures 4.2.i-iii*, indicating that no Au stripping has occurred during these experiments.

Significant differences are observed between the voltamassograms of *Figures 4.2.iv* and *4.2.v* and this is due to the sweep rate in the latter (20 mV/s) being sufficiently slow enough for Au dissolution to be the overriding process. This manifests itself in two ways.

(i) The appearance of a new feature with a peak potential of $E_p \approx +1.05$ V (vs. SCE) in the voltammogram of *Figure 4.2.v*. Peaks α and β can still be seen at peak potentials of +0.70 and +0.90 V (vs. SCE) respectively, as can peak OA_{3/4} at $E_p \approx +1.30$ V (vs. SCE), giving rise to the suspicion that this new feature is associated with Au stripping. This suspicion is supported by the observation that: its peak potential is co-incident with that recorded for peak OA₀, the Au/Au³⁺ oxidation process (*Reaction 3.17*) of *Figure 3.14* of **Chapter 3**; and there is a net mass loss between the start and end of the potential sweep.

(ii) The form of the voltamassogram of *Figure 4.2.v* has changed from that recorded at higher sweep rates, especially in *Zones III/IV, V and VIII*.

Taking *Zone VIII* of *Figure 4.2.v* first, it can be seen that a small mass increase occurs at the negative end of this zone. Comparing *Figure 4.2.v* with data recorded at the same electrode and sweep rate in pH 1 nitric in the absence of AHA indicates the presence of a similar feature and this has previously been attributed to the deposition of electrogenerated solution phase Au³⁺ ions as Au metal, or the re-adsorption of nitrate anions at the fresh Au surface revealed by the stripping of the gold oxide. However, *Zones III/IV and V* of *Figure 4.2.v* show significant differences from similar data recorded in the absence of AHA.

In the first instance, a mass loss is recorded in *Zones III & IV* that is co-incident with the occurrence of the new peak, tentatively labelled OA0, in the voltammogram. The size of this mass loss is much greater than any loss observed in the equivalent zone of data recorded in the absence of AHA. Again, this is strongly suggestive of the new peak being correctly labelled as OA0 and that the associated gold stripping reaction is AHA-assisted – specifically through the net solubility of Au³⁺ being increased by complexation with AHA.

In the second instance, a mass gain is recorded in *Zone V* that is co-incident with the occurrence of peaks OA3/4. Again, the size of this change is much greater than any gain observed in the equivalent zone in the absence of AHA. This may be due to:

- (a) a greater electrode surface at which oxide formation can take place, due to surface roughening generated by the AHA-assisted Au dissolution process; or
- (b) redeposition of gold from the gold-AHA complex at the electrode surface as the gold oxide.

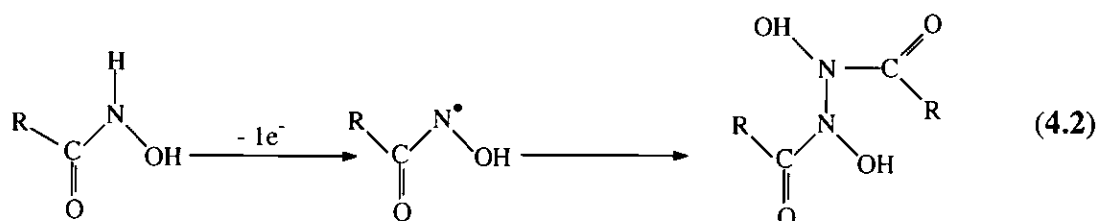
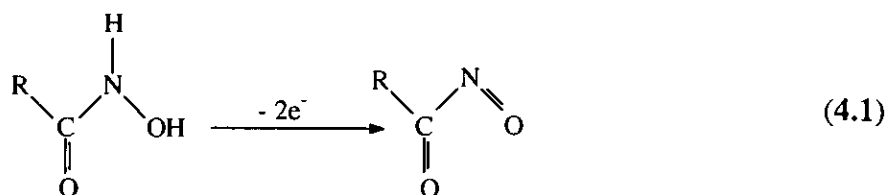
The origin of the oxide layer notwithstanding, as in the case of data recorded in the absence of AHA in **Chapter 3**, the formation of that layer ultimately leads to electrode passivation.

Further reduction in sweep rate from 10 mV/s to 1 mV/s in *Figures 4.2.vi-xi* results in an increase in the mass loss observed in *Zone IV* (due to the greater time afforded at lower sweep rates for Au stripping to occur) with a consequent increase in the net mass loss observed between the start and end of the potential scan. Peaks α and β can be observed throughout *Figures 4.2.vi-xi*, becoming more prominent in the cathodic going reverse sweep with decreasing v due to the proportionately smaller amount of gold oxide electrogenerated (in favour of Au stripping) as the value of v decreases.

Peaks OA0 and OA3/4 are also observed in *Figures 4.2.vi-xi*, the former appearing as a compound feature with peak β . The gold oxide reduction peak has almost completely vanished by *Figure 4.2.viii* due to the greater proportion of the current flow in the positive going scan being associated with the AHA-complexation assisted Au stripping reaction.

IV.4 - THE ELECTROCHEMISTRY OF ACETOHYDROXAMIC ACID STUDIED BY CYCLIC VOLTAMMETRY USING DISC MICROELECTRODES

Having assigned peaks α and β of *Figure 4.2.xi* to the intrinsic electrochemistry of AHA, we now attempt to assign those peaks to specific processes. As discussed in **Chapter 1**, Amberson *et al*, in their studies of Glutaro and Adipo dihydroxamic acids on glassy carbon electrodes, identify two oxidation processes, a two electron process and a single electron process, the latter occurring at a more positive potential than the former [4.1 & 4.2]. These are assigned to the following 2 and 1 electron oxidations respectively:



In light of the results of *Figures 4.1 & 4.2*, such an assignment seems inappropriate on Au electrodes as the more positive peak, β , is substantially larger than the more negative, α . The reverse assignment seems more likely and this is supported by two observations:

- (i) The ratio of peak currents at large v , $i_p(\alpha):i_p(\beta)$, is roughly 1:2 see *Figures 4.2.i-iv*
- (ii) At low sweep rates *Figures 4.2.vi-xi*, the peak currents associated with peak α are of the order predicted by the Randles-Sevcik equation *Equation 4.1* using $n=1$, n being the number of electrons, and an approximate value of D_0 , the diffusion coefficient of AHA of $4 \times 10^{-10} \text{ m}^2 \text{ s}^{-1}$

$$i_p = 0.4436 nFAC (nFvD_o/RT)^{1/2} \quad (4.1)$$

where F is the Faradays constant (96485 Cmol^{-1}), A is area of the electrode, R the gas constant (8.314 Jcmol^{-1}), T the temperature & C the concentration of reactant.

In order to verify the assignment of peaks α and β to *Reactions 4.2* and *4.1*, a voltammetric study of the electrochemistry of AHA on Au disc microelectrodes was conducted.

Figures 4.4.i-iv show the cyclic voltammetric profiles of 2 mol m^{-3} acetohydroxamic acid in 100 mol m^{-3} nitric acid electrolyte at gold polycrystalline disc microelectrodes with diameters of 250, 50, 25 & 5 μm respectively. They show typical cyclic voltammetric responses for gold oxidation in the positive-going forward scan (c.f. *Figure 1.6* in **Chapter 1**); however, on the negative-going reverse scan, AHA electrooxidation is observed c.f. *Figure 4.2.xi*. At first glance, little significant difference can be observed as a function of electrode diameter in either the positive or negative going scans. However, closer inspection of peak α indicates a negative shift in its half wave potential, $E_{1/2}$, with increasing electrode radius. This sort of dependency of $E_{1/2}$ on electrode radii can potentially be interpreted using the theoretical treatment of Oldham *et al* [4.8] which allows for the calculation from such data of the standard redox potential, E^\ominus , and / or the standard electrochemical rate constant, k^\ominus , and transfer coefficient, α , for the electrochemical process under study – in this case, the oxidation of AHA. This will be discussed in more detail below.

Considering the forms of *Figures 4.4.i-iv* in detail: two large oxidation peaks are seen in the positive going scan – a peak with an onset of +0.90 V (*vs.* SCE) and a smaller feature with an onset of $\sim +1.20$ V (*vs.* SCE). The forward going scan of these CVs was compared with voltammograms recorded in house on gold in background acid (see e.g. *Figure 1.6*) and AHA *Figures 4.1* and *4.2* and those reported in the literature by, *inter alia*, Burke *et al* [4.9],

Angerstein-Koslowska *et al* [4.7, 4.10, 4.11 & 4.12], Johnson and LaCourse [4.13] and Gerlache *et al* [4.14].

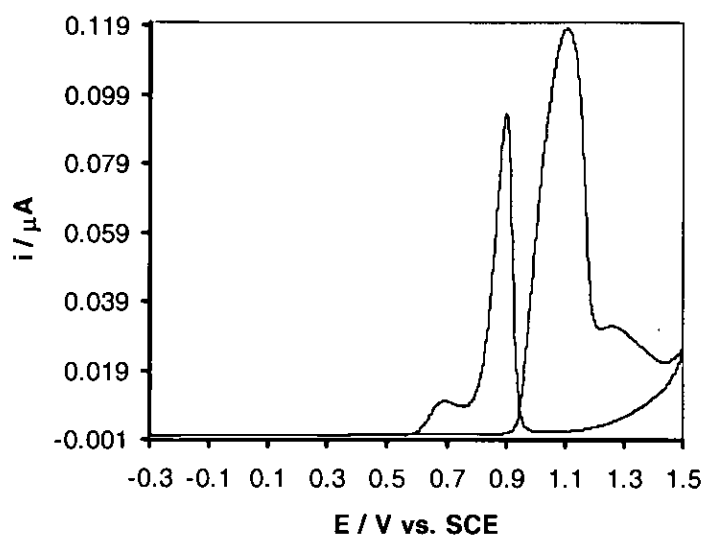


Figure 4.4.i: Cyclic voltammogram of 2 mol m^{-3} acetohydroxamic acid in 100 mol m^{-3} nitric (pH1) acid using a $250 \text{ }\mu\text{m}$ Au microdisc electrode at 1 mV/s .

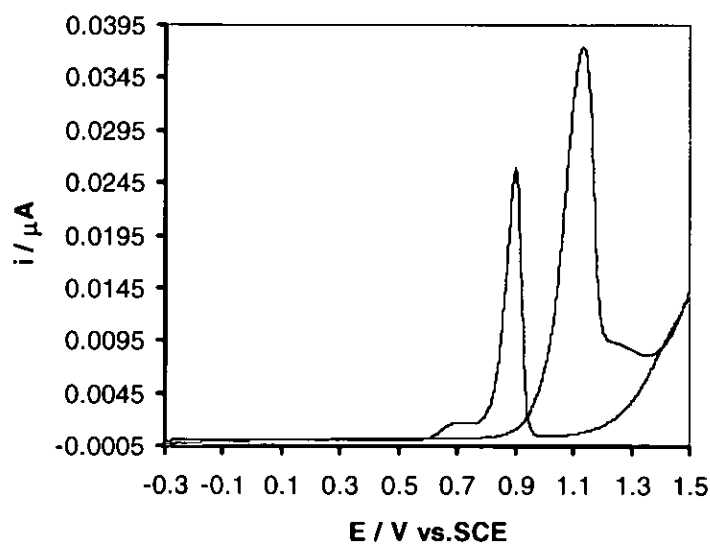


Figure 4.4.b: Cyclic voltammogram of 2 mol m^{-3} acetohydroxamic acid in 100 mol m^{-3} nitric (pH1) acid using a $125 \text{ }\mu\text{m}$ Au microdisc electrode at 1 mV/s .

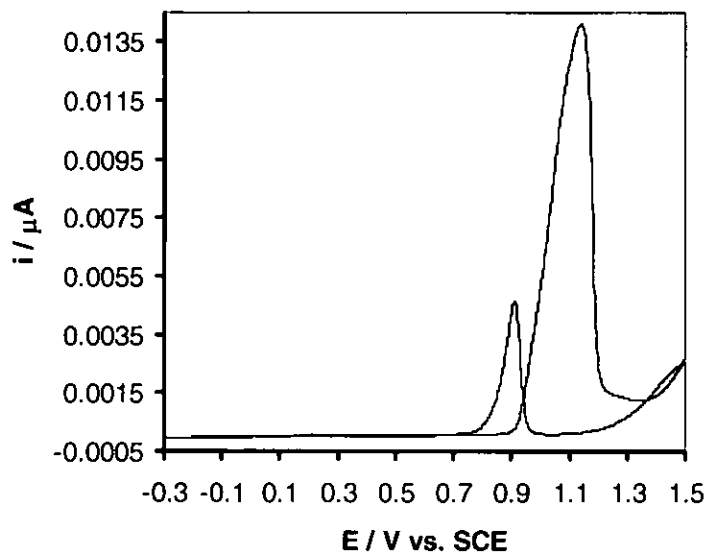


Figure 4.4.iii: Cyclic voltammogram of 2 mol m^{-3} acetohydroxamic acid in 100 mol m^{-3} nitric (pH1) acid using a $50 \text{ }\mu\text{m}$ Au microdisc electrode at $v 1 \text{ mV/s}$.

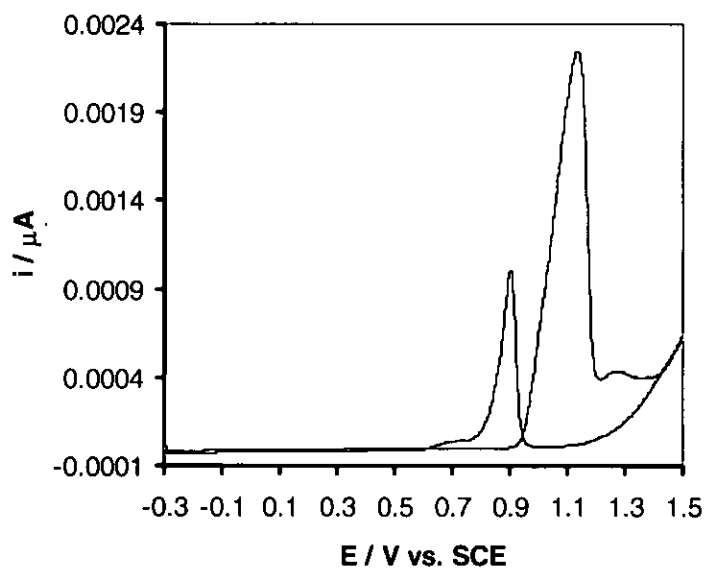


Figure 4.4.iv: Cyclic voltammogram of 2 mol m^{-3} acetohydroxamic acid in 100 mol m^{-3} nitric (pH1) acid using a $25 \text{ }\mu\text{m}$ Au microdisc electrode at $v 1 \text{ mV/s}$.

This comparison indicated that the oxidation waves at +0.90 V (*vs.* SCE) and +1.30 V (*vs.* SCE) are due to gold dissolution (peak OA0) and the formation of a passivating layer of gold oxide at the electrode surface (peaks OA3/4) respectively, as discussed in detail in **Chapter 3**.

Returning from the switching potential, positive oxidation currents associated with peaks β and α are observed superimposed over the negative current associated with the reduction of gold oxide. At pH 1, peaks β and α occur in the potential ranges +1.00 to +0.80 V (*vs.* SCE) and +0.80 V to +0.60 V (*vs.* SCE) respectively. This voltammetric behaviour of AHA on gold, also seen in *Figures 4.1 and 4.2*, is similar to that by Gerlache and co-workers for hydrogen peroxide on gold [4.15] and Johnson *et al* for glucose and sorbitol on gold [4.14]. Specifically, gold oxide formation during the forward going sweep inhibits the oxidation of H₂O₂ / glucose / sorbitol during the reverse sweep; reduction of gold oxide during the reverse sweep exposes a gold surface and oxidation of H₂O₂ / glucose / sorbitol at the electrode is then observed.

From *Figures 4.1 and 4.2* the negative going scans of *Figures 4.4.i-iv*, it can be seen that the onset of AHA oxidation is negative of the onset of gold dissolution / gold oxide formation. Thus, observation of a corresponding AHA oxidation wave during the forward going sweep of these experiments on microelectrodes would be expected, and is indeed observed during analogous experiments on 6 mm diameter Au piezoelectrodes *Figures 4.1 and 4.2.xi*. Several possible explanations can be offered for the lack of such a wave:

(i) Oxide formation and stripping activates the electrode surface to organic molecule oxidation. Burke *et al* [4.9] have suggested that the highly charged Au³⁺ species of the electrogenerated gold oxide / hydroxide species at the electrode surface does not lose many of its OH⁻ ligands before reduction *i.e.* the discharge occurs *via* an outer-sphere mechanism

to yield, as a primary product, non-lattice stabilised gold atoms. Burke further suggests that these active metal atoms quickly lose their excess energy by coalescing with one another and with the underlying metal lattice in a post-electrochemical step. Thus, it is possible that the surface rearrangement described by Burke, with its production of active, non-lattice stabilised gold atoms in low coordination states is responsible for the sensitisation of the electrode surface to AHA oxidation on the cathodic-going sweeps of *Figures 4.4.i-iv*. As stated in **Chapter 3**, surface roughening is removed when the electrode is returned to potentials negative of its pzc (ca. +0.16 V (vs. SCE) for Au) [4.15]. This would explain why, as the negative limit of the voltammograms in *Figure 4.4.i-iv* was -0.30 V (vs. SCE), the AHA oxidation peak is absent during the positive going sweep of voltammograms recorded immediately after those shown in *Figures 4.4.i-iv*.

(ii) A second explanation for the lack of the AHA oxidation peak during the forward going sweep derives from the fact that the gold microelectrodes of *Figure 4.4.i-iv* represent polished surfaces. No such polishing protocol is available for the piezoelectrodes employed in the experiments of *Figures 4.1 and 4.2*, the surface of which remains as deposited (see **Chapter 2**). A higher density of nitrate anion packing would be expected at such surfaces, said packing excluding AHA from the surface and so preventing its electrooxidation. As stated in reference to *Reaction 3.4* of **Chapter 3**, as surface coverage by adsorbed anions increases, the hydration number of those anions decreases. This would have the effect of suppressing surface Au-OH sublattice formation via *Reaction 3.5* of **Chapter 3**. Consequently, Au dissolution, peak OA0, described by *Reaction 3.15* of **Chapter 3**, occurs in preference to the surface passivation that follow on from *Reaction 3.5*. Dissolution continues until electrode passivation occurs through the processes of *Reactions 3.1b* and *3.7-3.9* of **Chapter 3**, peaks OA3/4. Dissolution roughens the gold surface which, when exposed upon reoxidation on the reverse sweep, is too rough to support its previous high levels of

anion packing, so allowing AHA molecules access to the electrode where they may be oxidised. As above, this roughening is removed when the electrode is taken to potentials negative of its pzc. Again, as the switching potential is negative of the pzc, the electrode is effectively electropolished at the end of the negative going reverse sweep, so allowing the close packing of nitrate anions at the electrode surface during the forward going sweep of an immediately subsequent potential cycle. This close packing again prevents access of AHA to the electrode surface, so preventing its oxidation during the forward going sweep of that cycle – and so on and so forth.

The first of these explanations can be discounted in light of the results of *Figures 4.1-4.2*, wherein the oxidation of AHA is observed during the positive going, forward potential sweep after the electrode has been swept to potentials negative of its pzc. The second explanation still holds in light of *Figures 4.1-4.2* as long as allowance is made for the influence of the underlying quartz crystal morphology in determining the form of the CV. Specifically, the underlying roughness of quartz crystal and presence of a Cr *Figure 4.1* or Ti *Figure 4.2* underlayer between the Au electrodes and the crystal surface prevents, during potential excursions negative of the pzc, the establishing at the gold surface of the piezoelectrode of a crystal plane orientation and smooth electrode morphology at which high levels of nitrate anion packing can occur. A consequence of this absence of dense packing is the observed AHA oxidation features during the forward going potential sweeps of *Figures 4.1 and 4.2*. The microelectrodes employed during the experiments of *Figures 4.4.i-iv* do not suffer from the sub-surface roughness problems that plague the piezoelectrodes: thus, their surfaces are “smooth” during the forward going sweep and are “roughened” by Au dissolution and gold oxide generation and its removal during the reverse sweep.

Further experiments will need to be conducted to verify this explanation – specifically, cyclic voltammetric studies on Au microelectrodes over the potential range +0.40 to +1.50 V (vs. SCE) at pH 1, so removing the potential induced removal of surface roughness that occurs negative of the pzc; and combined CV and gravimetric studies on Au piezoelectrodes constructed using *polished* quartz crystals over the potential range –0.30 to +1.50 V (vs. SCE) at pH 1. These experiments will form part of the further work for this project.

Returning to *Figures 4.4.i-iv*, for all electrode radii employed therein, a collection of small oxidation peaks can be observed in the potential region +0.30 to +0.70 V (vs. SCE) during the positive going forward scan. These peaks, which are shown in more detail in *Figures 4.5.a-d*, correspond to the peaks labelled D in *Figures 1.8 and 1.10* of Chapter 1, and can be associated with anion adsorption processes as described in Chapters 1 and 3 and the literature produced by Angerstein-Kosłowska and co-workers [4.10 to 4.13].

Interestingly, the current densities associated with peaks D recorded using microelectrodes during the experiments of *Figures 4.5.a-d* are substantially higher than those recorded using Au piezoelectrodes in *Figures 1.8 & 1.10* (>8000 and ~1000 nA m⁻² respectively). This observation indicates that anion adsorption is greater on the surface of the microelectrodes than on the piezoelectrodes, so supporting our explanation above as to why peaks α and β are not seen during the positive going forward potential scans of *Figures 4.4.i-iv*.

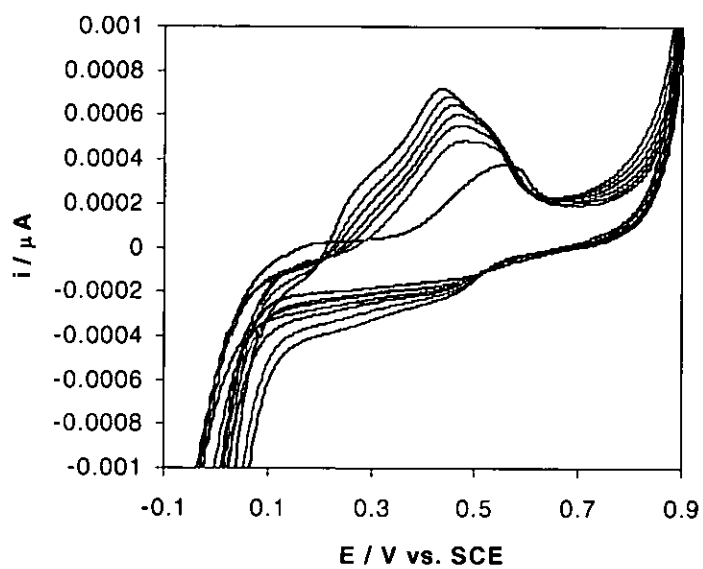


Figure 4.5.a: An enlarged CV profile of a 250 μm Au microdisc electrode for the double layer potential region for $100 \text{ mol m}^{-3} \text{ HNO}_3$ pH1 containing 2 mol m^{-3} acetohydroxamic acid at a scan rate of v 1 mV/s.

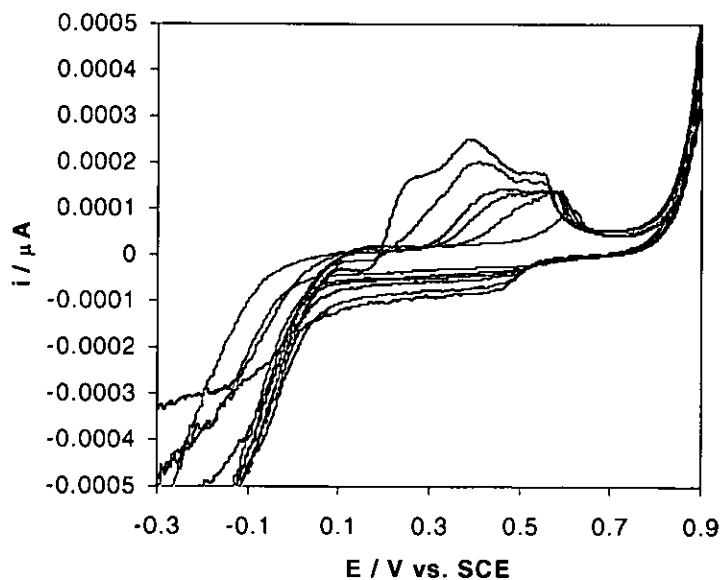


Figure 4.5.b: An enlarged CV profile of a 125 μm Au microdisc electrode for the double layer potential region for $100 \text{ mol m}^{-3} \text{ HNO}_3$ pH1 containing 2 mol m^{-3} acetohydroxamic acid at a scan rate of v 1 mV/s.

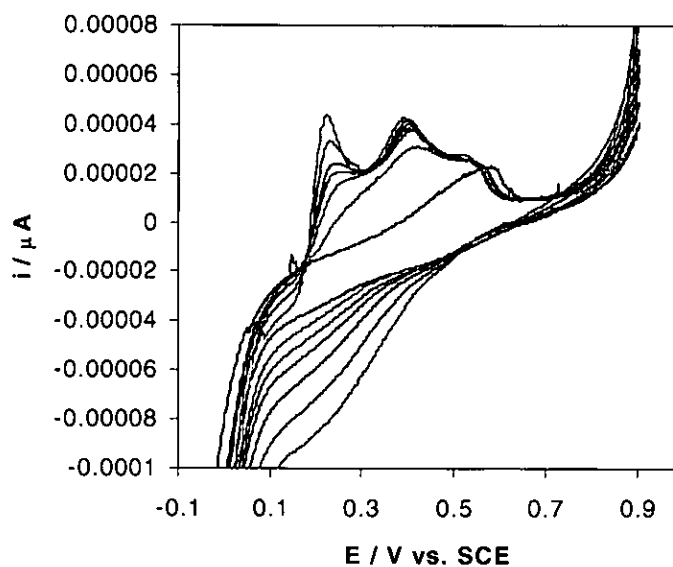


Figure 4.5.c: An enlarged CV profile of a 50 μm Au microdisc electrode for the double layer potential region for $100 \text{ mol m}^{-3} \text{ HNO}_3$ pH1 containing 2 mol m^{-3} acetohydroxamic acid at a scan rate of $\nu 1 \text{ mV/s}$.

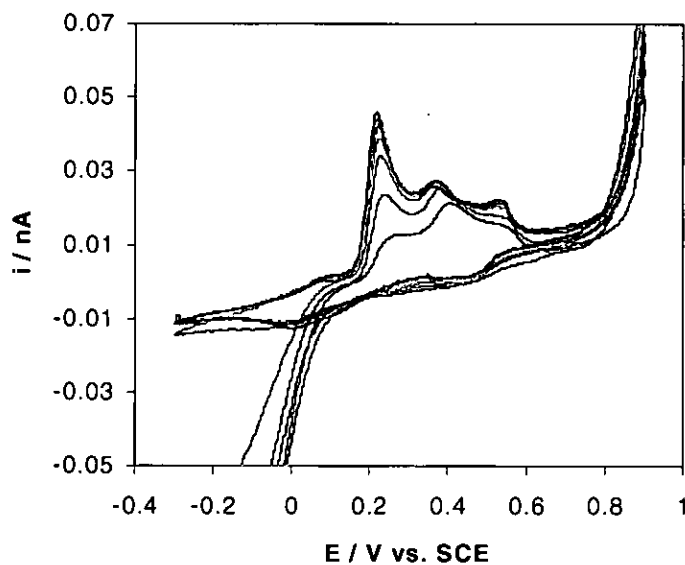


Figure 4.5.d: An enlarged CV profile of a 25 μm Au microdisc electrode for the double layer potential region for $100 \text{ mol m}^{-3} \text{ HNO}_3$ pH1 containing 2 mol m^{-3} acetohydroxamic acid at a scan rate of $\nu 1 \text{ mV/s}$.

Finally, let us return to the forms of the oxidation peaks in the potential range +0.60 to +1.00 V (*vs.* SCE) in **Figures 4.4.i-iv**. The form of these waves, which may also be seen in **Figures 4.1-4.2**, is suggestive of a diffusion controlled wave between +0.60 V and +0.80 V (*vs.* SCE) – peak α – followed by a further diffusion controlled wave between +0.80 V and +1.00 V (*vs.* SCE) – peak β . The first wave is due to the 1 electron transfer described in **Reaction 4.2** above, while the second wave is due to the reaction described in **Reaction 4.1**. Unfortunately, the diffusion-limited current plateau of peak β is not observed due to passivation of the electrode surface by gold oxide / hydroxide at $E > +1.00$ V (*vs.* SCE) during the negative going reverse sweep. Preliminary analysis would seem to indicate that such is not the case for peak α ; consequently, a more detailed examination of this peak was attempted using the methods devised by Oldham *et al* [4.8] for the analysis of families of polarograms recorded using microelectrodes of a range of radii. These methods are summarised in **Appendix A.1** and essentially involve an analysis of how $E_{1/2}$ and the Tomes potential, $(E_{3/4} - E_{1/4})$, vary with electrode radius.

Table 4.1 shows how the $E_{1/2}$, $E_{1/4}$, $E_{3/4}$ and $(E_{3/4} - E_{1/4})$ values for the reoxidation wave between +0.60 V and +0.80 V (*vs.* SCE) for varying electrode radii. Trends exhibited by $E_{1/2}$ and $(E_{3/4} - E_{1/4})$ would appear to be in keeping with those for diffusion controlled quasi-reversible / irreversible systems, as described by Oldham *et al* [4.8] but for two important observations:

(i) Using $n=1$ and an approximate value of the diffusion coefficient of AHA of $4 \times 10^{-10} \text{ m}^2 \text{ s}^{-1}$, **Equation A.1** from the **Appendices** predicts that, for a AHA concentration of 2 mol m^{-3} , such as that employed in **Figures 4.4.i-iv**, diffusion limited currents of ~4, 8, 19 and 38 nA should be obtained for electrodes of radii 12.5, 25, 62.5 and 125 μm respectively.

Electrode radii μm^{-1}	$E_{1/2}/\text{V}(\text{vs. SCE})$	$E_{1/4}/\text{V}(\text{vs. SCE})$	$E_{3/4}/\text{V}(\text{vs. SCE})$	$(E_{3/4} - E_{1/4})/\text{V}(\text{vs. SCE})$
12.5	0.649	0.624	0.670	0.046
25.0	0.652	0.626	0.675	0.049
62.5	0.645	0.622	0.663	0.041
125.0	0.640	0.620	0.659	0.039

Table 4.1 - Values of $E_{1/2}$, $E_{1/4}$, $E_{3/4}$ and $(E_{3/4} - E_{1/4})$ in Volts (vs. SCE) extracted from gold microdisc electrode cyclic voltammograms.

The actual values are substantially smaller, indicating that the negative current associated with gold oxide stripping is offsetting the positive current associated with AHA oxidation in the same potential range, so leading to a suppressed value of the diffusion limited current.

(ii) The Tomes potentials are substantially less than those that would be expected for even the most reversible 1 electron transfer process. Again, this is almost certainly due to the aforementioned suppression of the diffusion limited current plateau, so making the extraction of reliable $E_{1/2}$, $E_{1/4}$, $E_{3/4}$ and $(E_{3/4} - E_{1/4})$ values impossible.

It is expected that the future experiments mentioned above – specifically the cyclic voltammetric studies on Au microelectrodes over the potential range +0.40 to +1.50 V (vs. SCE) at pH 1 – will allow for the measurement of reliable diffusion limited currents for AHA oxidation in the forward going sweep. This will facilitate the extraction of reliable E^0 , k^0 and α values for the oxidation of AHA. In the meantime, and for the purposes of **Chapter 5**, we will discuss the susceptibility of AHA to electrochemical oxidation in terms of its oxidation onset potential of +0.55 V (vs. SCE).

IV.5 - CONCLUSIONS

An assessment of the thermodynamic and kinetic stability of HA ligands, in the form of the exemplar ligand acetohydroxamic acid, was conducted using the following electrochemical techniques (i) simultaneous cyclic voltammetric and voltamassogram profiles afforded by the EQCM (ii) cyclic voltammetry using a range of disc microelectrodes of various sizes. The studies revealed the following.

In total, three processes occur on or near Au piezoelectrodes at potentials in the vicinity of AHA oxidation at pH 0 & 1: (a) oxidation of the Au surface (see **Chapter 3**); (b) oxidation of the AHA itself; and (c) complexation of the AHA with electrogenerated Au^{3+} ions. The last process inhibits the passivation of the Au surface by gold oxide formation, so promoting the occurrence of the first two processes. Electrogravimetric analysis of the current peaks associated with AHA oxidation, peaks α and β in the potential range +0.60 to +1.00 V (*vs.* SCE) at pH 0 & 1, shows that no mass change is associated with those peaks and that the oxidation of AHA is therefore controlled by semi-infinite diffusion processes rather than surface adsorption processes. The first wave *alpha* is due to the 1 electron transfer described in *Reaction 4.2* above, while the second wave *beta* is due to the reaction described in *Reaction 4.1* a two electron transfer.

Polarograms recorded using microelectrodes reveal that the onset of peak α is in the vicinity of +0.55 V (*vs.* SCE) while that for peak β is in the vicinity of +0.80 V (*vs.* SCE) at pH 0 & 1. The oxidation appears to be irreversible and blocked at the surface of electrodes with minimal microscopic roughness by the close packing of nitrate ions at the electrode surface.

IV.6 - REFERENCES

- 4.1 J.A. Amberson. *Ph.D. Thesis*, Queens University Belfast. (1987)
- 4.2 J.A. Amberson and G.H. Svehla. *Anal. Pro.* **23**, (1986), 443
- 4.3 T.S.I. Cordoba, L.G.A. Hugot and R. Torresi. *J. Electrochem. Soc.* **138**, (1991), 1548
- 4.4 D.W.M. Arrigan, J.D. Glennon and G. Svehla. *Anal. Proc.* **30**, (1993), 141
- 4.5 D.W.M. Arrigan, B. Deasy, J.D. Glennon, B. Johnston and G. Svehla. *Analyst.* **118**, (1993), 355
- 4.6 S. Dong and Y. Wang. *Electroanalysis.* **1**, (1989), 99
- 4.7 H. Angerstein-Kozłowska, B.E. Conway, A. Hamelin and L. Stoicoviciu. *J. Electroanal. Chem.* **288**, (1987), 429
- 4.8 K.B. Oldham, J.C. Myland, C.G. Zoski and A.M. Bond. *J. Electroanal. Chem.* **270**, (1989), 79
- 4.9 L.D. Burke, D.T. Buckley and J.A. Morrissey. *Analyst.* **119**, (1994), 841
- 4.10 H. Angerstein-Kozłowska, B.E. Conway, B. Barnett and J. Mozota. *J. Electroanal. Chem.* **100**, (1979), 417
- 4.11 H. Angerstein-Kozłowska, B.E. Conway, A. Hamelin and L. Stoicoviciu. *Electrochimica. Acta.* **31**, (1986), 1051
- 4.12 L.D. Burke and J.F. O'Sullivan. *Electrochim. Acta.* **37**, (1992), 2087
- 4.13 D.C. Johnson and W.R. La Course. *Electroanalysis.* **4**, (1992), 367
- 4.14 M. Gerlache, Z. Seturk, G. Quarin and J.M. Kauffmann. *Electroanalysis.* **9**, (1997), 1088
- 4.15 R. Schumacher, G. Borges and K.K. Kanazawa. *Surf. Sci.* **163**, (1985), L621

**CHAPTER V - THE ELECTROCHEMICAL BEHAVIOUR
OF IRON (II/III) ON AHA IMPREGNATED NAFION®
COATED ELECTRODES**

CONTENT

<u>V.1 - ELECTROCHEMICAL BEHAVIOUR OF IRON (II/III) ON NAFION® COATED EQCM ELECTRODES</u>	<i>Page 188</i>
<i>V.1.1 - An EQCM Study of the Fe^{2+/3+} System using a Nafion® Modified Electrode</i>	<i>Page 193</i>
<i>V.1.2 - Response of the EQCM Piezoelectrode Nafion® / Fe II/III Redox System as a Function of Decreasing Sweep Rate</i>	<i>Page 200</i>
<u>V.2 - ELECTROCHEMICAL BEHAVIOUR OF IRON (II/III) IN A DEFERRIOXIMINE IMPREGNATED NAFION® COATED EQCM ELECTRODE</u>	<i>Page 220</i>
<i>V.2.1 - An EQCM Study of the Iron II/III System using a Nafion®/Desferrioximine Composite Modified Electrode</i>	<i>Page 222</i>
<u>V.3 - CONCLUSIONS</u>	<i>Page 242</i>
<u>V.4 - REFERENCES</u>	<i>Page 245</i>

V.1 - ELECTROCHEMICAL BEHAVIOUR OF IRON (II/III) ON NAFION® COATED
EQCM ELECTRODES

Polymeric coatings with incorporated electroactive compounds are capable of modifying electrode surfaces, and a large area of research has been devoted to the study of such systems because of their potential as electrochemical sensors [5.1 & 5.2]. Of particular utility to our ultimate sensor design are perfluorinated ion exchange polymer films that selectively preconcentrate hydrophobic ligands and ion selective chelating agents. Such films can enhance the electrochemical detection limit of the modified electrode compared to that of an uncoated electrode. Among the polymeric coatings that may serve such purposes, Nafion® is of special interest because of its high chemical stability, versatility and its ability to complex and retain organic cations. As a result of these features, Nafion® has been the subject of numerous investigations into the mechanisms of charge transport that occur for a range of redox couples incorporated into Nafion® as charge transport mediators.

Coatings can be prepared easily on electrode surfaces from commercially available Nafion® solutions, its ion-exchange properties usually discussed in terms of a cluster network model [5.3]. The structure of Nafion® is shown in *Figure 5.1*. Hydrophilic counter ions are thought to permeate the membrane through interconnected hydrophilic domains containing the fixed $-\text{SO}_3^-$ groups and solvent. Their mobility is therefore high. Conversely hydrophobic ion interacts strongly with the hydrophobic domains of the matrix which leads to significantly smaller transport rates of these entities.

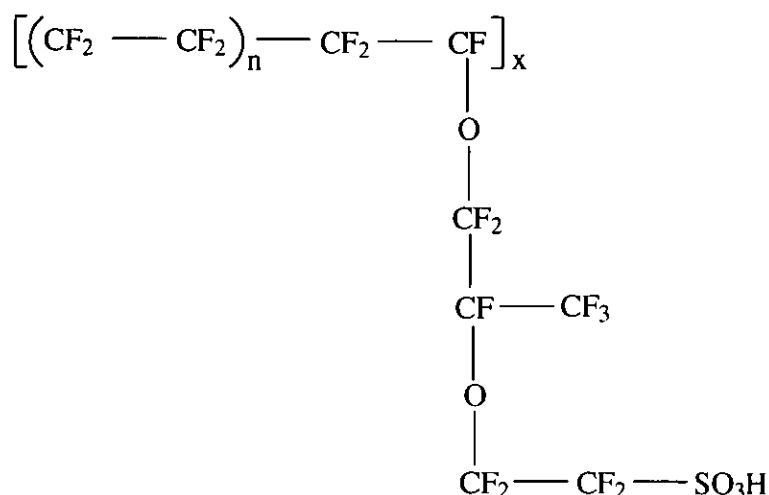


Figure 5.1: Structure of the perfluorosulphonate ionomer Du Pont Nafion[®].

Following the application of the EQCM technique to liquid media in the early eighties [5.4 & 5.5], it was quickly recognised that its exploitation in an electrochemical context would provide a means to simultaneously determine the changes in mass and electrochemical parameters (potential, current and charge) associated with a variety of reactions at electrode surfaces. Many applications of the EQCM in the study of adsorption, formation and removal of monolayers and multilayers, UPD metallic depositions and corrosion processes have been reported and reviewed [e.g. 5.6 & 5.7]. Consequently, application the EQCM to the investigation of Nafion[®] modified electrodes is an established area of study [5.8, 5.9 & 5.10].

Previous investigations of Nafion[®] coated electrodes have concentrated on hydrophobic redox-active cations such as ruthenium-bipyridine, cobalt-bipyridine and iron-phenanthroline complexes [5.11]. Consequently, there is ample evidence to demonstrate that Nafion[®] has an affinity for hydrophobic cations. We are interested in the interaction of Nafion[®] with the hydrophilic Fe²⁺/Fe³⁺ system [5.3, 5.12, 5.13, 5.14, 5.15 & 5.16] and the hydrophobic complexes iron yields with hydroxamic acids (HAs).

This interest arises from our efforts to develop a HA-based EQCM sensor for cations of interest to the nuclear industry and most especially the cations of the actinides. HAs show great affinity for actinides M^{4+} cations; however, they also show great affinity for Fe^{3+} . Given that Fe^{3+} is also redox active, it is an obvious candidate for a system on which to conduct development work on the sensor prior to investigating its utility for actinide sensing (with all the experimental difficulties that working with radioactive materials would entail). Thus, in the first instance, we shall explore the interaction $Fe^{2+/3+}$ with unmodified Nafion[®] layers before moving on to a consideration of the interaction of $Fe^{2+/3+}$ with HA-loaded Nafion[®] layers.

The $Fe^{2+/3+}$ / Nafion[®] system is shown schematically in *Figure 5.2*. The system has been electrochemically investigated by a number of workers, such as Ye and Doblhofer [5.3], who used a Pt rotating ring-disc electrode (RRDE) in aqueous H_2SO_4 electrolyte to study the effect of sweep rate and electrode rotation speed on membrane response. The iron system has also been studied both electrochemically and electrogravimetrically. For example, Belqat and co-workers have investigated the $Fe^{2+/3+}$ system on Au disc electrodes using potentiometric and voltammetric techniques. They found that the $Fe^{2+/3+}$ system is reversible in H_3PO_4 , becoming quasi-reversible upon addition of HF [5.16]. Juzeliunas and Juttner investigated the Fe (II) EDTA / Fe (III) EDTA system on an uncoated EQCM electrode at varying pH values in order to determine the mass deposition of iron on the EQCM electrode surface [5.15].

However, to date, and to our knowledge, there does not appear to have been any exhaustive studies conducted of the $Fe^{2+/3+}$ / Nafion[®] system using the EQCM. To this end, we initiated a series of EQCM studies into Nafion[®] incorporated $Fe^{2+/3+}$ in order to develop a better

understanding of the electrochemical behaviour of this composite membrane and its potential role as the transduction element of an EQCM-based iron sensor.

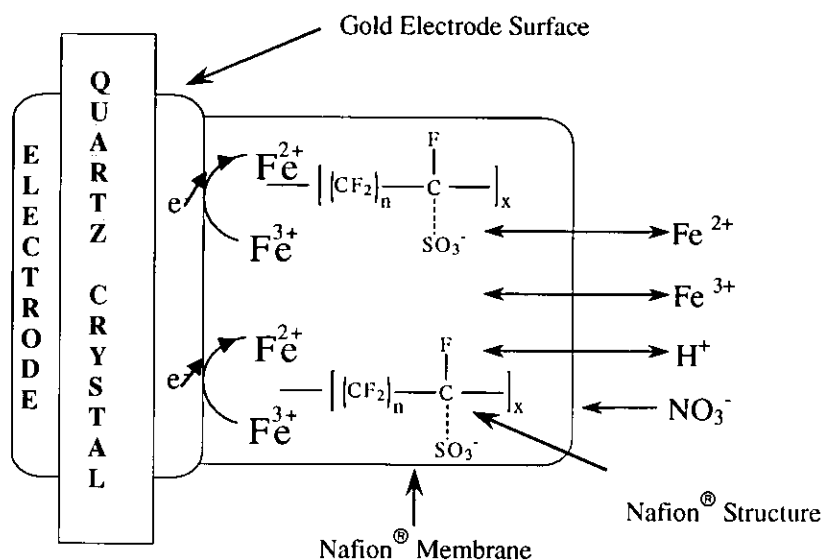


Figure 5.2: Representation of an Au piezoelectric electrode coated with Nafion[®] polymer in contact with the nitric acid electrolyte. The cations from the solution are partitioned into the fixed-charge polymer, Nafion[®], whose simplified chemical structure is also shown.

As stated in Chapter 2, the Nafion[®] films were of these experiments were prepared by drop deposition onto the crystal surface of 5 to 20 μl of a 5% solution of Nafion[®] in a mixed water / alcohol solvent. The majority of the data reported in this chapter, Figures 5.3-5.5, were obtained using Nafion[®] films prepared using drop volumes at the lower end of this range i.e. 5 μl . However, in order to maximise the voltammetric signal in experiments on the Fe^{3+} / DFA⁺ / Nafion[®] composite coated electrodes, the experiments of Figures 5.12-5.19 were conducted using the larger drop volume of 20 μl , and consequently thicker polymer layers. Unfortunately, these thicker layers, once impregnated with solvent, ligand and analyte ion, caused the gravimetric response of the device to crash, so rendering the recording of associated voltamassograms impossible.

Comparison of the preparation protocols of the thinner Nafion[®] layers employed in the experiments of *Figures 5.3-5.5* with the preparation protocols and results of Tjarnhage and Sharp [5.8] indicates that the polymer layers employed in the experiments of *Figures 5.3-5.5* display linearity between the measured frequency shift of the quartz crystal and the mass of the membrane. In our experiments, 5 μl of 5% Nafion[®] solution spread over a crystal surface corresponds to 162 μg of Nafion[®] per cm^2 of piezoelectrode surface. Tjarnhage and Sharp studied crystal response as a function of Nafion[®] loading in the mass range 48 to 435 μg of Nafion per cm^2 of piezoelectrode surface and found that energy losses associated with viscoelasticity within the polymer increased as the corresponding membrane thickness increased from 78 to 696 nm. However, this viscoelastic damping was not sufficient to invalidate the Sauerbrey relationship which received some support for its applicability through the linearity of a Δf vs. Nafion[®] film thickness plot over the thickness range 78-696 nm or 48-435 μg of Nafion[®] cm^{-2} . As the mass of our thinner membrane falls squarely within this range, we can assume that the Sauerbrey equation can be applied to the data of *Figures 5.3-5.5*.

V.1.1 - An EQCM Study of the $Fe^{2+/3+}$ System using a Nafion[®] Modified Electrode

This section presents a study of the behaviour of the hydrophilic $Fe^{2+/3+}$ redox system at a Nafion[®]-coated / Au electrode composite. Prior to recording data, the membrane coatings were treated in order to maximise the hydration state of the Nafion[®] layer (See **Section II.11**). Removing the effects of membrane dehydration as described by Shi and Anson (also see **Section I.8**) allowed for the generation of reproducible Nafion[®] coatings that were heavily loaded with electroactive counterions of the type examined in this study [5.17]. The resultant piezoelectric crystal / Nafion[®] / Fe composites were then cycled between the potential limits of the experiment until the ferric reduction and oxidation signals in the CV and voltamassogram became invariant with sweep number.

Cyclic voltammograms and voltamassograms were obtained in pH 1 nitric acid electrolyte from a Nafion[®] coated piezo Au electrode. The Nafion[®] coated piezo Au electrode had been pretreated by partitioning ferric ions into the polymer layer by immersion of the electrode in a 10 mol m^{-3} solution of $Fe(NO_3)_3$ in a background electrolyte of 100 mol m^{-3} HNO_3 at pH1 (see **Chapter 2, Section II.10** for full experimental protocol). The number of cations incorporated into the Nafion[®] membrane is limited by the number of sulphonate sites and the charge on the cation.

Figure 5.3 shows the CV obtained when a freshly prepared, Fe^{3+} -impregnated Nafion[®] coating is cycled between 0 and 1 V (vs. SCE). The starting potential of the cyclic voltammogram in **Figure 5.3** was 1 V (vs. SCE). Two prominent features are observed:

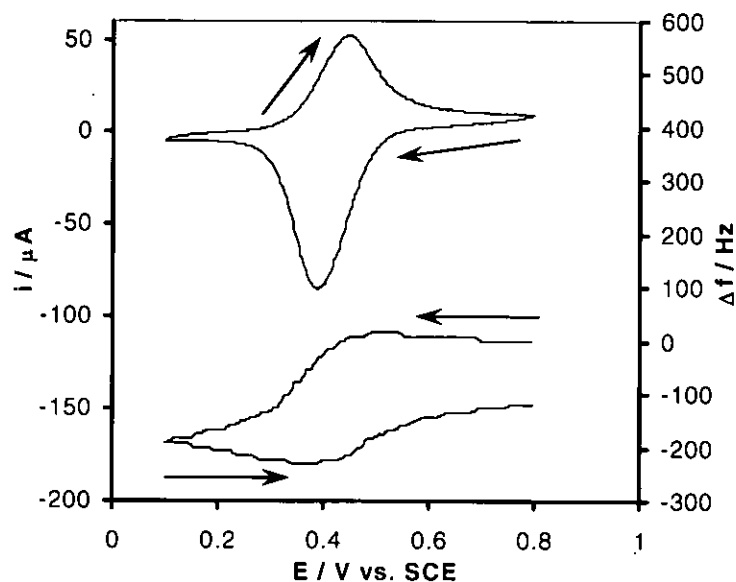


Figure 5.3: Cyclic voltammogram and corresponding frequency response for a Nafion[®] coating saturated with Fe III in 100 mol m⁻³ nitric acid pH1 using a 14mm Au(Cr) EQCM crystal at v 80 mV/s.

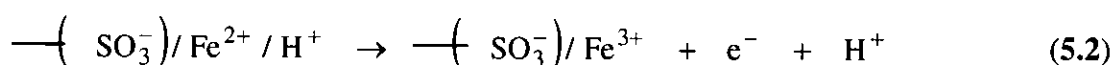
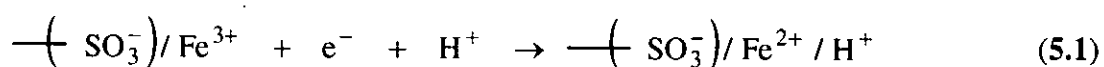
(i) a reduction wave, corresponding to the reduction of Fe³⁺ with a peak potential, E_p, of ~0.39 V (vs. SCE); and

(ii) an oxidation with E_p = of ~0.44 V (vs. SCE) corresponding to the oxidation of Fe³⁺.

The separation of the peak potentials is 51 mV, a value smaller than that expected for a process controlled by semi-infinite linear diffusion that being a peak separation of 59 mV, but consistent with thin layer cell behaviour with fast interfacial charge transfer and effective charge transport in the membrane coating. A comparison of **Figure 5.3** with that recorded using a similarly prepared Fe/Nafion[®] layer in 100 mol m⁻³ H₂SO₄ on a Pt RRDE [5.3] reveals the two to be virtually identical, suggesting that processes occurring on Pt in aqueous H₂SO₄ also occurs on the polycrystalline Au in HNO₃. Observations made by Ye and Doblhofer and Braun *et al* again suggest that the high mobility of the redox ions in the film is consistent with there being insignificant specific interaction between these ions and

the organic matrix [5.3 & 5.18]. The absence of any significant preference for either of the redox-ion species was endorsed by Ye and Doblhofer in their study as both Fe³⁺ reduction and Fe²⁺ oxidation peaks were found to be located in the same potential region when using coated and uncoated Pt RRD electrodes. As the CV response provided by Ye and Doblhofer appears to be identical to *Figure 5.3*, we can assume that any observations made can be transposed to our findings.

Possible processes associated with the reduction and oxidation waves of *Figure 5.3* are given by *Reactions 5.1 & 5.2* respectively:



where (-SO₃⁻) represents the sulphonate sites in Nafion[®] and (-SO₃⁻) / Mⁿ⁺ represents the coulombic affiliation between the sulphonate fixed charge and the free cations in solution necessary to maintain local electroneutrality.

The frequency response associated with the CV profile in *Figure 5.3* shows that the mass increases during the reduction of Fe³⁺. This frequency decrease commences at approximately at +0.45 V (vs. SCE), continues through the switching potential and continues until E = +0.40 V (vs. SCE) in the positive going reverse sweep, the onset of a frequency increase which continues until the end of the scan. The onset of this frequency increase is synchronous with the onset of the oxidation peak in the voltammogram i.e. it is associated with *Reaction 5.2*.

The frequency response of *Figure 5.3* exhibits a net frequency decrease of ~120 Hz over the entire potential cycle which corresponds to a mass change of ~150 ng or 530 ng cm⁻². In light of this result, it can be seen that *Reactions 5.1* and *5.2* oversimplify the physical reality of what is occurring. The only possible source of such a mass change is ingress of water into

the Nafion[®] coating occurring when Fe²⁺ and/or Fe³⁺ ions are transported into and/or out of the Nafion[®] membrane during potential cycling. The movement of anions can be eliminated as the membrane structure is permselective for cations and so repulses negative charges [5.8-5.10 & 5.17]. The most likely mechanism by which the water content of a previously fully hydrated membrane can increase is by a change in the solvation state of the cations occurring during their electroreduction. Such a change would not be expected for the Fe³⁺ to Fe²⁺ reduction. However, local electroneutrality must be maintained within the membrane and, as already stated, this cannot be achieved by anion movement, it must be achieved by ingress of some other cations – specifically protons. Thus, these H⁺ ions compensate for both the positive charge lost during electroreduction of the iron and diffusion of Fe²⁺ from the membrane, the latter facilitated by the lower charge density on the ferrous ion and so diminished strength of coulombic interaction with the fixed sulphonate groups compared with the ferric ion. The H⁺ ions will carry with them their own waters of solvation so accounting for the frequency decreases & increases associated with the respective reduction and oxidation processes in *Figure 5.3*.

It is well known that Nafion[®] exists in segregated phases with hydrophobic (fluorocarbons) and hydrophilic (clusters of sulphonate sites) each of which are interconnected as in other polyelectrolytes [5.3, 5.10 & 5.19]. The hydrophilic cluster size is therefore strongly dependent on the water content inside the polymer. This is related to the hydration state of the charged species inside the polymer, but also to the electrolyte concentration which affects the value of the water activity in the membrane and solution system [5.9 & 5.10].

Interestingly, the frequency decrease observed during the cathodic going scan is greater than the frequency increase observed in the anodic cycle of *Figure 5.3*. Tjarnhage and Sharp, in their study of the Os(bipy)₃^{2+/3+} / Nafion[®] system [5.8] proposed that this could be attributed

to most of the cations diffusing out of the polymer layer upon electroreduction during the negative-going forward scan so that only a fraction of the reduced ions can return to the coating during the positive going reverse sweep and be reoxidised.

Diffusion of the $\text{Fe}^{2+/3+}$ ions into the electrolyte must then allow for the diffusion of water molecules associated with H^+ ions into the membrane and the coulombic association of these solvated protons with polymer sulphonate sites, so reducing the Fe II/III electroactivity within the membrane. This theory is supported by a repetitive voltammetric and voltamassogram study in pH 1 nitric acid electrolyte, *Figure 5.4*, that shows that during continuous cycling, the concentration of Fe II/III in the membrane decreases with increasing scan number. Both the peak heights for oxidation and reduction of the Fe^{2+} and Fe^{3+} ions and the associated frequency changes decrease in magnitude after each cycle, suggesting that there is a net movement of ions from the Nafion[®] / iron composite coating into the initially Fe^{3+} -free electrolyte during each cyclic scan. As in the single scan experiment of *Figure 5.3*, the frequency decreases after each cycle, a decrease corresponding to an increase in total mass of the piezo crystal / Nafion[®] / $\text{Fe}^{3+/2+}$ composite. Interestingly, as the peak height for the oxidation and reduction processes decrease with each scan, corresponding to a $\text{Fe}^{3+/2+}$ concentration decrease within the membrane structure, one would expect a frequency increase should be observed as the cation content decreases and the membrane gets lighter. In fact the converse is observed, again suggesting there is ingress of water from the electrolyte which increases the mass of the electrode layer with each cycle.

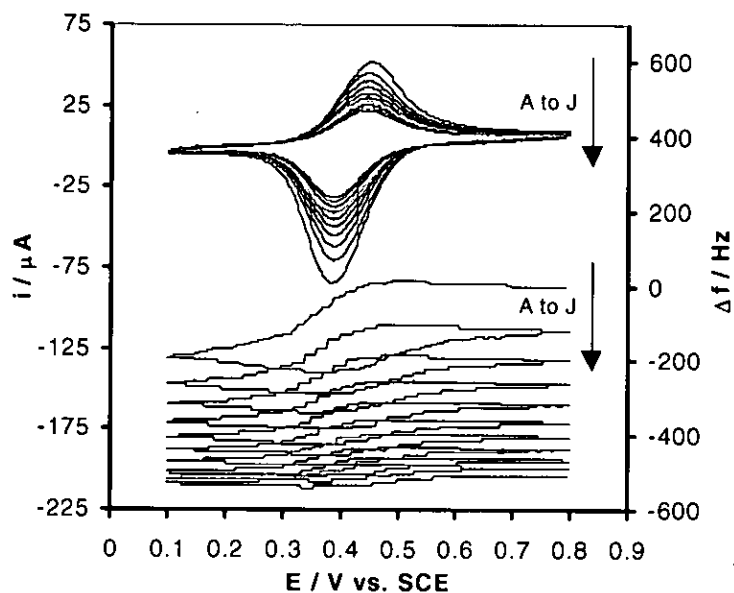


Figure 5.4: *Repetitive cyclic voltammogram and corresponding frequency response for a Nafion[®] coating saturated with Fe III in 100 mol m⁻³ nitric acid pH1 using a 14mm Au(Cr) EQCM crystal at v 80 mV/s.*

Tjarnhage and Sharp have proposed a method by which it is possible to determine the amount of water that accounts for the increase in mass over a potential cycle such as that shown in **Figure 5.3** [5.8]. By assuming that the charge balance within the membrane is maintained by the movement of cations, it is possible to calculate the difference in mass between fully oxidised and fully reduced coatings by equating the corresponding charge difference to an equivalent quantity of electroactive cations. They observed that mass changes in a range of electrolyte media were larger than those calculated for the transport of bare cations, which suggested that solvent molecules accompanied the charged species as a solvation shell [5.8]. As a consequence of this observation, a number of workers have suggested that the number of solvent molecules associated with each cation can be estimated from the difference in the mass change measured from the frequency change and the mass change calculated from the charge passed.

Gavach and coworkers and also Pourcelly *et al* calculated that, depending on the specific counterion, Nafion[®] could accommodate up to 28 molecules of water per sulphonate group [5.20 & 5.21]. Because of this and the recognised hygroscopic nature of Nafion[®], corrections may have to be made to the experimental data in order to obtain the mass change associated with the movement of Fe II/III ions into and out of the membrane system.

Thus, caution must prevail when interpreting the frequency changes of *Figures 5.3 & 5.4* as mass changes due to Fe^{2+/3+} movement, especially in view of discussions relating to solvent activity effects in polymers by Bruckenstein and Hillman [5.22]. They determined that a redox induced change in the ionic concentration in the polymer phase requires solvent movement. Being so, the changes in the film mass due to the solvent contribution may offset or overwhelm that due to ionic population effects [5.22].

V.1.2 - Response of the EQCM Piezoelectrode Nafion[®] / Fe II/III Redox System as a Function of Decreasing Sweep Rate

The role of the electroneutrality constraint within the Nafion[®] polymer and the extent to which, during potential cycling, it controls ingress and egress of cations and their accompanying molecules of solvation has been studied by a number of workers [5.8, 5.19 & 5.17]. In light of these studies, and in order to investigate the effects of solvation in *Figures 5.3 and 5.4*, a series of experiments were undertaken in a solution of 10 mol m⁻³ Fe(NO₃)₃ in 5 mol m⁻³ HNO₃ pH 2.3 electrolyte. *Figures 5.5.a-j* show a series of sequential cyclic voltammograms and voltamassograms recorded under these conditions. The Nafion[®] film was pre-saturated with Fe³⁺ partitioned from the bulk ferric nitrate electrolyte before the first voltammogram was recorded.

The objective of this study is to allow for reversible transport of the redox ions to and from the membrane thereby minimising any diffusion-derived Fe^{2+/3+} leaching effects such as those observed in *Figure 5.4*. Thus, in the absence of any irreversible structural change in the Nafion[®] polymer itself, this experiment should minimise variations in iron ion populations from one sweep to another and, consequently, their associated mass change, so allowing us to focus on mass changes derived from solvation effects. As can be seen from *Figures 5.5.a-j*, both the current and frequency response change with decreasing sweep rate. As would be expected, the peak currents, i_p , of the oxidation and reduction waves in the CV decrease with decreasing sweep rate – from +220 (oxidation) and -500 μ A (reduction) at 80 mV/s *Figure 5.5.a* to +12 (oxidation) and -50 (reduction) μ A at 1 mV/s *Figure 5.5.j*.

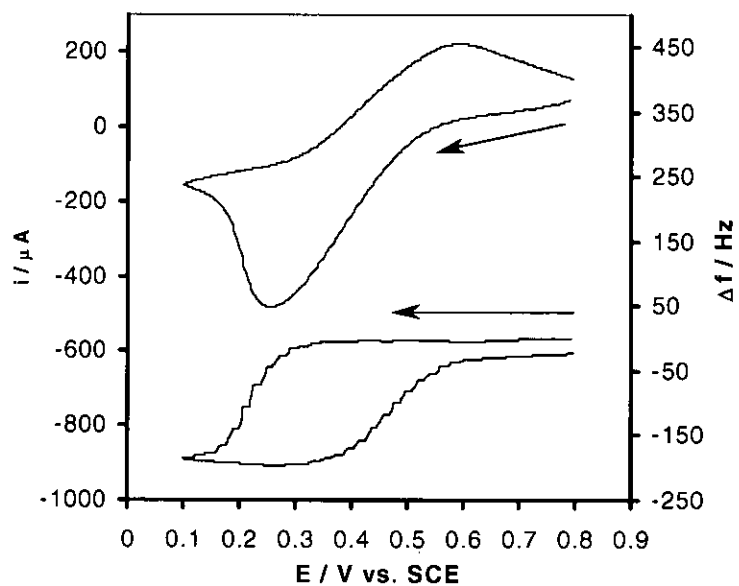


Figure 5.5.a: Simultaneous cyclic voltammogram and frequency response for a Nafion[®] coating in a solution of 10 mol m^{-3} Fe III nitrate and 5 mol m^{-3} nitric acid pH 2.3 using a 14mm Au(Cr) EQCM crystal at v 80 mV/s.

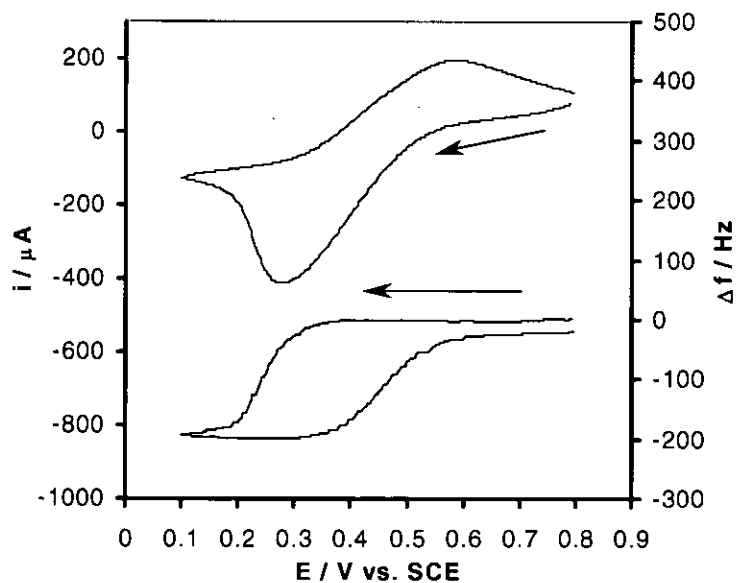


Figure 5.5.b: Simultaneous cyclic voltammogram and frequency response for a Nafion[®] coating in a solution of 10 mol m^{-3} Fe III nitrate and 5 mol m^{-3} nitric acid pH 2.3 using a 14mm Au(Cr) EQCM crystal at v 60 mV/s.

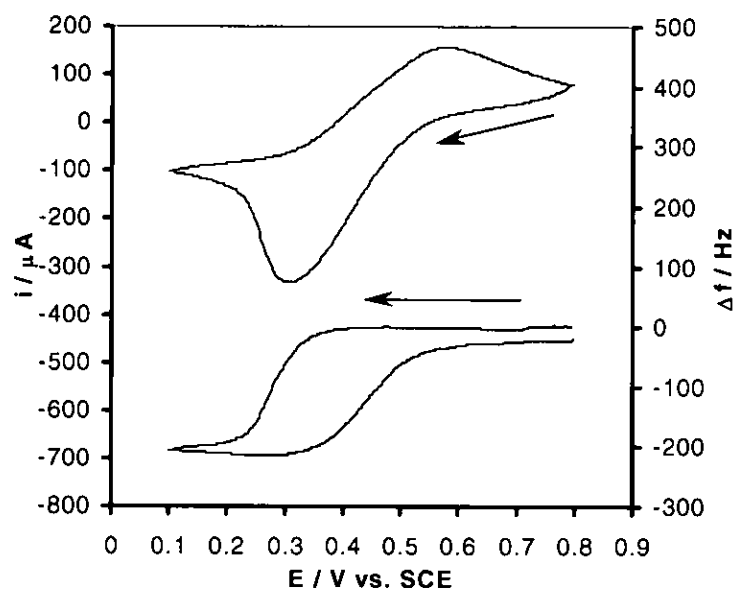


Figure 5.5.c: Simultaneous cyclic voltammogram and frequency response for a Nafion[®] coating in a solution of 10 mol m^{-3} Fe III nitrate and 5 mol m^{-3} nitric acid pH2.3 using a 14mm Au(Cr) EQCM crystal at v 40 mV/s.

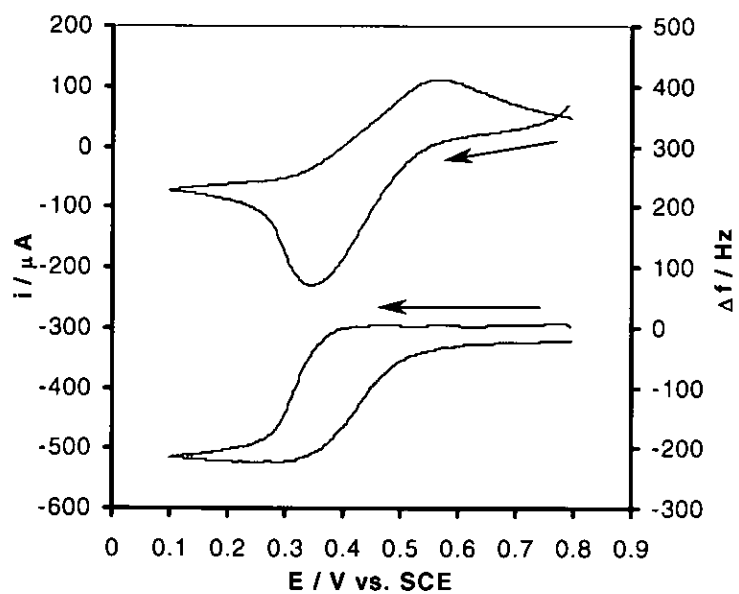


Figure 5.5.d: Simultaneous cyclic voltammogram and frequency response for a Nafion[®] coating in a solution of 10 mol m^{-3} Fe III nitrate and 5 mol m^{-3} nitric acid pH2.3 using a 14mm Au(Cr) EQCM crystal at v 20 mV/s.

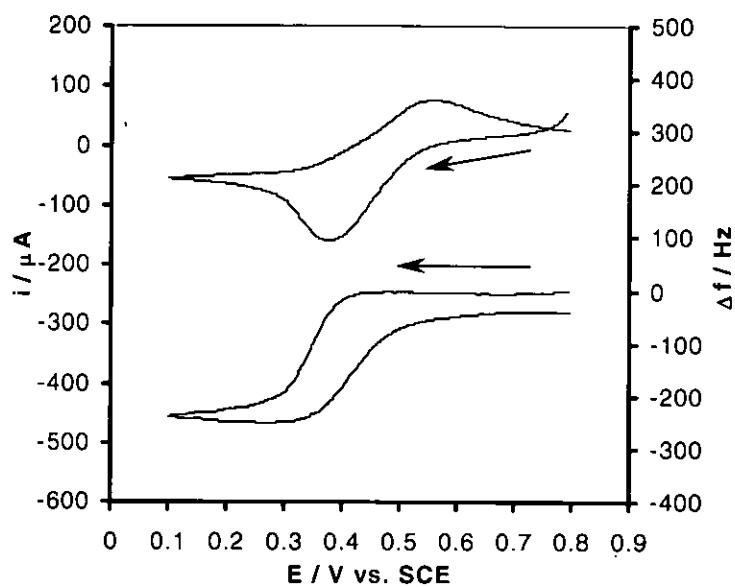


Figure 5.5.e: Simultaneous cyclic voltammogram and frequency response for a Nafion[®] coating in a solution of 10 mol m^{-3} Fe III nitrate and 5 mol m^{-3} nitric acid pH2.3 using a 14mm Au(Cr) EOCM crystal at v 10 mV/s.

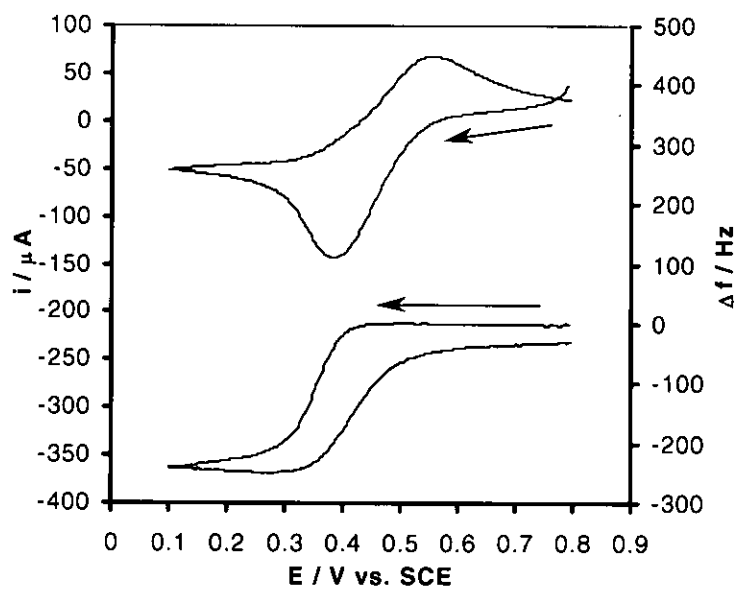


Figure 5.5.f: Simultaneous cyclic voltammogram and frequency response for a Nafion[®] coating in a solution of 10 mol m^{-3} Fe III nitrate and 5 mol m^{-3} nitric acid pH2.3 using a 14mm Au(Cr) EOCM crystal at v 8 mV/s.

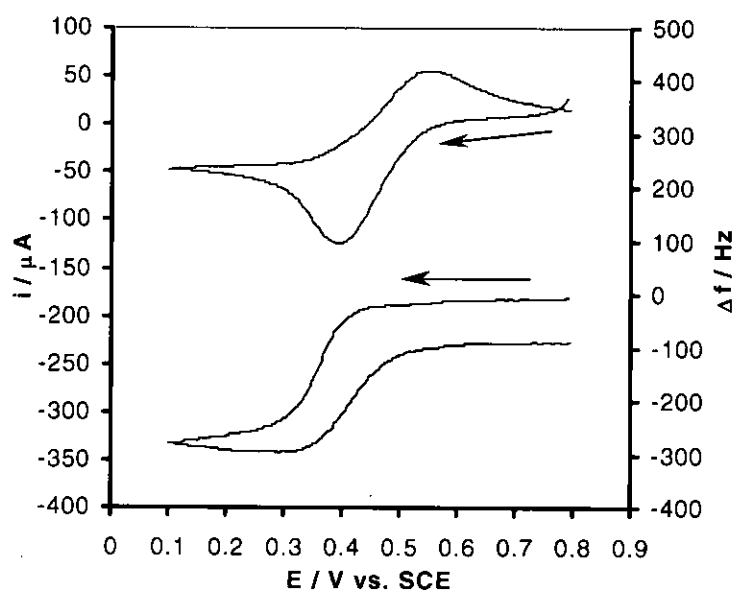


Figure 5.5.g: Simultaneous cyclic voltammogram and frequency response for a Nafion[®] coating in a solution of 10 mol m^{-3} Fe III nitrate and 5 mol m^{-3} nitric acid pH2.3 using a 14mm Au(Cr) EOCM crystal at v 6 mV/s.

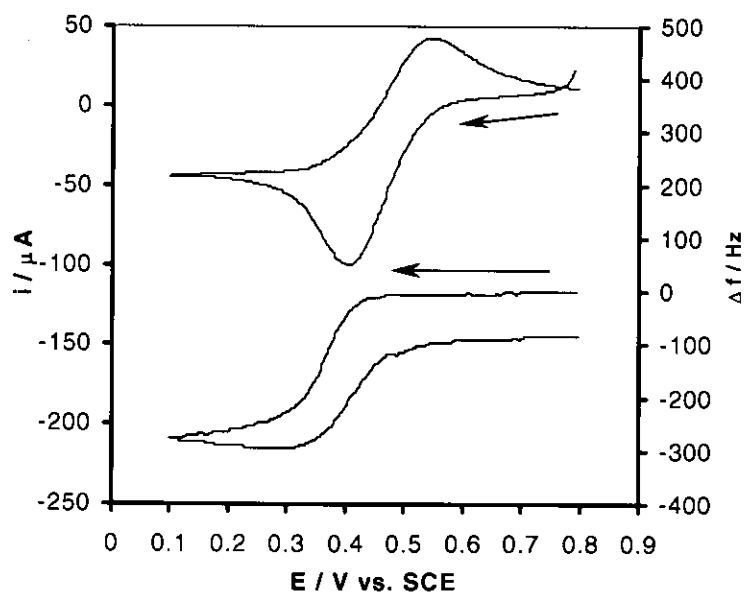


Figure 5.5.h: Simultaneous cyclic voltammogram and frequency response for a Nafion[®] coating in a solution of 10 mol m^{-3} Fe III nitrate and 5 mol m^{-3} nitric acid pH2.3 using a 14mm Au(Cr) EOCM crystal at v 4 mV/s.

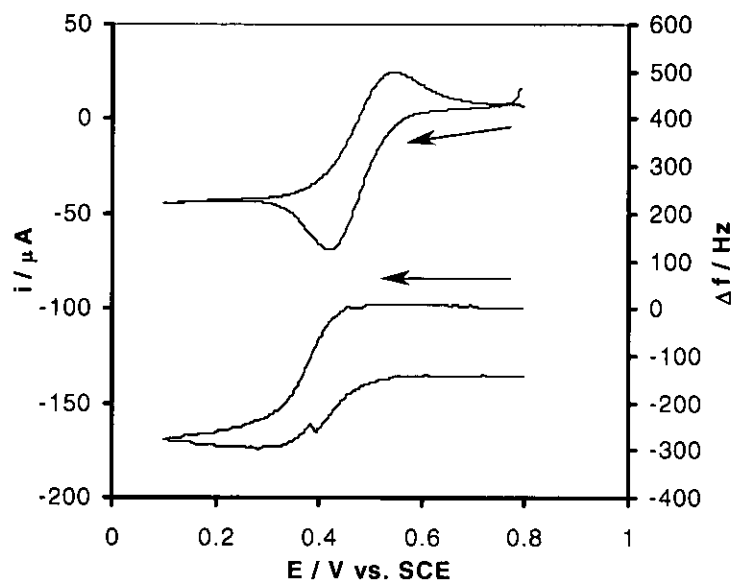


Figure 5.5.i: Simultaneous cyclic voltammogram and frequency response for a Nafion[®] coating in a solution of 10 mol m^{-3} Fe III nitrate and 5 mol m^{-3} nitric acid pH2.3 using a 14mm Au(Cr) EOCM crystal at v 2 mV/s.

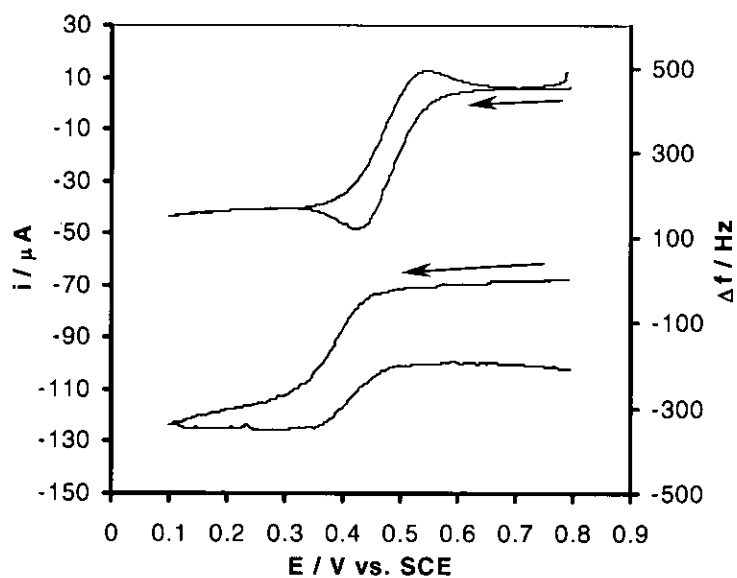


Figure 5.5.j: Simultaneous cyclic voltammogram and frequency response for a Nafion[®] coating in a solution of 10 mol m^{-3} Fe III nitrate and 5 mol m^{-3} nitric acid pH2.3 using a 14mm Au(Cr) EOCM crystal at v 1 mV/s.

The ratio of oxidative: reductive peak currents also decreases with sweep rate, reflecting the greater time allowed for diffusion of electrogenerated Fe^{2+} from within the polymer layer to the solution bulk at lower values of v . Comparison of the form of **Figures 5.3 and 5.5.a** indicates that, in the presence of Fe^{3+} in the bulk solution, the $\text{Fe}^{2+/3+}$ redox processes no longer exhibit thin layer cell behaviour. The Nafion membrane is acting as a blocking boundary between the bulk solution & the membrane solution hence the thin layer cell behaviour allows redox processes to occur only within the membrane but ultimately preventing diffusional effects from bulk solution to the electrode surface. The $\text{Fe}^{2+/3+}$ redox processes appear instead to be controlled by semi-infinite diffusion. That is the thickness of the diffusion layer defined by the redox species in the region next to the microdisc electrode surface is relatively small compared to the thickness of the diffusion media. Hence, the diffusional flux of the Fe^{3+} species from solution into the polymer layer, to the electrode is fast and maintained, a conclusion supported by

- (i) the larger currents observed in **Figure 5.5.a** than in **Figure 5.3**; and
- (ii) the linear dependence of the peak currents on the square root of the sweep rate for both the oxidation and reduction process **Figure 5.7, vide infra**.

Interestingly, the peak potential, E_p , separation increases with sweep rate in **Figure 5.5**, indicating a degree of irreversibility on the timescale these experiments, a component of which may be derived from the cation crossing the membrane-solution interface.

An analogous set of experiments to **Figures 5.5.a-j** were conducted using an uncoated Au piezoelectrode in $10 \text{ mol m}^{-3} \text{ Fe}(\text{NO}_3)_3$, pH 2.3, 5 mol m^{-3} nitric acid solution, from $v = 80$ to 1 mV/s . These are shown in **Figures 5.6.a-j**. The current responses can be seen to be broadly similar to those recorded in the presence of the pre-soaked Nafion[®] membrane **Figures 5.5.a-j**. However, there are two significant differences between the current responses of the

coated and uncoated piezoelectrodes. The first is the dependence of E_p , on sweep rate. The oxidative and reductive peak potentials for both coated and uncoated electrodes are shown in *Tables 5.1 and 5.2*. For both coated and uncoated electrodes, E_p for the reduction and oxidation peaks move to more positive and negative potentials respectively as sweep rate increases, indicating that the $Fe^{2+/3+}$ system is irreversible on both electrodes.

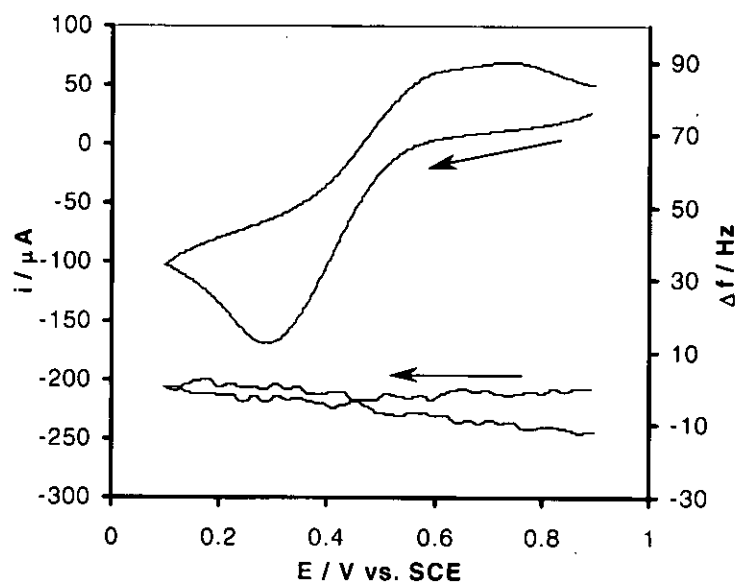


Figure 5.6a: CV and corresponding frequency response for uncoated 14mm Au(Cr) EQCM crystal recorded at v 80 mV/s in a solution of 10 mol m^{-3} Fe III nitrate in 5 mol m^{-3} nitric acid pH2.3.

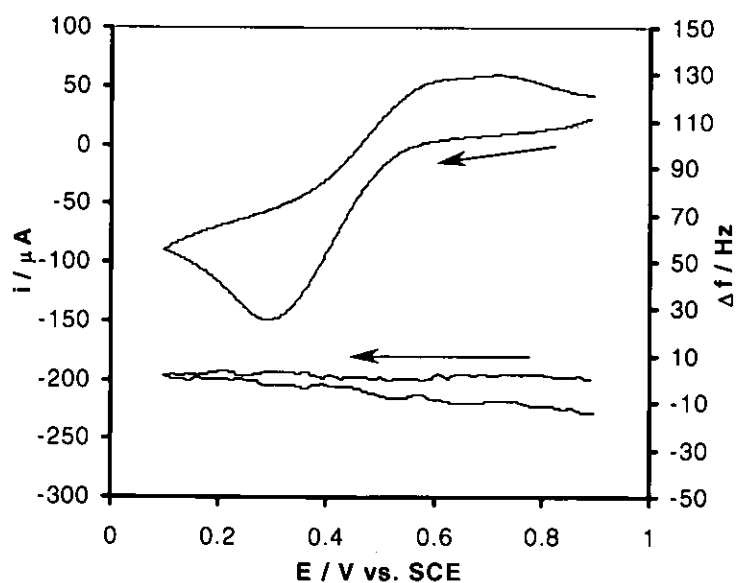


Figure 5.6b: CV and corresponding frequency response for uncoated 14mm Au(Cr) EQCM crystal recorded at v 60 mV/s in a solution of 10 mol m^{-3} Fe III nitrate in 5 mol m^{-3} nitric acid pH2.3.

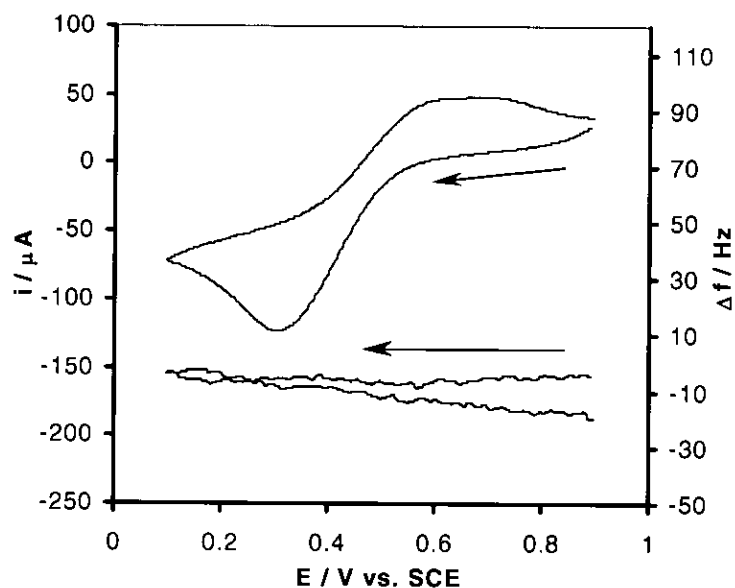


Figure 5.6.c: CV and corresponding frequency response for uncoated 14mm Au(Cr) EOCM crystal recorded at $v40$ mV/s in a solution of 10 mol m^{-3} Fe III nitrate in 5 mol m^{-3} nitric acid pH2.3.

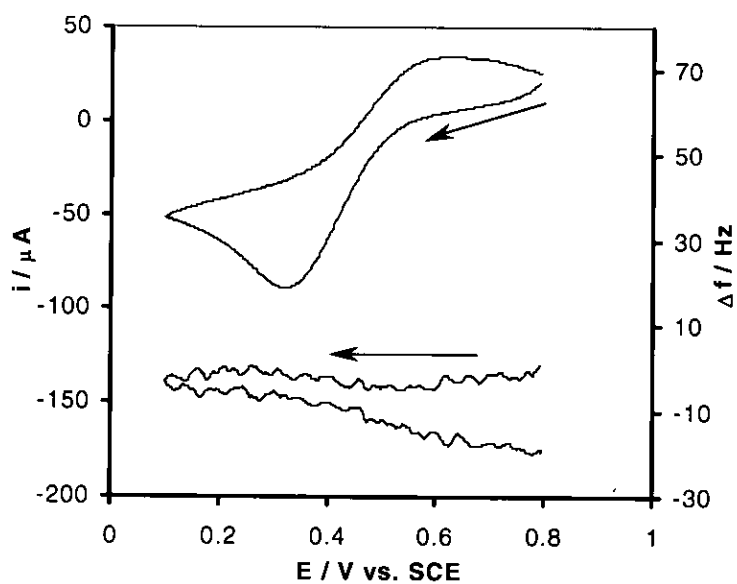


Figure 5.6.d: CV and corresponding frequency response for uncoated 14mm Au(Cr) EOCM crystal recorded at $v20$ mV/s in a solution of 10 mol m^{-3} Fe III nitrate in 5 mol m^{-3} nitric acid pH2.3.

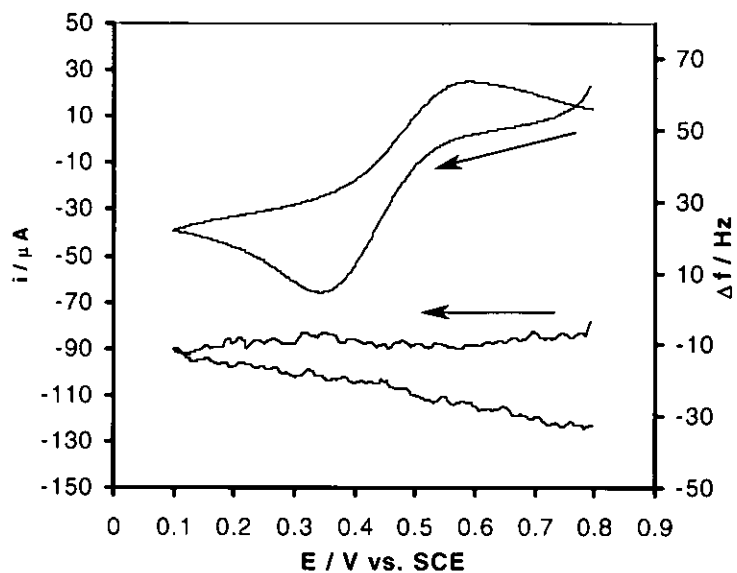


Figure 5.6.e: CV and corresponding frequency response for uncoated 14mm Au(Cr) EQCM crystal recorded at v 10 mV/s in a solution of 10 mol m^{-3} Fe III nitrate in 5 mol m^{-3} nitric acid pH2.3.

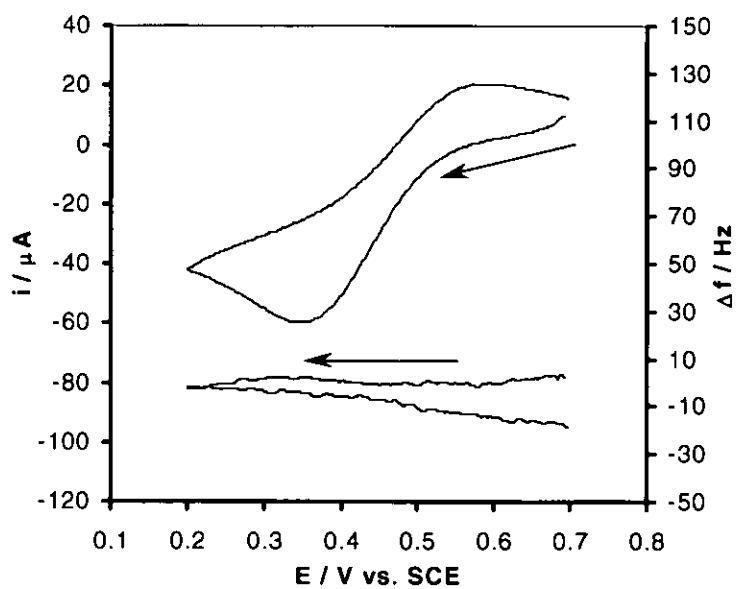


Figure 5.6.f: CV and corresponding frequency response for uncoated 14mm Au(Cr) EQCM crystal recorded at v 8 mV/s in a solution of 10 mol m^{-3} Fe III nitrate in 5 mol m^{-3} nitric acid pH2.3.

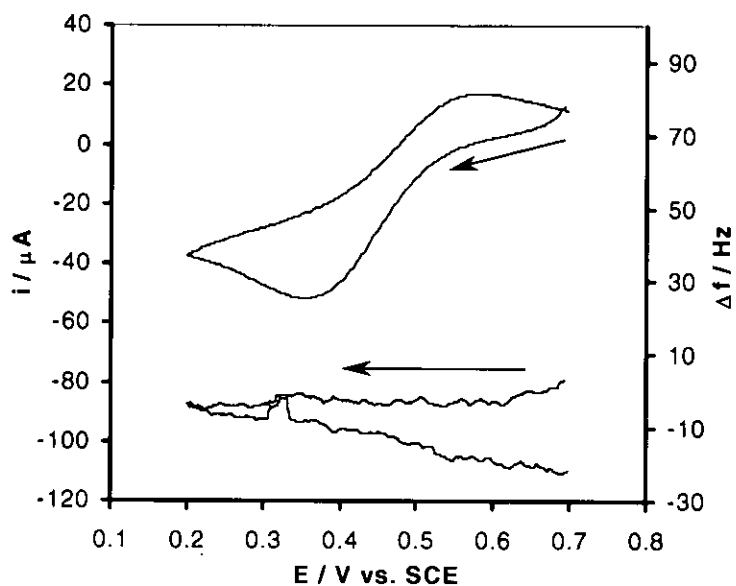


Figure 5.6.g: CV and corresponding frequency response for uncoated 14mm Au(Cr) EQCM crystal recorded at $v6$ mV/s in a solution of 10 mol m^{-3} Fe III nitrate in 5 mol m^{-3} nitric acid pH2.3.

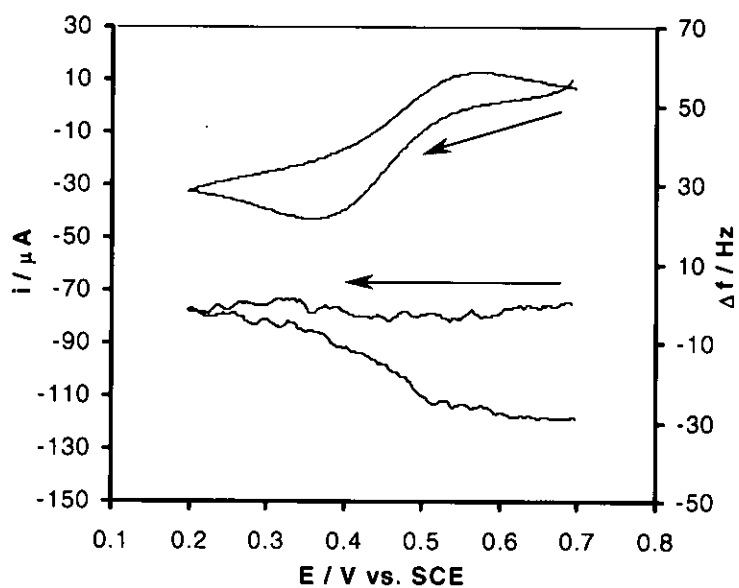


Figure 5.6.h: CV and corresponding frequency response for uncoated 14mm Au(Cr) EQCM crystal recorded at $v4$ mV/s in a solution of 10 mol m^{-3} Fe III nitrate in 5 mol m^{-3} nitric acid pH2.3.

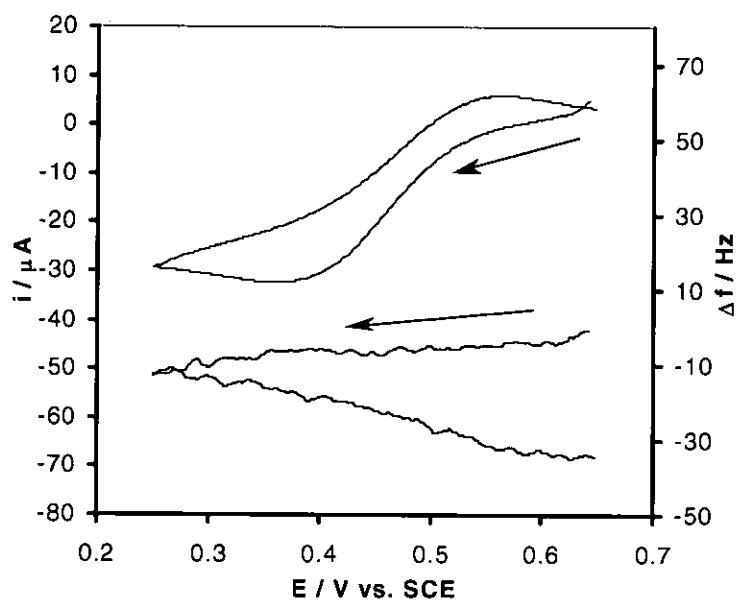


Figure 5.6.i: CV and corresponding frequency response for uncoated 14mm Au(Cr) EOCM crystal recorded at $v 2 \text{ mV/s}$ in a solution of 10 mol m^{-3} Fe III nitrate in 5 mol m^{-3} nitric acid pH2.3.

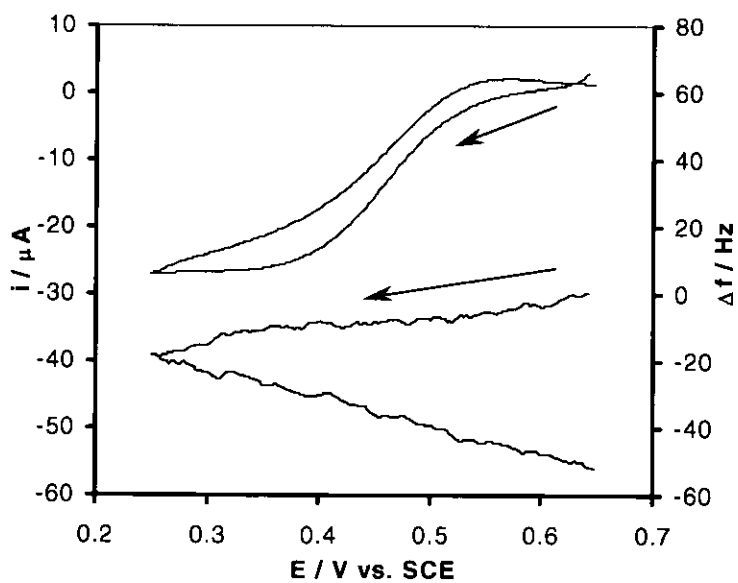


Figure 5.6.j: CV and corresponding frequency response for uncoated 14mm Au(Cr) EOCM crystal recorded at $v 1 \text{ mV/s}$ in a solution of 10 mol m^{-3} Fe III nitrate in 5 mol m^{-3} nitric acid pH2.3.

Table 5.1: - Analysis of peak potential data as a function of sweep rate for the reduction of Fe^{3+} at Nafion[®] coated *Figures 5.5.a-j* and uncoated Au piezoelectrodes *Figures 5.6.a-j*.

ν / mVs^{-1}	E_p / V (vs. SCE) for reduction of Fe^{3+} at a Nafion [®] coated electrode	E_p / V (vs. SCE) for reduction of Fe^{3+} at an uncoated electrode
80	0.263	0.295
60	0.285	0.299
40	0.312	0.314
20	0.353	0.329
10	0.383	0.348
8	0.392	0.353
6	0.400	0.361
4	0.412	0.363
2	0.424	0.364
1	0.429	0.357

Table 5.2: - Analysis of peak potential data as a function of sweep rate for the oxidation of Fe^{2+} at Nafion[®] coated *Figures 5.5.a-j* and uncoated Au piezoelectrodes *Figures 5.6.a-j*.

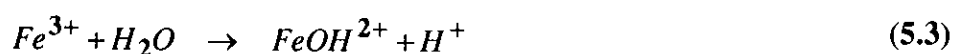
ν / mVs^{-1}	E_p / V (vs. SCE) for oxidation of Fe^{2+} at a Nafion [®] coated electrode	E_p / V (vs. SCE) for oxidation of Fe^{2+} at an uncoated electrode
80	0.580	0.631
60	0.583	0.629
40	0.575	0.624
20	0.563	0.619
10	0.553	0.588
8	0.553	0.585
6	0.546	0.576
4	0.544	0.566
2	0.539	0.557
1	0.500	0.567

Where the two systems differ is that, at the higher sweep rates e.g. 80 mV/s, coated and uncoated electrodes exhibit similar degrees of (ir)reversibility (peak separations of 317 & 336 mV for coated and uncoated electrodes respectively). While at lower sweep rates e.g. 1 mV/s, the uncoated system exhibits significantly greater irreversibility than the coated (peak separations of 71 and 210 mV for coated and uncoated electrodes respectively).

The irreversibility observed in *Figures 5.5.a-j* was discussed above. A clue to the origin of this irreversibility observed in *Figures 5.6.a-j* can be found in the second significant difference in the voltammetric responses of the two systems – the Fe²⁺ oxidation feature in the coated system appears as a single diffusion controlled peak whilst that in the uncoated system is a compound feature comprised of at least two peaks.

Inspection of the Pourbaix diagram for the Fe-H₂O system [5.23] reveals that, at pH 2.3, the ferric ion can exist as the FeOH²⁺ species which can react further to ultimately produce iron hydroxides / oxyhydroxides [5.24]. The higher the pH or concentration of ferric ions, the more facile hydroxide / oxyhydroxide generation becomes. Given the high ferric ion concentrations that will be generated at the electrode surface upon oxidation of Fe²⁺, it is not unreasonable to expect some ferric hydroxide / oxyhydroxide formation to occur at the electrode surface, so giving rise to the compound peak seen in uncoated systems *Figures 5.6.a-j*. That no such peak is observed in the coated system is indicative of:

(i) the local pH in the Nafion[®] layer being lower than that in bulk solution (possibly in part due to the influx of protons that occurs during the reduction of Fe³⁺ to Fe²⁺, *vide supra*), so suppressing the reaction *Reaction 5.3*.



(ii) the electrogenerated Fe^{3+} ions associate with the sulphonate groups in the Nafion[®] layer in such a way as to prevent hydroxide / oxyhydroxide formation on the timescale of the experiments shown in *Figure 5.5.a-j*.

We shall return to the matter of iron hydroxide/oxyhydroxide precipitation at the electrode surface when considering the voltamassograms of *Figures 5.5 & 5.6* below.

Closer inspection of the relative values of i_p for both the Nafion[®] and non Nafion[®] coated piezoelectrodes reveals that, at any given sweep rate, the ratio of peak height for reduction and oxidation of $\text{Fe}^{3+/2+}$ at the non-Nafion[®] coated electrode is $\sim 3 : 1$, whereas for the Nafion[®] coated electrode it is $\sim 2 : 1$. This observation shows that there is a larger concentration of the reduced species Fe^{2+} relative to Fe^{3+} at the electrode surface in the coated system than in the uncoated system. This is not surprising as the Fe^{2+} ion must be taking longer to diffuse out from the membrane structure of the coated electrode and as such must be retained for a longer period. Consequently, in the coated system, more Fe^{2+} can be reoxidised during the reverse sweep before potentially escaping to the bulk solution.

The permiselective membrane properties of Nafion[®] allow for the diffusion of charged cations in through the coating structure and out to the surrounding electrolyte thus ensuring electroneutrality. Using i_p - $v^{1/2}$ data from the Nafion[®] coated *Figures 5.5.a-j* and uncoated electrodes *Figures 5.6.a-j* it was found that both electrode systems exhibit linear i_p vs. $v^{1/2}$ plots for the reduction and oxidation peak *Figures 5.7* and *5.8*. The iron redox processes in both systems are therefore controlled by semi-infinite linear diffusion. Evidence for behaviour has also been reported by Belqat *et al* in their study of the Fe III/II system in H_3PO_4 -HF [5.16].

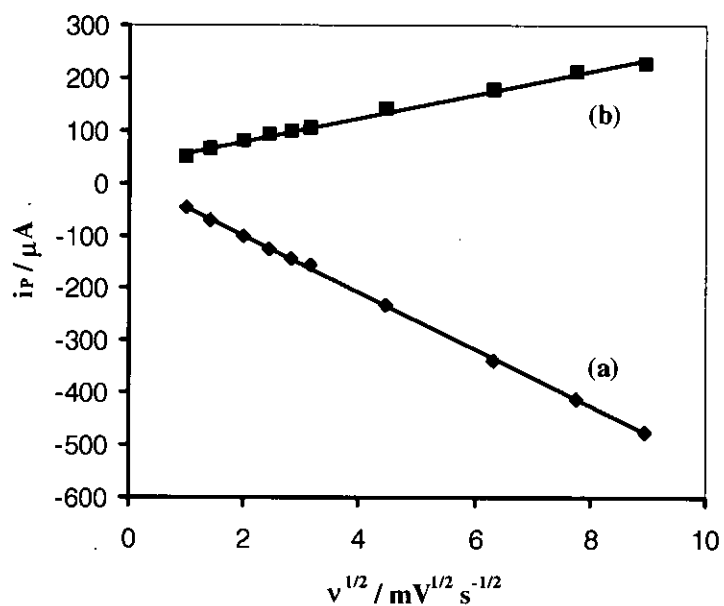


Figure 5.7.a & b: i_p vs. $v^{1/2}$ plots for (a) Fe^{3+} reduction and (b) Fe^{2+} oxidation at a Nafion[®] coated Au piezoelectrode, data taken from Figures 5.5.a-j.

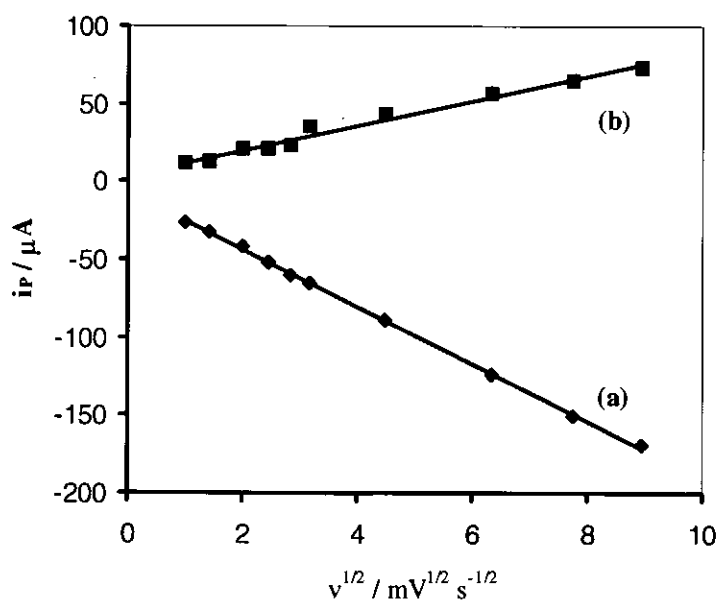


Figure 5.8.a & b: i_p vs. $v^{1/2}$ plots for (a) Fe^{3+} reduction and (b) Fe^{2+} oxidation at an uncoated Au piezoelectrode, data taken from Figures 5.6.a-j.

It can be seen from *Figures 5.7* and *5.8* that the slope of the i_p vs. $v^{1/2}$ plot for the oxidation of Fe^{2+} at the Nafion[®] membrane coated piezoelectrode is larger than that at the non-coated electrode. As we would expect cation diffusion to be slower within the Nafion[®] membrane than in free solution, this difference in slopes must be due to a concentration effect – the concentration of Fe^{2+} at the electrode surface being greater in the presence of the Nafion[®] membrane than in its absence. This is because the electrogenerated Fe^{2+} ion is impeded by the Nafion[®] structure to such an extent that it is slow to diffuse into the electrolyte beyond the diffusion limit and so is transported back to the surface promptly during oxidation. For the non-coated electrode, once reduction of the Fe^{3+} ions has taken place the so-formed Fe^{2+} ions are not restricted by the Nafion[®] membrane and so diffuse away from the electrode surface beyond the diffusion limit. Consequently, proportionately less Fe^{2+} is reoxidised in the uncoated system than the coated during the positive-going return sweep.

The frequency responses of *Figures 5.5.a-j* and *5.3* can be compared and be seen to be broadly similar in that the overall mass change of the coating was found to increase when comparing the initial and final frequency responses. Importantly, the frequency decrease (corresponding to a mass increase) is found to be 24 Hz for data recorded from solutions containing $10 \text{ mol m}^{-3} \text{ Fe}(\text{NO}_3)_3$ *Figure 5.5.a* compared with 120 Hz for data recorded using solutions containing no Fe *Figure 5.3*. Interestingly, the increase in mass during the cathodic going scan of *Figure 5.5* is very similar to that of *Figure 5.3*. Both being of the order of 196 Hz for *Figure 5.5* & 200 Hz for *Figure 5.3*, indicating that both changes arise from the same process: i.e. the reduction of Fe^{3+} to Fe^{2+} with subsequent diffusion of the latter to bulk solution, electroneutrality being maintained by an influx of highly hydrated protons, so giving rise to a frequency decrease.

As v is decreased to 1 mV/s *Figure 5.5.j* the net frequency change per cycle increases to ~200 Hz, the frequency response profile becoming more similar in shape to that of *Figure 5.3*. Thus, the slower cycle of *Figure 5.5.j* has allowed greater time for Fe^{2+} ions to diffuse away from the electrode surface / Nafion[®] film and beyond the diffusion layer, so reducing the fraction of these ions that can be reoxidised on the positive-going reverse sweep.

Thus, the net mass increases recorded at coated piezoelectrodes at 1 mV/s in the presence of solution phase ferric ions and at 80 mV/s in their absence arise from the same effect: the diffusive loss of the electrogenerated Fe^{2+} from the polymer layer. At 80 mV/s in $\text{Fe}(\text{NO}_3)_3$ solution, substantially more Fe^{2+} is electrogenerated than in the absence of ferric nitrate due to the replenishing of Fe^{3+} within the Nafion[®] layer by diffusion from solution. Thus, whilst during the return sweep at 80 mV/s the fraction of Fe^{2+} reoxidised is the same as in the presence and absence of $\text{Fe}(\text{NO}_3)_3$, because more Fe^{2+} is generated in the presence of ferric nitrate, the absolute amount reoxidised is higher than in the absence. In the former case, the electrogenerated local ferric concentration is capable of nearly fully resaturating the Nafion[®] layer with ferric ions and restoring it to its original mass *Figure 5.5.a*; in the latter case, the lower electrogenerated local ferric concentration cannot resaturate the Nafion[®] layer with ferric ions and so the electrode does not return to its original mass *Figure 5.3*.

Again, the net mass increase is due to

- (i) replacement of Fe^{3+} with Fe^{2+} and more highly hydrated H^+ in order to maintain electroneutrality; and
- (ii) replacement of Fe^{2+} , lost through diffusion out of the Nafion[®] layer, with highly hydrated H^+ ions.

Similar arguments can be applied to explain the electrogravimetric differences between *Figures 5.5.a & 5.5.j*. In the former, a high local concentration of Fe^{2+} is generated and, data

being recorded at a high sweep rate, a high fraction of these cations can be reoxidised to resaturate the Nafion[®] layer with Fe³⁺ ions. In the latter, a high local concentration of Fe²⁺ is again generated but, because we are now cycling at a lower sweep rate, a smaller fraction of the ferrous ions are reoxidised and this amount is insufficient to achieve total resaturation of the Nafion[®] layer with Fe³⁺, so resulting in the retention within the polymer film of some H⁺ ions and their waters of solvation.

As we have highlighted in this section, the above is suggestive of the fact that in a solution that contains bulk Fe³⁺ ions the Nafion[®] film see *Figure 5.5.a* is able to maintain electroneutrality through ion transportation. Any leaching from the membrane of Fe^{2+/3+} can then be replaced by the bulk ion electrolyte being so mass gain is less pronounced in *Figure 5.5.a* than in 5.3.

Examination of the frequency responses of *Figure 5.6.a-j* shows that there is little or no mass change over the negative going forward scan. However, a slight frequency decrease, consistent with a mass increase, can be seen on the positive going reverse scan. As discussed above, the possibility exists that, on an uncoated electrode and at the pHs used in *Figure 5.6*, some of the electro-regenerated Fe³⁺ ions may precipitate at the electrode surface as iron hydroxides/oxyhydroxides. This would account for the frequency decrease observed during the reverse scan – the slower the scan, the larger the decrease because of the greater time afforded for the iron hydroxide polymerisation reaction to take place.

To summarise: *Figures 5.3, 5.4 & 5.5* exhibit mass changes associated with ingress and egress of Fe^{3+/2+} and H⁺ ions and their associated waters of solvation into and out of the Nafion[®] layer. No such processes occur in *Figure 5.6*, although some iron hydroxide / oxyhydroxide precipitation is observed.

V.2 - ELECTROCHEMICAL BEHAVIOUR OF IRON (II/III) IN A DESFERRIOXIMINE
IMPREGNATED NAFION[®] COATED EQCM ELECTRODE

This section presents an investigation of the feasibility of using electrodes modified with Nafion[®] polymer films, functionalised with an appropriate hydroxamic acid, for performing electroanalysis of iron in solution. The proposed approach takes advantage of the pre-concentration derived sensitivity of chemically modified electrodes and the fact that ligand incorporation provides for a controllable and variable specificity. The method is simple in application and is based on the use of polymer films that are impregnated with an electroactive centre and co-ordination site selected the basis of the species that is of interest.

As is universally accepted iron is an essential element of all living systems. For this reason microorganisms produce a class of molecules, siderophores, which selectively bind and transport iron from the environment to cell. Generally siderophores selective to Fe³⁺ contain catecholates in *Figure 5.9.a* and hydroxamate groups *Figure 5.9.b*. The hydroxamate group is one of the most common found in siderophores produced by molds, fungi and yeast. These compounds are predominately trihydroxamic acids, such as ferrichrome and ferrioxamine, which form very stable complexes with iron III.

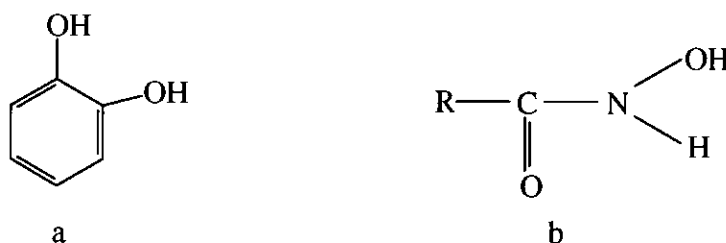


Figure 5.9.a&b: Structural formula of catecholates (a) and the basic structure of hydroxamate (b).

There has been considerable interest in the development of new siderophore analogues and their potential use in modified electrodes [5.25, 5.26 & 5.27]. As these new, synthetic hydroxamic ligands form stable complexes with a range of metals, this has allowed for their characterisation using potentiometric and spectrophotometric techniques [5.25 to 5.27 & 5.28].

The availability of potentiometric techniques to investigate the mechanism of electron transfer in the hydroxamic iron complex and the kinetics of dissociation of the iron complex allows for the investigation of this system with Au electrodes on the EQCM. This will be the main topic of the following section.

V.2.1 - An EQCM Study of the Iron II/III System using a Nafion[®]/Desferrioximine Composite Modified Electrode

The immobilisation of metal binding reagents within the polymer layer of a chemically modified electrode surface can lead to selective accumulation of analytes of interest to the electroanalytical chemist. Arrigan *et al* have reported the incorporation of hydroxamic acid ligands in the form of desferrioxamine (DFA⁺), a natural trihydroxamic acid and glycine hydroxamic acid (GHA⁺) into Nafion[®] coated glassy carbon electrodes (GCEs) [5.27]. As Fe (III) forms a deep red colour characteristic of octahedral Fe (III) complexes with HA-based ligands, the approach taken by Arrigan *et al* allowed for the detection of the ligand in the Nafion[®] film visually, colorimetrically, and electrochemically by cyclic voltammetry. Complexation of the Fe (III) by the HA allowed for pre-concentration at the electrode surface.

However, the surface properties of carbon electrodes are not thoroughly understood due to the variety of procedures used to prepare these electrodes and the large number of electrochemical variables and electrochemically active surface groups that occur at the electrode surface e.g. -OH, >C=O, -CHO, -COOH groups [5.29]. In **Chapter 3**, we characterised the oxidative electrochemistry of the gold surface presented to solution by Au piezoelectrodes. Thus, the development of an EQCM/HA based sensor for metal ions using Au electrodes would produce a better characterised device than one employing GCEs.

As mentioned in **Section V.1**, the proposed EQCM sensor under development in this project involves the incorporation of a suitable HA ligand into the Nafion[®] ion exchange polymer for the purposes of detecting metal ions of interest to the Nuclear Industry. For developmental purposes, we have opted to investigate the feasibility of using such a device

in the detection of ferric and/or ferrous ions. The HA within the polymer layer will selectively sequester Fe^{3+} which will be detected both gravimetrically and electrochemically.

The hydroxamic ligands to be utilised must be of a large molecular size and preferably have a positive charge to allow for the ease of partitioning and retention into the Nafion[®] membrane. Moreover, in this developmental situation, the standard electrochemical oxidation potential of the hydroxamic acid must be greater than the redox potential of the $\text{Fe}^{2+/3+}$ couple in order to allow for oxidation of Fe^{2+} to Fe^{3+} with its subsequent sequestration by the HA, but also to avoid the irreversible oxidation of the HA ligand itself by either the electrode or the ferric ions.

Importantly, the potential for the oxidation of the HA group exhibits little dependence upon its substituents. Thus, in order to characterise the redox behaviour of the HA, an investigation into the electrochemical oxidation of acetohydroxamic acid was undertaken in **Chapter 4**. As has been stated earlier, Amberson and co-workers have conducted voltammetric studies on synthetically prepared HA [5.25 & 5.26]. Amberson *et al* have found that the reagents are irreversibly oxidised at glassy carbon electrodes via a one proton, two electron mechanism, followed by hydrolysis to give the carboxylic acid and various nitrogen species [5.25 & 5.26]. Our own studies indicate that, at pH 1 on gold, HAs can be oxidised by either a one or two electron process, the former occurring at a potential negative of the latter (peaks α and β respectively in *Figures 4.1 & 4.2*). Comparison of the potential for the onset of AHA oxidation of $\sim +0.55$ V (vs. SCE), $\sim +0.79$ V (vs. SHE) obtained in **Chapter 4** with the Pourbaix diagrams for Fe (the development metal *Figure 5.10.a*) and Pu, Np & U (the metals on which it is intended the sensor will eventually be deployed *Figures 5.10.b to d*) indicates that HA ligands will be susceptible to irreversible oxidation by Pu^{4+} , PuO_2^+ , PuO_2^{2+} , NpO_2^+ and NpO_2^{2+} [5.30]. Thus modified ligands need to be

identified which are not subject to these reactions, or the sensor must be deployed in situations where these ions are not present. This would obviously limit the application of the sensor within process streams containing those ions.

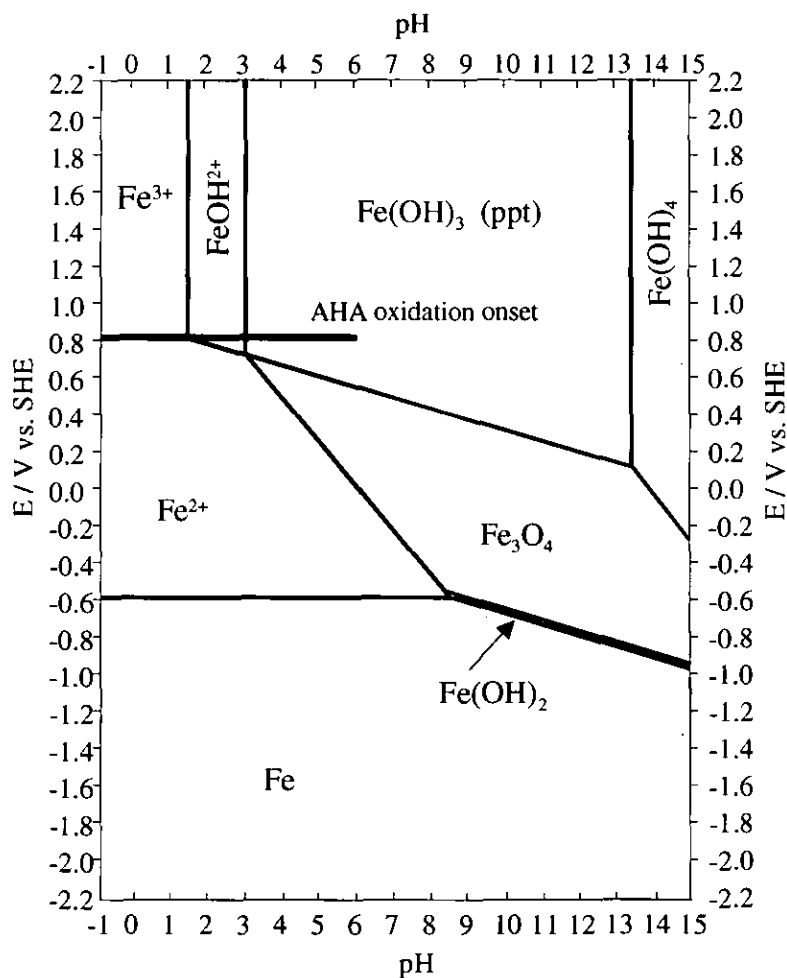


Figure 5.10.a: Pourbaix potential-pH diagram for the Fe-H₂O system at 298 K, for FeII/III solution activities of 0.1 mol m⁻³.

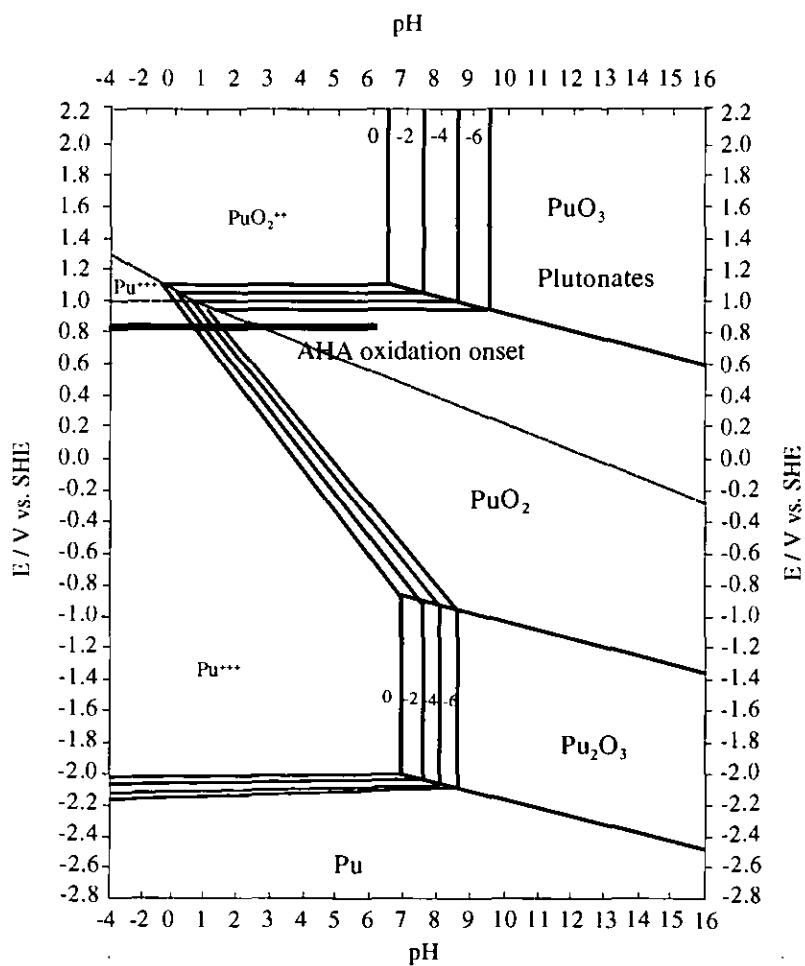


Figure 5.10.b: Pourbaix potential-pH diagram for the Pu-H₂O system at 298 K, for Pu³⁺ / Pu⁴⁺ solution activities of 0.1 mol m⁻³.

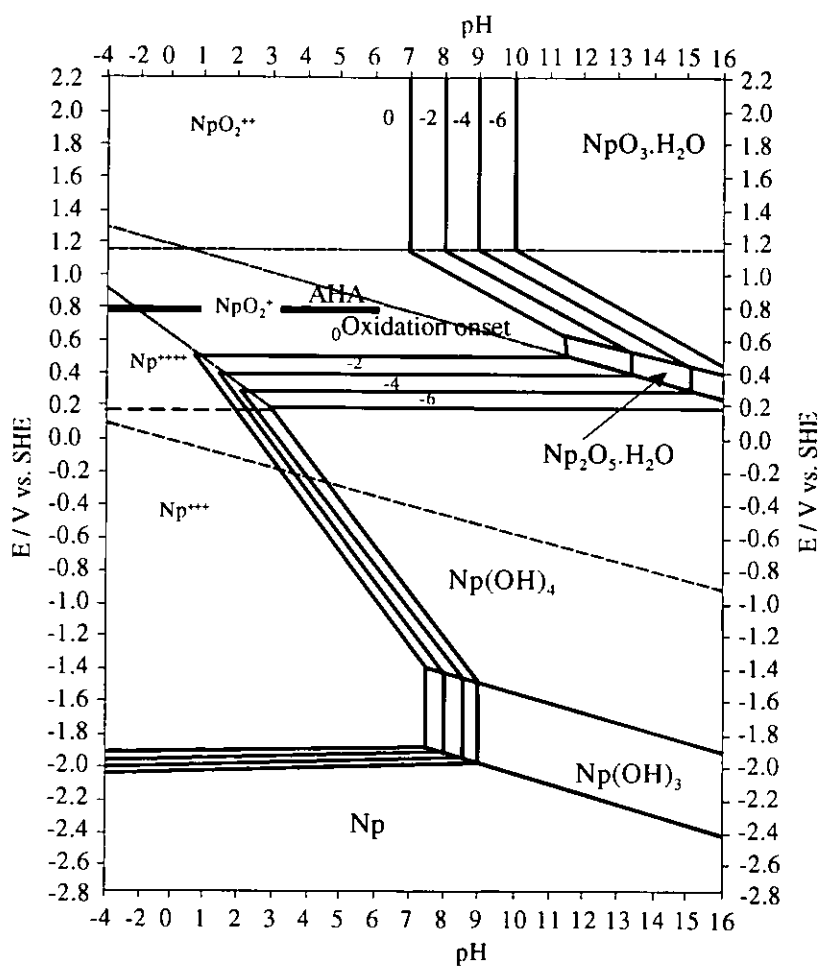


Figure 5.10.c: Pourbaix potential-pH diagram for the Np-H₂O system at 298 K, for Np³⁺ / Np⁴⁺ solution activities of 0.1 mol m⁻³.

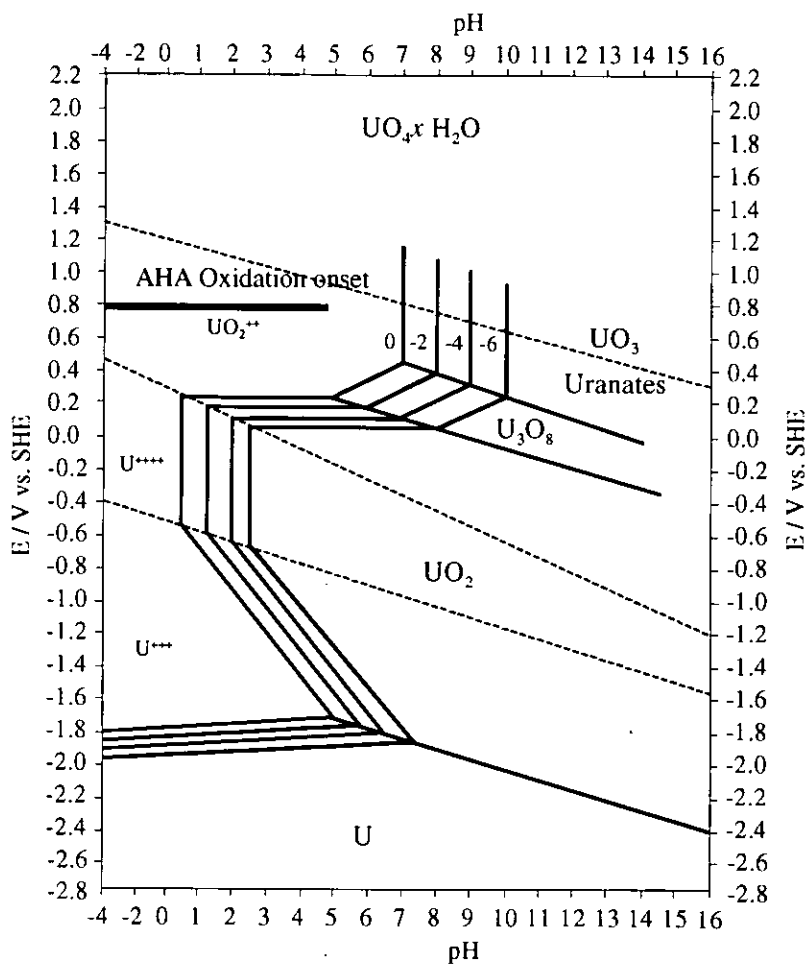


Figure 5.10.d: Pourbaix potential-pH diagram for the U-H₂O system at 298 K, for U³⁺ / U⁴⁺ solution activities of 0.1 mol m⁻³.

However an alternative is provided by the electrochemical control of the solution environment adjacent to the QCM electrode surface available within the EQCM configuration. Hence, if the electrode were poised at a potential cathodic of the onset potential for HA oxidation, any species capable of oxidising the HA would be itself be reduced by the biased electrode; the HA would therefore be protected from oxidation **Figure 5.11**.

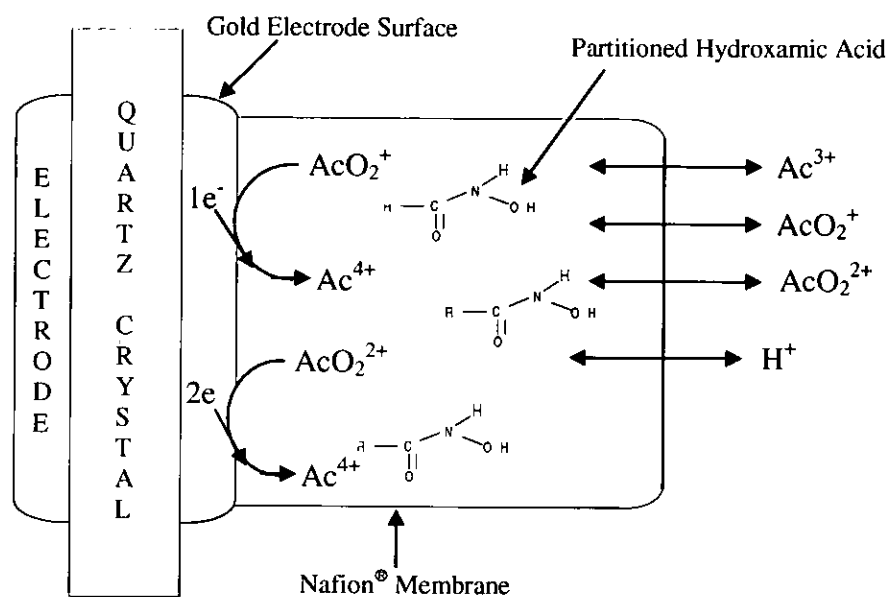


Figure 5.11: Representation of the Au piezoelectric electrode coated with a hydroxamic acid (whose simplified chemical structure is included) partitioned Nafion[®] polymer in contact with the nitric acid electrolyte. Analyte cations which may irreversibly oxidise the ligand, are reduced at the piezoelectrode surface to an oxidation state incapable of oxidising the ligand. In this way, the ligand is protected by the electrochemical conditioning of the polymer layer.

To this end a series of investigations were conducted to observe and develop control of the solution environment within the Nafion[®] / HA composite layer and adjacent to the EQCM electrode surface. Nafion[®] / HA composite layers were prepared on the surfaces of Au piezoelectrodes as described in Chapter 2. As stated in the same chapter, Section II.10, the presence of HA ligands within the Nafion[®] film was confirmed visually by placing the modified electrodes in a solution of $10 \text{ mol m}^{-3} \text{ Fe}(\text{NO}_3)_3$ for 1 min. Removal of the electrode and examination of the film for colour allowed the deep red colour characteristic of octahedral Fe (III) hydroxamate complexes to be observed. Using this method, it could be determined that three hydroxamate/Fe (III) complexes – those formed with AHA, GHA^+ and DFA^+ - exhibited film retention difficulties. Leaching of the complex from the film could be seen with the naked eye when the Nafion[®]/hydroxamate/Fe (III) composite was placed in

the background electrolyte solution ($100 \text{ mol m}^{-3} \text{ HNO}_3$) prior to voltammetric investigation. However, the DFA^+ showed the best retention within the Nafion[®] membrane of the three ligands and so was chosen for this series of preliminary investigations.

The CVs obtained from EQCM Nafion[®]/ DFA^+ /Fe (III) electrodes *Figures 5.12-5.19* are consistent with those reported by Arrigan *et al* for a GC GHA^+ /Nafion[®] composite electrode [5.28]. The reduction wave observed in the cathodic sweep of *Figure 5.12* at -0.70 V (vs. SCE) can be interpreted as being due to the reduction of DFA^+ -complexed Fe^{3+} within the membrane.

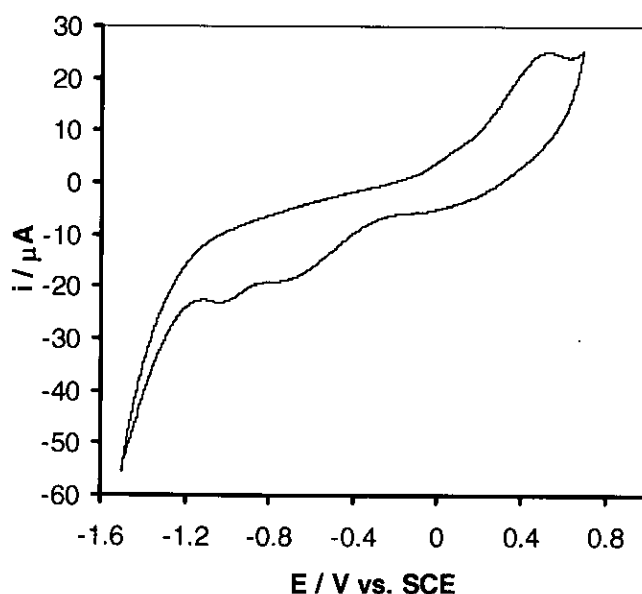
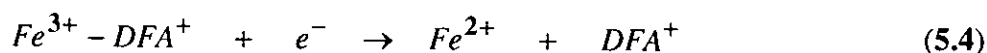


Figure 5.12: Cyclic voltammogram for a Nafion[®] coating partitioned with DFA and saturated with Fe^{3+} in 100 mol m^{-3} nitric acid pH1 using a 14mm Au(Cr) EQCM crystal at $v 80 \text{ mV/s}$.

Returning from the switching potential, the anodic scan shows an oxidation wave at $+0.55 \text{ V}$ (vs. SCE), which can be attributed to the oxidation of free Fe^{2+} within the Nafion[®] film. The peak potential of this latter feature is co-incident with that recorded for Fe^{2+} oxidation at DFA^+ -free, Nafion[®] coated electrodes *c.f. Figure 5.5.a*, indicating that the electrogenerated

Fe²⁺ is not complexed by the DFA⁺. The reduction peak of non-complexed Fe³⁺ to Fe²⁺, observed at ~+0.25 V (vs. SCE) within HA-free Nafion[®] membranes see *Figure 5.3* is not observed in *Figure 5.12*. This is strongly suggestive that the Fe³⁺ ion is complexed with the DFA⁺ ligand partitioned within the Nafion[®] composite layer, so preventing the reduction of non-complexed Fe³⁺ in this potential region. The absence of a reoxidation peak associated with a Fe(II)-DFA⁺ complex (generated by the electroreduction of the Fe(III)-DFA⁺ complex) in the range -1.20 to -0.90 V (vs. SCE) of *Figure 5.12* is indicative of complex dissociation upon reduction according to *Reaction 5.4*:



This in turn is strong evidence for the valence selectivity of DFA⁺ toward Fe³⁺ as opposed to Fe²⁺ ions and raises an interesting possibility. The mode of action of many QCM-based sensors for metal ions involves complexation of the metal ion with an ion-selective ionophore / ligand at the piezoelectrode surface. However, due to the (desirable) strength of interaction between the metal ion and the ionophore in the resultant metal-ligand complex at the QCM surface, it is then difficult to expel the metal ion from the transduction layer once analyte quantitation has taken place. Indeed, analyte retention in the sensing layer is often cited as being a major barrier to commercialisation of ion selective, thin polymer layer-based QCM sensors. Analyte expulsion is usually accomplished by eluting with excess solvent – however, if deployed to sense metal ions of interest to the Nuclear Industry, this elution would produce a large amount of contaminated waste solvent with all the waste management issues that that would entail. Given that HA ligands are complexation specific to iron in its 3+ oxidation state as Fe³⁺ ions and actinides in their 4+ oxidation state as Ac⁴⁺ ions, the results of *Figure 5.12* and *Equation 5.3* suggest that it should be possible to electrochemically expel the analytes, Fe³⁺ or Ac⁴⁺, from the layer once measurement has

taken place, simply by electrochemically reducing the complexed Fe and Ac ions to their 2+ and 3+ oxidation states respectively, whereupon decomplexation would occur and the reduced metal ions would simply diffuse out of the polymer layer and back out into solution.

The success of this electrochemical expulsion mechanism relies on our being able to control the speciation of the analyte metal ion throughout the polymer layer. Electrochemical control of analyte speciation within the composite polymer layer on the EQCM is also the basis of the method by which we propose to protect the HA ligands from irreversible oxidation by actinide cations such as Pu^{4+} , PuO_2^+ , PuO_2^{2+} , NpO_2^+ and NpO_2^{2+} within certain nuclear industrial environments. Thus, in order to investigate within our device the feasibility of electrochemical expulsion of the analyte and, by implication, control of the metal ion speciation throughout the DFA^+ / Nafion[®] composite layer, a study was conducted wherein the underlying Au piezoelectrode was held at a range of lengths of time at a potential where reduction of the Fe(III)-HA complex would be expected to take place.

The cyclic voltammetric results of this study are shown in *Figures 5.13-5.19*. As for the data of *Figure 5.12*, the Nafion[®]/ DFA^+ /Fe (III) composite electrode was prepared by pre-soaking a gold piezoelectrode-mounted Nafion[®] / HA composite layer, prepared as described in **Chapter 2**, in a 10 mol m^{-3} solution of $\text{Fe}(\text{NO}_3)_3$. Immediately before measurement, the resultant electrode was removed from the soaking solution, rinsed and placed in a solution of the background electrolyte. The Nafion[®]/ DFA^+ /Fe III composite electrode was initially cycled between potential limits of +0.70 to -1.50 V (vs. SCE) to confirm the presence of Fe species in the Nafion[®] membrane by observation of their oxidation and reduction waves *Figure 5.13.a*. The cycle was repeated *Figure 5.13.b* and the voltage was held at the switching potential of -1.50 V (vs. SCE) for 30s before embarking on the return sweep in order to allow the Fe(III) species within the membrane to be

electroreduced to Fe^{2+} and diffuse from the membrane coating. A third scan, identical to the first, was then conducted *Figure 5.13.c* in order to investigate the effects of diffusive depletion of the total iron concentration within the membrane. It was expected that current peak sizes should have diminished in the third scan with respect to the first scan due to this concentration change. This protocol was repeated on a series of electrodes freshly soaked in $\text{Fe}(\text{NO}_3)_3$, the period at which the electrode was held at the switching potential being increased sequentially from 30s to 10 min. Results are shown in *Figures 5.13-5.19*. Once the electrochemistry of the iron species was no longer detectable in the scan recorded directly after the potential had been held, the electrode was regenerated by soaking in $\text{Fe}(\text{NO}_3)_3$ solution and retested. Results are shown in *Figures 5.19.a-c*.

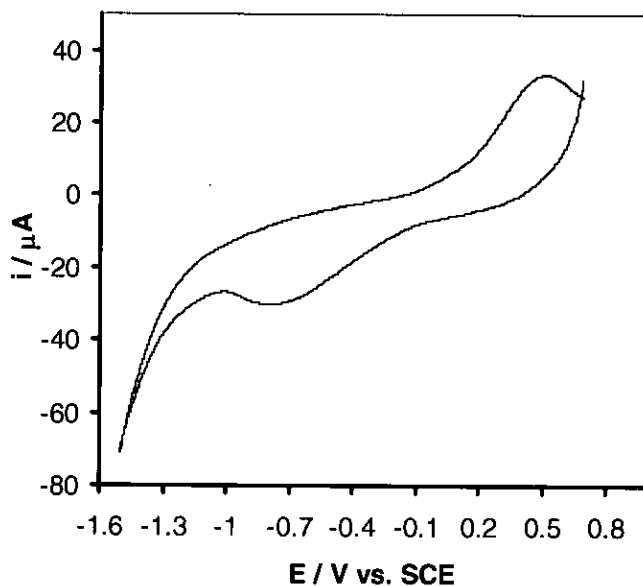


Figure 5.13.a: CV of a Nafion[®] coating partitioned with DFA⁺ and pre-saturated with Fe³⁺ recorded in 100 mol m⁻³ nitric acid pH1 using a 14mm Au(Cr) EQCM crystal at v 80 mV/s.

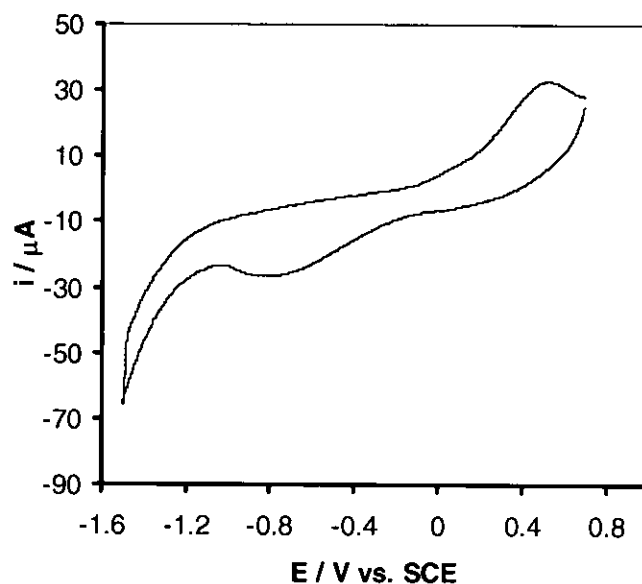


Figure 5.13.b: CV of a Nafion[®] coating partitioned with DFA⁺ and pre-saturated with Fe³⁺ recorded in 100 mol m⁻³ nitric acid pH1 using a 14mm Au(Cr) EQCM crystal at v 80 mV/s. The cycle was held at -1.50 V (vs. SCE) for 30s after the negative-going, forward scan to allow for the Fe²⁺ ion to diffuse from the membrane.

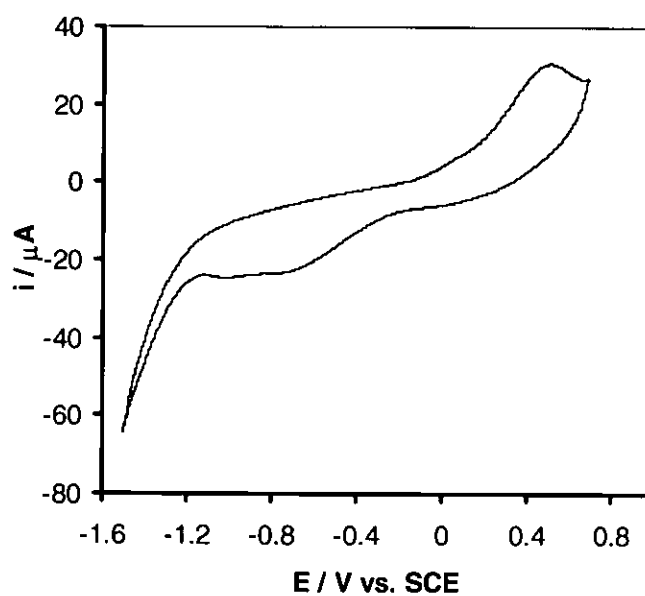


Figure 5.13.c: As Figure 5.13.a, immediately post-treatment shown in Figure 5.12.b.

Figures 5.14-5.17 & 5.18.a exhibit a general form similar to that of Figure 5.12 but with diminishing size of Fe(III)-DFA⁺ reduction peak and Fe²⁺ reoxidation peak with increasing

residence time at the switching potential. The CV of *Figure 5.18.b*, recorded directly after 5 minutes residence at the switching potential of -1.50 V (vs. SCE) is virtually featureless, indicating that; (i) nearly all of the iron has diffused out of the ligand-polymer composite layer on the time scale of the experiment; and consequently (ii) electrochemical control of the speciation of the analyte within the ligand-polymer layer is possible. The CV of *Figure 5.19.a* was recorded over a potential range of $+0.90$ to -1.50 V (vs. SCE). *Figure 5.19.b* was recorded over the same range, but was held at the cathodic switching potential, -1.50 V (vs. SCE) for 10min. On the return sweep, the Fe^{2+} oxidation peak usually observed at $+0.50$ V (vs. SCE) has disappeared suggesting that the Fe^{2+} ion has diffused out of the membrane. After regeneration of the Nafion[®]/DFA⁺/Fe(III) composite by submersion of the electrode in $10 \text{ mol m}^{-3} \text{ Fe}(\text{NO}_3)_3 / 5 \text{ mol m}^{-3}$ nitric acid for 1 min, a CV identical to that of *Figure 5.19.a* is obtained *Figure 5.19.c* indicating that the electrode can be recycled.

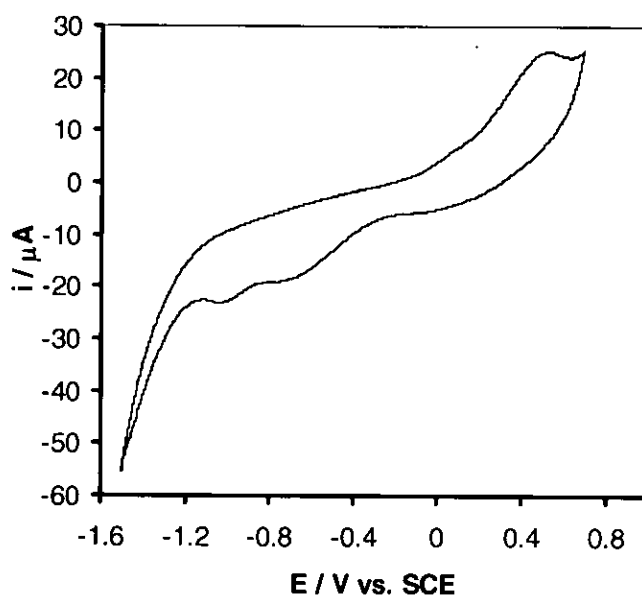


Figure 5.14.a: CV of a Nafion[®] coating partitioned with DFA⁺ and pre-saturated with Fe^{3+} recorded in 100 mol m^{-3} nitric acid pH1 using a 14mm Au(Cr) EQCM crystal at v 80 mV/s.

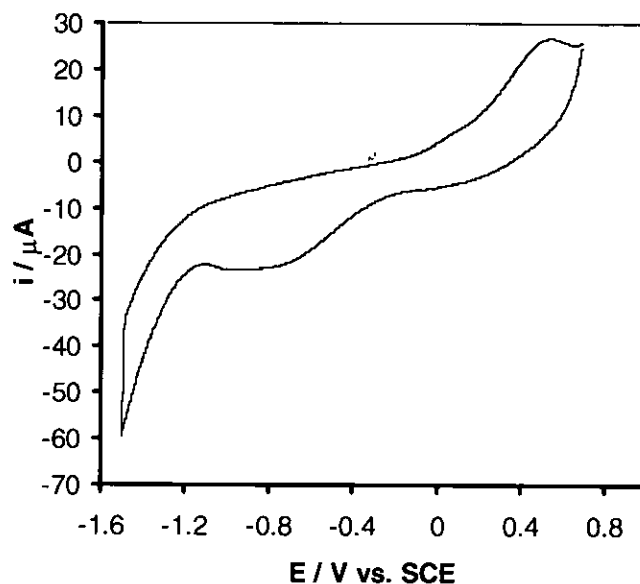


Figure 5.14.b: CV of a Nafion[®] coating partitioned with DFA⁺ and pre-saturated with Fe³⁺ recorded in 100 mol m⁻³ nitric acid pH1 using a 14mm Au(Cr) EQCM crystal at v 80 mV/s. The cycle was held at -1.50 V (vs. SCE) for 1 min after the negative-going, forward scan to allow for the Fe²⁺ ion to diffuse from the membrane.

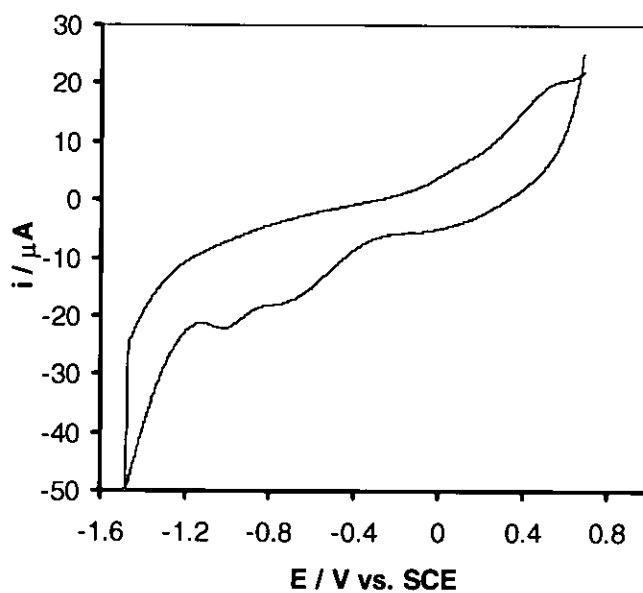


Figure 5.15.a: CV of a Nafion[®] coating partitioned with DFA⁺ and pre-saturated with Fe³⁺ recorded in 100 mol m⁻³ nitric acid pH1 using a 14mm Au(Cr) EQCM crystal at v 80 mV/s. The cycle was held at -1.50 V (vs. SCE) for 2 min after the negative-going, forward scan to allow for the Fe²⁺ ion to diffuse from the membrane.

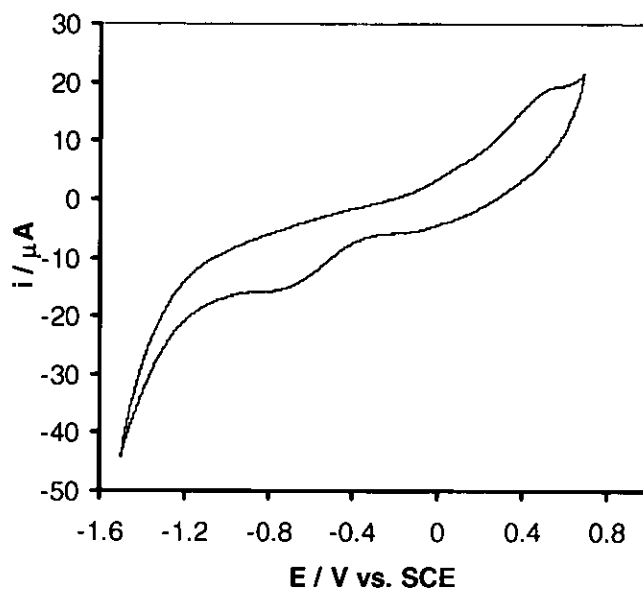


Figure 5.15.b: As Figure 5.14.a, immediately post-treatment shown in Figure 5.15.a.

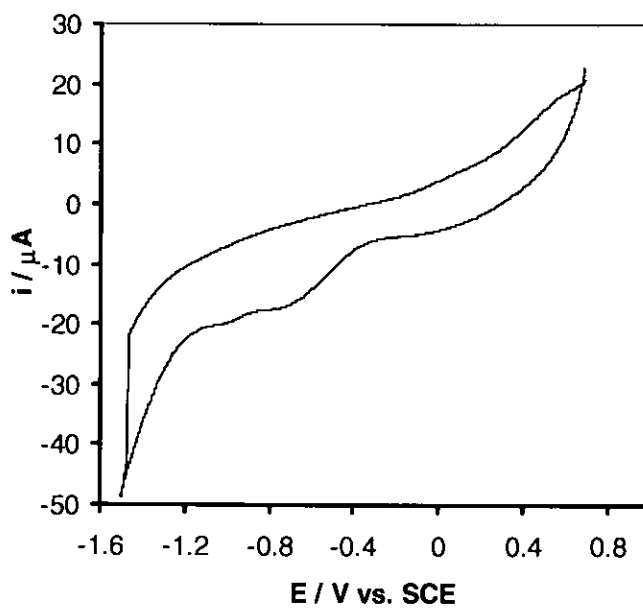


Figure 5.16.a: CV of a Nafion[®] coating partitioned with DFA⁺ and pre-saturated with Fe³⁺ recorded in 100 mol m⁻³ nitric acid pH1 using a 14mm Au(Cr) EQCM crystal at v 80 mV/s. The cycle was held at -1.50 V (vs. SCE) for 3 min after the negative-going, forward scan to allow for the Fe²⁺ ion to diffuse from the membrane.

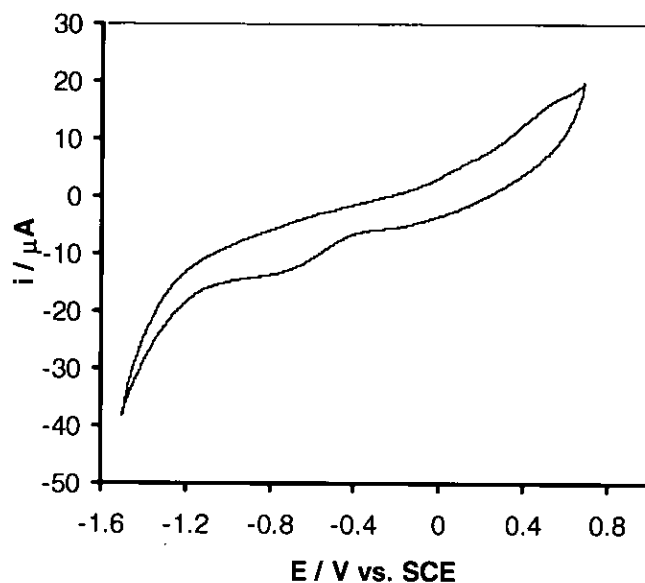


Figure 5.16.b: As Figure 5.14.a, immediately post-treatment shown in Figure 5.16.a.

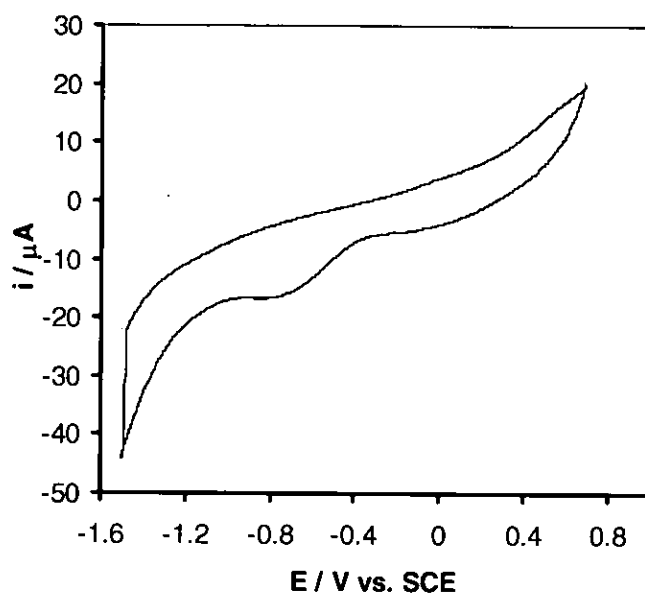


Figure 5.17.a: CV of a Nafion[®] coating partitioned with DFA⁺ and pre-saturated with Fe³⁺ recorded in 100 mol m⁻³ nitric acid pH1 using a 14mm Au(Cr) EQCM crystal at v 80 mV/s. The cycle was held at -1.50 V (vs. SCE) for 4 min after the negative-going, forward scan to allow for the Fe²⁺ ion to diffuse from the membrane.

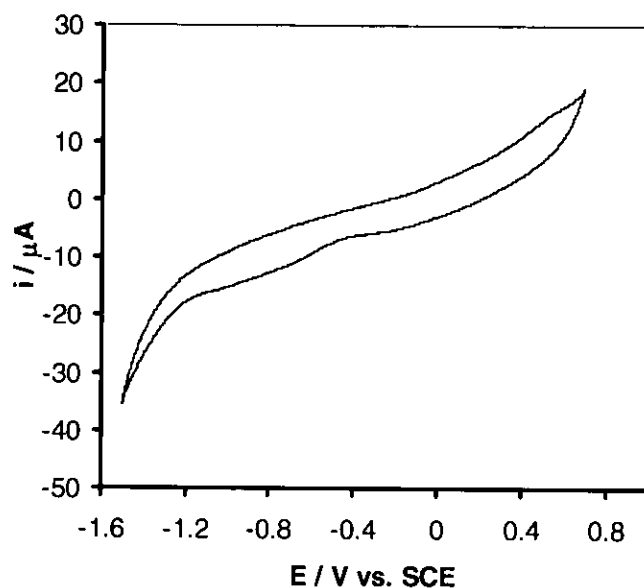


Figure 5.17.b: As Figure 5.14.a, immediately post-treatment shown in Figure 5.17.a.

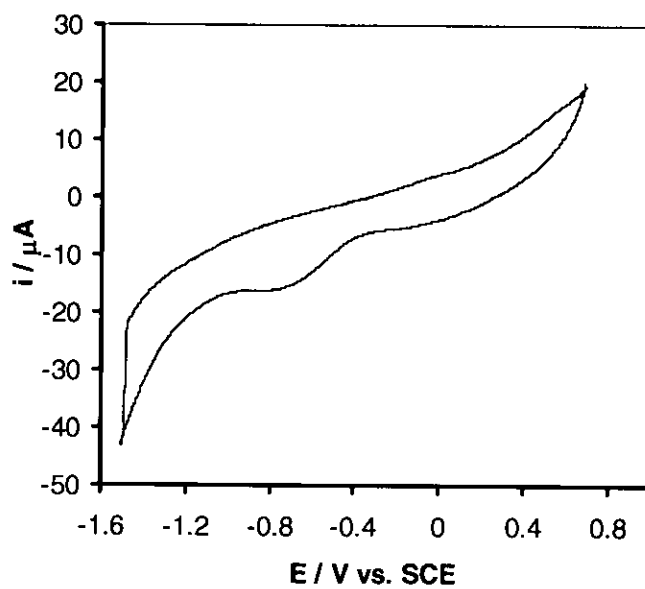


Figure 5.18.a: CV of a Nafion[®] coating partitioned with DFA⁺ and pre-saturated with Fe³⁺ recorded in 100 mol m⁻³ nitric acid pH1 using a 14mm Au(Cr) EQCM crystal at v 80 mV/s. The cycle was held at -1.50 V (vs. SCE) for 5 min after the negative-going, forward scan to allow for the Fe²⁺ ion to diffuse from the membrane.

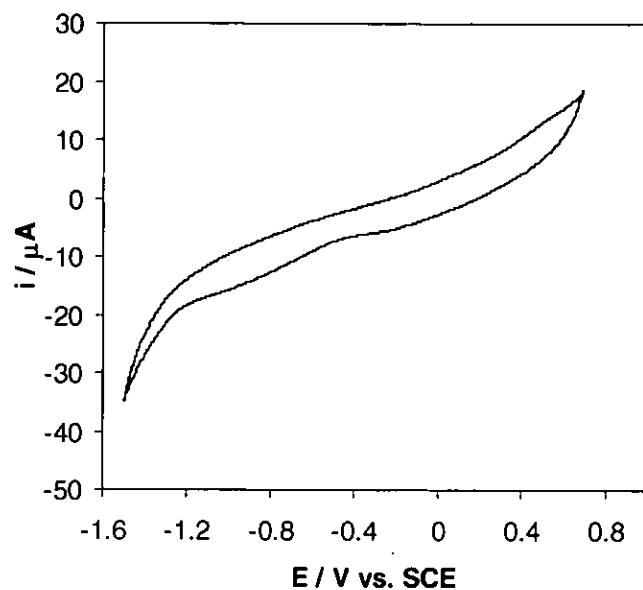


Figure 5.18.b: As Figure 5.14.a, immediately post-treatment shown in Figure 5.18.a.

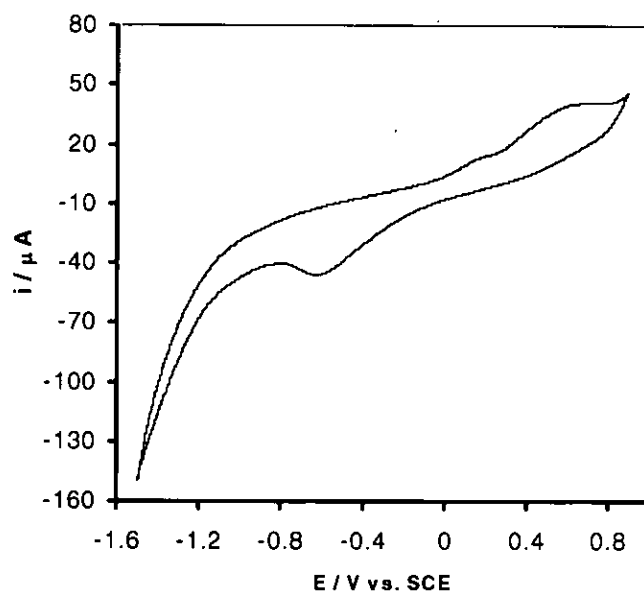


Figure 5.19.a: CV of a Nafion[®] coating partitioned with DFA⁺ and pre-saturated with Fe³⁺ recorded in 100 mol m⁻³ nitric acid pH1 using a 14mm Au(Cr) EOCM crystal at v 80 mV/s.

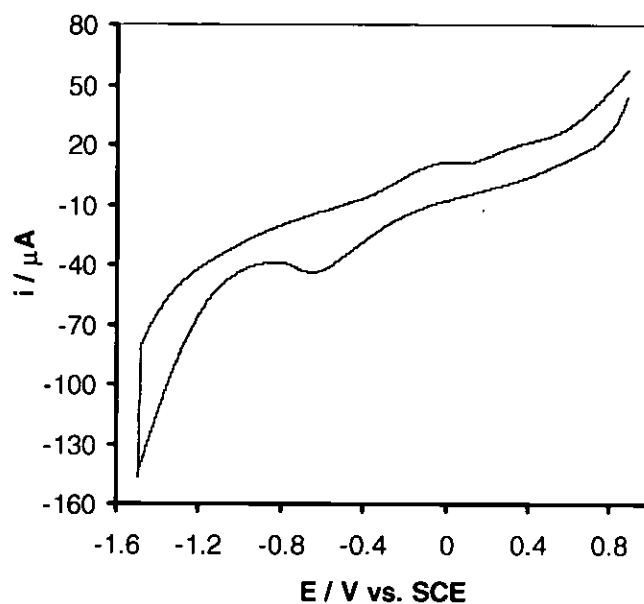


Figure 5.19.b: CV of a Nafion[®] coating partitioned with DFA⁺ and pre-saturated with Fe³⁺ recorded in 100 mol m⁻³ nitric acid pH1 using a 14mm Au(Cr) EOCM crystal at v 80 mV/s. The cycle was held at -1.50 V (vs. SCE) for 10 min after the negative-going, forward scan to allow for the Fe²⁺ ion to diffuse from the membrane.

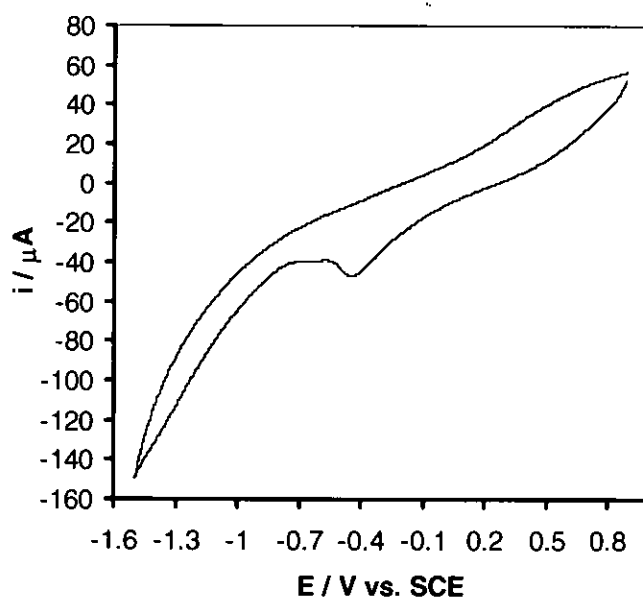


Figure 5.19.c: As Figure 5.19.a, recorded after the treatment shown in Figure 5.19.b, followed by electrode regeneration by soaking in 10 mol m⁻³ Fe(NO₃)₃ / 5 mol m⁻³ nitric acid for 1 min.

The reason the cyclic voltamassogram responses associated with *Figures 5.12-5.19* have been omitted is as follows. The Nafion[®] film thickness that was drop deposited onto the surface of the piezoelectrode varied from 5 to 20 μl . As was stated in the introduction to this chapter, the results of *Figures 5.12-5.19* were obtained using Nafion[®] layers prepared using drop sizes at the top end of this range. However, partitioning of the DFA⁺ ligand into the membrane followed by binding of the Fe³⁺ ions with their associated molecules of solvation leads to the quartz crystal crashing as described in **Chapter 1, Section I.4.3**. Reducing the amount of Nafion[®] drop coated onto the surface of the piezoelectrode leads to a smaller voltammetric response and a diminished gravimetric response that, at the moment, is beyond the resolution of the EQCM. Resolution of this problem will form a substantial part of the further work for this project.

V.3 - CONCLUSIONS

An EQCM study of Nafion[®] modified Au piezoelectrodes was conducted. The microelectrogravimetry of the Fe^{2+/3+} couple was studied at bare Au, Nafion[®] modified Au and Nafion[®] modified Au impregnated with DFA⁺ ionophore / ligand. These investigations were conducted in order to develop a better understanding of the electrochemical behaviour of Fe³⁺ / DFA⁺ / Nafion[®] composite membranes and their potential role as the transduction element of an EQCM-based sensor.

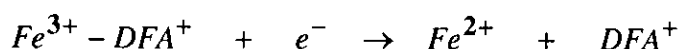
The results indicate that, in background electrolyte (nitric acid, pH 1 & 0), the electrochemistry of Nafion[®] layer partitioned Fe^{2+/3+} ions is consistent with thin layer cell behaviour with fast interfacial charge transfer and effective charge transport in the membrane coating. The polymer layer appears to increase in mass during reduction of Fe(III) to Fe(II) due to an influx of highly hydrated H⁺ ions necessary to maintain electroneutrality within the polymer.

That the current signals derived from the Fe^{2+/3+} redox processes in the polymer layer were not significantly displaced from the potential at which the same processes would occur in free solution was indicative of there being no specific interaction between the various sites within Nafion[®] and ferrous / ferric ions. Indeed, upon repetitive cycling, the iron content of the membrane gradually decreases. This is most readily observed by a gradual increase in the mass of the membrane as ferrous / ferric ions leach out and, in order to fulfil the electroneutrality requirement within the membrane, are replaced by highly solvated H⁺ ions. Microelectrogravimetry studies of Fe³⁺ solutions at pH 2 at bare and Nafion[®] modified Au piezoelectrodes indicate that electrogenerated Fe³⁺ (produced as a result of re-oxidation of electroreductively generated Fe²⁺) can precipitate at the surface of bare Au electrodes as iron

oxyhydroxides. Such a process is not observed during analogous experiments at Nafion[®] modified electrodes, most likely due to the lower pH generated within the polymer layer as a result of the influx of H⁺ ions discussed previously. Importantly in solutions of Fe(NO₃)₃, both the oxidation and reduction of Fe^{2+/3+} ions at bare and Nafion[®] modified electrode surfaces appear to be controlled by semi-infinite linear diffusion rather than displaying behaviour consistent with that of a thin layer cell.

For completeness a series of investigations were conducted to observe and develop control of the solution environment within the Nafion[®] / HA composite layer and adjacent to the piezoelectrode surface in a solution of 10 mol m⁻³ Fe(NO₃)₃. Results demonstrated while Fe³⁺ ions within the polymer layer are complexed by partitioned DFA⁺ ligands, Fe²⁺ is not. This was suggested by the fact that, while the reduction peak of non-complexed Fe³⁺ to Fe²⁺, within HA-free Nafion[®] membranes is not observed, the oxidation peak of non-complexed Fe²⁺ is seen.

The absence of a reoxidation peak associated with a Fe(II)-DFA⁺ complex (generated by the electroreduction of the Fe(III)-DFA⁺ complex) is indicative of complex dissociation upon reduction according to *Reaction 5.4*:



This in turn is strong evidence for the valence selectivity of DFA⁺ toward Fe³⁺ as opposed to Fe²⁺ ions and raises the possibility of electrochemically assisted expulsion of the analyte – in this case, the Fe³⁺ demonstrator ion. Repetitive potential cycling experiments show that complete expulsion is possible and that, upon exposure to a solution containing Fe³⁺ ions, the Fe(III)-DFA⁺ complex reduction current signal is regenerated. These results indicate that: (i) electrochemical control of the environment within the polymer layer is possible and

so, consequently, is protection of the HA ligand against analyte driven oxidation; and (ii) the sensor can be used repeatedly.

V.4 - REFERENCES

- 5.1 L.D. Whiteley and C.R. Martins. *Anal. Chem.* **59**, (1987), 1746
- 5.2 M.W. Espenchied, A.R. Ghatak-Roy, R.B. Moore III, R.M. Penner, M.N. Szentirmay and C.R. Charles. *J. Chem. Soc. Faraday Trans.* **82**, (1986), 1051
- 5.3 J. Ye and K. Doblhofer. *Ber. Bunsenges. Phys. Chem.* **92**, (1988), 1271
- 5.4 A. Kanazawa and J.G. Gordon. *Anal. Chem.* **57**, (1985), 1770
- 5.5 T. Nomura and O. Hattori. *Anal. Chim. Acta.* **115**, (1980), 323
- 5.6 D.A. Buttry, in: “*Electroanalytical Chemistry*”, A.J. Bard, (Ed.), Marcel Dekker, New York. **17**, (1990), 1
- 5.7 D.A. Buttry and M.D. Ward. *Chem. Rev.* **92**, (1992), 1355
- 5.8 T. Tjarnhage and M. Sharp. *Electrochimica Acta.* **39**, (1994), 623
- 5.9 Y.K. Agrawal and R.D. Roshania. *Bull. Soc. Chim. Belg.* **89**, (1980), 159
- 5.10 K.N. Raymond and T.P. Tufano, in: “*The Biological Chemistry of Iron*”, H.B. Dunford, D. Dolphin, K.N. Raymond and L. Sleiker, (Eds.), D. Reidel Publishing Co, Dordrecht Holland. (1982), 85
- 5.11 D.A. Buttry and F.C. Anson. *J. Electroanal. Chem.* **130**, (1981), 333
- 5.12 J. Langmaier, A. Trojanek, I. Weber and Z. Samec. *J. Electroanal. Chem.* **469**, (1999), 11
- 5.13 Z. Lu and S. Dong. *J. Electroanal. Chem.* **233**, (1987), 19
- 5.14 C.P. Andrieux, P. Audebert, B. Divisia-Blohorn, P. Aldebert and F. Michalak. *J. Electroanal. Chem.* **296**, (1990), 117
- 5.15 E. Juzeliunas and K. Juttner. *Electrochimica Acta.* **43**, (1998), 1691
- 5.16 B. Belqat, A. Laghzizil, K. Elkacimi, A. Bouhaouss and S. Belcadi. *J. Fluor. Chem.* **105**, (2000), 1

-
- 5.17 M. Shi and F.C. Anson. *J. Electroanal. Chem.* **425**, (1997), 117
- 5.18 H. Braun, W. Storck and K. Doblhofer. *J. Electrochem. Soc.* **130**, (1986), 93
- 5.19 M. Shin, E-Y. Kim, J. Kwak and I.C. Jeon. *J. Electroanal. Chem.* **394**, (1995), 87
- 5.20 C. Gavach, G. Pamboutzoglou, N. Nedyalkov and G. Poucelly. *J. Membr. Sci.* **45**, (1989), 37
- 5.21 G. Poucelly, A. Lindheimer, G. Pamboutzoglou and C. Gavach. *J. Electroanal. Chem.* **259**, (1989), 113
- 5.22 S. Bruckestein and A.R. Hillman. *J. Phys. Chem.* **92**, (1988), 4837
- 5.23 C. Boxall, G. Kelsall and Z. Zhang. *J. Chem. Soc. Faraday Trans.* **92**, (1996), 791
- 5.24 M.A. Blesa and E. Matijevic. *Advances in Colloid & Interface Science.* **29**, 1989, 173
- 5.25 J.A. Amberson. *Ph.D. Thesis*, Queens University Belfast. (1987)
- 5.26 J.A. Amberson and G.H. Svehla. *Anal. Pro.* **23**, (1986), 443
- 5.27 M.A. Santos, M.A. Esteves, M. Candida, T. Vaz and M.L.S.S. Goncalves. *J. Chem. Soc. Dalton Trans.* (1993), 927
- 5.28 D.W.M. Arrigan, B. Deasy, J.D. Glennon, B. Johnston and G. Svehla. *Analyst.* **118**, (1993), 355
- 5.29 M.T. McDermott, C.A. McDermott and R.L. McCreery. *Anal. Chem.* **65**, (1993), 937
- 5.30 M. Poubaix in: "*Atlas of Electrochemical Equilibria in Aqueous Solutions*". 2nd Ed. Nat. Assoc. Corro. Eng. Houston Texas USA. (1974), 208

**CHAPTER VI - ELECTROCHEMICAL AND
MICROELECTROGRAVIMETRIC STUDIES OF
METHYLENE BLUE**

CONTENT

<u>VI.1 - INTRODUCTION</u>	<i>Page 248</i>
<u>VI.2 - THE ELECTROCHEMICAL BEHAVIOUR OF METHYLENE BLUE AT GOLD MICRODISC ELECTRODES</u>	<i>Page 251</i>
<u>VI.3 - MICROELECTROGRAVIMETRIC BEHAVIOUR OF METHYLENE BLUE</u>	<i>Page 259</i>
<u>VI.4 - CONCLUSIONS</u>	<i>Page 273</i>
<u>VI.5 - REFERENCES</u>	<i>Page 276</i>

VI.1 - INTRODUCTION

As discussed in **Chapter 1** and **Chapter 5**, electrochemical conditioning of the oxidation state of the actinide metal ions under analysis is a key feature of the mechanism by which our proposed sensor will eventually function. This conditioning occurs for two reasons:

- (i) to convert the actinide (Ac) ions into an oxidation state that exhibits a high complexation constant with HA – specifically the Ac^{4+} ion; and
- (ii) to protect the HA ionophore against irreversible oxidation by Pu^{4+} , PuO_2^+ , PuO_2^{2+} , NpO_2^+ and NpO_2^{2+} ions. By poisoning the electrode at a potential cathodic of the onset potential for HA oxidation, any species capable of oxidising the HA would be itself be reduced by the biased electrode; the HA is then protected from oxidation. In practise, this involves reduction of the actinide cations into their Ac^{3+} or Ac^{4+} state.

Apart from the $\text{Pu}^{4+} \rightarrow \text{Pu}^{3+}$ conversion, all of the other actinide reductions of interest to us involve the breaking of metal-oxygen bonds and so will exhibit some degree of electrochemical irreversibility. This is certainly the case for the reduction of UO_2^{2+} to U^{4+} on gold electrodes at pH 0. According to thermodynamics, the E^0 value for this process is +0.03 V (vs. SCE) see **Figure 5.10.d**. In contrast to this, U(VI) reduction to U(IV) on glassy carbon at pH 0 exhibits a half wave potential at +0.026 V (vs. SCE) [6.1] while in-house measurements indicate $E_{1/2} = -0.20$ V (vs. SCE) under the same conditions on gold. Thus, as we were restricted to using Au piezoelectrodes, and in order to avoid problems derived from the irreversibility of (some) actinide reductions on Au, we elected to explore the potential role of redox mediators in achieving our target actinide reduction reactions. A mediator for actinide reduction within the Nafion[®] polymer layer would necessarily have to be retained within that layer during operation of

the sensor, a problem that has been the subject of a substantial research effort in the field of enzyme-modified electrode based biosensors.

As opposed to the transducing film being comprised of ligand, mediator and polymer as in our device, the film material of enzyme electrocatalysis based sensors is typically comprised of the enzyme, a redox mediator and the supporting polymer matrix. Electropolymerised semiconducting film materials that have been widely studied as support matrices for biosensor applications include those derived from monomers such as pyrrole, thiophene and aniline [e.g. 6.2, 6.3, 6.4, 6.5 & 6.6 and references therein].

Recently, in order to combine the functions served by the mediator and polymer support, attention has focused on the preparation of semiconductor films from monomers that are themselves redox mediators. Thus, polymer film-modified sensing electrodes have been prepared by the electropolymerisation of, *inter alia*, viologen, phenoxazine and phenothiazine derivatives [again, see 6.2 to 6.6 and references therein].

Methylene blue (MB) is a phenothiazine dye that behaves as an efficient two electron transfer mediator in electrochemical systems [6.7 & 6.8] and as such, has attracted attention as a potential mediator in enzyme electrode based biosensors [6.9]. Recently, MB was found to form conductive and electrocatalytically active polymer films on both graphite [6.2] and gold [6.6] electrodes when polymerised electrochemically under anodic conditions. The polymer films retained monomer-type redox activity and were shown to electrocatalyse the oxidation of nicotinamide adenine dinucleotide hydrogenase (NADH), so finding utility in reagentless amperometric dehydrogenase based electrochemical sensors [6.3 & 6.6]. Methylene blue is especially attractive for acting as a mediator for actinide reduction in Nafion[®] films as:-

- (i) it has an E^0 at pH 0 of +0.19 V (vs. SCE) [6.10] and so in its reduced state is thermodynamically capable of reducing Pu species to Pu³⁺, U species to U⁴⁺ and Np species to Np⁴⁺ at pH 0 (c.f *Figures 5.10* in Chapter 5); and

- (ii) it is known to be strongly retained in Nafion[®], so obviating any problems associated with mediator dissolution upon deployment of the sensor [6.11].

However, before being deployed as a mediator in a Nafion[®]-modified microelectrogravimetric sensor, the behaviour of methylene blue at unmodified Au piezoelectrodes must be characterised.

The electrochemistry of MB has been studied using an extensive range of electrode techniques and materials including Hg [6.12, 6.13 & 6.14], Pt [6.15], carbon [6.16] and Au [6.11 & 6.17], as well as electrodes that have been modified with Nafion [6.18, 6.19 & 6.20] and sulphur [6.21, 6.22, 6.23, 6.24, 6.25 & 6.26]. However, comparatively few reports have appeared concerned with the behaviour of MB at microelectrodes [6.27, 6.28 & 6.29] or on the EQCM [6.30 & 6.31]. As many enzyme-based sensors are developed as "micro-miniaturised" devices, a microelectrode study of MB was viewed within these laboratories as being particularly apposite. Such a study was conducted by Pennarun [6.32] and Xiao [6.10] and their results are summarised in the next section.

Kertész *et al* have used the EQCM to study the formation and redox transformations of poly-MB at gold electrode surfaces [6.30], while Hepel and Janusz have used voltamassogram measurements to study the reductive growth and reoxidation of LMB films at sulphur-modified gold electrodes at an indeterminate pH [6.31]. However, neither report describes the use of the EQCM in the investigation of the electroreduction of MB at bare Au electrodes in buffered solutions. Thus, in keeping with our requirement for characterising the behaviour of MB at unmodified piezoelectrodes, the final two sections of this chapter will be concerned with microelectrogravimetric studies on methylene blue on bare gold and the conclusions that can be drawn from them.

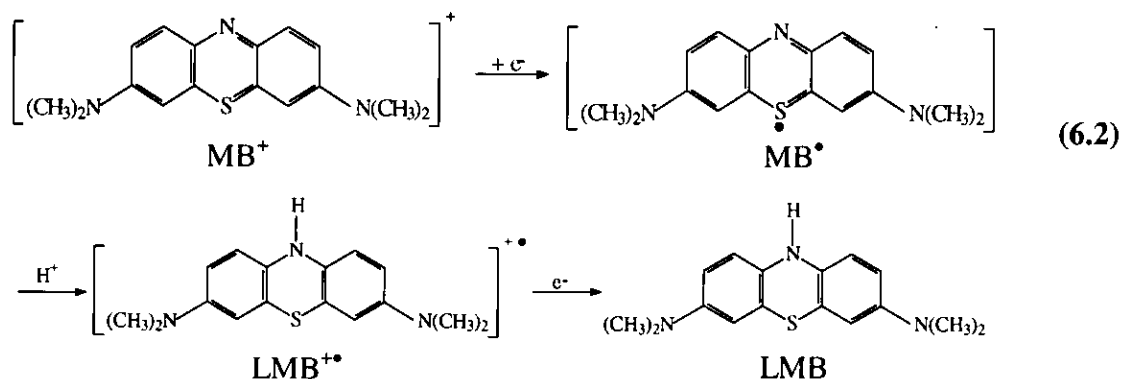
VI.2 - THE ELECTROCHEMICAL BEHAVIOUR OF METHYLENE BLUE AT GOLD

MICRODISC ELECTRODES

Reactions 6.1.a-c show what is believed to be the sequence of reactions during the electrochemical reduction of MB to LMB [6.11 to 6.17 & 6.27].



Structurally, the reaction of MB to produce LMB can be represented as follows.



The protonation reaction has been observed to be very fast or virtually complete in near neutral or acidic medium and so the ECE process appears as EE over a wide range of scan rates [6.33]. As the overall electrode process has been considered to be a reversible reaction on many electrode materials, very few kinetic parameters have been reported. Using fast cyclic voltammetry on 10 μm Hg microelectrodes, Chen *et al* [6.28] have reported a surface reaction rate constant, k_s , for the $2e^-$ reduction of MB of $5.4 \times 10^5 \text{ s}^{-1}$. Using the treatment of Brown and Anson which, by applying Marcus's theory, relates k_s and the *standard heterogeneous reaction rate constant* for electron transfer, k^0 [6.34], a value of k^0 of $9 \times 10^{-6} \text{ m s}^{-1}$ may be obtained for the $2e^-$ reduction of MB. Oldham *et al*

[6.35] found that processes at microelectrodes may be described in terms of a dimensionless parameter κ^0 :

$$\kappa^0 = \frac{\pi k^0 r}{4D_0} \quad (6.2)$$

where D_0 is the *diffusion coefficient* of the electroreactant ($\text{m}^2 \text{s}^{-1}$) and r is the *radius* of a disc microelectrode (m). The reversibility of a process at a microelectrode can then be described according to the following classification:

$\kappa^0 > 40$:	effectively reversible
$0.2 \leq \kappa^0 \leq 20$:	effectively quasi-reversible
$\kappa^0 < 0.1$:	effectively irreversible

Experiments in the quasi-reversible regime are the most advantageous for kinetic studies. For $k^0 = 9 \times 10^{-6} \text{ m s}^{-1}$ and $D_0 \approx 10^{-9} \text{ m}^2 \text{ s}^{-1}$, one needs to use a disc microelectrode with a radius in the range 0.03 to 3 mm to attain quasi-reversibility. Therefore, microelectrode voltammetry of MB using disc electrodes with a radius of < 1 mm at more moderate sweep rates than those used by Chen *et al* [6.28] may provide previously unavailable kinetic and mechanistic information about the ECE reduction of MB.

The most recently published study of the behaviour of MB at microelectrodes employed carbon fibre microcylinder electrode [6.29]. However, the surface properties of carbon electrodes are not thoroughly understood due to the variety of procedures used to prepare these electrodes and the large number of variables at the surface [6.36].

It was against this background that Pennarun and Xiao [6.10 & 6.32] studied the electrochemistry of MB at Au microelectrodes. Further, in order to decrease the rate of the protonation reaction in order to study the chemical step of the overall ECE process of *Reaction 6.1.a-c*, they conducted their studies at low H^+ concentrations, specifically pH 7.9. Pennarun and Xiao findings are as follows.

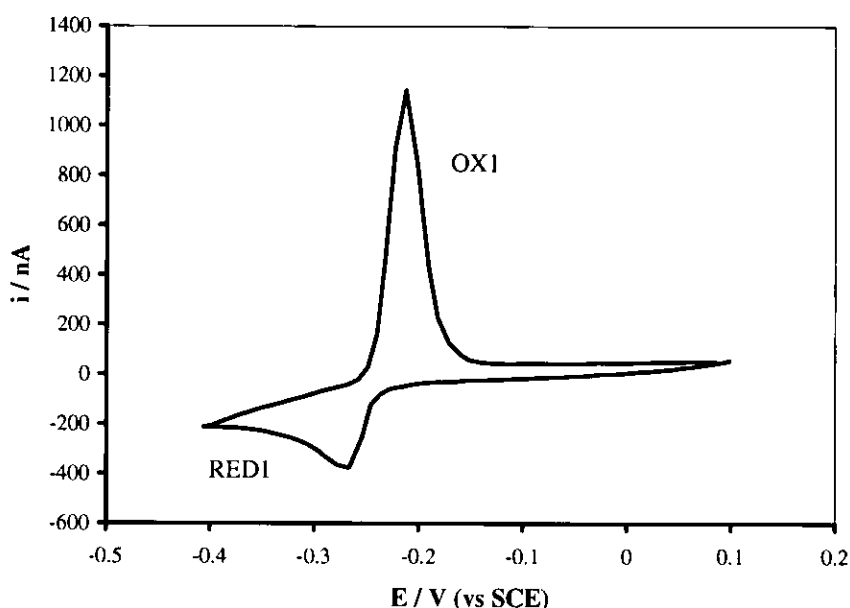


Figure 6.1: CV of MB on a 250 μm Au microdisc electrode $1 \text{ mol m}^{-3} \text{ MB}^+$, Phosphate buffer pH=7.9, scan rate $v 100 \text{ mVs}^{-1}$.

The electrochemistry of MB on Au microdisc electrodes at pH 7.9 exhibits two modes of behaviour that depend critically upon the state of MB adsorption at the electrode surface and the time spent at potentials negative of the MB reduction potential.

The first mode of behaviour, which is most readily seen by cycling between the potential limits of +0.10 and $-0.40 \text{ V (vs. SCE)}$ at a freshly cleaned electrode, is shown in **Figure 6.1**. A reduction peak, peak RED1, appears at $-0.27 \text{ V (vs. SCE)}$ while a sharp reoxidation peak, peak OX1, appears at $-0.22 \text{ V (vs. SCE)}$. The latter has the appearance of a metal film stripping peak. Importantly, the voltammogram may be reproduced time and again during repetitive cycling without recourse to mechanical cycling.

Pennarun and Xiao analysis of RED1 and OX1 reveals that $E_p(\text{RED1})$ and $E_p(\text{OX1})$ are independent of sweep rate over $v = 0.001$ to 0.5 V s^{-1} and may therefore be considered reversible over that range of sweep rates. The form of the cyclic voltammogram for an electrochemically reversible metal deposition / stripping process has been analysed by Berzins and Delahay [6.37], White and Lawson [6.38] and Schiffrin [6.39]. Pennarun

and Xiao have adapted this approach for the involvement of H^+ and a possible dimeric precursor of MB to LMB and obtained the following expressions involving the peak current, i_p , peak potential and the half peak potential, $E_{p/2}$ [6.10 & 6.32]

$$|E_p - E_{p/2}| = 0.7876 \left(\frac{mRT}{nF} \right) = 20.23 \frac{m}{n} \text{ mV at 298 K} \quad (6.1)$$

$$i_p = 0.6105 \frac{n}{m} FA [MB] \left(\frac{nF}{mRT} \right)^{1/2} D_{MB}^{1/2} v^{1/2} \quad (6.2)$$

$$i^2 = \left(\frac{n}{m} FA [MB] \left(\frac{nF}{mRT} \right) D_{MB}^{1/2} v^{1/2} \frac{2}{\pi^{1/2}} \right)^2 (E_r - E) \quad \text{for } E_p < E < E_r \quad (6.3)$$

where n is the number of electrons of a reacting species and m the molar mass.

$$E_r = E^0 + \frac{RT}{nF} \ln [MB]^m [H^+] \quad (6.4)$$

Use of Equation 6.1 in the analysis of peak RED1 of **Figure 6.1** gives an n/m value of 1.49 ± 0.09 , indicating that each molecule of MB requires 1.5 electrons for reduction at $E = -0.25 \text{ V (vs. SCE)}$ [6.10 & 6.32].

In keeping with data obtained by Clavilier *et al* on Au and Pt macroelectrodes [6.11 & 6.15], this result is strongly suggestive of the reduction product being a quasi-metallic, electronically conducting, mixed valence salt of the radical cation $LMB^{+\bullet}$ and the expected product LMB. Clavilier *et al* provided little in terms of numerical analysis of the reduction peak associated with the formation of this salt due to the instability of the phase on macroscopic electrodes. The overall process of the salt formation may be represented as:



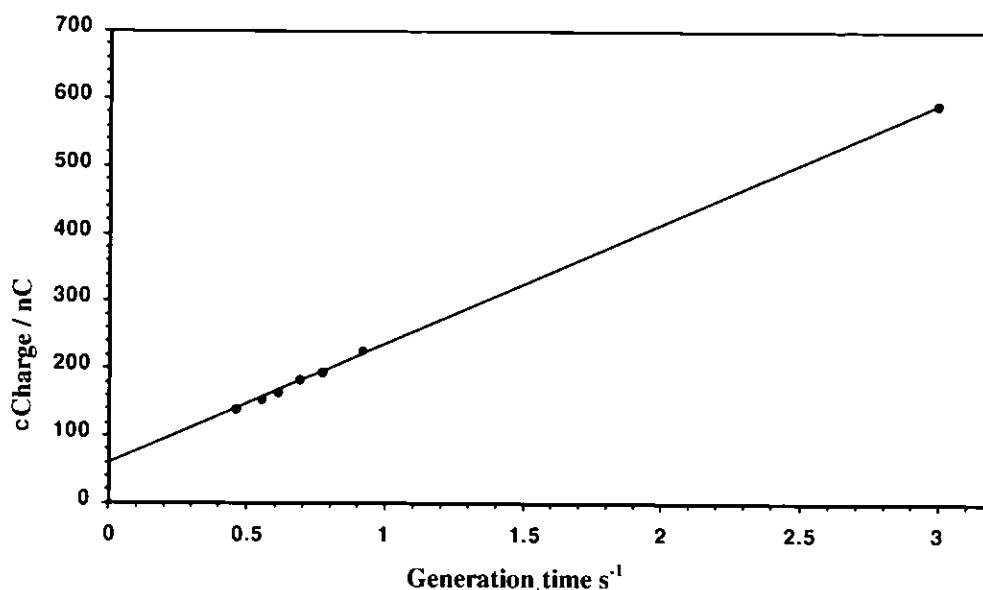


Figure 6.2: Reoxidation charge of OX1 versus generation time.

Pennarun and Xiao analysis of *Figure 6.1* in accordance with *Equation 6.3* gives an n/m of 1.40 from the slope of a typical plot of i^2 vs. E in the potential range $E_p < E < E_r$ of peak RED1 [6.10 & 6.32]. Using similar data obtained from the same gold disc microelectrode at a range of sweep rates faster than 0.14 V s^{-1} , an average value of n/m of 1.51 ± 0.05 was obtained, which is in excellent agreement with the value obtained from the peak potential data [6.10 & 6.32].

Inspection of peak OX1 indicates that its current drops rapidly to zero after rising to its maximum value, a characteristic of the dissolution of metallic films [6.40]. Pennarun and Xiao observed from *Figure 6.2*, that the integrated charge beneath OX1 it is found to be linearly proportional to t_G , the generation time, which is simply the amount of time the applied potential is negative of E_r (see *Equation 6.4*) during the forward and reverse sweeps of the potential cycle [6.10 & 6.32]. Further, $E_{p,a}$ is independent of t_G and thus, by implication, layer thickness supporting the idea that a quasi-metallic phase with electronic conductivity has been formed during the reaction corresponding to RED1 [6.10 & 6.32].

The integrated charge that is under the oxidation peak OX1 is found to equal to that under the reduction peak RED1. The area occupied by a molecule of MB at the electrode surface depends upon its orientation. Values of 0.55 nm^2 and $1.25\text{-}1.3 \text{ nm}^2$ have been cited for molecules orientated perpendicular and parallel to the surface respectively [6.13, 6.14 & 6.31]. Using the value of $n = n/m = 1.5$ derived above, and depending upon the molecular orientation, the total charge passed during either the reduction or reoxidation reaction corresponds to some 30-60 layers of MB.

Extending the cathodic limit of the potential sweep to -0.90 V (vs. SCE) leads to a time-dependent response at gold microelectrodes, as shown in *Figures 6.3.a-c*. The first point to note is the presence of a broad cathodic peaks between -0.40 and -0.80 V (vs. SCE), peak RED2. Upon repetitive cycling between potential limits of -0.90 and 0.10 V (vs. SCE), OX1 gradually diminishes in size, to be replaced with a second anodic peak, OX2, for which $E_{p,a} = -0.14 \text{ V}$ (vs. SCE). Interestingly, if the sweep rate is sufficiently slow, a voltammogram of the form of *Figure 6.3.c* is obtained first sweep illustrating the time dependence of this process [6.32].

After reaching a maximum value, the current of OX2 decays proportionally to $t^{1/2}$, suggesting that the electrooxidation is diffusion controlled [6.32]. In a similar experiment on gold macroscopic electrodes, Clavilier *et al* [6.11] noted that the current was not affected by stirring the solution during the anodic scan but did depend upon the type and concentration of the anions present. This suggests that the mass transport is confined to within a solid, electrically non-conducting layer over the electrode surface.

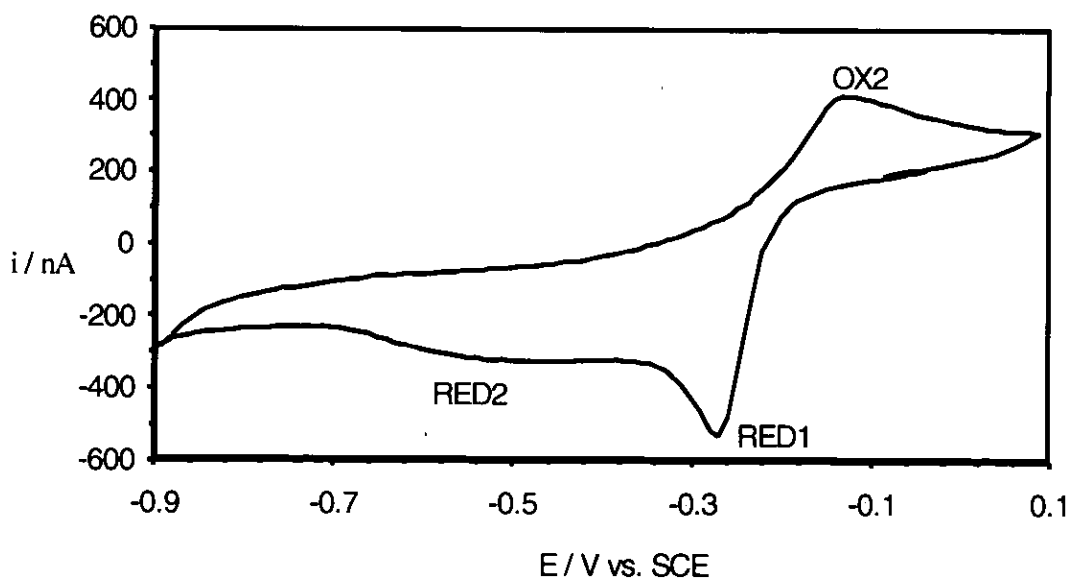
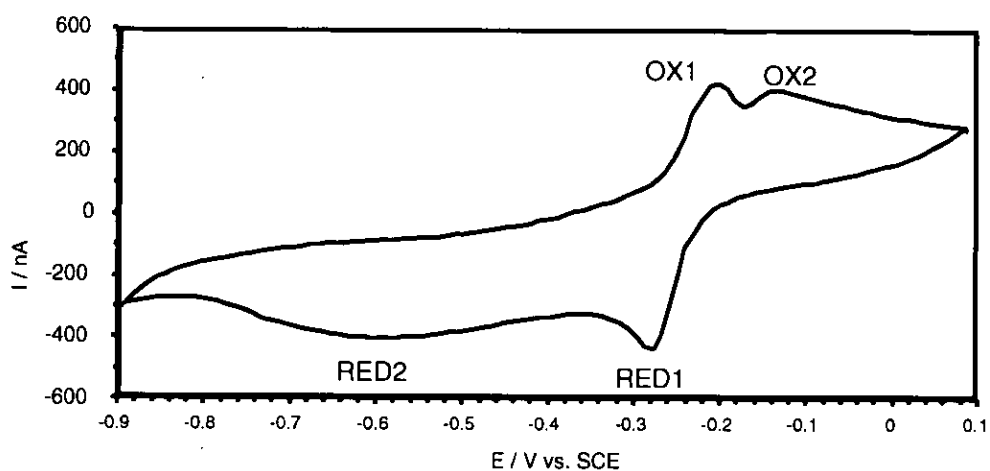
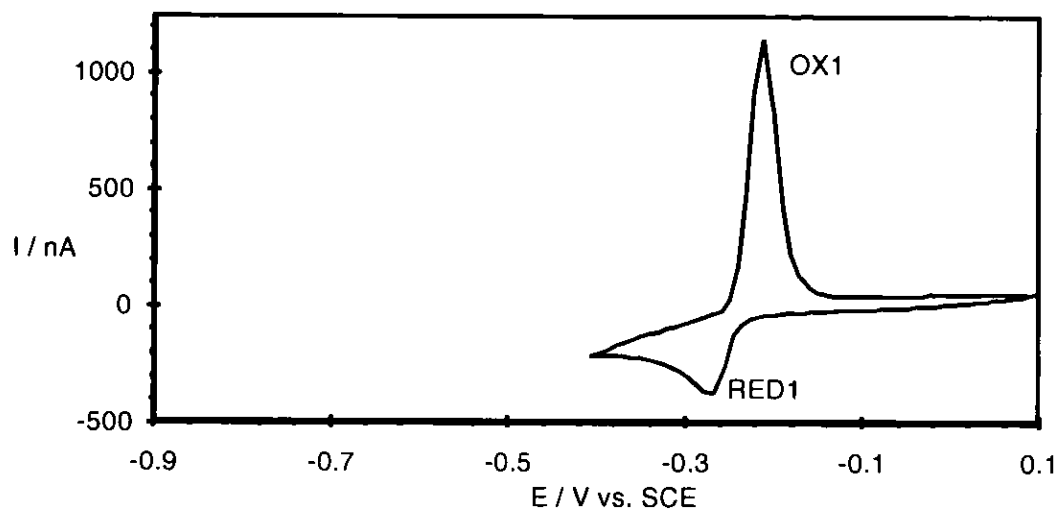


Figure 6.3.a-c: CVs of MB on a 125 μm Au microdisc electrode $1 \text{ mol m}^{-3} \text{ MB}^+$, Phosphate buffer pH=7.9, scan rate 100 mV.s^{-1} . Note that the negative potential limit has been extended in (b) & (c). Also note that, while (b) and (c) form part of a single uninterrupted, repetitive cycling experiment on the same microdisc, several cycles were performed between (b) and (c).

Corn *et al* [6.17] have used polarisation modulated-FTir (PM-FTir) spectroscopy to investigate the composition of the MB reduction product formed as a surface layer on polycrystalline gold by holding the electrode at -0.50 V (*vs.* SCE) at pH 7.9 for 3-20 minutes and found it to be LMB. From Corn *et al* [6.17], Clavilier *et al* [6.11] and their own results [6.10 & 6.32], Pennarun and Xiao conclude that RED2 corresponds to the $\text{LMB} \rightarrow \text{MB}^+$ stripping peak and that OX2 must therefore be a result of the solid state reduction of the $\text{LMB/LMB}^{+\bullet}$ mixed valence salt to generate LMB. Such a reduction would be expected to be accompanied by a change in the crystal phase of the surface layer and therefore be electrochemically irreversible; this conclusion is borne out by the broadness of RED2 and its displacement to more cathodic potentials with increasing v .

The time evolution of the relative intensities of the OX1 and OX2 peaks may be explained as follows. OX1 is present during the first cycle over the extended potential limits of *Figure 6.3.b*, but gradually diminishes in size with each subsequent cycle until it is no longer distinguishable from OX2, as seen in *Figure 6.3.c* [6.32]. The non-completion of the reductive transformation of the surface layer observed during the early cycles is a function of the slowness of the solid state reaction associated with RED2 and the comparatively high sweep rates that may be employed with microelectrodes during this work. With each subsequent sweep, the solid state transformation appears to get faster until, as in *Figure 6.3.b*, it has gone to completion within the time scale of the experiment and no trace of $\text{LMB/LMB}^{+\bullet}$ is seen on the anodic return sweep.

Having summarised the observations made by Pennarun and Xiao from microelectrode experiments on the MB system at pH 7.9, let us now proceed to discuss the microelectrogravimetric behaviour of the MB system under similar conditions and so address why the reduction of $\text{LMB/LMB}^{+\bullet}$ to LMB appears to occur with increasing facility with each sweep in *Figures 6.3.a-c*.

VI.3 - MICROELECTROGRAVIMETRIC BEHAVIOUR OF METHYLENE BLUE

The methylene blue cation has long been known to adsorb at both inorganic and biological aqueous interfaces [see *e.g.* 6.11-6.17]. As a result of this adsorption, many workers studying the electrochemistry of methylene blue have developed robust cleaning procedures to enable them to examine the behaviour of MB on virgin electrode surfaces [*e.g.* 6.11, 6.15 & 6.17]. For example, in their study of the electrochemistry of MB on macroscopic gold electrodes, Zutic, Clavilier *et al* clean the electrode surface by melting the component metal in a flame [6.11, 6.41 & 6.42].

Such a cleaning procedure would be detrimental to piezoelectric state of the quartz crystal. Therefore with all gold piezoelectrode experiments, a fresh crystal was used for each investigation. Pretreatment to obtain a clean surface is described in the experimental section **Chapter 2**. Flame cleaning of the microelectrodes used in the experiments summarised in **Section VI.2** was also impossible due to failure of the electrode-insulator seal derived from the differential thermal expansions of gold and borosilicate glass. Thus, an analogous cleaning procedure to that employed for the piezoelectrodes, combined with a rigorous mechanical polishing regimen, was used for the microelectrodes.

For the purposes of these experiments, the initial state of both types of electrode is taken to be that described by the voltammogram of *Figure 6.1* over the appropriate potential limits (+0.10 to -0.40 V (*vs.* SCE) for microelectrodes, +0.10 to -0.40 V (*vs.* SCE) for piezoelectrodes). Though the resultant surface on both the piezoelectrodes and microelectrodes may indeed be characterised by significant levels of MB adsorption, the fact that it may be consistently regenerated (without recourse to thermal cleaning) provides us with a reproducible initial electrode state. For simplicity, this will be referred to as a “clean” surface.

Figure 6.4 shows the CV and EQCM response taken simultaneously during the first cycle after the cleaning procedure under near-identical conditions to those employed in **Figures 6.1 & 6.3.a**. Apart from the electrode size, the most significant difference between the two experiments is the truncated cathodic potential limit of -0.30 V (vs. SCE) employed in **Figure 6.4** compared to that of -0.40 V (vs. SCE) in **Figure 6.1**. The truncation was necessary in order to arrest a change in the form of the CV observed with increasing sweep number and analogous to that seen in **Figures 6.3.b** and **6.3.c** over wider potential windows. Only the first voltammogram recorded on a freshly cleaned crystal has the form of that in **Figure 6.4**, subsequent CVs resemble that in **Figure 6.3.b**.

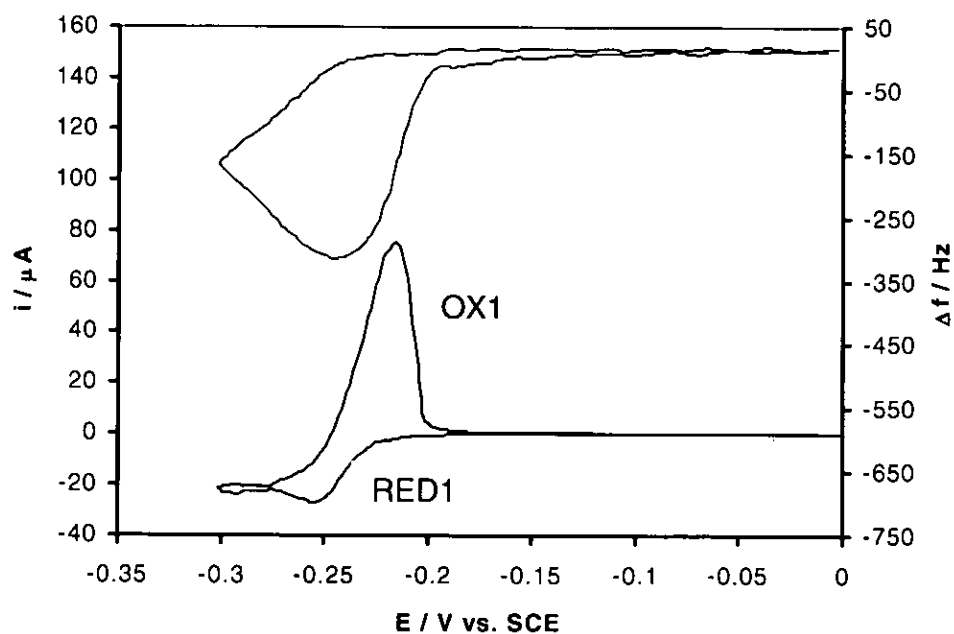


Figure 6.4: CV of MB on a 14mm Au EQCM crystal electrode $1 \text{ mol m}^{-3} \text{ MB}^+$, Phosphate buffer pH=7.9, scan rate 6 mV s^{-1} .

The CV of **Figure 6.4** strongly resembles that of **Figure 6.3.a** i.e. it has a form directly analogous to that of simple metal deposition (RED1) and stripping (OX1). In the voltammetric response, the charge transfer complex generation peak occurs at ~ -0.26 V

(vs. SCE) and the stripping peak occurs at ~ -0.22 V (vs. SCE). The essential features of the frequency response of the EQCM measurement are **Figure 6.4**:

- (i) on the cathodic scan, the mass begins to increase at $E = -0.20$ V (vs. SCE), coincident with the onset of the cathodic reduction current; and
- (ii) on the return anodic sweep, the mass begins to sharply decrease at -0.24 V (vs. SCE), coincident with the onset of the anodic reoxidation current.

According to Hepel and Janusz [6.31], films of MB reduction product that are electrodeposited onto gold-coated quartz crystals under experimental conditions analogous to those employed in this study exhibit no visco-elastic resonance damping effects and that, consequently, the Sauerbrey equation is applicable. Thus, assuming a direct proportionality between mass and frequency change, the mass change during the forward sweep is 660 ng or 0.0233 g m⁻². This is equal to that observed during the reverse sweep. Hence, there is no net mass change / imbalance during the first cycle, indicating that film dissolution occurs quickly and to completion (within the limits of detection of the EQCM).

Hepel and Janusz [6.31] record that the respective masses of one monolayer of MB adsorbed at the electrode surface as a flat monomer (molecular axis parallel to the electrode surface), flat dimer and vertical monomer (molecular axis perpendicular to the electrode surface) are: 3.51×10^{-4} , 7.02×10^{-4} and 6.96×10^{-4} g m⁻² respectively. Svetlicic *et al* have suggested that both MB and the charge transfer complex are adsorbed at bare Au surfaces in flat / planar orientation [6.14]. Thus, a mass increase of 660 ng corresponds to the deposition/adsorption of 66.5 monolayers of MB monomer with a flat orientation at the electrode surface.

The molar mass, M , of an electrodeposited species can be obtained by two methods if the resultant film is thin, rigid and of a defined stoichiometry. The first, or integral method,

is suitable for systems when a constant or slowly changing current is observed during electrodeposition or dissolution. M is then given by

$$M/n = \Delta m F/|Q| \quad (6.6)$$

where Q is the *total faradaic charge* passed during the electrode reaction. The second, or differential, method is suitable for systems where the faradaic current is changing rapidly. M is then given by:

$$\frac{M}{n} = \frac{F}{i} \left(\frac{dm}{dt} \right)_{at\ i} \quad (6.7)$$

In accordance with the approach described by Hepel and Janusz [6.31], M/n is given by

$$\frac{M}{n} = \frac{M_{MB} + M_{H^+} + xM_{A^{z-}} + yM_{H_2O}}{2 - z x}, \quad \text{where } n = 2 - zx. \quad (6.8)$$

where A^{z-} is the adsorbed anion species, x the number of reacting anions and z their associated charges.

Given the 50-fold excess of phosphate over chloride, and that, at pH 7.9, $[HPO_4^{2-}] \approx 43 \text{ mol m}^{-3}$ and $[H_2PO_4^-] \approx 7 \text{ mol m}^{-3}$, we expect that HPO_4^{2-} will act as a counterion in any electrodeposited solid phase formed at the electrode surface. Svetlicic *et al* have already demonstrated the role of phosphate as a counterion in the electrochemistry of the MB system [6.11]. If we assume that $y = 0$, $M_{MB} = 285$, $M_{H^+} = 0$, $M_{A^{z-}}$ for $[HPO_4^{2-}] = 96$ & $z = 2$ then M/n is then given by:

$$\frac{M}{n} = \frac{285 + 96x}{2 - 2x} \quad (6.9)$$

Analysis of the current and mass deposition data at -0.30 V (*vs.* SCE) in *Figure 6.4* in accordance with *Equation 6.7* indicates that $M/n = 193$ which, upon substitution into *Equation 6.19*, gives $n = 1.58$. Use of *Equation 6.6* and the total charge associated with

peak OX1 in the analysis of the mass loss observed during the return sweep of *Figure 6.4* gives an M/n value of 205.4. Substitution of this value into *Equation 6.19* gives $n = 1.50$. Both of these values of n are in excellent agreement with the values of n/m of 1.49 & 1.51 obtained from by microelectrode measurements of Pennarun and Xiao, summarised in **Section VI.2**. Thus, the values of n obtained from the microelectrogravimetric measurements strongly support the findings of the microelectrode study so confirming that, in accordance with *Equation 6.5*, the electrodeposited phase observed in *Figures 6.1, 6.3.a* and *6.4* is the mixed valence LMB/LMB^{+•} charge transfer complex.

Figure 6.5 shows a suggested mechanism for the repetitive deposition and stripping of the quasi-metallic LMB/LMB^{+•} salt at the surface of gold microelectrodes. In summary, deposition probably occurs initially at the electrode/solution interface and subsequently at the film/solution interface. Due to the metallic nature of the film, stripping most likely occurs from the film/solution interface into the film.

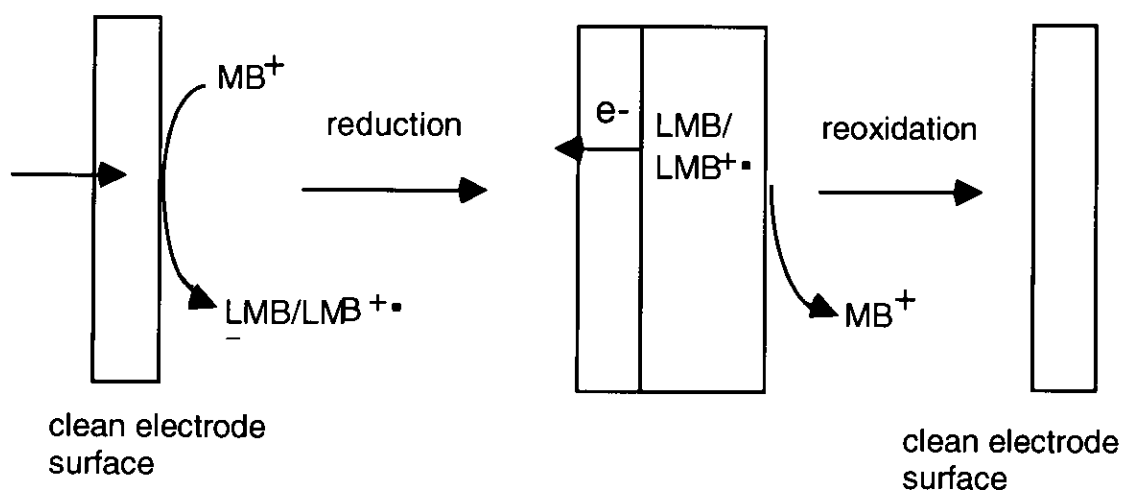


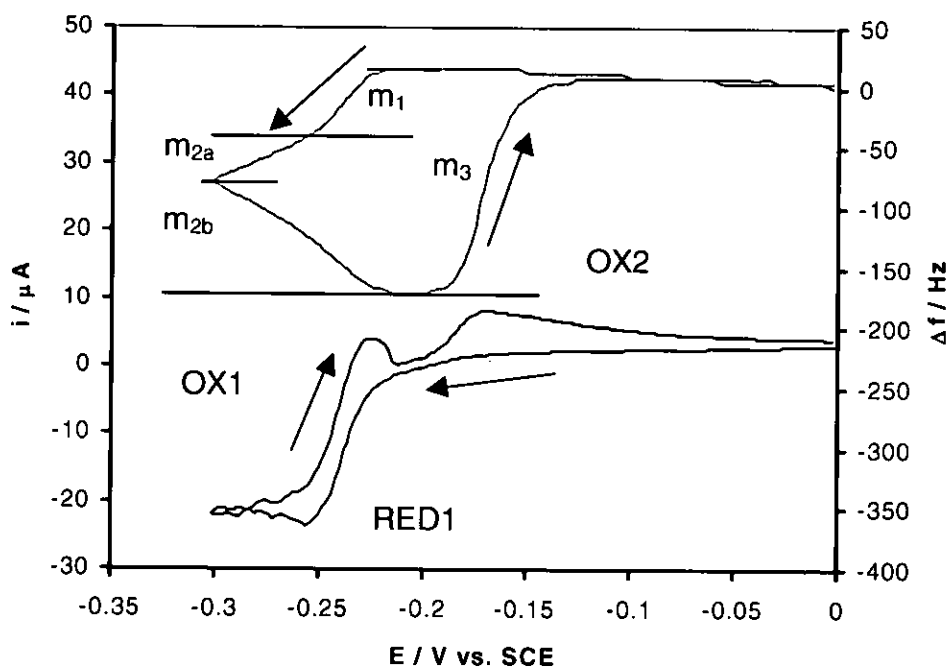
Figure 6.5: A schematic of the electrochemistry of MB on a "Clean" gold electrode.

Let us now consider the microgravimetric responses associated with peaks RED2 and OX2. As can be seen from *Figure 6.6.a*, the cyclic voltammograms and

voltamassograms recorded on macroscopic Au piezoelectrodes are broadly similar to those recorded on Au microelectrodes shown in *Figure 6.3.b*.

However, in the absence of the irreversibility imposed by microelectrode geometry on the reaction associated with RED2, the transformation from LMB/LMB⁺ to LMB occurs within sweep limits of 0.00 to -0.30 V (vs. SCE) *Figure 6.6.a* as opposed to 0.00 to -0.90 V (vs. SCE) *Figure 6.3.b*. Thus, voltammograms with a final form similar to that of *Figure 6.3.c* are obtained after repetitive cycling within the narrower potential window of *Figure 6.6.a*. Let us consider the final form of the cyclic voltammogram / voltamassogram shown in *Figure 6.6.b*.

On the cathodic sweep, the voltamassogram exhibits the following features:



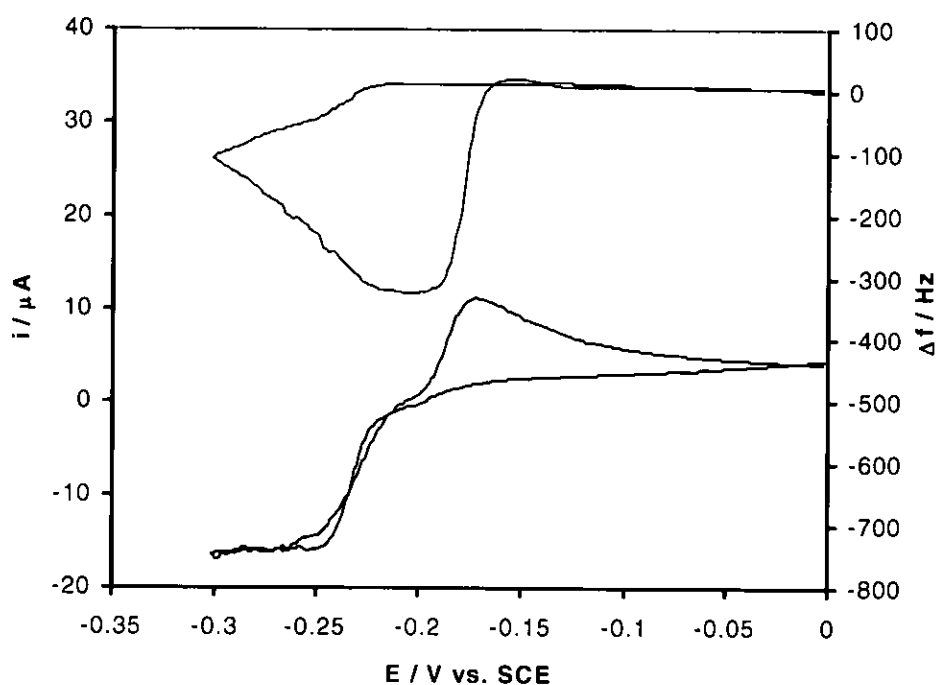


Figure 6.6: CV of MB on a 14mm Au EQCM crystal electrode $1 \text{ mol m}^{-3} \text{ MB}^+$, Phosphate buffer pH=7.9, scan rate (a) 3 mV.s^{-1} (b) 1 mV.s^{-1} .

- (i) a mass increase, m_1 , the onset of which at $\sim -0.22 \text{ V}$ (vs. SCE) is coincident with the onset of a cathodic reduction wave;
- (ii) an inflexion at -0.245 V (vs. SCE); and
- (iii) a second mass increase, m_{2a} , that continues to the switching potential.

On the return anodic sweep:

- (i) the mass continues to increase by an amount m_{2b} , until the potential at which the associated cathodic reduction current returns to zero; and then
- (ii) the mass begins to sharply decrease by an amount m_3 at -0.195 V (vs. SCE); coincident with the onset of the anodic reoxidation current associated, by comparison with **Figure 6.3.c**, with OX2.

The mass change m_1 is 77 ng or $2.72 \times 10^{-3} \text{ g m}^{-2}$ which, using the monolayer mass data of Hepel and Janusz [6.31], corresponds to the deposition / adsorption of 7.8 monolayers

of MB monomer or 3.9 monolayers of dimer with a flat orientation at the electrode surface. Analysis of the Δm -Q data in the vicinity of m_1 in accordance with *Equation 6.6* gives $M/n = 195.7$ which, upon substitution into *Equation 6.9*, gives $n = 1.56$. This is in excellent agreement with the values of $n = 1.50$ and 1.58 obtained from *Figure 6.4*, allowing us to conclude that the phase electrodeposited during the cathodic going sweep at potentials anodic of the inflexion at -0.245 V (vs. SCE) is the mixed valence LMB/LMB^{+•} charge transfer complex.

Inspection of *Figures 6.4* and *6.6.a* indicates that peak OX2 is only observed when the inflexion is present in the cathodic going sweep *i.e.* the inflexion at -0.245 V (vs. SCE) corresponds to the onset of the solid state reduction of LMB/LMB^{+•} to LMB. To our knowledge, the onset of this process has never been directly observed before.

The mass change observed at potentials cathodic of the inflexion, m_{2a} , is therefore a function of two parallel processes: the electrodeposition of LMB/LMB^{+•} and its subsequent solid state reduction to LMB with accompanying counterion expulsion. The form of the voltamassogram consequently defies simple analysis by *Equations 6.6* and *6.7*, although a qualitative consideration of the values of dm/dE pre- and post-inflexion is instructive. Pre-inflexion electroreduction involves the deposition of 1 mass equivalent of LMB and half a mass equivalent of chloride per 1.5 equivalents of electrons passed *i.e.* from *Equation 6.19*, $M/n = 206$. Post-inflexion electroreduction involves the deposition of the mixed valence salt followed by its reduction to LMB *i.e.* the effective deposition of 1 mass equivalent of LMB per 2 equivalents of electrons passed, for which $M/n = 142.5$. Pre-and post-inflexion, $dm/dE = 5160$ ng V⁻¹ and 3050 ng V⁻¹ respectively in *Figure 6.6.b*, values which qualitatively reflect the M/n values of the associated section of the voltamassogram. The post-inflexion value of dm/dE is lower than might be expected based on the post and pre-inflexion M/n values, although this may be due to a hindering of diffusive mass transport to and from the electrode by a surface layer of

electrogenerated LMB. Therefore, it may be no coincidence that the potential of the inflexion coincides with the onset of the plateau of the cathodic wave.

The mass changes m_{2a} and m_{2b} arise from the same processes and so can be considered as a single mass change $m_2 = m_{2a} + m_{2b}$. Mass change m_2 in *Figure 6.6.b* is 690 ng or 0.0244 g m^{-2} which, using the monolayer mass data of Hepel and Janusz [6.31], corresponds to the deposition of 70 monolayers of MB monomer with a flat orientation at the electrode surface or 35 monolayers with a vertical orientation.

As stated above, mass change m_3 in *Figure 6.6.b* is a sharp decrease with an onset at $-0.195 \text{ V (vs. SCE)}$, coincident with the onset of the anodic current associated the LMB \rightarrow MB oxidation described by OX2. Interestingly, the rapid mass decrease is completed before the potential reaches $-0.15 \text{ V (vs. SCE)}$ on the anodic scan. This occurs before the current ceases on the anodic side of OX2. Hepel and Janusz [6.31] have observed a similar phenomenon when reoxidising LMB films at S-modified Au electrodes, which they attribute to the disintegration of the LMB film after it has been only partially oxidised. The same explanation may be applied to the data of *Figure 6.6.b*. Such a process would lead to the release of a substantial amount of dissolved LMB in the vicinity of the electrode surface which would be subsequently oxidised in the potential range $E = -0.15 \text{ to } 0.00 \text{ V (vs. SCE)}$. To the best of our knowledge, is the first time such an effect has been observed on bare gold electrodes.

It is interesting now to examine the mass changes that occur during the anodic sweep of *Figure 6.6.a*. The mass of the electrode increases during the return sweep (the ultimate increase being m_{2b}) until the potential reaches $-0.225 \text{ V (vs. SCE)}$, which is coincident with the peak potential of the LMB/LMB⁺ stripping peak, OX1. The mass of the electrode is then constant until the potential of the onset of the LMB \rightarrow MB oxidation peak, OX2, at which point the mass decreases sharply as in *Figure 6.6.b*. Two conclusions can be made from these observations.

- (i) No mass increase is observed at potentials anodic of the LMB/LMB⁺⁺ stripping peak during the forward or reverse sweeps of *Figures 6.4* or *6.6.a*. Thus, whilst the final composition of the electrodeposited layer immediately prior to the first reoxidation process on the return sweep may be predominantly LMB, LMB/LMB⁺⁺ is a necessary precursor to its formation and hence in determining the ultimate size of m_2 .
- (ii) There is no mass decrease associated with the reduction of LMB/LMB⁺⁺ to MB (OX1), indicating that the electrogenerated MB is still bound in some manner to the piezoelectrode surface. This behaviour is in contrast to that of *Figure 6.4* where, in the absence of reductively generated LMB in the surface layer, the cyclic voltammetric current peak OX1 is accompanied by a sharp mass decrease in the voltamassogram. A possible explanation of this observation is that the semi-reduced, mixed LMB- LMB/LMB⁺⁺ layer present at on the electrode surface immediately prior to the first reoxidation described by OX1 has a three-dimensional bicontinuous mesh structure. Upon reoxidation of the LMB/LMB⁺⁺ component of the mesh to MB, the “holes” in the remaining LMB-only structure are small enough to restrict the diffusion of the MB molecules out of the surface layer. Such trapped entities will still contribute to the measured electrode mass and only be released to free solution upon the dissolution of the porous LMB layer at \sim 0.19 V (vs. SCE). It is therefore expected that this mesh structure could be observed using in-situ AFM and studies to this effect are underway in our laboratory.

A bicontinuous, mixed LMB- LMB/LMB⁺⁺ mesh would most likely arise as a result of the solid state LMB/LMB⁺⁺ \rightarrow LMB reduction occurring via a crystallization process involving simultaneous dendritic growth from a number of nucleation sites on the

electrode surface. With this hypothesis in mind, we now address the time evolution of the relative intensities of the OX1 and OX2 peaks in *Figures 6.3 & 6.6*.

The progression in the forms of the CVs presented in *Figures 6.3, 6.4* and *6.6* may be understood in terms of the orientation and electrochemical activity of the first adsorbed monolayers of MB and its reduction products at the electrode surface. Svetlicic *et al* have suggested that MB is adsorbed at bare Au surfaces in a flat orientation [6.14] with primary interactions from the aromatic rings and the exocyclic nitrogens and heterocyclic sulphur. In that orientation, the first monolayer of MB adsorbed on the bare Au is electrochemically inactive [6.43]. Further, it appears that MB molecules in the first adsorbed monolayer only exhibit an electrochemical activity if tilted or perpendicular to the electrode surface as this allows the MB cation to interact with the Au substrate through the S heteroatom (see structure in *Reaction 6.2*).

Hepel and Janusz [6.31] suggest that the reduction of MB from solution on the first adsorbed planar monolayer is possible, so forming a deposition product on top of the inactive layer of MB. Svetlicic *et al* [6.14] propose that the charge transfer complex has a planar orientation at the electrode surface. Thus, the CVs of *Figures 6.3.a* and *6.4* can be understood in terms of the deposition (via peak RED1) of planar orientated LMB/LMB⁺ over a layer of similarly orientated MB at the electrode surface followed by its oxidative electrodisolution during the reverse sweep (via peak OX1).

Now let us consider the situation when LMB is the apparent principle reduction product. Corn *et al* [6.17] found that electrogenerated LMB is orientated perpendicularly to the gold electrode surface; given the known strength of the gold-sulphur interaction, LMB is almost certainly adsorbed at the electrode surface through the heterocyclic S atom of its central ring. Indeed, adsorption of both MB and LMB at gold has been enhanced by derivatising the Au surface with a layer of S atoms [6.21-6.26]. Importantly, MB bonds with the S-modified Au surface by a sulphur adatom-sulphur heteroatom bond, so

forming a dense, self-assembling monolayer of perpendicularly orientated molecules [6.21]. Reduction of MB over such a layer yields similarly orientated LMB as its sole product [6.31]. In support of these findings, Kuwabata *et al* note that MB is restricted to a perpendicular orientation at Nafion modified electrodes and that, under such circumstances, LMB is the sole reduction product detected [6.18]. Thus, the CVs of *Figures 6.3.c* and *6.6.b* can be understood in terms of the electrogeneration and oxidative redissolution of perpendicularly orientated LMB at the electrode surface. Given the presence of the inflexion at -0.245 V (*vs.* SCE) in the voltammogram of *Figure 6.6.b*, the formation of LMB at the electrode surface is a two step process. The first process being the electrodeposition of planar orientated LMB/LMB⁺ followed by the solid state reduction of the charge transfer complex to form perpendicularly orientated LMB.

It is apparent from the CVs of *Figures 6.3*, *6.4* and *6.6* that, if the cathodic potential limit is sufficiently negative, the rate of the solid state reduction increases with each subsequent potential sweep. This may be understood by consideration of the orientation of MB generated as a result of the reoxidation of LMB in the first monolayer.

Within the sequence of voltammograms presented in *Figure 6.3*, comparatively little LMB is generated during the timescale of the first cathodic sweep to -0.90 V (*vs.* SCE). This is because the reduction of LMB/LMB⁺ to LMB will be accompanied by a change in the crystal structure of the electrodeposited layer due to the component molecules changing from a planar to perpendicular orientation. Essentially this is because the electronegative portions of the LMB/LMB⁺ and LMB will be repelled by the negative potential of the working electrode during cathodic excursions forming a more stable monolayer in the favoured perpendicular orientation and ultimately be expected to be electrochemically irreversible. During the reverse sweep, those perpendicular LMB molecules that have been produced are reoxidised to form MB. MB molecules generated in this way would also be orientated perpendicular to the electrode surface, so enabling

the cation to interact with, and absorb onto, the Au substrate through the sulphur heteroatom. Whereas the reorientation of planar molecules to perpendicular is thermodynamically driven by the electrochemical reduction of LMB/LMB⁺⁺ to LMB during the forward going sweep, no such electrochemical process is available to drive the perpendicularly orientated MB molecules, once formed, into a planar configuration. Significant proportions of those molecules retain their perpendicular orientation for the commencement of the next sweep. Such perpendicularly orientated MB molecules would then be reduced directly to LMB during that sweep with an onset potential either coincident with or, more likely given the inflexion in the voltammogram of *Figure 6.6.b*, just cathodic of the onset of LMB/LMB⁺⁺ generation. The LMB sites so formed may then act as nucleation centres for the electrogeneration of perpendicularly oriented LMB from LMB/LMB⁺⁺, so facilitating the solid state reductive transformation of the charge transfer complex to the leuco form. With each subsequent sweep, the number of LMB, and consequently MB, molecules with a perpendicular orientation at the electrode surface increases, with a consequent increase in the rate of the reductive conversion of LMB/LMB⁺⁺ to LMB. Eventually, the number of perpendicular nucleation centres is high enough to facilitate the complete reductive transformations of the solid surface layer on the time scale of a single voltammogram. Under such circumstances, voltammograms similar to those seen in *Figures 6.3.c* and *6.6.b* are observed.

The process by which the electrode surface is progressively covered with perpendicularly orientated MB molecules, which promote the formation of the LMB phase at the electrode surface, is illustrated in *Figure 6.7*.

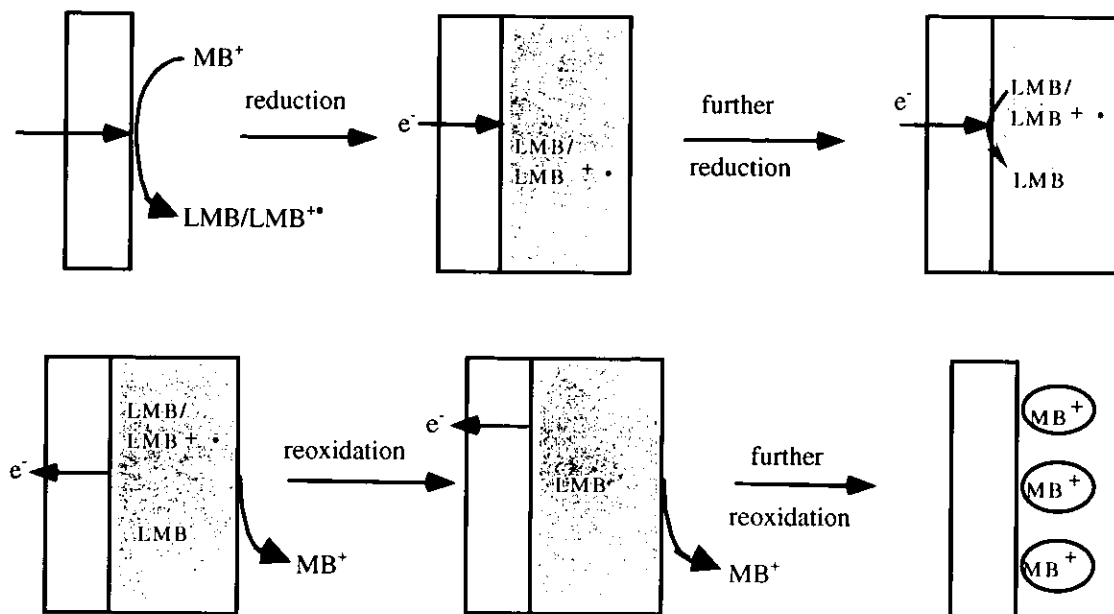


Figure 6.7: Electrochemistry of MB on gold electrode surface.

VI.4 - CONCLUSIONS

The electrochemistry and microelectrogravimetric behaviour of MB has been examined as part of a larger study into its suitability as a redox mediator in a Nafion[®] polymer modified EQCM-based sensor for actinide metal cations. The reduction of MB to leucomethylene blue, LMB, occurs via an ECE mechanism where the chemical step corresponds to the protonation of the product of the 1 e⁻ reduction of MB. Even though the sensor will ultimately be deployed at pH ≤ 1, measurements were conducted at pH 7.9 in order to maximise any potential problems that may arise due to the protonation step.

In keeping with results of Clavilier *et al* [6.11] and Corn *et al* [6.17], as well as previous results obtained from a microelectrode study of MB conducted in this laboratory [6.10 & 6.32], EQCM experiments indicate that the reduction of MB to solid LMB occurs in two steps. During the first step, LMB is formed which subsequently undergoes a complexation reaction with its immediate electrochemical precursor to form a solid charge transfer complex, LMB/LMB^{+•} which electrodeposits at the electrode surface. The formation of the charge transfer complex therefore corresponds to a net 1.5 electron transfer per molecule of MB reduced, a number confirmed by analysis of the voltamassograms. The second step involves the reduction of the charge transfer complex to solid phase LMB at the electrode surface. The electrode kinetics of the latter step are found to be highly irreversible, a result consistent with the fact that a solid phase change occurs when the conducting charge transfer complex is reduced to the insulating leuco form. On the other hand, the kinetics of charge transfer complex formation are found to be electrochemically reversible over all times time domains studied in this work, implying that the direct reduction of MB to LMB must also be highly reversible.

In keeping with results obtained on microelectrodes, EQCM experiments indicate that the relative amounts of reductively generated charge transfer complex and leuco form produced during the negative going, forward are highly dependent upon the timescale of the experiment – essentially, the longer the applied potential is held at values negative of the standard potential for the reduction of MB, the higher the proportion of LMB generated (the greater the proportion of charge transfer complex reduced). Importantly, the onset of charge transfer complex reduction to LMB can be directly observed as an inflection in the voltamassogram. We believe that this is the first time that this has been reported.

While charge transfer complex oxidation is reversible, the reoxidation of the solid leuco form is an irreversible process, presumably due to the effect of the solid overlayer of insulating LMB. For layers that are composed of a mixture of charge transfer complex and LMB, no significant mass change is observed in the voltamassogram upon oxidation of the former back to MB, even though a significant passage of charge is recorded. However, a sudden and large mass loss is observed upon oxidation of the LMB to MB, indicating that (i) the MB generated as a result of the reduction of the charge transfer complex is retained at the piezoelectrode surface in the remaining LMB structure; and (ii) upon reduction of the first layer of LMB molecules at the electrode surface, the structure of the LMB layer disintegrates, releasing LMB and MB to solution, the former of which is then reduced in a semi-infinite linear diffusion controlled process see *Figure 6.6.b*.

It is suggested that the solid phase conversion of the charge transfer complex, wherein the component phenothiazine nuclei are adsorbed planar / parallel to the electrode surface, to the leuco form, wherein the LMB molecules are adsorbed perpendicular to the electrode surface, occurs with greater facility when perpendicularly adsorbed MB molecules are present at the electrode surface. Essentially, the more LMB generated

during a cycle, the greater the number of perpendicularly adsorbed MB molecules at the electrode surface at the end of the cycle. These perpendicularly adsorbed molecules then act as nucleation centres for LMB formation, leading to the generation of an even greater amount of LMB during the immediately subsequent cycle. That no net mass change is observed between the beginning and the end of the cycles shown in *Figure 6.6* indicates that, while their orientation may alter, the total surface population of adsorbed MB molecules (both planar and perpendicular) does not change.

The reversibility of the MB to LMB reduction within the context of charge transfer complex electrogeneration is highly encouraging evidence that MB may be a suitable mediator for actinide cation reduction within the polymer layer of the proposed sensor. It is well known that the pendular amino-groups of LMB are protonated below pH 1, so rendering the resultant LMBH_2^{2+} soluble in aqueous solution. This means (a) difficulties associated with the irreversible reoxidation of the solid phase LMB generated at pH 7.9 will be obviated; and (b) being a large cation, we could expect LMBH_2^{2+} to be retained within the Nafion[®] layer. Further work will therefore involve an EQCM study of the reduction of MB at $\text{pH} \leq 1$ at bare gold piezoelectrodes and at Nafion[®]-coated electrodes. Ultimately, the feasibility of accomplishing MB-mediated reduction of actinide metal cations such as UO_2^{2+} will also be investigated.

VI.5 - REFERENCES

- 6.1 H. Aoyagi, Z. Yoshida and S. Kihara. *Anal. Chem.* **59**, (1987), 400
- 6.2 A.A. Karyakin, A.K. Strakhova, E.E. Karyakina, S.D. Varfolomeyev and A.K. Yatsimirsky. *Bioelectrochem. Bioenergetics.* **32**, (1993), 35
- 6.3 A.A. Karyakin, E.E. Karyakina, W. Schuhmann, H.-L. Schmidt and S.D. Varfolomeyev. *Electroanalysis.* **6**, (1994), 821
- 6.4 D.D. Schlereth, W. Schuhmann and H.-L. Schmidt. *J. Electroanal. Chem.* **381**, (1995), 63
- 6.5 D.D. Schlereth and A.A. Karyakin. *J. Electroanal. Chem.* **395**, (1995), 221
- 6.6 A. Silber, N. Hampf and W. Schuhmann. *Biosensors and Bioelectronics.* **11**, (1996), 215
- 6.7 J. Kulys, G. Gleixner, W. Schumann and H-L. Schmidt. *Electroanalysis.* **5**, (1993), 201
- 6.8 Y. Ye and R. Baldwin. *Anal. Chem.* **60**, (1988), 2263
- 6.9 Y. Liu, H. Liu, J. Qian, J. Deng and T. Yu. *Anal. Chim. Acta.* **316**, (1996), 65
- 6.10 S. Xiao, PhD Thesis, University of Central Lancashire, 2000
- 6.11 V. Zutic, V. Svetlicic, J. Clavilier and J. Chevalet. *J. Electroanal. Chem.* **219**, (1987), 183
- 6.12 R.H. Wopschall and I. Shain. *Anal. Chem.* **39**, (1967), 1527
- 6.13 G. Papeschi, M. Costa and S. Bordi. *J. Electrochem. Soc.* **128**, (1981), 1518
- 6.14 V. Svetlicic, J. Tomaic, V. Zutic and J. Chevalet. *J. Electroanal. Chem.* **146**, (1983), 71
- 6.15 V. Svetlicic, V. Zutic, J. Clavilier and J. Chevalet. *J. Electroanal. Chem.* **195**, (1985), 307
- 6.16 T. Sagara and K. Niki. *Langmuir.* **9**, (1993), 831
- 6.17 E.I. Sáez and R.M. Corn. *Electrochim. Acta.* **38**, (1993), 1619
- 6.18 S. Kuwabata, J. Nakamura and H. Yoneyama. *J. Electroanal. Chem.* **261**, (1989), 363
- 6.19 A.R. Guadalupe, K.E. Liu and H.D. Abruña. *Electrochim. Acta.* **36**, (1991), 881
- 6.20 S.A. John and R. Ramaraj. *J. Chem. Soc. Faraday Trans.* **90**, (1994), 1241
- 6.21 V. Svetlicic, V. Zutic, J. Clavilier and J. Chevalet. *J. Electroanal. Chem.* **233**, (1987), 199
- 6.22 J. Clavilier, V. Svetlicic, V. Zutic, B. Ruscic and J. Chevalet. *J. Electroanal. Chem.* **250**, (1988), 427

-
- 6.23 R.O. Lezna, N.R. de Tacconi, F. Hahn and A.J. Ariva. *J. Electroanal. Chem.* **306**, (1991), 259
- 6.24 B.J. Barner and R.M. Corn. *Langmuir*. **6**, (1990), 1023
- 6.25 R.R. Naujok, R.V. Duevel and R.M. Corn. *Langmuir*. **9**, (1993), 1771
- 6.26 V. Svetlicic, J. Clavilier, V. Zutic, J. Chevalet and K. Elachi. *J. Electroanal. Chem.* **344**, (1993), 145
- 6.27 P.R. Unwin and A.J. Bard. *Anal. Chem.* **64**, (1992), 113
- 6.28 X. Chen, J. Zhuang and P. He. *J. Electroanal. Chem.* **271**, (1989), 257
- 6.29 H. Ju, J. Zhou, C. Cai and H. Chen. *Electroanalysis*. **7**, (1995), 1165
- 6.30 V. Kertész, J. Bácskai and G. Inzelt. *Electrochimica Acta*. **41**, (1996), 2877
- 6.31 M. Hepel and W. Janusz. *Electrochimica Acta*. **45**, (2000), 3785
- 6.32 G.A. Pennarun, PhD Thesis, University of Central Lancashire, 1999.
- 6.33 A.S.N. Murthy and K.S. Reddy. *J. Chem. Soc. Faraday Trans. I*. **80**, (1984), 2745
- 6.34 A.P. Brown and F.C. Anson. *J. Electroanal. Chem.* **92**, (1978), 133
- 6.35 K.B. Oldham, J.C. Myland, C.G. Zoski and A.M. Bond. *J. Electroanal. Chem.* **270**, (1989), 79
- 6.36 M.T. McDermott, C.A. McDermott and R.L. McCreery. *Anal. Chem.* **65**, (1993), 937
- 6.37 T. Berzins and P. Delahay. *J. Am. Chem. Soc.* **75**, (1953), 555.
- 6.38 N. White and F. Lawson. *J. Electroanal. Chem.* **25**, (1970), 409.
- 6.39 D.J. Schiffrin, *J. Electroanal. Chem.* **201**, (1986), 199.
- 6.40 G. Gunawardena, G. Hills and I. Montenegro. *J. Electroanal. Chem. Interfacial Electrochem.* **184**, (1985), 371
- 6.41 J. Clavilier and J.P. Chauvineau. *J. Electroanal. Chem.* **97**, (1979) 199
- 6.42 J. Clavilier. *J. Electroanal. Chem.* **107**, (1980), 211
- 6.43 V. Svetlicic, J. Clavilier, V. Zutic and J. Chevalet. *J. Electroanal. Chem.* **312**, (1991), 205

CHAPTER VII – CONCLUSIONS AND FURTHER WORK

The objective of this project was the development of a prototypical *electrochemical quartz crystal microbalance* (QCM)-based sensor specifically tailored for the nuclear industry for the determination of isotope pollutant levels in plant process streams. The sensor was to consist of a **gold piezoelectrode** support modified by a **Nafion[®] polymer layer**, said layer impregnated with an oxidation state specific ligand – specifically a cationic **hydroxamic acid** showing selectivity towards actinide 4+ ions and the non-radioactive **demonstrator ion**, Fe³⁺. Further, and if appropriate, in order to mediate the electrochemical conditioning of actinide (V) and (VI) species to actinide (IV) and so render them detectable by the sensor, the possibility of including a **redox mediator** within the film will also be investigated.

While the realisation of the sensor prototype remains to be achieved and will form a substantial part of the further work for this project, the following results have been obtained for each of the component parts.

The Gold Piezoelectrode

The dissolution and redeposition processes of Au in HNO₃ solution at pH 1 & 0 were investigated as a function of sweep rate by in situ EQCM experiments. The results demonstrate that, at pH 1 and $v \leq 10 \text{ mV s}^{-1}$, Au dissolves through a $3e^-$ oxidation at $E > +1.00 \text{ V (vs. SCE)}$, a process that, at $v \leq 10 \text{ mV s}^{-1}$, is kinetically hindered with respect to upd of OH surface sublattices and subsequent 2-D-phase oxide formation. The inhibition arises from the presence of a closed packed layer of nitrate oxyanions at the gold surface,

although the layer is disrupted and the inhibition removed by the gold dissolution and reprecipitation processes that occur during potential cycling at low v .

To better understand the processes involved in gold dissolution and redeposition it would be advantageous to continue to investigate this topic by researching other acid based environments such as HClO_4 , H_2SO_4 etc more extensively especially under steady state conditions. Investigation into single crystal gold structures namely 100, 101 & 110 would complete this study especially utilising the EQCM and microdisc techniques already developed.

The Hydroxamic Acid Ligand

Utility of an ideally suited sequestration agent was investigated using primarily hydroxamic acids (i.e. acetohydroxamic acid) investigation into kinetic and thermodynamic stability properties were assessed. It was observed that the onset of AHA oxidation was negative of the onset of gold dissolution / gold oxide formation. The AHA oxidation wave was studied by using a range of disc microelectrodes radii and during analogous Au piezoelectrodes experiments.

The observations from this series of studies show that corresponding voltamassogram recordings in nitric acid in the absence of AHA show no mass change associated with peaks identified as being associated with AHA oxidation and designated as peaks *alpha* & *beta*. This observation suggests that, during AHA oxidation, all processes are controlled by solution diffusion and not surface processes. The electron transfer processes associated with the waves *alpha* and *beta* are found to be 1 and 2 electron reactions respectively.

Further measurements obtained using the EQCM show that the total mass loss observed in a solution containing AHA was ~750ng, observed in *Zones III & IV* of *Figure 4.1*. A corresponding mass loss observed in nitric only was found to be ~360ng, this strongly indicates the presence of another process, that being the AHA assisted electro-dissolution of gold, almost certainly driven by AHA complexation of electrogenerated Au³⁺ ions.

Finally, the absence of an AHA oxidation wave prior to the onset of Au oxidation during the positive-going, forward sweep of the gold microelectrode investigations can be attributed to the following: the microelectrode surface in contact to the solution phase was presented as a polished surface. Conversely, no such polishing protocol was available for the piezoelectrode study, the surface of which remained as deposited and so microscopically rough. Hence, a higher density of nitrate anion packing would be expected at the former surfaces, said packing excluding AHA from the surface and so preventing its electrooxidation during the anodic going sweep.

In order to confirm the findings stated further experiments will need to be conducted to verify this explanation – specifically, cyclic voltammetric studies on Au microelectrodes over the potential range +0.40 to +1.50 V (*vs.* SCE) at pH 1. By conducting the study in this fashion we hope to remove the potential induced surface roughening that occurs negative of the pzc; and combined CV and gravimetric studies on Au piezoelectrodes constructed using *polished* quartz crystals over the potential range –0.30 to +1.50 V (*vs.* SCE) at pH 1.

The Polymer Layer and the Demonstrator Ion, Fe³⁺

Having characterised the electrochemistry of the Au piezoelectrode and the HA under conditions where the sensor may be deployed, an investigation of Nafion[®] membranes incorporated with DFA⁺ sequestering reagent specific toward cations of analytical interest was undertaken.

The microelectrogravimetry of the non-radioactive demonstrator Fe^{2+/3+} couple was studied at bare Au, Nafion[®] modified Au and Nafion[®] modified Au impregnated with DFA⁺ ionophore / ligand. These investigations were conducted in order to develop a better understanding of the electrochemical behaviour of Fe³⁺ / DFA⁺ / Nafion[®] composite membranes and their potential role as the transduction element of an EQCM-based sensor.

The results indicate that, in background electrolyte (nitric acid, pH 1 & 0), the electrochemistry of Nafion[®] layer partitioned Fe^{2+/3+} ions is consistent with thin layer cell behaviour with fast interfacial charge transfer and effective charge transport in the membrane coating. The polymer layer appears to increase in mass during reduction of Fe(III) to Fe(II) due to an influx of highly hydrated H⁺ ions necessary to maintain electroneutrality within the polymer.

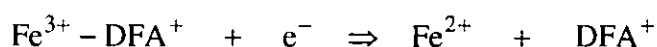
That the current signals derived from the Fe^{2+/3+} redox processes in the polymer layer were not significantly displaced from the potential at which the same processes would occur in free solution was indicative of there being no specific interaction between the various sites within Nafion[®] and ferrous / ferric ions. Indeed, upon repetitive cycling, the iron content of the membrane gradually decreases. This is most readily observed by a gradual increase in

the mass of the membrane as ferrous / ferric ions leach out and, in order to fulfil the electroneutrality requirement within the membrane, are replaced by highly solvated H^+ ions.

Microelectrogravimetry studies of Fe^{3+} solutions at pH 2 at bare and Nafion[®] modified Au piezoelectrodes indicate that electrogenerated Fe^{3+} (produced as a result of re-oxidation of electroreductively generated Fe^{2+}) can precipitate at the surface of bare Au electrodes as iron oxyhydroxides. Such a process is not observed during analogous experiments at Nafion[®] modified electrodes, most likely due to the lower pH generated within the polymer layer as a result of the influx of H^+ ions discussed previously. Importantly in solutions of $Fe(NO_3)_3$, both the oxidation and reduction of $Fe^{2+/3+}$ ions at bare and Nafion[®] modified electrode surfaces appear to be controlled by semi-infinite linear diffusion rather than displaying behaviour consistent with that of a thin layer cell.

For completeness a series of investigations were conducted to observe and develop control of the solution environment within the Nafion[®] / HA composite layer and adjacent to the piezoelectrode surface in a solution of $10 \text{ mol m}^{-3} Fe(NO_3)_3$. Results demonstrated while Fe^{3+} ions within the polymer layer are complexed by partitioned DFA^+ ligands, Fe^{2+} is not. This was suggested by the fact that, while the reduction peak of non-complexed Fe^{3+} to Fe^{2+} , within HA-free Nafion[®] membranes is not observed, the oxidation peak of non-complexed Fe^{2+} is seen.

The absence of a reoxidation peak associated with a $Fe(II)\text{-}DFA^+$ complex (generated by the electroreduction of the $Fe(III)\text{-}DFA^+$ complex) is indicative of complex dissociation upon reduction according to the following reaction:



This in turn is strong evidence for the valence selectivity of DFA^+ toward Fe^{3+} as opposed to Fe^{2+} ions and raises the possibility of electrochemically assisted expulsion of the analyte – in this case, the Fe^{3+} demonstrator ion. Repetitive potential cycling experiments show that complete expulsion is possible and that, upon exposure to a solution containing Fe^{3+} ions, the Fe(III)-DFA^+ complex reduction current signal is regenerated. These results indicate that: (i) electrochemical control of the environment within the polymer layer is possible and so, consequently, is protection of the HA ligand against analyte driven oxidation; and (ii) the sensor can be used repeatedly.

Further work will involve an examination of ligand leaching effects from the Nafion[®] membrane; an effect that was highlighted in **Chapter V**. Problems associated with crystal overload effects observed when using DFA^+ impregnated polymer layers need to be addressed, possibly by investigating the effect of membrane thickness on the crystal. The successful solution to this problem should be immediately followed by: (a) Calibration studies using the demonstrator ion; (b) a study of oxidation state specific sequestration, ligand protection and electrochemical expulsion of cations of depleted uranium; and (c) an assessment of the feasibility of the measurement of total Fe or U in a mixture of the two.

The Redox Mediator

The electrochemistry and microelectrogravimetric behaviour of methylene blue (MB) has been examined as part of a larger study into its suitability as a redox mediator in a Nafion[®] polymer modified EQCM-based sensor for actinide metal cations. The reduction of MB to

leucomethylene blue, LMB, occurs via an ECE mechanism where the chemical step corresponds to the protonation of the product of the $1 e^-$ reduction of MB.

Under conditions where the chemical step might be expected to be hindered, i.e. pH 7.9, EQCM experiments indicate that the reduction of MB to solid LMB occurs in two steps. In the first step, LMB is formed which subsequently undergoes a complexation reaction with its immediate electrochemical precursor to form a solid charge transfer complex, LMB/LMB^{**} which electrodeposits at the electrode surface. The formation of the charge transfer complex therefore corresponds to a net 1.5 electron transfer per molecule of MB reduced, a number confirmed by analysis of the voltamassograms.

The second step involves the reduction of the charge transfer complex to solid phase LMB at the electrode surface. The electrode kinetics of the latter step are found to be highly irreversible, a result consistent with the fact that a solid phase change occurs when the conducting charge transfer complex is reduced to the insulating leuco form.

The EQCM experiments indicate that the relative amounts of reductively generated charge transfer complex and leuco form are produced during the negative going, forward scan and highly dependent upon the timescale of the experiment – essentially, the longer the applied potential the higher the proportion of LMB generated. Importantly, the onset of charge transfer complex reduction to LMB can be directly observed as an inflection in the voltamassogram. We believe that this is the first time that this has been reported.

The reversibility of the MB to LMB reduction within the context of charge transfer complex electrogeneration is highly encouraging evidence that MB may be a suitable mediator for actinide cation reduction within the polymer layer of the proposed sensor. It is well known that the pendent amino-groups of LMB are protonated below pH 1, so rendering the resultant LMBH_2^{2+} soluble in aqueous solution. This means (a) difficulties associated with the irreversible reoxidation of the solid phase LMB generated at pH 7.9 will be obviated; and (b) being a large cation, we could expect LMBH_2^{2+} to be retained within the Nafion[®] layer. Further work will therefore involve an EQCM study of the reduction of MB at $\text{pH} \leq 1$ at bare gold piezoelectrodes and at Nafion[®]-coated electrodes. Ultimately, the feasibility of accomplishing MB-mediated reduction of actinide metal cations such as UO_2^{2+} will also be investigated.

Final Comments

This study has shown that a chemically modified EQCM sensor has the potential to provide quantitative data for use with an industrial environment. Furthermore, the investigations that have been conducted using microelectrodes combined with extensive use of the EQCM have allowed for detailed investigation into Au / nitric system, AHA kinetics & thermodynamics, electrochemical interrogation of the $\text{Fe}^{2+/3+}$ Nafion[®] DFA composite and finally the potential of MB as a redox mediator.

APPENDICES

CONTENT

<u>A.1 - KINETIC PARAMETERS FROM STEADY-STATE VOLTAMMOGRAMS AT MICRODISC ELECTRODES</u>	<i>Page 286</i>
<u>A.2 - REFERENCES</u>	<i>Page 294</i>

A.1 - KINETIC PARAMETERS FROM STEADY-STATE VOLTAMMOGRAMS AT
MICRODISC ELECTRODES

At low scan rates, the voltammograms on microelectrodes are sigmoidal in shape because diffusion to the electrode is predominantly at steady state. This occurs because a significant fraction of the current is passed at the edges of the electrode [A.1-A.3]. The relationship for the limiting current (I_d) given by *Equation A.1 & 2*, has been derived previously for the current under mass-transport controlled, steady-state conditions at a microdisc electrode [A.1 & A.4].

$$I_d = 4nrFD_0C \quad (\text{A.1})$$

At low scan rates, the current-potential curve at a microelectrode for a reversible system and soluble reactants/products without pH effect should follow the *Equation A.2* [A.4]

$$E = E_{1/2} + \frac{RT}{nF} \ln\left(\frac{I_d - I}{I}\right) \quad (\text{A.2})$$

where E is the applied potential. $E_{1/2}$ is the half-wave potential, given by

$$E_{1/2} = E^0 - \frac{RT}{nF} \ln \gamma \quad \gamma = m_o/m_R \quad (\text{A.3})$$

where m_o and m_R are the mass transfer coefficients for the oxidised and reduced species respectively, which corresponds to D_o/δ_o and D_R/δ_R respectively, where δ_o and δ_R are the thickness of the hypothetical diffusion layer of oxidised and reduced species. Because the diffusion coefficient (D_R) of the product of the electrode reaction rarely differs significantly from that of the reactant, the half wave and standard formal potentials (E^0) are identical for a reversible electrode reaction. A useful way of quantifying the slope of a voltammetric wave was pioneered by Tomes [A.5] and involves measuring the difference between the one-quarter-wave potential and three-

quarter-wave potential. From *Equation A.2-4*, it can be shown that, for a reversible n -electron reduction wave, this potential difference is given by

$$|E_{3/4} - E_{1/4}| = \frac{RT}{nF} \left| \ln \left(\frac{1}{9} \right) \right| \quad (\text{A.4})$$

Oldham, *et al.* [A.6], classify electrode reactions according to seven cases, *Figure A.1*, showing how the reversible, quasi-reversible and irreversible kinetic regimes reflect $\log \kappa^0$. κ^0 is defined as the dimensionless parameter by *Equation A.5*.

$$\kappa^0 = \frac{k^0 r \pi}{4D_o} \quad (\text{A.5})$$

The kinetic parameters such as α (the charge transfer coefficient), k^0 (the standard rate constant), and thermodynamic parameter E^0 are measured by use of steady-state voltammograms recorded at a range of radii in microelectrodes and *Figures A.2-A.5*. Procedures to be adopted in each case are summarised as follows:

1) CASE 1 - Reversible / near-reversible reaction

Case I in *Figure A.1* shows a situation in which the accessible range of κ^0 includes portions of both the reversible and quasi-reversible regimes. The difference is that $n|E_{3/4} - E_{1/4}|$ will obey *Equation A.4* on the largest disc radii; under these circumstances, $E_{1/2} = E^0$. For the voltammograms recorded on the smaller discs, we may then calculate the coordinates $n(E_{1/4} - E_{3/4})$ and $n|E^0 - E_{1/2}|$ on a set of kinetic indicator diagrams derived by Oldham *et al* [A.6] and given in *Figures A.2 & A.3*. The location of this point on the kinetic indicator diagram permits the simultaneous estimation of α and $\log \kappa^0$. The standard rate constant may be determined by *Equation A.6*.

$$k^0 = \frac{4D_o \kappa^0}{\pi r} \quad (\text{A.6})$$

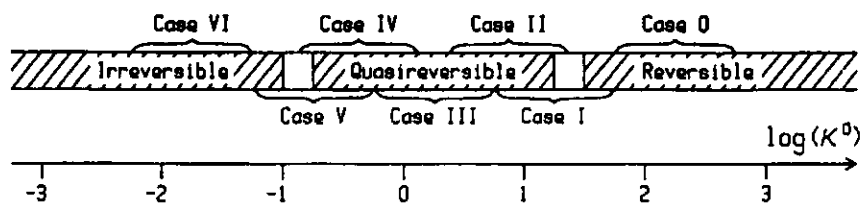


Figure A.1. The 'spectrum' of voltammograms for different reaction systems.

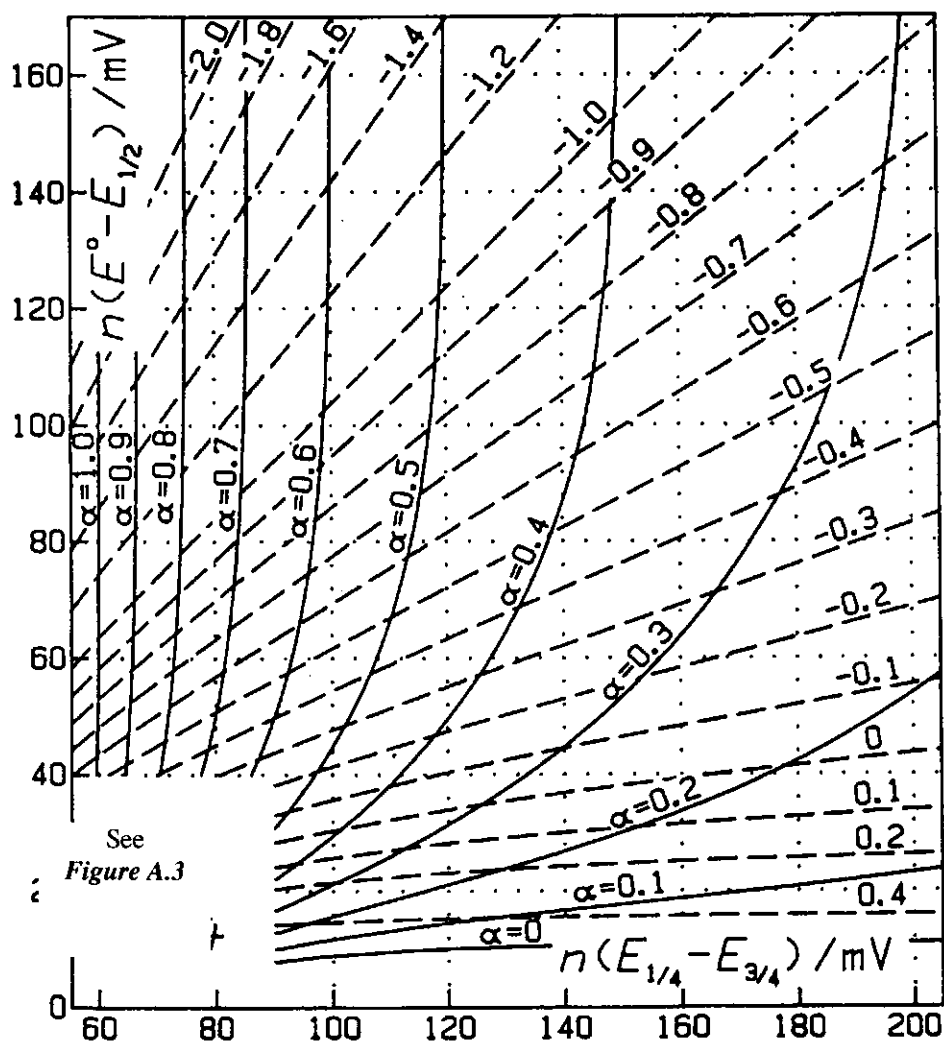


Figure A.2. A small-scale kinetic indicator diagram which shows the relationship between $n(E^0 - E_{1/2})$ and $n(E_{1/4} - E_{3/4})$ at constant α or $\log \kappa^0$ for steady-state voltammograms at microdisc electrodes.

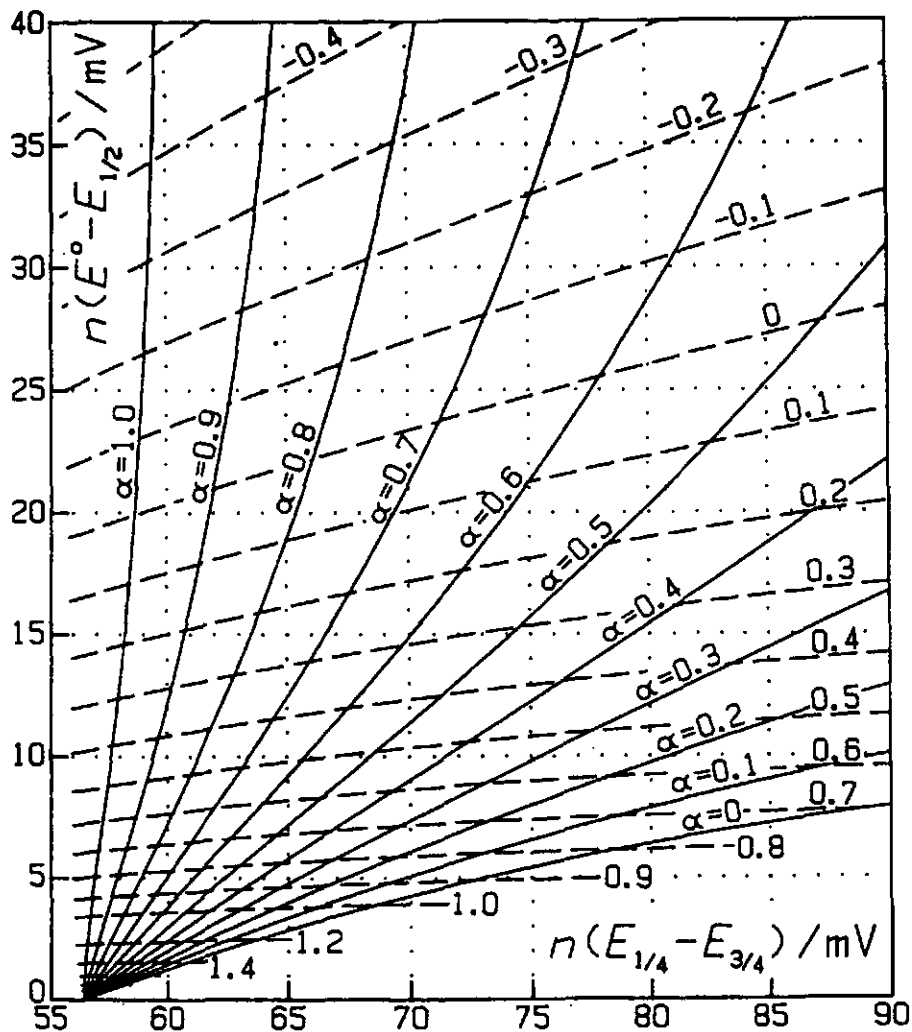


Figure A.3. The expanded inset of **Figure A.2.**

2) CASE II – Near-reversible / quasi-reversible reaction

This case in **Figure A.1** corresponds to a situation in which the accessible values of κ° do not enter the reversible region: $n|E_{1/4} - E_{3/4}|$ exceeds RT/F and approaches this value for the largest disc. A plot of $nE_{1/2}$ vs $1/r$ will yield a straight line of slope $-2RTD_0/Fk^\circ$ and intercept nE° , thus providing a convenient method for determining both k° and E° .

Alternatively, in the region of near-reversibility, there exists a linear relationship between $n|E_{1/2} - E^\circ|$ and $n|E_{1/4} - E_{3/4}|$ for discs of differing radii. For a plot $E_{1/2}$ versus

$n|E_{1/4} - E_{3/4}|$; the intercept, $|E_{1/4} - E_{3/4}| = |E^\circ + \frac{RT \ln(9)}{(3^{1-\alpha} - 3^{\alpha-1})nF}|$, is E° , while the slope, $1/(3\alpha - 1 - 3^{1-\alpha})$ of the line can be used to provide a value of α .

Another alternative method of determining α is obtained from the kinetic indicator diagrams given by *Figures A.2 & A.3*. Knowing E° and k° (and hence κ°) from a graph of $nE_{1/2}$ vs. $1/r$, a series of points along one of the α contours can be easily located.

3) CASE III – Quasi-reversible reaction

The values of κ° will lie in the quasi-reversible region for case III shown in *Figure A.1*. This situation will be reflected in the $n|E_{1/4} - E_{3/4}|$ potential separations, which will not approach a limit at either the smallest or the largest disks studied. $nE_{1/2}/d \log(r)$ must be determined, which permits values of α and $\log \kappa^\circ$ (and hence k° via *Equation A.6*) to be determined simultaneously using *Figures A.4 & A.5*. Values of α and $\log \kappa^\circ$ in addition to $n|E_{1/4} - E_{3/4}|$ provide the necessary information for locating a point for each voltammogram on *Figures A.2 & A.3*, which relate $n|E^\circ - E_{1/2}|$ and $n|E_{1/4} - E_{3/4}|$. From a particular value of $n|E^\circ - E_{1/2}|$ for each voltammogram, a unique E° value may be found.

4) CASE IV - Near-irreversible reaction

Case IV in *Figure A.1* corresponds to a situation in which the accessible values of κ° do not enter the irreversible regime, but lie close to it. The $n|E_{1/4} - E_{3/4}|$ separations, which will increase with decreasing disk size and approach a limit (the $2.342RT/\alpha F$ irreversible limit) with the smallest disks. If L is given by

$$L = 0.3564 \exp\left\{\frac{n(E_{1/4} - E_r)}{25.7 \text{ mV}}\right\} - 3.472 \exp\left\{\frac{n(E_{3/4} - E_r)}{25.7 \text{ mV}}\right\} \quad (\text{A.7})$$

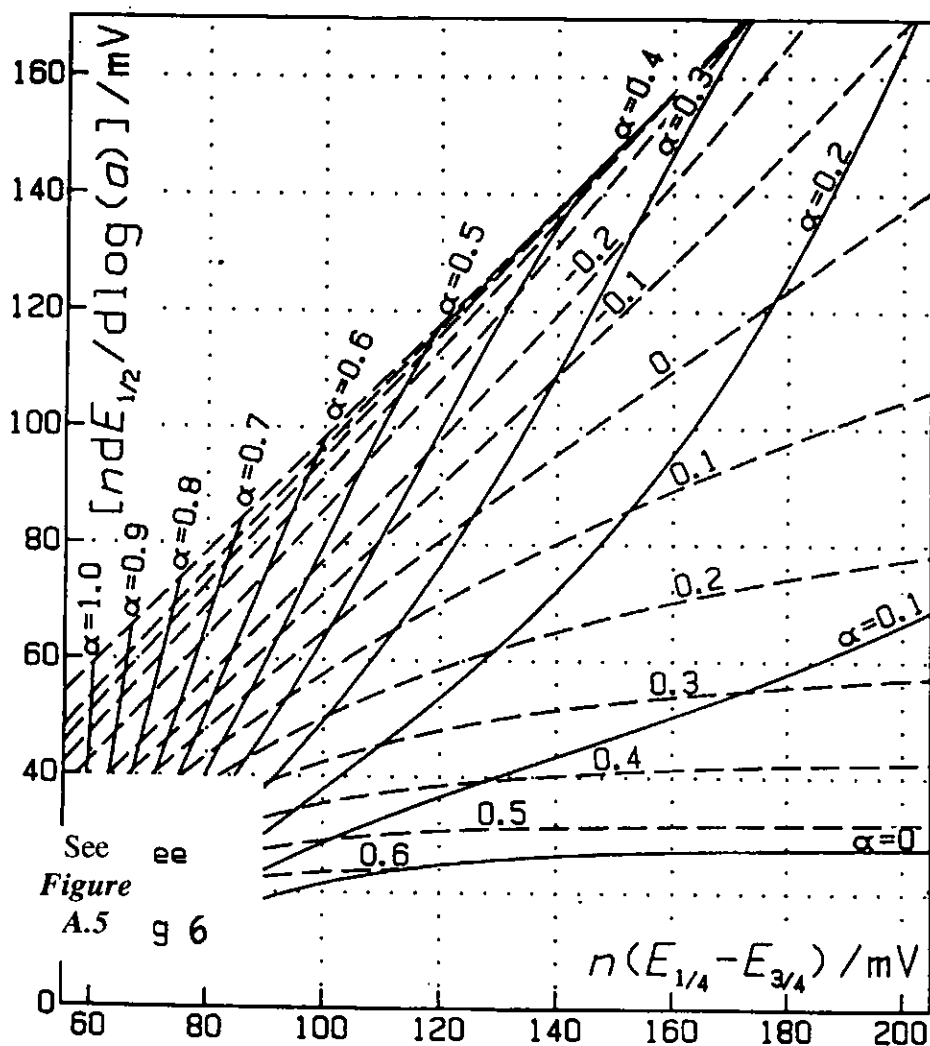


Figure A.4. A small-scale kinetic indicator diagram which portrays the relationship between $ndE_{1/2}/d\log(r)$ and $n(E_{1/4}-E_{3/4})$ at constant α or $\log \kappa^{\circ}$ for steady-state voltammograms at microdisc electrodes. The unlabelled $\log \kappa^{\circ}$ lines correspond to $-0.4, -0.6, -0.8, -1.0$ and $-\infty$.

Here E_T is any constant reference potential in the vicinity of the voltammetric waves; it could, for example, be the half-wave potential of one of the voltammograms. Then, in this instance, a plot of L versus $n|E_{1/4}-E_{3/4}|$ will be approximately linear and may be extrapolated to intersect the $n|E_{1/4}-E_{3/4}|$ axis at $2.342RT/\alpha F$. This intercept permits a determination of α , while the standard potential is then calculable from the slope by Equation A.8.

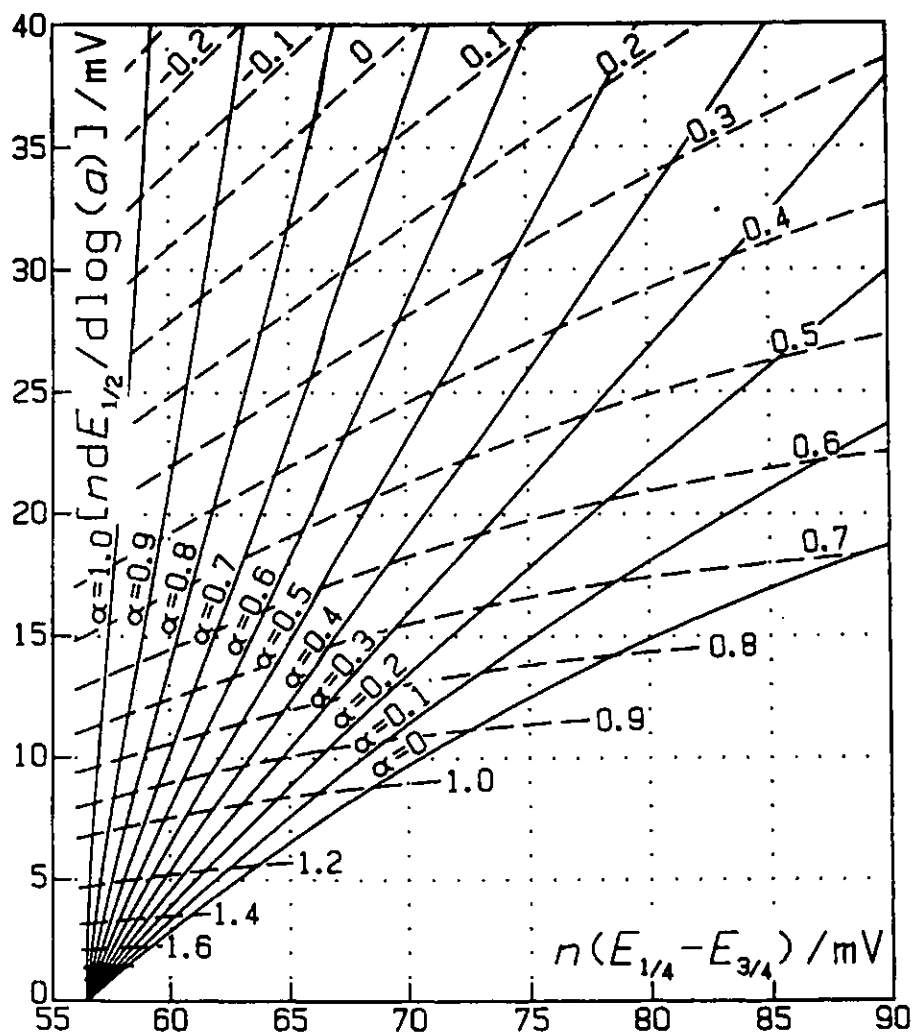


Figure A.5. The expanded inset of Figure A.4.

$$nE^{\circ} = nE_r + (25.7\text{mV})\ln\left\{-\frac{(25.7\text{mV})(\text{slope})}{\alpha}\right\} \quad (\text{A.8})$$

For the voltammogram from each disk, the coordinates $n|E^{\circ} - E_{1/2}|$ and $n|E_{1/4} - E_{3/4}|$ of a point on kinetic indicator diagram *Figure A.2* can be calculated according to α and E° . $\log \kappa^{\circ}$ is obtained from *Figures A.2 & A.3* and hence k° from *Equation A.6*.

5) CASE V – Near-irreversible/irreversible

In this case, the range of κ° values includes portions of both the quasi-reversible and irreversible kinetic regimes. This case can be identified from the fact that the smallest disks will have identical $n|E_{1/4} - E_{3/4}|$ separation, whereas larger disks will generate

voltammograms whose one-quarter and three-quarter potentials are less separated. For the smallest disks, the $n|E_{1/4} - E_{3/4}|$ separation will be obey *Equation A.9*,

$$n | E_{1/4} - E_{3/4} | = | \frac{2.342RT}{\alpha F} | \quad (\text{A.9})$$

allowing α to be calculated. We can then locate the appropriate α contour on *Figures A.2 & A.3*, and insert points corresponding to the larger disks at the intersections of this contour with the measured $n|E_{1/4} - E_{3/4}|$ abscissae. From each such point, values of $n|E^\circ - E_{1/2}|$ and $\log \kappa^\circ$ can be read off. E° is calculable using the measured $E_{1/2}$, while k° may be found via *Equation A.6*.

If $E_{1/2}$ shifts negatively for a reduction reaction, positively for an oxidation reaction with decreasing electrode size, but $|E_{1/4} - E_{3/4}|$ is uniformly constant, α can be calculated by *Equation A.9*. The parameters E° and k° are separately inaccessible, but a composite parameter is obtained by *Equation A.10*

$$nE^\circ + \frac{RT}{\alpha nF} \ln k^\circ = nE_{1/2} + \frac{RT}{\alpha nF} \left\{ 0.3118 + \ln \frac{D}{r} \right\} \quad (\text{A.9})$$

A.2 - REFERENCES

- A.1. Y. Saito. *Rev. Polarogr.* **15**, (1968), 178
- A.2. K. Aoki and J. Osteryoung. *J. Electroanal. Chem.* **122**, (1981), 19
- A.3. A. Shoup and A. Szabo. *J. Electroanal. Chem.* **140**, (1982), 237
- A.4. A. M. Bond, K. B. Oldham and C. G. Zoski. *J. Electroanal. Chem.* **245**, (1988), 71
- A.5. J. Tomes. *Collect. Czech. Chem. Commun.* **9**, (1937), 150
- A.6. K. B. Oldham and J. C. Myland. *J. Electroanal. Chem.* **270**, (1989), 79